Micro and nanoactuators based on bistable molecular materials

Maria Dolores Manrique-Juarez

Université Fédérale
Toulouse Midi-Pyrénées

THÈSE

En vue de l'obtention du

DOCTORAT DE L'UNIVERSITÉ DE TOULOUSE

Délivré par :

Université Toulouse 3 Paul Sabatier (UT3 Paul Sabatier)

Présentée et soutenue par :
MARIA DOLORES MANRIQUE JUAREZ
le 28/11/2017

Titre :

Micro and nanoactuators based on bistable molecular materials

---

École doctorale et discipline ou spécialité :
ED SDM : Sciences et génie des matériaux - CO034

Unité de recherche :
Laboratoire de Chimie de Coordination (UPR 8241)

Directeur/trice(s) de Thèse :

Gabor Molnar and Azzedine Bousseksou

Jury :

M. Nicolas GIUSEPPONE, Président du Jury
Mme Birgit WEBER, Rapporteur
M. Pance NAUMOV, Rapporteur
M. Eric DANTRAS, Examinateur
M. Liviu NICU, Membre Invité

A los ángeles de tu luz

Acknowledgments

This work has been achieved thanks to the collaboration of many people and different institutions that I will mention as follows:

The Switchable Molecular Materials team, the Laboratory of Coordination Chemistry (LCC), the MEMS team, the Laboratory of Analysis and Architecture of Systems (LAAS) and the Mexican National Council for Sciences and Technology (CONACYT) for hosting me and funding this thesis.

I am deeply grateful with all the members of the jury: Prof. Nicolas Giuseppone (*President*) from the University of Strasbourg, Prof. Birgit Weber (*referee*) from the University of Bayreuth, Prof. Pance Naumov (*referee*) from the New York University of Abu Dhabi, Dr. Eric Dantras (*inspector*) from the University of Toulouse, Dr. Liviu Nicu (*invited member*) from the Laboratory of Analysis and Architecture of Systems of Toulouse, Dr. Gabor Molnar (*supervisor*) and Dr. Azzedine Bousseksou (*co-supervisor*), from the Laboratory of Coordination Chemistry of Toulouse, for agreeing to read the manuscript and to participate in the defense process of this thesis.

I would like to thank my supervisors from LCC, Azzedine Bousseksou and Gabor Molnar for giving me the opportunity to join their research team and putting in my hands this fascinating project. They shared with me their expertise and scientific knowledge through discussions and ideas to enrich this work all along my thesis. I appreciate the fact they always pushed me beyond my limits. I am grateful for their guidance, support and capacity to put in value all the results obtained during this work.

I warmly thank Liviu Nicu, director of LAAS and member of the MEMS team, who three years ago gave me the first brick from which everything was triggered. Along with him I would like to thank Thierry Leichle, also member of the MEMS team. Together they put in place the several human and technological resources I needed. They followed very close this project with enthusiasm, always giving time for discussions and feedback. It was an honor for me to share with them not only their scientific knowledge, but also their extraordinary human qualities which helped me a lot to lead this project with confidence.

I would like to thank the members of the I2C team in LAAS. In special manner I want to thank the engineer Fabrice Mathieu in charge of the MEMS transduction and improvements in the characterization set-up. His enthusiasm, curiosity and expertise made him an essential part of this thesis and the first witness of the results harvested from it. I thanks his implication and the fact he never gave up each time we faced a new challenge. Fabrice became one of the best colleagues and friends I keep from this thesis.

I thank the Chemists from LCC, Sylvain Rat, Lea Godard and Lionel Salmon, who provided me with the spin crossover materials. Besides providing the material, I would like to thank Sylvain for his dynamism and interest to each result emerging from this project, Lionel Salmon for the interesting discussions about these materials which helped me to understand and evaluate better their properties. I also thanks Iurii Suleimanov for the discussions and preliminary tests we did together, Lea who did an excellent work for the last part of this project. I also want to thank Victoria Shalavaeba and Isabelle Seguy (LAAS) for their implication with the thermal vapor depositions of these compounds.

I want to thank all the members from the clean room in LAAS, especially to my responsible Laurent Mazenq for all his guidance on the microfabrication process and SCO integration ideas. Benjamin Reig for all the assistance with the characterization equipment and Adrian Laborde for his help with the spray coating depositions. I also thank Jean Cacheux and Daisuke Saya for providing some of the devices I used during my thesis.

I would also thank to the technical and administrative staff from LCC and LAAS who made my stay very pleasing.

If I enjoyed these three years of thesis it was in big part due to the atmosphere in both laboratories, for this reason I want to thank all my colleagues and friends from both research teams Equipe P (Mirko, Sylvain, Edna, Costel, Elias, Lucy, William, Victoria, Alin, Iurii, Olena, Lea, Karl, Mario, Haonan, Jose, Jackie, Carlos) and LAAS (Cécile, Douglas, Pierre, Denis, Adhythia, Christian, Sabrina, Bernard, Ali, Arushee, Mathieu, Angelo, Francisco, Vincent, Jean, Daisuke). In special way I want to thank my friends Sara and Kayum who made me feel closer to my home town and made me laugh all along these years.

I would like also thank my emotional support, my family. They gave me the courage and warmed me with their constant messages letting me know they were always there for me. I want to thank also Babeth and Olivier who made me feel part of their family since the first time I met them.

Finally I want to thank my life advisor, my dear Mirko Mikolasek who has been there supporting me with love, kindness and patience (24/7). He shared with me this journey behind the scenes. I appreciate our long conversations and his understanding not only emotional but also scientific which inspired me in many senses.

Micro and nanoactuators based on bistable molecular materials

Table of contents

List of Tables

List of Figures

Acronyms

AFM	Atomic force microscopy
SEM	Scanning electron microscopy
TEM	Transmision electron microscopy
MEMS	Micro electromechanical systems
NEMS	Nano electromechanical systems
DMA	Dynamical Mechanical Analysis
SOI	Silicon on Insulator
NIS	Nuclear Inelastic Scattering
VNA	Vectorial Network Analyzer
SCO_PNC	Spin Crossover Polymeric Nanocomposite
SCO_PC	Spin Crossover Composite
PEB	Post-exposure baking
FIB	Focused Ion Beam
XRR	X-Ray Reflection
XRD	X-Ray Difraction
GIXRD	Grazing incidence X-Ray diffraction
RIE	Reactive ion etching
MEMS-PNC	MEMS/SCO_PNC bilayer system
Polymer-PNC	Polyester/SCO_PNC bilayer system
SPR	Surface plasmon resonance
LIESST	Light-Induced Excited Spin-State Trapping

General Introduction

The possibility of harnessing useful work from bistable molecular switches led to the development of hundreds of compounds with a remarkable degree of sophistication. These 'molecular actuators' display distinct molecular geometries, which can be reversibly interconverted in response to some form of chemical or physical stimuli. They include various structural switches (e.g. stereoisomers, linkage isomers, etc.) as well as coupled electronic/structural switches (e.g. valence tautomers, Jahn Teller switches, etc.) [**Feringa and Browne, 2011**]. The most sophisticated ones (e.g. rotaxanes, catenanes, etc.) are often termed as 'molecular machines' or 'molecular muscles' for their large amplitude of motion [**Balzani et al., 2003, Sauvage and Amendola, 2001**]. Beyond purely mechanical applications, these compounds represent a particularly attractive scope for developments of chemomechanical, biomimetic and other complex systems [**Abendrot et al., 2015**]. Their potential application is not restricted to the molecular scale, but includes also mesoscopic and truly macroscopic systems. Obviously, in each case, the molecules must be properly interfaced with their environment in order to produce a useful work and also to allow for external control. This issue has been identified long ago as the main bottleneck for the development of useful devices using switchable molecules [**Coskun et al., 2012**]. Yet, the integration of 'molecular actuators' into functional systems has remained in its infancy and most of the reported examples, despite being scientifically frontier, concern rather simple devices and techniques from a technological point of view. Among the most remarkable ones one can cite (electro)chemically actuated rotaxane coated cantilevers [**Juluri et al., 2009**], photochromic molecule based polymer actuators [**Yu et al. 2003**], liquid crystalline materials doped with photoswitches [**Browne and Feringa et al., 2006**], clamped single crystals of photo responsive molecules [**Morimoto et al. 2010**], photo responsive organic nanostructures [**Al-Kayisi et al., 2006**], motion controlled jumping/twisting/bending molecular crystals [**Naumov et al., 2015]**, muscle-like supramolecular polymers [**Du et al., 2012**] and micro cantilevers functionalized with natural polymers [**Shu et al., 2005]**.

In this context, spin crossover (SCO) molecular actuators can provide not only good actuating performance, but they also offer various smart features (e.g. shape memory), a high degree of synthetic versatility and multifunctionality, such as the coupling of optical, electrical, magnetic and mechanical properties. Furthermore, it has been demonstrated that SCO complexes can display useful mechanical response even at the single molecule level [**Harzmann et al., 2015**]

and as such there is no fundamental restriction on their functionality at the nano-scale. As a macroscopic proof of concept, the Switchable Molecular Materials team (LCC-CNRS) recently studied a bilayer cantilever architecture in which a single crystal of the SCO complex {Fe(3-CNpy)[$Au(CN)_2]_2$}·$2/3H_2O$ (py = pyridine) was strongly bonded to a passive metallic coating [**Shepherd et al., 2013**]. The differential expansion of the two strata at the spin transition led to dramatically amplified motion at the macroscopic scale. Indeed, the experimentally observed volumetric work density (~1 Jcm^{-3}) is several orders of magnitude greater than that expected from thermal expansion alone. The versatility of this approach was also demonstrated by using different SCO materials embedded in various polymer matrices [**Guralskiy et al., 2014**].

This thesis has been developed with the aim to demonstrate the coupling of SCO molecular switches with microelectromechanical systems (MEMS). Since their implementation in the 70's, MEMS based on silicon technologies have shown a remarkable development, primarily for sensor and actuator technologies leading to commercial successes. Nevertheless, MEMS are still very attractive for the scientific community due to their broad application field and also for the possibility of further miniaturization to obtain more sensitive nanoscale devices (NEMS). The development of NEMS, however, requires significant challenges to be solved, including the integration of smart actuating materials into nanoscale systems [**Leondes 2006**]. Traditional materials used in the fabrication of MEMS are typically limited to silicon, ceramics, metals and polymers. However, the challenges associated with size reduction of these technologies means that while materials and processes for the construction of MEMS are well established, there exist only a few, if any, high-performance materials available for NEMS operation. As the demand for smaller systems with ever more complex functionality grows, novel materials with diverse properties, capable of operation at small scales will need to be developed. Creating these materials is only the first step, understanding and predicting their behavior is crucial to optimization of function and requires an intimate knowledge of structure–property relationships. Furthermore, the successful integration of novel materials into useful devices requires appropriate fabrication protocols tailored to the production and operation of such unconventional systems. Thus an interdisciplinary approach to this problem that brings together aspects of chemistry, physics and nano-technological engineering is required.

During this thesis work we thus developed original materials, MEMS fabrication and characterization protocols with the aim to (i) demonstrate the possibility of efficient integration of SCO molecular actuators into sophisticated microsystems and (ii) extract information on the mechanical properties and actuation performance of these materials.

Chapter 1 provides an overview of advances and presents the prospects for integrating switchable molecular materials as active elements into actuator devices, with particular emphasis on micro- and nanoscale mechanical systems.

Chapter 2 introduces the SCO phenomenon and discusses the different stimuli to trigger it. The conventional characterization techniques to detect and measure the SCO are also exposed. Since the strain and mechanical properties are the outstanding parameters regarding actuating performance, this chapter places a particular emphasis on the structural aspects of the SCO, from the molecular to the macroscopic scale and their repercussion on the volume change.

Chapter 3 gives a brief introduction about the basic principles of MEMS devices. Concepts regarding actuation, detection and miniaturization are discussed. The possible strategies for integration of SCO actuators into MEMS are also discussed.

Chapter 4 describes the first achievement of this thesis to integrate spin crossover molecules as nanometric thin films into silicon MEMS devices. For this, a high quality thin layer of [$Fe^{II}(H_2B(pz)_2)_2(phen)$] (pz = pyrazol-1-yl and phen = 1,10-phenantroline) was deposited by thermal evaporation onto freestanding silicon bridges and cantilevers. From the mechanical response of the bilayer system it was possible to extract the relevant mechanical properties of the SCO material. Additionally, we also demonstrated the light-induced excited spin-state trapping (LIEEST) phenomenon by tracking the MEMS resonance frequency.

As a substantial step towards technological applications, we describe in Chapter 5 a MEMS device in which the SCO molecules are not only used to tune the device mechanical properties, but also perform controlled and reversible macroscopic work under ambient conditions. To this aim we developed and characterized high-quality films of [$Fe^{II}(HB(tz)_3)_2$] (tz = 1,2,4-triazol-1-yl) which were deposited by thermal evaporation onto MEMS devices.

Even though the thermal evaporation technique to integrate SCO materials into MEMS is highly efficient, it is limited to a few compounds which can be readily sublimated. Hence in Chapter 6 a more versatile alternative technique is described. Nanoparticles of the SCO complex [$Fe^{II}(Htrz)_2(trz)](BF_4)$ (Htrz = 1H-1,2,4-triazole, trz = 1,2,4-triazolato) were deposited on the MEMS devices in the form of polymer nanocomposite material by spray coating. Using this approach SCO actuators were efficiently integrated not only in micro-systems, but also into macroscopic soft actuators (*sic* artificial muscles).

Chapter 1. Molecular actuators

Molecular switches rely on various physico-chemical phenomena, and in most cases the switching event is accompanied by a significant rearrangement of atomic positions. At the macroscopic level the long range order of switching molecules usually results in a collective, or even cooperative volume change, which can be readily exploited for actuating purposes. These molecular (or molecule-based) systems can provide multiple advantages for this type of application due, primarily, to their intrinsic chemical and functional versatility and the small size of their functional units. This chapter provides an overview of advances and presents the prospects for integrating switchable molecular materials as active elements into actuator devices, with particular emphasis on micro- and nanoscale mechanical systems.

1.1 What is an actuator?

By definition an actuator is a device that converts a source of energy into motion. From the muscle which converts chemical energy in the form of food into bodily motion, to the motors that power the machines we rely on, actuators are a fundamental part of everyday life. Actuators are indeed created and applied in many different fields of science and technology, including – for example – automotive [**Eddy et al., 1998**], aerospace [**Loewy R. G., 1997**] and robotic [**Sreenivasa et al., 2012**] applications, but an important driving force of the current developments comes from the recent progress of micro- and nano-electro-mechanical systems (MEMS/NEMS). MEMS technology involves structures and devices that perform mechanical tasks at microscopic scales. Components with moving parts are integrated with microelectronics to produce electromechanical systems.

Since the early conceptual ideas of silicon-based MEMS technology proposed by Petersen in 1982 [**Petersen, 1982**], there has been a remarkable development of the materials employed in this field: soft technologies based on passive polymers and the use of active materials. Piezoelectrics are an example of an active material used in MEMS technology for highly accurate positioning and sensing tasks in a wide variety of applications from printing and data communications to biological and pressure sensors [**Pons, 2005**]. Traditional materials used in the fabrication of MEMS are typically limited to silicon, ceramics, metals and polymers. However, the challenges associated with size reduction of these technologies means that while

materials and processes for the construction of MEMS are well established, there exist only a few, if any, high-performance materials available for NEMS operation. Any new material would have to satisfy a number of disparate requirements in terms of force, displacement, work density, operation speed, repeatability and the ability to be integrated into devices; no single material is currently able to offer these attributes simultaneously at the nanoscale. As the demand for smaller systems with even more complex functionality grows, novel materials with diverse properties, capable of operation at small scales will need to be developed. Creating these materials is only the first step, understanding and predicting their behavior is crucial to optimization of function and requires an intimate knowledge of structure–property relationships. Furthermore, the successful integration of novel materials into useful devices requires appropriate fabrication protocols tailored to the production and operation of such unconventional systems. Thus an interdisciplinary approach to this problem that brings together aspects of chemistry, physics and nano-technological engineering is required. In this context molecular switches, including photochromic, spin-crossover and many other bistable molecular or molecule-based systems, may provide interesting prospects as their properties can be finely tuned chemically and they are sensitive to a wide range of stimuli, including light, temperature, pressure, magnetic and electric fields. In most cases the molecular switching event is associated with the change of various material properties(optical, electrical, magnetic) beyond the mechanical strain, which can allow the development of smart systems combining sensor and actuator functions, even within the same material. In addition, by virtue of their molecular nature, there is no fundamental restriction on their functionality at the nanoscale. Indeed, recent work in this field has led to several encouraging prototype actuating devices, even if – to the best of our knowledge – none has yet been commercially exploited. This chapter assesses these results with the aim of clarifying the real prospects, identifying the main challenges and providing a useful guide for future work.

As a starting point the most significant smart actuating materials currently being investigated and their associated technologies are briefly described. Then, switchable molecular materials with actuating functionality are reviewed. At this point it is necessary to clarify a few definitions. Throughout the literature there is some confusion between the concepts of molecular switches and molecular machines. One might consider the requirements of the former as having at least two stable molecular states between which one may switch reversibly and in a controlled manner. In the case of the latter, we may consider an additional requirement for these molecules to perform useful work on their surroundings. With a few notable exceptions, molecular

switches have rarely been converted into molecular machines capable of doing useful work. Another important point we must mention at the beginning is that the exciting and also very challenging field of single molecule machines is not covered by the present work. Here we focus on materials based on molecular switches.

1.2. Conventional actuating materials

A large variety of actuator technologies exist, and they can be classified in several different ways (**Figure 1**). For example they could be classified by their application or function (medical devices, diagnostics, switches, microrobotics, artificial muscles, etc.), by their material nature (polymers, carbon nano-materials, alloys, composites, crystalline inorganic materials, etc.) or energy sources (thermo-mechanical, magneto-mechanical, electro-mechanical, fluid-mechanical, biochemical actuation, etc.). For the purpose of this thesis the classification will be made according to the actuation mechanism – by focusing on the technologically most important families.

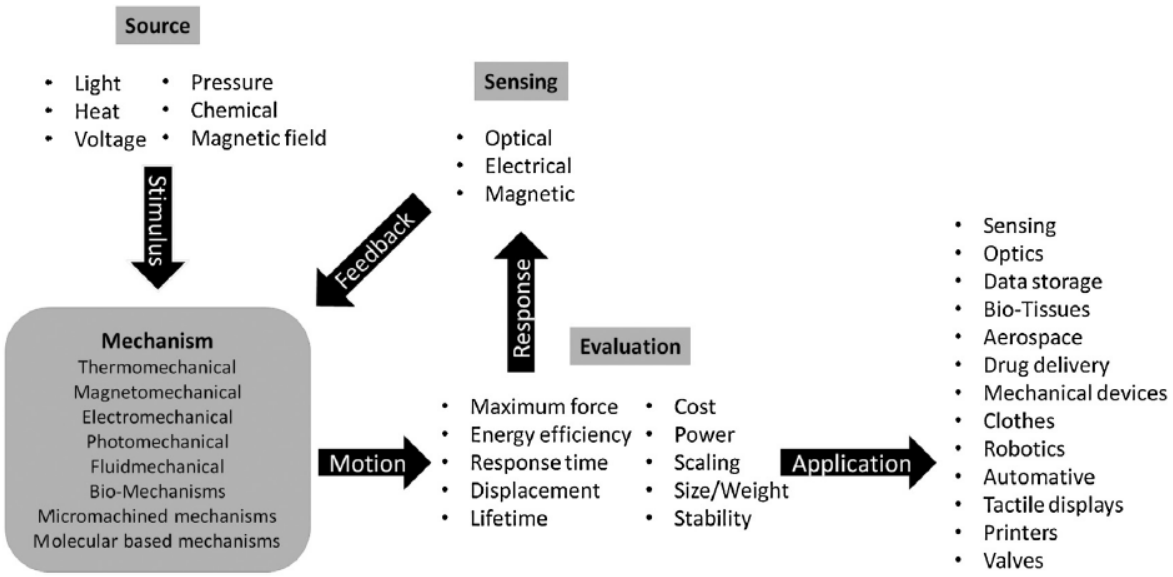

Figure 1: *Schematic principles of smart actuators.*

It is important to note here that traditional actuating technologies (electromagnetic motors, pneumatic and hydraulic systems) are not based on a specific material property, but rely usually

on a geometric concept (e.g. electrostatic comb actuators or a hydraulic piston-cylinder system), while more recent technologies (piezoelectric ceramics, shape memory alloys or thermal expansion actuators) are constructed starting from a material attribute. These latter are often defined as smart materials, which signifies that they possess in-built sensing and actuating capabilities.

Table 1: *Different actuating mechanisms for conventional smart materials.*

Actuation Mechanism	Driving power	Materials	Principle	Applications	Related literature
Shape Memory alloys	Thermal	Alloys: Nitinol (Ni50-Ti50), Cu-Zn-Al and Cu-Al-Ni.	Reversible Phase transition	Sensing, robotics, positioning systems, microvalves , micropumps, etc.	Pons 2005, Nespoli 2010, Huang 2002, Van Humbeeck 1999, Ikuta 1988.
Thermo-responsive polymers	Thermal	Poly(N-isopropyl acrylamide) (PNIPAM), liquid crystals	Conformational rearrangements (Shrinking and swelling), phase transition.	Bio-medical, artificial muscles.	Ionov 2010, Yang 2009, De Gennes 1969.
Magnetostrictive	Magnetic field	Alloys: Ni based, Fe-Al, ferrite and amorphous Fe-Si-B, Tb-Dy, Tb-Dy-Fe , $SmFe_2$, $ErFe_2$.	Alignment of magnetic domains Vs mechanical stress.	Electrohydraulic servo valves, strain sensing, and vibration control, etc.	Pons 2005, Angelos 2014, Tianli 2004.
Piezoelectric	Electric Field	Ceramics: zirconate titanate (PZT). Polymers: PVDF (polyvinylidene fluoride), polyamides, parylene-C and liquid crystal polymers	Crystal lattice or polymer deformation as consequence of the applied electric field. An applied pressure also generates the inverse phenomenon.	Ink jet printers, hard disk drivers, positioning systems in microscopes and vibration suppressors.	Ramadan 2014, Uchino 1986, Kyser 1980, Dosch 1992. Hunter 1992.
Electrostricitive	Electric field	Ceramics: lead magnesium niobate (PMN). Polymers	Ion displacements generate lattice deformation	Ceramics:deformable mirrors, printers, ultrasonic motors, optics and ultraprecision machining. Polymers:artificial muscles and acoustic actuator applications.	Damjanovic 1992, Hom 1996, Uchino 1986, Kornbluh 1998, Heydt 1998.
Thermal expansion	Thermal	Polymers, metals or ceramics	Increasing inter-atomic distances and atomic vibrations. Used in bimorph systems.	In inkjet printing heads and temperature sensing.	Miller 2009, Pons 2005, Comtois 1997, Jarrold 2003.
Biochemical	Chemical	Organic materials, natural and synthetic polymers.	Redox, charge grouping on polymer chains	Bio-devices, microgrippers, microcages.	Ionov 2010, Randhawa 2011, Bashir 2004, Kumar 2009.

Table 1 summarizes the main actuating mechanisms for conventional smart materials, and **Figure 2** position them according to their mechanical properties, work density and bandwidth.

1.3. Evaluate actuating performance

Whichever actuation mechanisms and materials are used, they must fulfill a large number of disparate specifications. Some of the most important to be considered are power (or work) density, energetic efficiency, response time (or frequency bandwidth), maximum achievable force and displacement, size/weight, linearity, scaling properties, stability (including environmental effects), cost, ease of processing and integration with current fabrication technologies, etc. Obviously the relative importance of these requirements will depend on the targeted application. Nevertheless, following the proposition of Liu et al. [**Liu et al., 2012**], a very useful classification is possible if one plots the Young's modulus of the material versus the maximum achievable linear strain (**Figure 2a**).

Strain (ε) is a very important property because it indicates the amplitude of actuation of a given material. On the other hand, the Young's modulus (E) determines the magnitude of the applied force. These two outputs are linked together through the volumetric work density (W/V), i.e. the maximum mechanical work output per unit volume of the active material, by **Equation 1**.

$$\frac{W}{V} = \frac{E\varepsilon^2}{2} \qquad (1)$$

For example, large forces with small displacements are achieved using piezo-electric materials, while large displacements capable of moving small loads would be expected from electrostrictive polymers. For many applications in the MEMS/NEMS context it is desirable to achieve high work densities due to the space (and mass) limitations. This requirement is currently fulfilled only by shape memory alloys, but their further development is hampered by the degradation of their properties at sub-micrometric sizes [**Liu et al., 2012**, **Krilevitch et al., 1996**]. Beside stiffness and strain, the speed of response (or frequency bandwidth) is also an important attribute in the MEMS/NEMS technology. This property is more elusive in that in many cases it is limited by the actual device structure and size besides the material used, but as

a general guide the typical bandwidth of different active materials is shown in **Figure 2b**. A range of frequencies from a few Hz to a few Mhz can be attained using these actuating technologies.

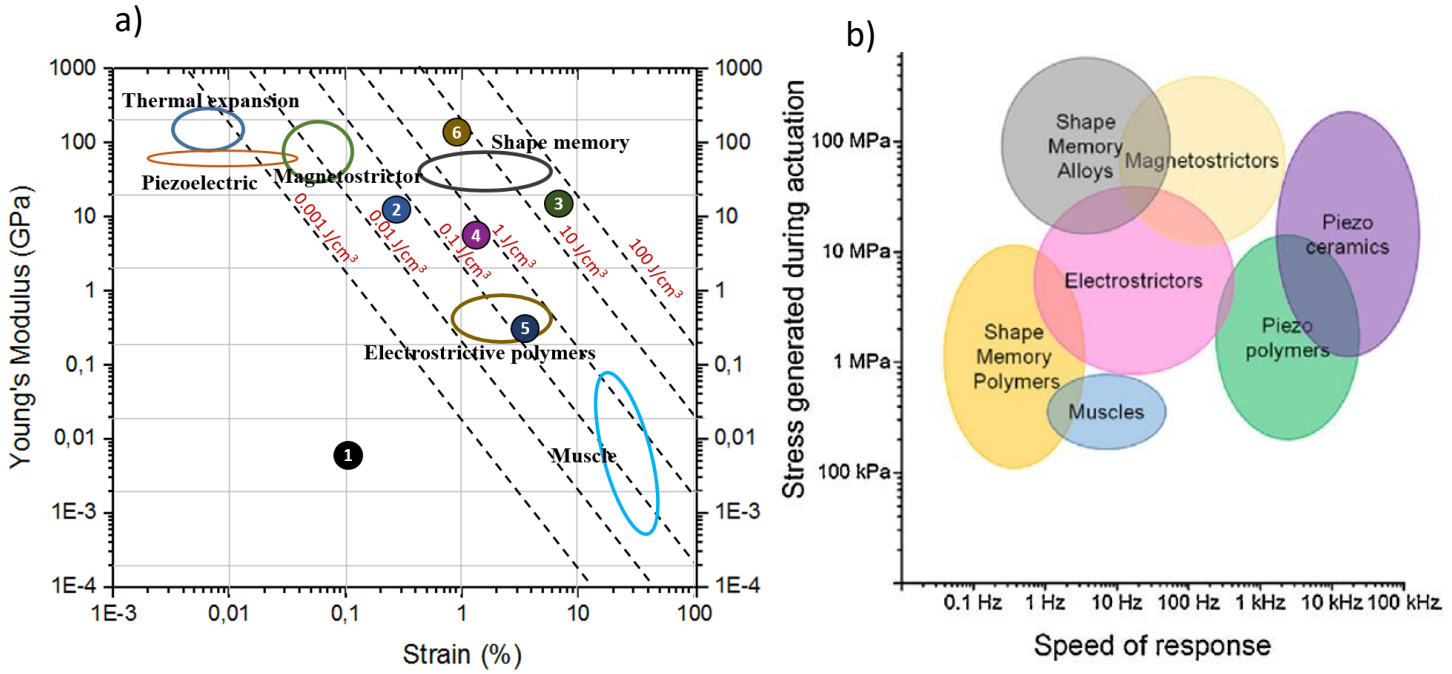

Figure 2: *Actuation performance: a) Young's Modulus versus linear strain, plot for the selected actuation materials families [Adapted from* ***Liu et al., 2012****]. The contours of equal volumetric work density are also shown by dashed lines. Encircled numbers represent compound. 1-Ruthenium sulfoxide-polymer composite [****Jin et al., 2011****], 2-diarylethene single crystal [****Morimoto Et al., 2010****], 3-Fe(pyrazine)[Pt(CN)$_4$] single crystal [****Felix et al., 2015****, ****Cobo et al., 2008****], 4- {Fe(3-CNpy)[Au(CN)$_2$]$_2$}2/3H$_2$O single crystal [****Shepherd et al., 2013****], 5-[Co(NH$_3$)$_5$(NO$_2$)]Cl(NO$_3$) single crystal [****Naumov et al., 2013****], 6-VO$_2$ single crystal [****Liu et al., 2012****], b) Maximum achievable stress versus actuation bandwidth for selected actuator materials families [Adapted from* ***Lantada, 2011****].*

1.4. Molecular switches

A molecule is considered as a molecular switch if it has (at least) two molecular states – or isomers – between which a controlled and reversible transformation can be achieved using an external stimulus. The two isomers represent two different local minima on the potential energy surface and correspond (usually) to a stable and a metastable state (**Figure 3**).

By convention we consider the system as a molecular switch if the energy barrier between these two potential wells is larger than the thermal energy – at the temperature of observation. This rather loose definition gives a large freedom in what can be considered as a molecular switch.

Indeed, molecular switching phenomena comprise a vast variety of molecules (both organic and inorganic) and physico-chemical mechanisms. Somewhat arbitrarily we will classify molecular switches into four families: (i) Structural switches (ii) Electronic switches and (iii) Redox/pH switches.

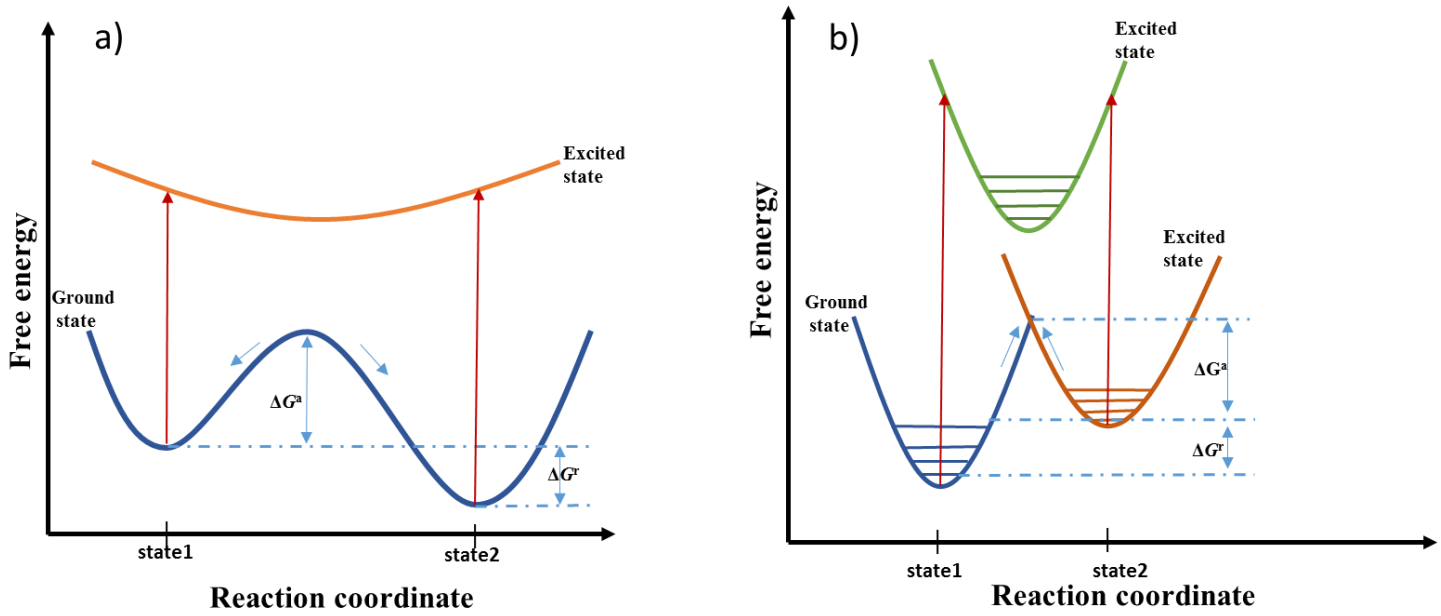

Figure 3: *Typical potential energy surfaces of two-state molecular switches exhibiting metastable states either on the ground a) or excited b) state potential energy surface. Switching mechanism via higher excited states and analog the energy barrier are shown.*

1.4.1. Structural switches for actuation

A structural switch implies a change in the spatial arrangement of the atoms in a molecule. If this occurs without a change in their connectivity, i.e. the formal "line structure" of the molecule remains the same and only the atomic positions change in space the phenomenon is often referred to as stereoisomerism or occasionally conformational switching. Probably the most famous example of this type of molecular switch is azobenzene [**Natanshon et al., 2002**]. On the other hand, the switching event may involve a molecular rearrangement with bond formation and/or breaking. Examples include diarylethenes [**Morimoto et al., 2010**] and naphthalocyanine [**Liljeroth 2007**]. Linkage isomers are an interesting class of coordination complexes, which have one (or more) ligands with switchable connectivity to the metal ion [**Warren et al., 2014**]. In all of the above cases, the two states of the molecule correspond to local minima in the ground-state potential energy surface.

These compounds have been primarily investigated for their photomechanical properties (i.e. light induced actuation). Nevertheless it may be useful to note that other stimuli (temperature, pressure, etc.) can be also used in several cases to induce switching. Photochromism is the term used for a reversible light-induced color change of a material. In the case of molecular materials this is the result of a photo-activated transformation of a molecule between two states with distinguishably different absorption spectra in the visible range. The photoproduct usually generates a change in the shape and/or volume of the material. [**Agolini et al., 1970, Matejka et al., 1979, Kim et al., 2014, Priimagi et al., 2014**]

While bulk single crystals of photochromic molecules have in fact been reported to exhibit macroscopic deformations upon light irradiation, switching in the bulk form remains often difficult due to the large energy barriers, which arise from steric hindrance. Additional difficulties with bulk materials may result from the generally very incomplete light penetration and the integration of such samples into functional devices is not straightforward either. To overcome these problems photochromic units were incorporated on several instances into different matrices (liquid crystalline elastomers, cross-linked polymers, etc.) allowing for better processability and more complete photo-switching. The most significant trade off with this strategy is that the dilution of photochromic units leads to reduced mechanical performance in terms of strain, work density, elastic moduli, response time, etc. For example, Jin et al. [**Jin 2011, Jin et al., 2014**] reported a dilute, photochromic ruthenium sulfoxide-based polymer composite that efficiently deforms at room temperature under laser irradiation (**Figure 5a**). The active material has a rather low concentration within the polymeric structure (2–4%) and a high level of crosslinking is present to ensure efficient propagation of the desired photomechanical effect. The work density for these materials remains rather moderate when referring to **Figure 2**. This can be explained by the small strain (<0.001) and relatively low Young's modulus (<700 MPa) of these materials. Interestingly, though not unexpectedly, a photo-induced change of the Young's modulus (up to ~30%) was also reported [**Jin et al., 2011, Jin et al., 2014**].

Light is an interesting energy source for actuating purposes in that it allows for remote control with high temporal and (reasonably) high spatial resolution. In addition, other properties of the electromagnetic wave (wavelength, polarization, coherence, etc.) may be also exploited. For example the polarization direction of light was used to achieve directional motion in photo stimulable actuators by Choi et al. [**Choi et al. 2009**]. Photo-switchable liquid crystal elastomers (LCE) containing azo-benzene moieties have been also reported by several other authors who demonstrated various macroscopic motion [**Yamada et al 2008, Takashima et**

al., 2012]. A particular interest of LCE materials is that they are amenable for film fabrication, which is an important issue in the MEMS/NEMS context [**Eelkema et al., 2006, Li et al., 2003, Jia and Li, 2014**].

While the photomechanical response of polymeric systems has been studied for many years, single crystal studies are more recent, this is the case of diarylethenes. [**Irie et al., 2001, Kobatake et al., 2007**].

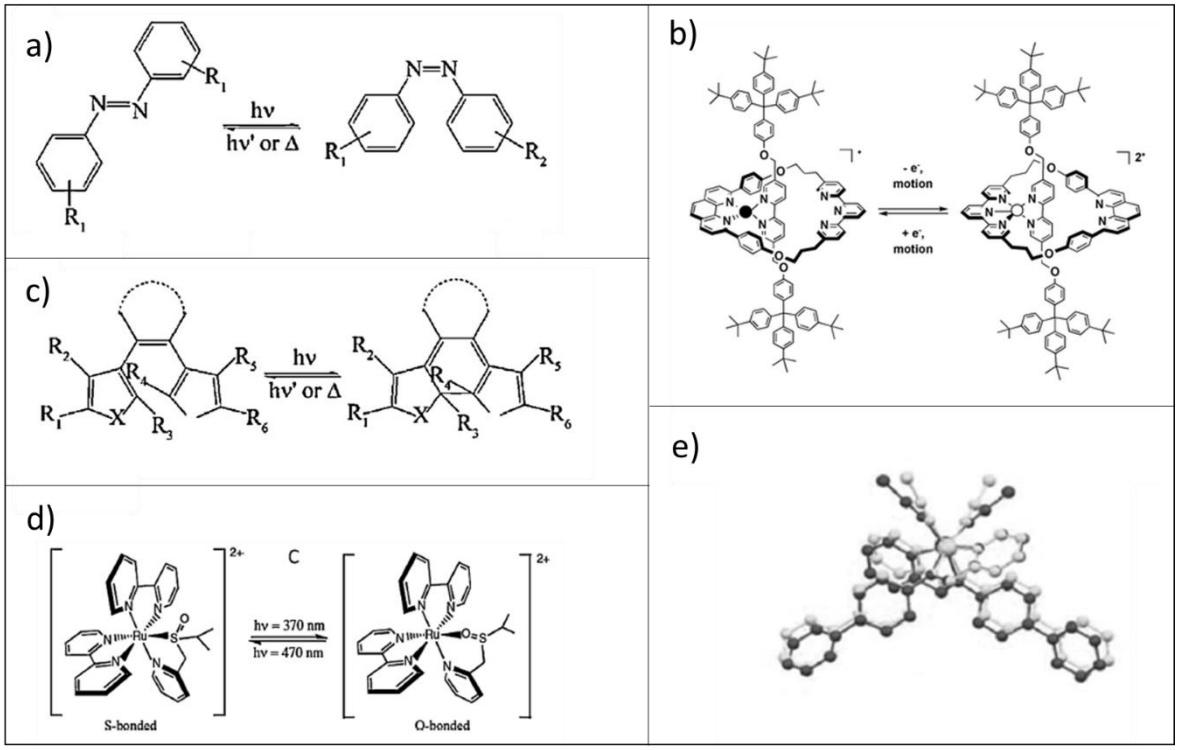

Figure 4: *Examples of some molecular switches: a) azobencene, b) rotaxane, c) diarylethene, d) rutenium sulfoxide and e) spin crossover compound.*

The Irie group has studied several cases and one of the recent examples involved the photo-isomerisation of macroscopic (1–5 mm) diarylethene crystals [**Morimoto et al., 2010**]. These molecules undergo a solid state reaction from an open-ring isomer to a closed-ring isomer under irradiation with UV-light. The reverse process is also readily achieved through irradiation at visible wavelengths. The change in shape of an individual molecule is relatively small during this process; however, the perfect alignment of the molecules in the crystal ensures that all individual molecular motions occur in unison, and in the same direction. An interesting feature of this type of systems serves to further amplify the motion of these crystals: the isomerization reaction occurs only at the surface. The result of this poor penetration of light into the sample

for the dramatic actuating response may be understood through analogy to bimetallic strips, wherein the strain mismatch of the two components leads to the bending of the strip, allowing the movement of relatively large loads (**Figure 5c**) through rapid (<5 μs) and reproducible movements over (at least) 250 cycles. A detailed photo-crystallographic study of the sample revealed a linear strain of 0.29% along the crystallographic b-axis, which corresponds to the long axis of the crystal. The Young's modulus was determined as high as 11 GPa and the work density was calculated to be ca. 0.046 J/cm^3. Koshima et al. [**Koshima et al., 2009**] described a similar experiment using an azo-dye crystal. Under UV irradiation of the (0 0 1) surface, the crystal bent away from the light source, reaching a maximum deflection after 0.2 s, as measured at the tip of the crystal. The bent crystal returned to the initial, straight form 3.8 s after the illumination was stopped (**Figure 5b**). This reversible bending was observed over 100 cycles.

Optical spectroscopic and crystallographic studies and their correlation with the photoactuation properties are obviously very important in this family of materials and have been carried out by several groups. For example, Bushuyev et al. [**Bushuyev et al., 2013**] investigated the influence of electronic structure, molecular geometry, long-range crystal packing and macroscopic crystal orientation on the photo actuation performance of different azobenzene dyes and established a few useful "rules of thumb" for the design of more efficient systems. Photoexcitation conditions have been also quite thoroughly investigated and in some cases a rather high degree of spatio-temporal control of crystal motion could be achieved using sophisticated photoexcitation methods [**Good et al., 2009**].

1.4.2. Electronic switches for actuation

An electronic switch is based on a change of the electronic state of the system, i.e. a switch between the ground and a close-lying electronic state, separated by a sufficiently large energy barrier. We can further classify these systems in different sub-families: Spin-crossover occurs in octahedral $3d^4$–$3d^7$ transition metal complexes wherein switching takes place between the high spin (HS) and low spin (LS) states of the central metal ion [**Gutlich and Goodwin, 2004, Bousseksou et al., 2011**]. Jahn-Teller switching results from the distortions of Jahn-Teller active ions and involves either a static or dynamic orbital ordering in crystalline solids [**Halcrow, 2013**]. Redox isomerism (touted in a few specific cases also as valence tautomerism) leads to a change of the charge distribution within the molecule hence the switching can be

described as an intramolecular electron transfer between a donor and accept or moiety of the molecule [**Pierpont, 2001**].

To date, the only class of electronic molecular switches that have been investigated and reported for actuating applications is spin crossover systems. The spin crossover (SCO) phenomenon leads to a redistribution of electrons within the 3d-orbitals of some transition metal complexes, which results in weaker metal–ligand bonds in the HS state. Hence the transition from the LS to the HS state typically involves a spontaneous increase of a few percent in the volume of the material. For example, Young's modulus up to 15 GPa, linear strain up to 7 % and work densities up to 37 Jcm^{-3} (values 10^4–10^5 times greater than that expected from thermal expansion alone for a same ΔT) were reported for the SCO complexes Fe(pyrazine)[$Pt(CN)_4$]. Such high work density together with the possibility of room temperature operation is obviously very appealing for actuation purposes [**Cobo et al.,, 2008, Felix et al., 2015**]. Starting from these facts, in our research group a series of actuating devices were developed from a range of spin crossover materials as a macroscopic proof of concept [**Shepherd et al.,, 2013**]. The approach is based on a bilayer cantilever architecture in which an active SCO material is strongly bonded to a passive coating. The differential expansion of the two strata as the phase transition occurs, results in dramatically amplified motion at the macroscopic scale, as demostrated for the case of an actuator that uses a single crystal of the SCO complex{Fe(3-CNpy)[$Au(CN)_2]_2$}·$2/3H_2O$ as the active layer [**Shepherd et al., 2013**]. The versatility of this approach was demonstrated by using active layers composed of either single crystals of an SCO complex or SCO/polymer composites (**Figure 5e-f**) [**Guralski et al., 2014, Chen et al., 2015, Shepherd et al., 2013**]. Light-induced actuation was also demonstrated. Indeed, switching between HS and LS states is possible in response to several different external stimuli (temperature, light, pressure, magnetic field) [**Gutlich and Goodwin, 2004**]. In addition the SCO is often cooperative in the solid state, producing first-order phase transitions with hysteresis (i.e. memory effect), but can be also very gradual without hysteresis. As such, SCO can be considered as a very versatile transducer, capable of converting many forms of energy into motion. Another advantage is the hundreds of known SCO compounds available with a variety of active working ranges from cryogenic to ambient temperature. Since this thesis is focused on actuators based on SCO materials, chapter 2 is dedicated to describe more in detail the main mechanisms, which govern this phenomenon.

1.4.3. Redox and pH switches for actuation

Redox switches and pH switches are based on the charging of the molecule by an electron or a proton, respectively. These events are usually accompanied by a significant change of the geometry and/or the electronic configuration of the molecule, but the distinction with structural and electronic switches described above is clear since the latter phenomena are not associated with a change of the molecular charge. Strictly speaking in this class of system, switching does not take place between two isomers, since the charge (and/or the atomic composition) of the molecule is not the same in the two states. Furthermore the definition of this family refers more to a stimuli than to the actual change in the state of the molecule. Nevertheless we feel these compounds, including rotaxanes, catenates [**Bruns and Stoodart, 2014, Durot et al., 2010**], etc.,are important in the field and thus deserve separate discussion.

Electrochemical, ion-, pH-, or solvent-driven (i.e. host–guest) molecular switching phenomena have been described in different systems, but the development of these switching events toward actuating purposes is undoubtedly the most advanced in the field of bistable rotaxane-based molecular switches. Rotaxanes are mechanically interlocked molecules typically composed of a ring that can reversibly shuttle between two (or more) stations of a dumbbell [**Sauvage and Amendola, 2001**].

These systems have been designed to achieve translational motion and very high linear strains up to 67% [**Liu et al., 2005**]. At the molecular scale these systems can be used for example to modulate electronic communication between different molecular fragments [**Bruns and Stoddart, 2014**] or can be operated as nanovalves [**Saha et al., 2007**]. Synthesizing rotaxane based molecular muscles has recently become a major focus for several research groups [**Bruns and Stoddart, 2014, Jimenez-Molero et al., 2003, Du et al., 2012**]. Rotaxane-based molecular switches are excellent candidates to build artificial molecular muscles, because their architectures possess molecular units similar to the sarcomeric human muscle structure, they respond to (electro-) chemical stimuli and they are potentially biocompatible. One of the main limitations of rotaxanes, however, is the difficulty to scale up these molecular phenomena and create motion at the macroscopic scale. Thus recent investigations have focused on the development of “bottom-up” assembly approaches that can produce long-range order of molecular units with the aim of achieving their collective motion in nano and microscale

devices. This goal was first attained by the Stoddart group [**Huang et al., 2004**] who self-assembled redox-switchable rotaxanes on the surface gold-coated silicon cantilevers (500 × 100 × 1 μm, spring constant 0.02 Nm^{-1}).The rotaxane comprised two rings, which were linked to the gold surface by a disulphide moiety. Oxidation/reduction led to the contraction/elongation of the inter-ring distance and the concerted motion of these molecular units resulted in the macroscopic upward (oxidation) or downward (reduction) bending of the cantilevers (**Figure 5d**).

It should be noted that the molecules were not aligned in the monolayer hence the contribution of individual molecules to the bending depends on their relative orientation versus the long axis of the cantilever. A more detailed report from the same group later quantified the average force per molecule of a similar device at ca. 10 pN [**Liu et al., 2005**]. In the next step an

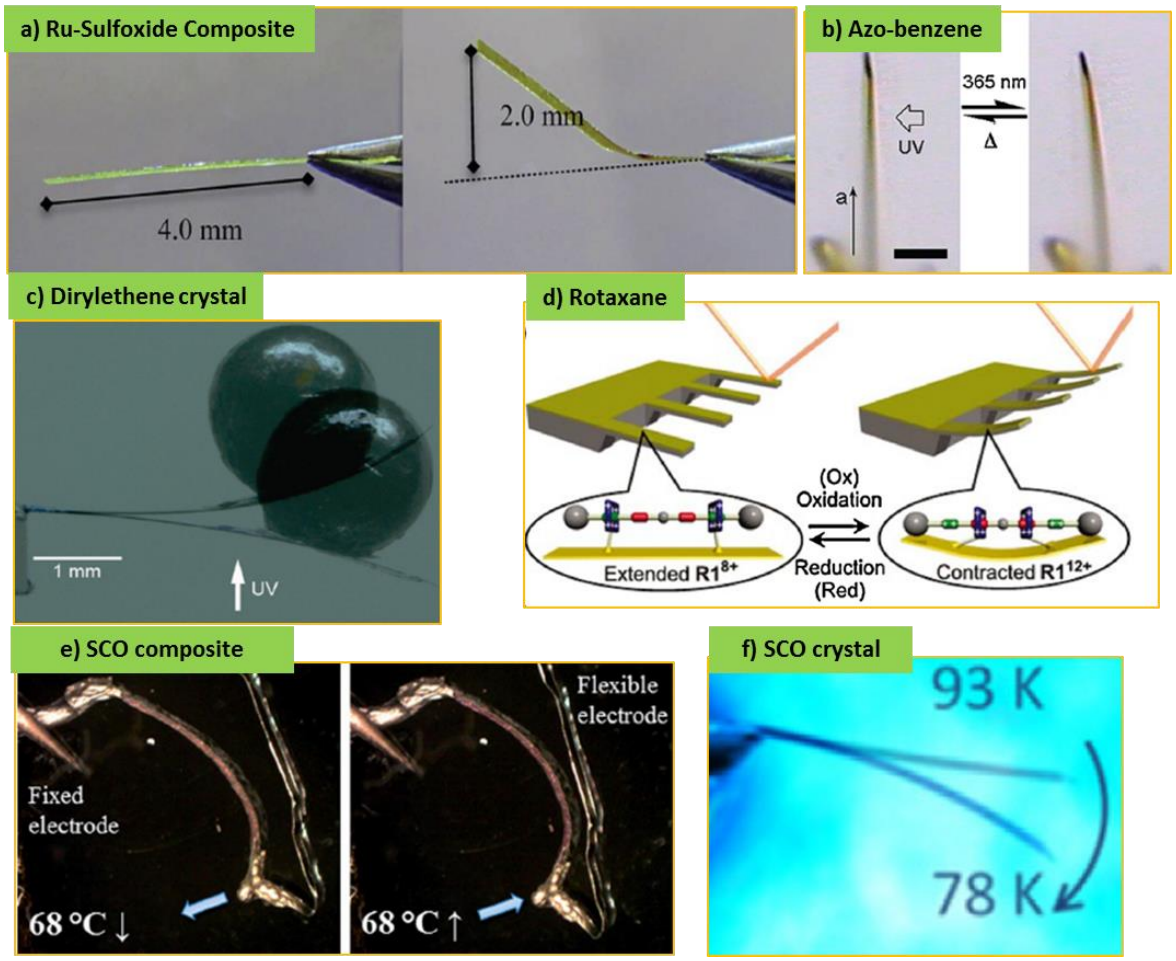

Figure 5: *Cantilever switch based on different molecular actuators stimulated by: a)-c) light, d) redox reaction and e)-f) temperature [**Jin et al., 2014, Koshima et al., 2009, Morimoto et al., 2010, Huang et al., 2004, Shepherd et al.,2013, Guralski et al., 2014**].*

electrochemical cell was used in conjunction with the rotaxane-based cantilever device to achieve significantly better control of the redox switching process [**Juluri et al., 2009**].

This device, using palindromic [**Sreenivasa et al., 2012**] rotaxane molecules, allowed improvement of both the static (force and stroke) as well as the dynamic response of the system, paving the way for true MEMS operation. In a completely different approach, rotaxane units were linked together through polymerization reactions with the aim of amplifying molecular motion and demonstrating thus actuation at mesoscopic scales [**Du et al., 2012, Dauwson et al., 2008, Clark et al., 2009, Hmadeh et al., 2010**].

1.4.4. Macroscopic shape change and motility

There are many examples in the literature where single crystals of molecular compounds undergo intricate shape changes when excited by heat or light and some of them exhibits even significant motility, a phenomenon which is described as a thermosalient or photosalient effect [**Sahoo et al., 2013, Naumov et al. 2015**], depending on the excitation source. These different phenomena provide obvious visual evidence for the conversion of thermal or photon energy into macroscopic work and thus for the amplification of individual molecular movements due to the collective behavior of molecules in the crystal. Even if these phenomena remain rather case specific and difficult to quantify, the underlying mechanistic and structural aspects have recently been investigated more deeply for several different (mainly organic) compounds [**Kim et al., 2014, Naumov et al., 2015**]. Strictly speaking some of the examples are not molecular switches because the photo-induced changes are more related to a variation of the crystal packing (dimerization, etc.) than to a well-identifiable intramolecular structural change. Obviously there is always a coupling between the molecular and crystal structures and the distinction between the cause and the effect is not always trivial. In the case of the 9-anthracenecarboxylic acid UV light irradiation of high aspect ratio micro ribbons led to a twisting motion, which is reversible (when the light is turned off the crystal relaxes back to its initial shape in ambient conditions) and reproducible [**Zuh et al., 2011**]. A detailed structural analysis revealed that the molecules undergo a reversible photo-dimerization, which drives the deformation of the crystal, while the twist period is controlled by the number of absorbed photons as well as by the geometry of the ribbon. The authors suggested that this specific shape

is the consequence of the coexistence in the structure of photo-reacted dimers and unreacted monomers. Jumping and other motility phenomena are ubiquitous in crystals exhibiting phase transitions with significant internal stress and strain. Recently, these phenomena have received more attention and detailed structural investigations allowed more insight into the physical mechanisms behind them to be obtained. For example, Naumov et al. [**Naumov et al., 2013**] reported on various spectacular kinematic effects (splitting, explosion, jumping, etc.) of crystals of the coordination complex $[Co(NH_3)_5(NO_2)]Cl(NO_3)$ under UV light irradiation. This compound exhibits a nitro–nitrito linkage isomerism, which develops in a homogenous fashion, i.e. no phase separation and volume discontinuity is observed. Nevertheless the stress which develops as a result of this relatively small structural change (the highest linear strain is ca. 3.5%) is able to propel millimeter-sized crystals to several tens of centimeters from their initial position.

1.5 Prospects of molecular switches for MEMS/NEMS devices

With the advent of the nanotechnology era attention has turned more and more toward the fascinating potential for molecular devices in different fields (molecular electronics, molecular magnetism, etc.). While custom-designed single molecule device is a captivating idea, for the moment this field remains a topic of fundamental nanoscience. On the other hand molecular materials may readily find technological applications. Fields as MEMS/NEMS technologies, or artificial muscles are areas in which actuators based on active molecular components may find useful application. A major point of interest for these systems is their high degree of versatility, bolstered by advances in modern synthetic chemistry. Beyond molecular design, efforts are increasingly devoted also to rationalization and control over supramolecular organization, something which may be key to device integration [**Breuning et al., 2000**]. The potential to graft molecular switches onto polymeric chains, inorganic nanoparticles and surfaces, or even on macromolecules of biological interest is certainly a huge advantage over other actuating materials. Another key point is their multi functionality, which confers to them appealing smart features. Beyond the strain, which always accompanies a molecular switching event, other material properties often change in unison (including color, refractive index, magnetic susceptibility, conductivity, etc.). This provides interesting possibilities for combining built-in actuator and sensor functions and, by appropriate feedback design, a control function can be also established.

Beyond smart and specialized features the good overall actuating performance of these materials must be also highlighted. The primary material performance meters are stiffness, strain, work density and bandwidth. Molecular actuators have moderate to low performance in terms of force/stiffness, which is simply related to the (relative) weakness of intermolecular forces. On the other hand, they display more promising strain (displacement) and work density characteristics. For example, the work density of certain spin crossover complexes is comparable with that of shape memory alloys. This arises from a dramatic change in the molecular geometry of these systems. The bandwidth in molecular systems can be inherently very high, since these molecular switching events occur usually at the ns (structural switches) – ps (electronic switches) time scales. However at the material and device levels this intrinsic bandwidth may be significantly reduced [**Lorenc et al., 2009**].

One of the main promises of molecular materials is operation at reduced sizes, but this requires processing, integration and testing at these scales. A basic requirement for device integration is micro- and nanoscale organization and compatibility with silicon-based technologies. The main challenge here is to provide approaches that are compatible with the MEMS/NEMS fabrication steps (in particular taking into account the fragility of the structures once liberated) and that allow the preservation of molecular switching functionality and performance. A straightforward way to introduce these molecules into real applications might be through their incorporation into polymeric materials, which can be readily processed using well-established methods, such as spin coating or micro molding. The recent spectacular advances in the field of spin crossover thin films and nano-objects [**Bousseksou et al., 2011, Cavallini 2012, Gentili et al., 2014**] provide some confidence that this can be a viable approach.

The next step is the analysis of actuating performance of these devices, some-thing that is almost completely missing from the current literature, and which may be significantly different when compared to the actuating performance of bulk single crystal materials. Indeed, a polycrystalline film with randomly oriented active molecules may exhibit significantly reduced effective strain; depending on the actuation method the bandwidth and efficiency may also be seriously reduced. Other properties such as linearity and stability must be also investigated. Rather surprisingly the mechanical properties of molecular switches are also not well established. While the strain associated with the switching event is usually well characterized by crystallographic methods, the elastic moduli and their correlation with the molecular structure have been analyzed only in a very few cases. This is all the more surprising given that mechanical properties play often a pivotal role in the switching phenomena. Accumulation of

experimental data including nano indentation, atomic force microscopy, inelastic scattering techniques and high pressure crystallography would be extremely useful and should be accompanied by a more widespread use of computational methods. Recent progress in the study of other molecular materials may serve as a useful guide for this task [**Reddy et al., 2006, Reddy et al., 2010**].

Conclusions

In this chapter, some of the main advances of molecular switches as actuators were discussed, the parameters to evaluate their actuating performance were set as well as their applicative potential with respect to other conventional actuating materials. The different actuating mechanisms were exposed (structural, electronic, redox switching). The actuating proof of concept for most of them have been already achieved using either single crystals or composite materials. The next step is their successful integration into useful devices for future applications. In order to succeed, the combination of fundamental principles governing molecular actuators, their mechanical performance evaluation and the introduction of appropriate fabrication protocols is needed. This thesis is focused on SCO molecular actuators and has been developed to advance some of these issues.

Chapter 2. The spin crossover phenomenon

Introduction

Among the different types of molecular actuators, spin crossover compounds are well-known to display a reversible switching between the high spin (HS) and low spin (LS) states of the central metal ion. This phenomenon can be induced by different physical and chemical stimuli. The electronic switching is associated with a significant change in molecular volume and shape, which can be harnessed to produce useful mechanical work. This chapter introduces the SCO phenomenon and discusses the different stimuli to trigger it. The conventional characterization techniques to detect and measure the SCO properties are also exposed. Since the strain and mechanical properties are the outstanding parameters regarding actuating performance, this chapter gives a particular emphasis on structural aspects of the SCO, from the molecular to the microscopic scale and their repercussion on the volume change. An overview of the SCO mechanical properties is also discussed.

2.1 Spin crossover: general principles

The spin crossover phenomenon occurs in some $3d^4$ - $3d^7$ transition metal compounds with a pseudo-octahedral molecular symmetry where six donor atoms form an octahedron around the metal ion. Depending on the ligand field strength, these metal ions can adopt two spin states called low spin (LS) and high spin (HS).

The SCO phenomenon was observed for the first time in 1931 by Cambi and Gagnasso reporting a strange magnetic behavior in a set of compounds of Fe(III) based on the dithiocarbamate ligand. They observed a reversible conversion of the spin state as a result of temperature variation [**Cambi and Gagnasso, 1937**]. Twenty years later, in 1956, the notion of spin equilibrium behavior was evoked [**Griffith, 1956**]. The first occurrence of SCO phenomenon in an iron(II) complex was reported by Baker et al [**Baker and Bobonich, 1964**]. This finding led to countless other complexes and the effect is currently found in iron(II), iron(III), cobalt(II) and less frequently in cobalt(III), manganese(II), chromium(II) and manganese(III). However, the majority of the studied complexes have an iron(II) central ion [**Gutlich and Goodwin, 2004**]. For this reason, in the following the general principles which govern the spin transition will be discussed for iron(II).

2.1.1 Ligand-field theory

If an iron(II) ion is set in a perfectly octahedral coordination, its five d orbitals are split into three orbital subsets, dxy, dyz, dxz, which represent the basis of the irreducible representation t_{2g}, and another subset of two orbitals, namely dz^2 and dx^2-y^2 which are basis of the e_g irreducible representation. The t_{2g} orbitals are non-bonding and therefore at lower in energy than the antibonding e_g orbitals (**see Figure 6a**). The difference in energy between these two levels is given by the ligand field strength 10Dq, and depends on the metal-ligand distance $1/r^n$, with n = 5, 6. In addition to this energy, the electron-electron repulsion, also called the spin pairing energy Π has to be taken into account. In the case of iron (II), it is possible to define two ground states with different distributions for the six d electrons depending on the magnitudes of 10Dq and Π.

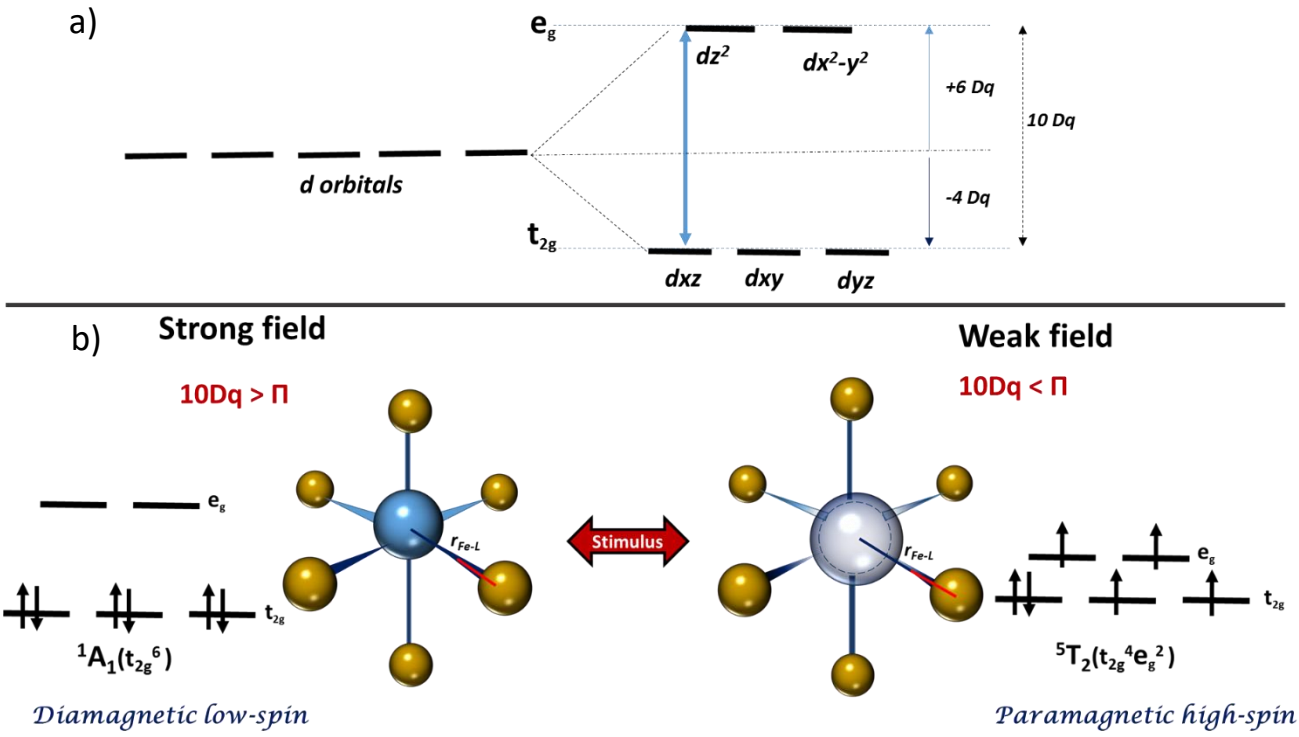

Figure 6: *a) Separation of the d orbitals in an octahedral ligand field induced by the ligand strength 10Dq, b) Diagram of the electronic configuration for the two possible ground states for iron (II) in an octahedral complex.*

If Π is larger than 10Dq the electrons will occupy the five d orbitals according to Hund's rule, with maximum spin multiplicity as for the free ion. This results in a paramagnetic state S=2, the so-called high-spin $^5\mathbf{T_2(t_{2g}^4e_g^2)}$ ground state. In case that 10Dq is larger than Π, the six d electrons will pair up in the t_{2g} orbitals, resulting in a diamagnetic state S=0, the so-called low-spin $^1\mathbf{A_1(t_{2g}^6)}$ ground state (**Figure 6b**). In case Π ≈ 10Dq, the SCO phenomenon can occur [**Gutlich and Goodwin, 2004**].

During the SCO the metal-ligand bond length changes abruptly and therefore 10Dq changes abruptly too. As a general rule, in the case of an octahedron FeN_6, the bond lengths are approximately r_{LS} = 1.92 -2.00 A° in the LS state and r_{HS} = 2.12 – 2.18 A° in the HS state, giving a variation $\Delta r_{LS\text{-}HS} \approx 0.2$ A° (10 %), which means an increase of 25 % in the octahedral volume from the LS to the HS state. For a configurational coordinate diagram (see **Figure 7a**) one can see that the minima of the two potential wells (HS and LS) are displaced, both horizontally (Δr_{HL}) and vertically (ΔE^0_{HL}) to each other.

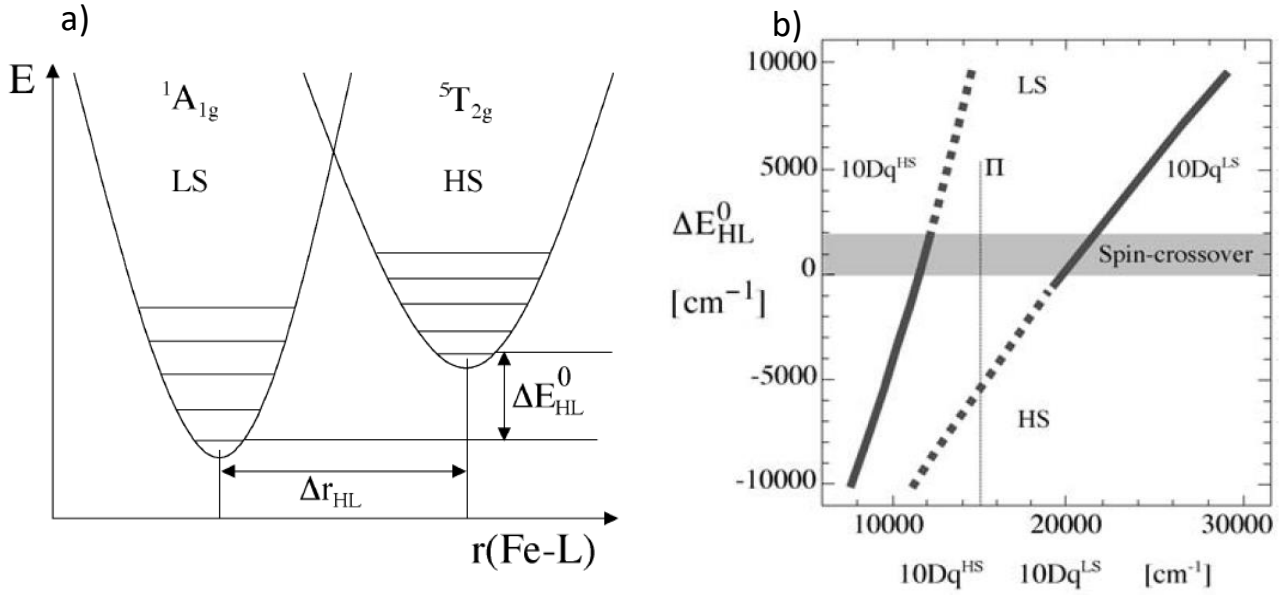

Figure 7: *a) Adiabatic potentials for the HS and LS states as a function of the totally symmetric metal-ligand stretch vibration denoted r(Fe-L). b) Stability regions of the LS and HS states as a function of 10Dq [**Gutlich and Goodwin, 2004**].*

Taking into account the bond length dependence of 10Dq and the fact that Π does not vary with, the ground state energy ΔE^0_{HL} between the HS and LS states can be estimated as a function of

$10Dq^{HS}$ and $10Dq^{LS}$ respectively, as illustrated in **Figure 7b**, where three regimes can be observed [**Gutlich and Goodwin, 2004**]:

i) $10Dq^{HS} < 10000cm^{-1}$, $\Delta E^0_{HL} < 0$. Here the HS state is the quantum mechanical ground state and is thermodynamically stable at all temperatures at atmospheric pressure.

ii) $10Dq^{LS} > 23000\ cm^{-1}$, $\Delta E^0_{HL} > 2000\ cm^{-1}$. Here the LS state is the quantum mechanical ground state and is thermodynamically stable state up to very high temperatures.

iii) $10Dq^{HS} = 11000 – 12500\ cm^{-1}$, $10Dq^{LS} = 19000 – 22000\ cm^{-1}$ and $\Delta E^0_{HL} = 0\text{- }2000\ cm^{-1}$. This narrow region represents the area where thermal spin crossover may occur.

2.1.2 Different stimuli to induce spin transition.

The spin transition can be triggered by different stimuli, but the most accessible experimentally is the thermo-induced spin transition. Nevertheless other stimuli have been also explored such as the pressure and light-induced spin state change, which will be briefly discuss below. Let us also note that SCO can be also induced by gas/molecule absorption or by an intense magnetic field.

2.1.2.1 Thermally-induced spin transition.

The thermally induced spin transition is an entropy driven process. This is the most common way to trigger the switch between the LS and HS states. The two spin states are in thermodynamic competition. The phase change that can be associated to the spin crossover phenomenon can be analyzed through the Gibbs free energy.

$$\Delta G = G_{HS} - G_{LS} = \Delta H - T\,\Delta S \tag{2a}$$

$$\Delta H = H_{HS} - H_{LS} \tag{2b}$$

$$\Delta S = S_{HS} - S_{LS} \tag{2c}$$

The equilibrium temperature $T_{½}$, at which the quantity of molecules in the HS and LS states are the same, is defined by:

$$T_{1/2} = \frac{\Delta H}{\Delta S} \quad (3)$$

The complexes will be in the low-spin state at very low temperatures, where the enthalpy term dominates. On the other hand at elevated temperatures the entropy-driven almost quantitative population of the high-spin state may be observed. The entropy difference between the two states is based on two contributions, i) the higher spin multiplicity of the high-spin state, and ii) a vibrational contribution due to the generally lower vibrational frequencies and the resulting higher density of vibrational states in the high-spin state. The low-spin state, in fact, remains the quantum mechanical ground state at all temperatures, but the high-spin state becomes the thermodynamically stable state at elevated temperatures.

2.1.2.2 Photo-induced spin transition.

The first occurrence of light induced spin crossover was reported in 1982 by McGrarvey and Lawthers [**McGravey and Lawthers, 1982**], which had a big impact on the spin crossover research field. They have shown that by using a pulsed laser they could perturb the equilibrium between the two states in several Fe(II) SCO compounds in solution. Later, Decurtis [**Decurtis et al., 1984**] discovered that by irradiating a solid Fe(II) SCO sample with green Ar+ laser (λ = 514.5 nm) he could excite the LS state into a metastable state until the complete population of the HS state, presenting a long lifetime at sufficiently low temperatures (10^6 s for $[Fe(ptz)_6(BF_4)_2]$ at 20 K). This solid state effect was named "Light Induced Excited Spin State Trapping" or LIESST effect. The reverse-LIESST effect was soon reported by Hauser [**Hauser 1986**], and was obtained by converting the HS state into the LS state using red light (λ = 820 nm). The Jablonski diagram, illustrates the LIESST and reverse LIESST effects with vertical transitions and relaxation processes (s**ee Figure 8**).

The light induced switching process is thought to occur with the excitation of the sample into the $^1T_1$ energy level (or MLCT levels – depending on the experimental conditions), followed by a first relaxation into the $^3T_1$ level.

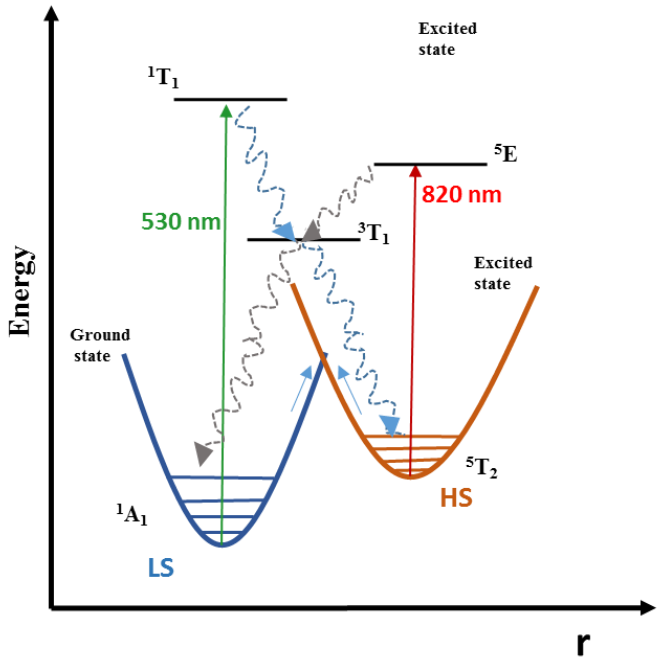

Figure 8: *Jabloski diagram showing LIESST and reverse LIESST effects [**Hauser, 1991**].*

The second relaxation may occur into the $^5T_2$ (HS) state, where the molecule remains trapped due to the large energy barrier between the HS and LS states. Because the energy level $^3T_1$ is below ^5E state for SCO compounds, this suggests a possible reversibility of the LIESST effect. This is possible by irradiation with λ = 820 nm, which induces a transition between the $^5T_2$ and ^5E levels, where it relaxes via $^3T_1$ to the $^1A_1$ (LS) state. It is worth underlying that the HS trapping is only efficient at cryogenic temperatures (typically below 50 K) because at higher temperatures the photo-induced HS state relaxes rapidly to the ground state. (The life time of the state at room temperature is typically a few μs-ns. [**Hauser, 1991**].

2.1.2.3 Pressure-induced spin transition.

Pressure is another perturbation which can trigger or alter the spin transition. Due to the fact that the SCO molecule has a smaller molecular volume in the LS state than in the HS one, pressure is favoring the LS state [**Gutlich and Goodwin, 2004, Varret et al., 2002**]. When low - moderate pressures (< 1 - 10 GPa) are applied the potential wells suffer only a relative vertical displacement, and the gap between the LS and the HS states increases by $p\Delta V$ where ΔV represents the volume difference in the two spin states (**Figure 9**). The energy gap between the two spin states can be expressed by **Equation 2**.

$$\Delta E_{HL}^{0}(p) = \Delta E_{HL}^{0} + p\Delta V_{HL} \quad (2)$$

For iron(II) compounds the transition temperature variation under hydrostatic pressure is about 15-20 K/kbar (Slichter 1972).

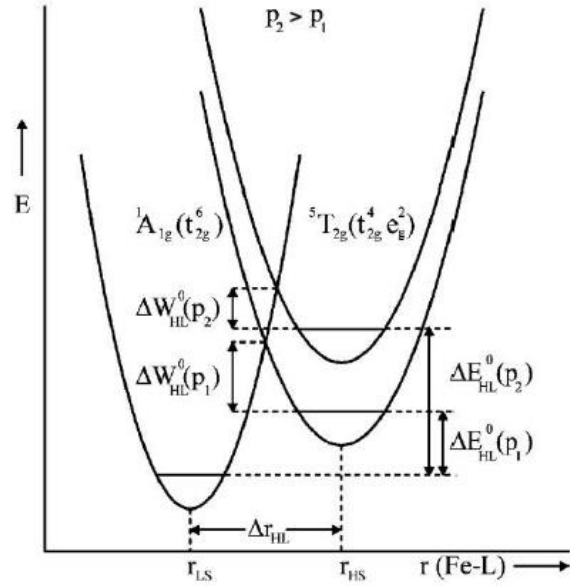

Figure 9: *Schematic representation of pressure effect on LS and HS potential wells of Fe(II) compounds [**Gutlich and Goodwin, 2004**].*

2.2. Methods to detect and measure SCO properties

During the spin transition physical phenomena at different levels may occur (electronic, molecular, structural, micro structural) which produce changes of different properties (color, volume, magnetic, electrical, etc.) **Table 2** lists the properties changes that can be triggered during the SCO and the most typical characterization techniques used to determine them.

For the purpose of this thesis, we will focus on the structural and the mechanical changes and how these parameters need to be considered for actuation purposes. For instance, the strain during the spin transition is governed by the structural changes and it will determine the amplitude of actuation. On the other hand, the Young's modulus which determines the output force is determined mainly by the lattice dynamical properties. Below we discuss how these two parameters are affected by the spin transition.

Table 2 : *Characterization techniques to detect and evaluate SCO properties.*

Property	Technique	
Magnetic	SQUID	Magnetic moment, Magnetic susceptibility
	Mossbauer	Hyper-fine properties
Lattice dynamics	NIS	Acoustic phonon, sound velocity
	FT-IR, Raman	Optical phonons
	Mossbauer	Debye Temperature (+ electronique configurations)
Optical	UV-Vis	Transmission/Absorption/Reflectance
	Ellipsometry, SPR	Refractive index
	Diffraction	Refractive index
Structural	DRX	Lattice parameters, molecular structure, microstructure
Thermophysical	DSC	Entropy, Enthalpy, Heat capacity
Electrical	Dielectric spectroscopy	Permitivity, conductivity

2.2.1 Strain and cooperativity: Structural and Microstructural aspects

As mentioned before, the SCO is accompanied by significant structural changes. Up to now the main principles has been described from the electronic and thermodynamic perspectives, but the bulk physical properties go beyond the electronic or molecular transformation and the physical property changes will be a consequence of various phenomena at different structural organization scales. Guionneau has discussed this issue based on X-ray diffraction studies providing information about the different structural levels to consider during the strain of the SCO material (**see Figure 10**) [**Guionneau, 2014**]. In the following a summary of these structural considerations is given.

2.2.1.1 SCO at the level of coordination octahedron

Since the reversible spin transition triggers length changes between the metal-ligand bonds, information about the spin transition itself is provided from this parameter which can be

determined by the study of the crystal structure, giving information of the atomic position of a given metal site. Not only the bond lengths change, but the ligand-metal-ligands angles as well, producing a distortion of the octahedron geometry and influencing directly the SCO properties. Remarkably for most compounds with $Fe(II)N_6$ core the volume change of the octahedron was found nearly the same $\Delta V \approx 25$ % (13 $Å^3$) [**Halcrow, 2011, Guionneau, 2014**].

2.2.1.2 SCO at the molecular level

When the octahedral deformation occurs during the spin transition, this is propagated through the whole molecule whose geometry is affected depending on the set of ligands used. The main events which can be encountered at the molecular level are: i) an aperture angle producing flapping/bending of the ligands, ii) no geometry alteration, iii) dissymmetry and, in some extreme cases, iv) metal-ligand bond breaking. The SCO at the molecular level will not be affected only by the modifications at the octahedral level, but also by the inter-molecular interactions.

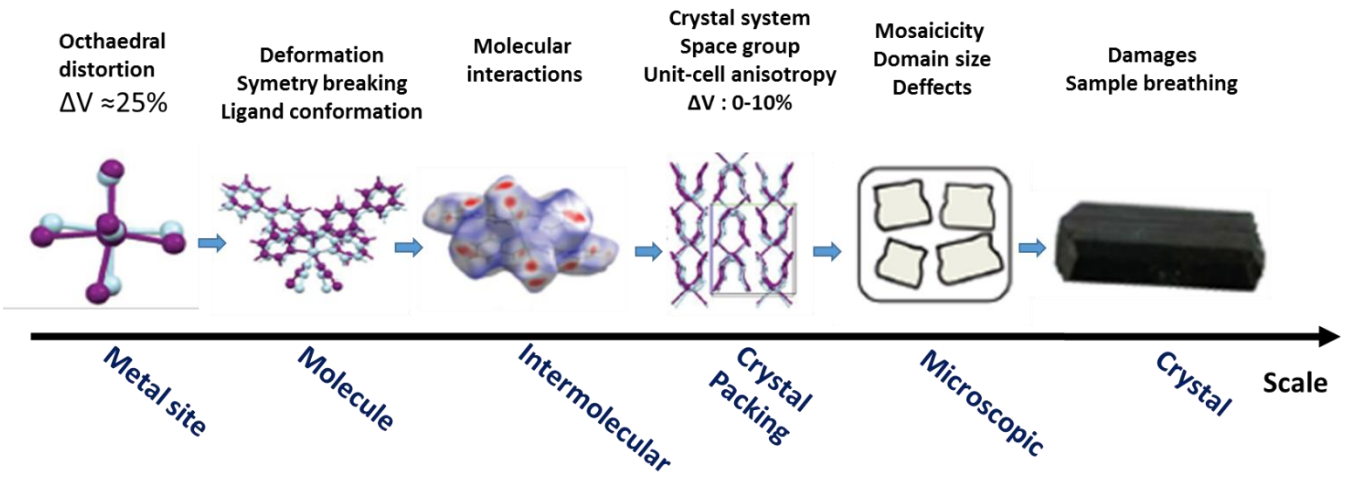

Figure 10: *Multiscale view of possible structural modifications connected with the SCO phenomenon on the example of [Fe(PM-BiA)$_2$(NCS)$_2$]. [Adapted from* ***Guionneau, 2014****].*

2.2.1.3 SCO at the inter-molecular level

The influence of the SCO phenomenon at this level is very important since the complexity of these materials rely on interactions between molecules. These interactions are mainly hydrogen bonds, van der Waals contacts and π-π stacking, which are directly correlated with the

cooperativity of the SCO. However, it is difficult to stablish general rules due to the diversity of structural situations.

2.2.1.4 SCO and the crystal packing

It is useful to follow the structural modification through the unit cell parameters values. This is one of the most used approaches since the unit cell can be determined quickly both from powder and single crystal diffraction experiments. In fact, it allows to quantify the final amplitude of the SCO breathing on the material. For most of compounds based on Fe(II) the volume change ΔV in the unit cell varies from 1 to 5 % and in some special cases, such as for the $[Fe(Htrz)_2(trz)](BF_4)$ and $Fe(pyrazine)[Pt(CN)_4]$ compounds, this value can reach 10-13 %. This value is significantly smaller than the octahedral volume change because the cell volume change is a consequence of the rearrangement of the whole molecule and the crystal packing. Moreover it is important to consider the anisotropy changes during the SCO, which may favor a specific strain direction. This aspect must be carefully considered during their integration in MEMS devices. The X-ray diffraction patters can be also useful to follow the evolution of the unit cell during the temperature ramp and deduce accurately the thermal expansion of the material far from the SCO [**Guionneau, 2014**].

2.2.1.4 SCO at the microscopic and macroscopic levels

The propagation of the SCO strain at the micro and macroscopic scales does not related only to the crystal unit cell, but also to the defects and damages in the crystal. Some of the structural aspects to take into account during the SCO at the micro and macroscale are the particle size, domain size, mosaicicity, crystal defects, and long range damages. For instance the mosaicicity of a single crystal is strongly affected during the first thermal cycles. Fatigability has been reported in recent research using either Reflectivity measurements, X-ray diffraction or by AFM microscopy [**Lefter et al., 2015, Guionneau et al., 2012, Grosjean et al., 2016, Manrique-Juarez et al., 2016**]. All these aspects affect obviously on the SCO performance for application purposes. Nevertheless for some cases it seems there is a critical point where SCO prevails without no significant further structural modifications [**Guionneau et al., 2012**]. Indeed, interestingly Guionneau et al. noticed that the fatigue of the structure had almost no

influence on the transition temperature after a few thermal cycles [**Forestier et al., 2009, Grosjean et al., 2016**], but it still plays an important role for strain harvesting.

2.2.1.5 Cooperativity of the SCO

In the case of a crystalline lattice, the change of volume and shape of a molecule upon its spin transition triggers important repercussions to its close environment, but also to the long range environment affecting the energy of the whole lattice.

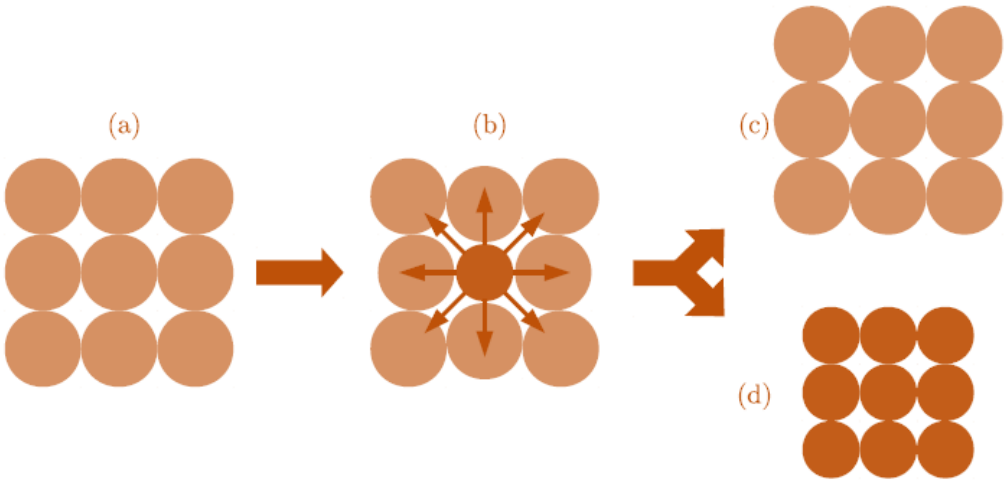

Figure 11: *Simplified representation of collective mechanisms in the case of a highly cooperative SCO compound a) Molecules in the HS state. b) The central molecule transits towards the LS state, which implies a lattice deformation and tensile stress from its neighbors (arrows). As a result, c) either the molecule returns to the HS state or d) the neighbors transit towards the LS state [**Mikolasek 2016**].*

For instance, if a HS molecule in a HS molecular environment switches to the LS state, this will lead to important stress and strain (**Figure 11**) and thus an increase of the elastic energy of the crystal lattice. For strong elastic interactions, the intermediate states between the pure LS and HS states are very unstable and the material is blocked in its current state until the intake energy is large enough to exceed the energy barrier. These collective phenomena are called cooperativity. They may lead in some cases to a first-order phase transition with an elastically-driven memory effect (hysteresis).

Figure 12 shows typical plots of the high spin fraction (Υ_{HS}) vs temperature presenting a large diversity of behaviors ranging from gradual to very abrupt transitions with hysteresis as well as multi-step or incomplete SCO. The main source of the variety of the presented spin crossover curves is the degree of cooperativity between the molecules, which is determined by the lattice properties, notably by the way that metal-ligand deformations are propagated through the solid.

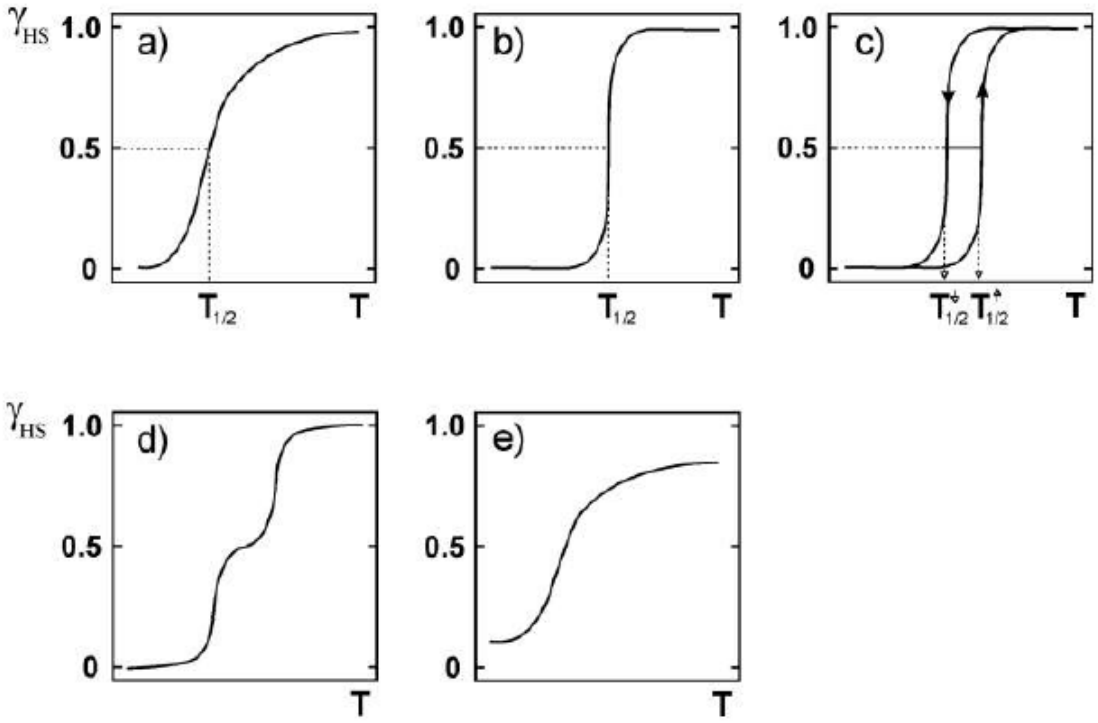

Figure 12: *Representation of a a) gradual, b) abrupt, c) hysteresis, d) multi-step, and e) incomplete spin transition [**Gutlich and Goodwin, 2004**].*

One of the most common behavior found in SCO systems is the gradual conversion (**Figure 12a**), denoting relatively weak cooperative interactions. If the degree of cooperativity in the system is increased, an abrupt transition can be found (**Figure 12b**). When a high degree of cooperativity is present in the system, the transition has a hysteretic behavior as illustrated in **Figure 12c**. For a narrow category of materials, a transition that occurs in two or even more steps can be detected (**Figure 12d**). This behavior happens in systems where the metal ions occupy at least two different lattice sites in the material. Alternatively it may also occur in systems with single metal site due to the preferential formation of LS-HS pairs caused by the competition of long and short range interactions [**Bousseksou et al., 1992-1993**]. The incomplete transition (**Figure 12e**) can be usually explained by the presence of some defects in

the lattice capable of preventing the formation of LS and/or HS species. Another cause may be a kinetic effect at low temperatures, when the conversion rate from one state to another becomes extremely low or even quenched.

The link between cooperativity and crystal structure is obvious, but remains extremely difficult to quantify. Intermolecular contacts between spin centers can lead to strong cooperativity. These contacts might arise through strong or weak hydrogen bonding, from π-π interactions, or simply van der Waals forces. Cooperativity is also transmitted mechanically in a molecular crystal, between molecules with a high degree of surface contact. Large structural differences between the high and low-spin states can lead to strong cooperativity, as long as the lattice is sufficiently flexible to accommodate these changes [**Halcrow, 2011**].

2.2.2 Mechanical properties of SCO materials

As we have seen above, the knowledge of the elastic constants of SCO materials and their spin-state dependence is of primary interest since the mechanical properties play an important role in the spin-transition behavior of SCO solids. Indeed, cooperative phenomena can be rationalized only by taking into account the volume misfit of the HS and LS states and the concomitant elastic interactions between the SCO centers [**Spiering et al., 1982**]. Obviously, the use of SCO materials in actuators also requires a detailed knowledge of their mechanical properties. Taking into account their central role in the SCO phenomenon, it is thus rather surprising to realize that the elastic constants of spin-transition materials have been determined only in a few occasions (and usually in only one spin state) using high pressure X-ray diffraction [**Shepherd et al., 2012, Granier et al., 1993**], Brillouin spectroscopy [**Jung et al., 1996**], AFM [**Hernandez et al., 2014**], and NIS (nuclear inelastic scattering) [**Rat et al., 2016a**], reporting values between ~1.5-8 GPa with $E_{LS \rightarrow HS}$ variations up to 30%. The main reason of this lack of information is that SCO materials are commonly obtained as nanoparticles, powders or microscopic crystals, which hinders the extraction of their mechanical properties using conventional characterization methods at the macroscopic scale. Additionally the extraction of such properties in tunable temperature is not obvious and instrumental challenges need to be overcome in order to obtain reliable data.

As a general rule, in the LS state the SCO molecule occupies smaller volume, has a higher density and higher stiffness with respect to the HS state. Due to the lack of complete elastic

data, the mechanical properties of SCO materials were often discussed on the basis of the Debye model, which assumes a simplified phonon spectrum based on a single parameter, the Debye temperature Θ_D or the Debye sound velocity v_D. In particular ^{57}Fe Mössbauer spectroscopy studies revealed approximately 10 % increase of Θ_D and v_D in the LS state in line with the expected stiffening of the lattice [**Felix et al., 2015**]. In the course of this thesis we used the NIS technique to extract mechanical properties of SCO powder samples, while SCO thin films and SCO polymer composite samples were analyzed using MEMS and DMA (dynamical mechanical analysis), respectively. These methods will be introduced in the next chapters.

Conclusions

In this chapter a global overview about the main principles governing the thermal, light and pressure-induced SCO phenomenon was provided. In particular we highlighted that structural aspects at different scales (coordination sphere, molecule, crystal packing …) have important consequences on the spin crossover properties in the solid state. The very important volume change of the coordination octahedron (ca. 25 %) is strongly attenuated at the macroscopic level, but still has significant consequences on the material properties (e. g. cooperativity) and provides scope for actuating applications. While the strain associated with the SCO is usually well characterized by crystallographic methods, the mechanical properties of these materials remain largely unknown. For this reason one of the objectives of this thesis was to develop an appropriate methodology to collect mechanical data for different forms of SCO materials.

Chapter 3. Microelectromechanical systems

Microelectromechanical systems (MEMS) are microscale devices able to transform a mechanical signal into an electrical one and vice-versa. They are widely spread in our daily life, but - even if recent technological progress has allowed a considerable advancements of these devices - several challenges remain. The coupling of SCO materials with MEMS brings promising opportunities not only for MEMS actuation, but also for the exploration of SCO mechanical properties. In order to succeed the fusion of these two well-known scientific worlds, efficient engineering strategies need to be set first. This chapter gives an introduction about the advancements, challenges and general principles of MEMS devices. Key parameters for actuation, detection and miniaturization are discussed. The integration of SCO actuators in MEMS is also overviewed.

3.1 Miniaturized electromechanical systems

The term of MEMS (micro-electromechanical system) makes reference to a miniaturized device which is built of mechanical and electronic components with feature sizes at the microscale. In a broad and most complete sense, MEMS devices comprise microfabricated sensors, actuators and electronics that function as integrated systems designed to interface directly with their environment. Such systems are constructed from materials that exhibit favorable mechanical, electrical and/or chemical properties. MEMS devices have significant impact in modern life. Some of their application in the commercial sector are vehicle safety, entertainment and recreation, healthcare instrumentation, telecommunications and information technologies (see an example in **Figure 13**). Some other technology areas start also to benefit from continuous advancements in MEMS technologies including medicine, aerospace, and energy. MEMSs are still very attractive for the scientific community due to their broad application field and also for the possibility of further miniaturization to obtain more sensitive nanoscale devices (NEMS, nanoelectromechanical systems). [**Graighead, 2000**]. In the following their main functions as sensors and actuators are described.

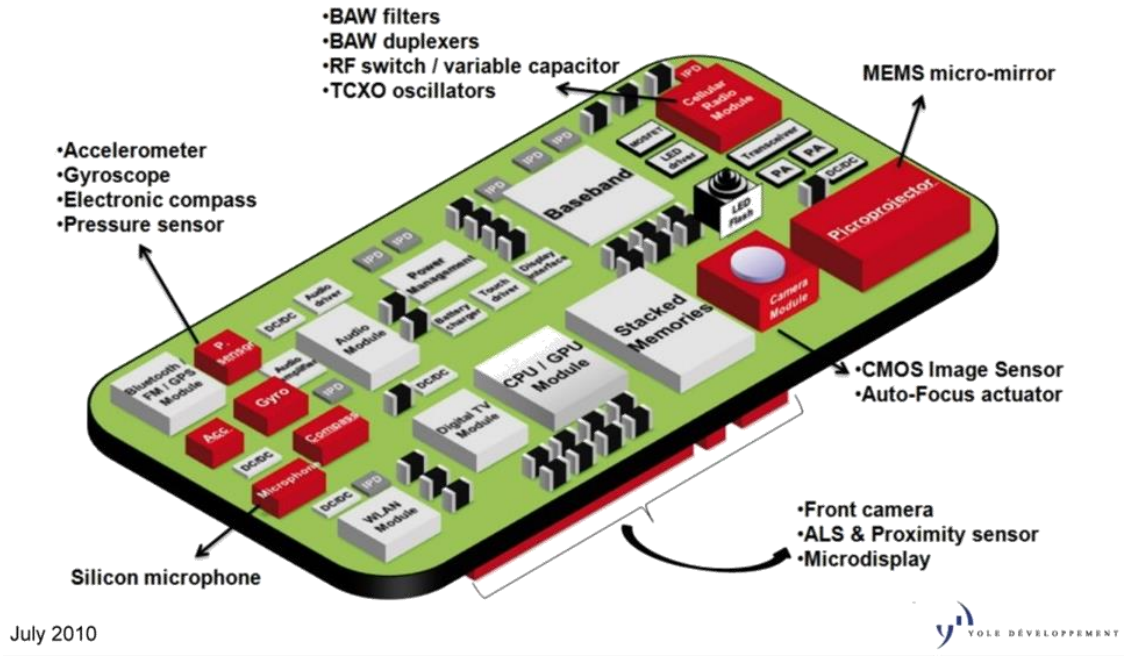

Figure 13: *Simplified view of a smart-phone board integrated by MEMS (in red) [**Scansen 2013**].*

3.2 MEMS as sensors

The main function of MEMS sensors is to generate an electrical signal once they are submitted to an external perturbation. The nature of the perturbation can be physical, chemical or biological.

MEMS sensors can be classified in different ways: i) by their transduction principle (physical, chemical, biological, optical, etc.), ii) by the measured parameter (pressure, acceleration, gas concentration) or iii) by their application (automobile, aerospatial or biomedical). For the purpose of this thesis, in the following we make reference to mechanical microsensors which are defined by their physical transduction. Mechanical microsensors transform a mechanical signal (mass, displacement, force, pressure etc.) into an electrical one (voltage, current etc). They can operate in two different modes: the dynamical regime and the static regime. In the dynamic regime (vibration), the applied perturbation is periodic in time. In the static regime (deformation) the perturbation can be considered constant or with slow variation.

3.2.1 Operation (Static vs. Dynamic regimes)

3.2.1.1 Static regime

MEMSs (for example a micro-cantilever) operating in the static regime, transform a static deformation (surface stress induced by an external perturbation (**Figure 14b**) into an electrical variation of current or voltage. Most of these microsystems require an external detection commonly achieved by optical deflection (**see Figure 16a**). The sensitivity of MEMS which operate in the static regime is closely related to the spring constant (k) of the mechanical part. This constant depends of the device geometry and the elastic properties of the integrated materials. The deflection amplitude ($\Delta\delta$) for these systems can be obtained by applying Stoney's equation:

$$\Delta\delta = \frac{4\,(1-v)L^2}{Eh^2}\Delta\sigma \qquad (3)$$

where υ, L, h , E and Δσ are the Poisson's coefficient, length, thickness, Young's modulus and stress difference, respectively, induced by the external perturbation (molecules absorbed on surface, mismatch bilayer properties etc.) [**Nicu, 2000, Dezest, 2015, Boisen et al., 2011**]

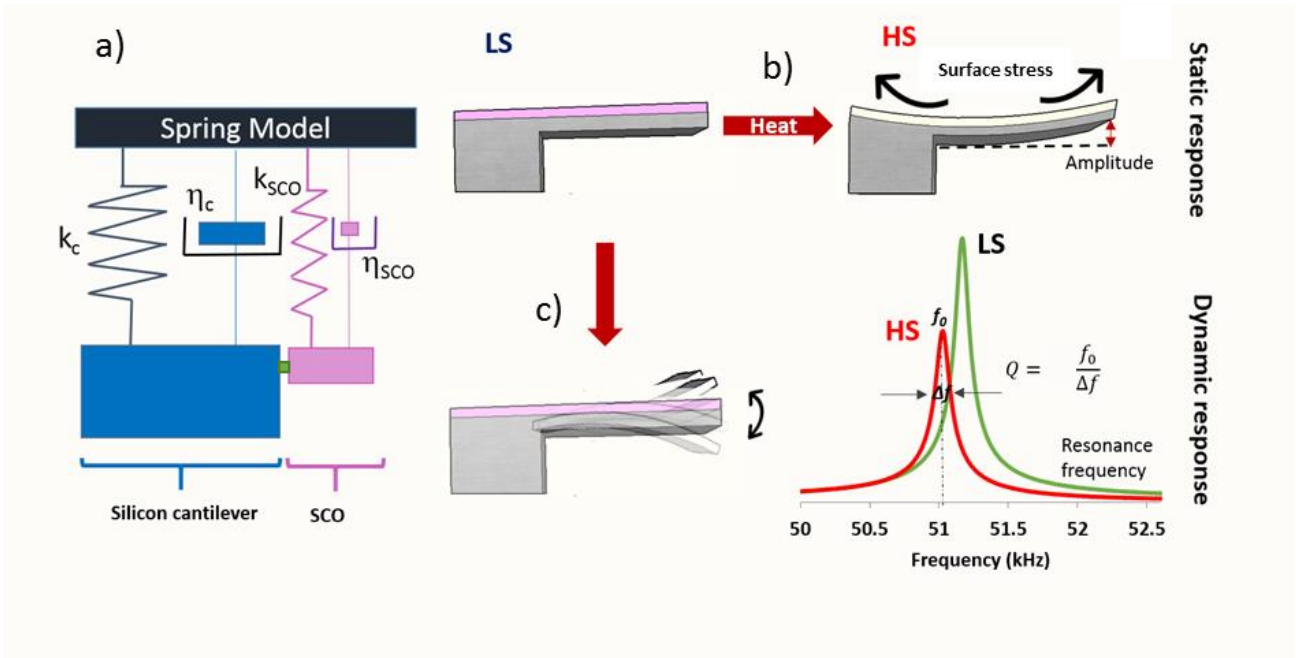

Figure 14: *Schematic representation of the possible mechanisms induced by the SCO phenomenon over a microcantilever. a) The elasticity and mechanical losses of the cantilever are modeled by a spring and a damper in parallel with spring constant k and damping coefficient η, respectively. Upon the thermally induced spin crossover the active compound generates a surface stress, which can be transduced b) as a displacement of the equilibrium position or c) as a shift of the resonance frequency of the system.*

The stress above and under the neutral bending line of a cantilever (the neutral bending line is located in the middle of the cantilever system) is responsible for the direction of the deflection, because stress causes forces which result in the bending moments. If the sum of the moments under the neutral bending line is larger than above, then the deflection is upward, otherwise downward. Let us consider the case of a thin film deposited on the upper surface of a cantilever (**Figure 15**). If the film contracts the cantilever bends upwards and the stress in the film is tensile (by convention, positive), while the stress in the top side of the cantilever is compressive (by convention, negative), i.e. the stress created in the cantilever balances the stress in the thin film whose compression is hindered by the supporting cantilever. *Vice versa* if the film expands the cantilever bends downward, the stress in the film is compressive while the stress on the top side of the supporting cantilever is tensile [**Boisen et al., 2011, Hollauer, 2007**].

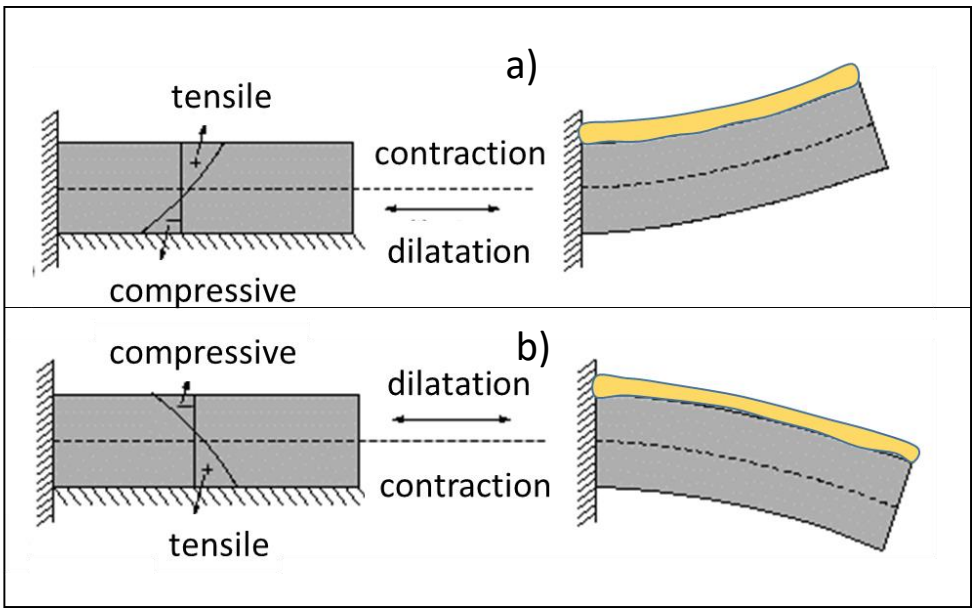

Figure 15: *Stress distributions in a fixed cantilever and its respective deflection after release of a tensile (a) or compressive (b) stress in the film [Adapted from* ***Boisen et al., 2011****].*

3.2.1.2 Dynamic regime

For MEMS in the dynamic regime (**Figure 14c**), a resonance shift results from the influence of an external excitation over the natural frequency of the mechanical structure. In the spectrum of the natural frequency of the system (amplitude vs. frequency) a resonance peak will have higher sensitivity if it is associated with a large amplitude and a high quality factor (Q). This

sensitivity is directly related to f_r and could be also affected by surface stress effects. The resonance frequency depends on the geometry, size and clamping configuration (**see Equation 6**). It is essential to be able to indicate or control the external factors (out of the one of interest) that can influence the natural resonance of the mechanical device. For instance the damping induced by environmental conditions is directly related to the quality factor. On the other hand internal stresses can induce a deformation and affect the linearity of the global mechanical response of the device. The Q factor characterizes the total stored energy in the system by the energy dissipated per radian of vibration during each cycle [**Kim et al., 2008**]. Q can be expressed by **Equation 4**:

$$Q = \frac{2\pi W_s}{W_d} \tag{4}$$

where W_s is the stored vibrational energy and W_d is the energy lost per cycle of vibration. Damping mechanisms can include thermoelastic losses, viscous damping and acoustic losses. This parameter determines the accuracy of the resonance frequency measurement as it relates the slope of the amplitude and phase curves near resonance. Therefore Q is also defined as:

$$Q = \frac{f_0}{\Delta f} \tag{5}$$

where f_0 is the resonance frequency, Δf is the full-width 3dB down from the resonance frequency peak.

As mentioned above, in the static regime surface stress affects directly the cantilever bending. In the case of the dynamic regime this parameter may have different effects depending on the system geometry. In the case of a double clamped cantilever the surface stress induces a force along the beam axis that modifies the resonance frequency. In contrast, for a single clamped cantilever the free end allows deformation and releases most of the stress influence over the resonance frequency [**Tamayo 2013**].

In the dynamic regime MEMS sensors can be made with either i) an integrated detection, where the mechanical signal is directly converted by the MEMS itself into an electrical signal, or ii) with an external detection, where the microsensor requires an external system in order to generate the electrical signal.

(i) *Microsensors with external detection in the dynamic regime*: Most of these types of microsensors are coupled with an optical detection system in order to generate the

electrical signal which translates the influence of the external perturbation. For this aim two common optical methods are described in literature: Interferometry and optical beam deflection. The latter is the most used and consists of a laser beam which is focalized over the mechanical vibrating part and it is reflected on a position sensitive photodetector. The amplitude variation induces a shift on the detected photocurrent. On the other hand in the interferometric method, light from a single source is split into two beams that travel through different optical paths which are reflected by mirror-like surfaces (*e.g.* silicon substrate) and combined again to produce interferences. The resulting interference fringes give information about the difference in the optical path length. This technique is widely used to measure small displacements.

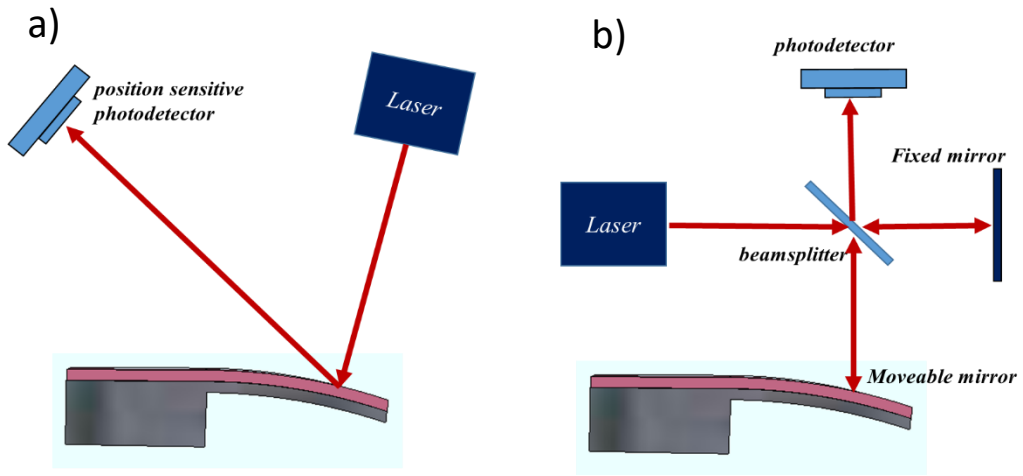

Figure 16: *Different optical detection methods used in the dynamical regime: a) beam deflection, b) interferometry (Michelson interferometer).*

(ii) *Microsensors with integrated detection in the dynamic regime:* This kind of microsensors can use three physical mechanisms: i) direct piezoelectric, ii) piezoresistive and iii) capacitive effects.

a. *MEMS with piezoelectric effect*. The piezoelectric effect represents the properties of certain materials to transform an electrical signal into mechanical deformation and *vice versa*. When a piezoelectric film is integrated into the mechanical cantilever, the piezoelectric effect allows to induce typically a displacement in the order of nanometers and force gradients in the order of nN/m [**Dezest, 2015**].

b. *MEMS with piezoresistive effect*. The piezoresistive effect represents the change in the resistivity of certain materials under the effect of a mechanical stress. In general polysilicon is used as a piezoresistive material. However, it is ca. 10 times less sensitive than monocrystalline silicon. For this reason, ionic implantation is used to diffuse boron atoms in monocrystalline silicon MEMS to form the piezoresistive zones and to obtain an optimal efficiency [**Dufour et al., 2012, Li et al., 2007**].
c. *MEMS with capacitive effect*. The principle of capacitive detection is based on the measurement of the maximum equivalent admittance of the microsensor. The device is integrated by two plane structures suited in a way they can form a flat capacitor. One of the structures is static. The second electrode is a microcantilever (or bridge) with a weak spring constant (≈10 N/m). The vibration of the structure modifies the space between the electrodes of the microsensor, therefore also modifies its admittance [**Nicu, 2000, Pelesko and Berstein 2002**].

3.3 MEMS as actuators

As seen in chapter 1, an actuator can be defined as a device capable to transform a source of energy into motion. MEMS actuators are deformable microstructures such as cantilevers, bridges or membranes. The most common energy transduction mechanisms in MEMS actuators are piezoelectric, magnetic, thermal and capacitive. For the purpose of this thesis we used the three former methods which will be briefly described in the following.

3.3.1 Piezoelectric actuation

This actuation method relies on the inverse piezoelectric effect where the materials deforms upon an applied electric field. Once a piezoelectric material is submitted to a sinusoidal electric field, the material vibrates. This material can be part or independent of the microdevice. If the piezoelectric is part of the mechanical device, this can be sandwiched between two electrodes on the resonator surface. When a transverse electrical field is applied an axial asymmetric stress induces a bending moment with respect to the neutral bending line. In the case of an external

piezoelectric drive the MEMS is glued on a piezoelectric transducer ceramic (**see Figure 21**). In comparison with other transduction methods, the piezoelectric approach has several advantages in terms of transduction efficiency and low power operation [**Dezest, 2015, Masmanidis et al., 2007**].

3.3.2 Magnetostatic actuation

In this kind of transduction, an alternative current is passed through a conductive loop, which is part of the mechanical structure. The presence of a static magnetic field will then induce a Lorenz force leading to the vibration of the microstructure. Depending on the direction of the magnetic field, the force can induce in plane or out of plane displacements. The amplitude of the excitation force $F_{Lorentz}$ is proportional to the intensity of the magnetic field and the applied electric current I, as well as the cantilever length (**Equation 5**). The main advantage of this transduction method is that it can achieve frequencies up to the GHz range [**Cleland and Roukes, 1996**].

$$F_{Lorentz}(\omega) = LBI(\omega) \tag{5}$$

3.3.3 Thermal actuation

This kind of actuation relies on the difference of thermal expansion coefficients between two different materials in a bilayer system. Upon temperature variation, the thermal expansion mismatch between the two different materials is responsible of axial stresses at the origin of the bending moment. The heat source can be electro-thermal (Joule effect) or photo-thermal (light irradiation) energy. Periodic temperature changes allow to put in vibration the mechanical structure. The efficiency of this actuating method relies on the capacity of the system to follow the frequency imposed by the excitation source [**Bargatin et al., 2007**]. The smaller the size of the system the higher the cut-off frequency.

3.4 Strategies to integrate SCO materials into MEMS devices

At the beginning of this thesis no single work related to the coupling between MEMS and SCO compounds was reported. To our best knowledge, apart from the experiments of the Stoddart team with rotaxane molecules (see Chapter 1), no other molecular actuators have been

interfaced with MEMS devices. A first challenge emerges from this fact since it is necessary to assess several technical aspects (active/passive material properties, device dimensions, actuation method, detection method, fabrication issues, etc.) to implement efficient strategies for the design and evaluation of MEMS-SCO performance (see **Figure 17**). For instance, a MEMS, which is developed to characterize the mechanical properties of SCO compounds requires a protocol, which is not appropriate to detect the spin transition and *vice versa* (see Chapter 4). In general, we should consider the following:

(i) The fabrication method needs to be adapted in order to maintain the integrity of the SCO material, but also to avoid the damage of the fragile mechanical parts during the microfabrication process.

(ii) The characterization set-up needs to be adapted to the environmental conditions required to induce the SCO (temperature, pressure, light, etc.) and/or preserve the material properties.

In the following we will briefly discuss these issues.

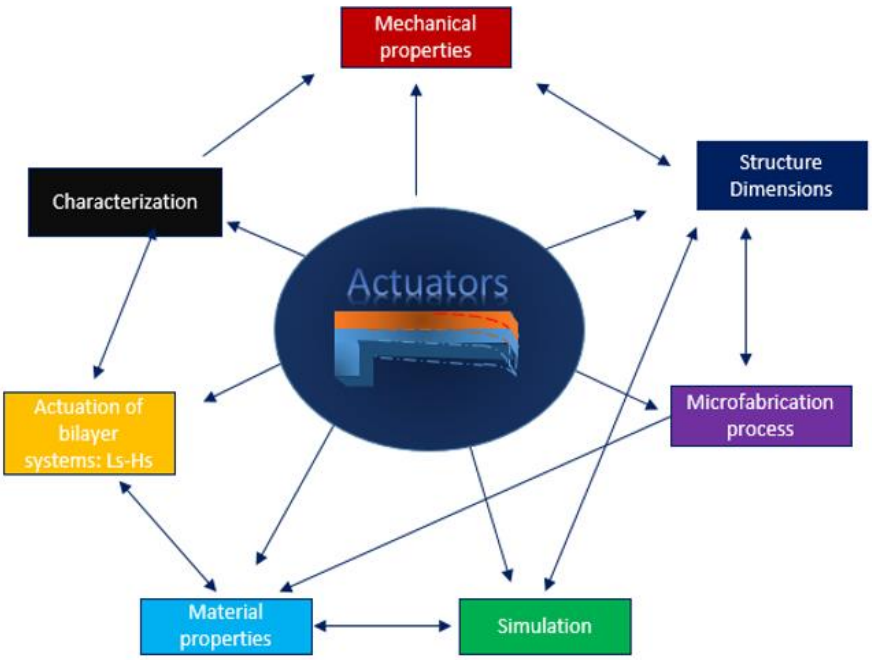

Figure 17: *Different parameters involved in the design and development of actuator devices.*

3.4.1 Silicon MEMS and their bulk micromachining

Most MEMS are made of silicon, even if other technologies using ceramics or polymers have been also developed. Similar to semiconductor integrated circuit manufacturing, MEMS devices are manufactured on a silicon or glass "wafer". This platform provides an economy of scale as hundreds or thousands of devices are manufactured at once in a batch process. In addition, many wafers can be processed simultaneously using automated or semi-automated equipment. The implementation of efficient ways to produce MEMS at large-scale offers significant cost benefit, high reliability and performance. The main steps to produce a standard silicon-MEMS process consist of (i) the mask design, (ii) photolithography patterning, and (iii) dry and wet etching [**Spearing, 2000**].

3.4.2 Alternatives to integrate SCO materials

Different approaches were studied in order to integrate SCO materials into silicon devices. One of the main issues to consider is the damage the SCO material may suffer during the silicon-MEMS fabrication (plasma cleaning, photoresist deposition, pattern transfer by solvents, etching etc. **See Annexes A1.3**). For this reason the SCO materials cannot be easily integrated before the very last stage of the process.

Some of the available deposition options to use at the final microfabrication step are: drop casting, spin coating, dip coating, thermal evaporation, and spray coating, though other techniques such as soft patterning or ink-jet may be also feasible. Below are described the techniques we used for the preliminary tests of this project.

- *Drop casting*: It consists of the deposition of a drop of solution followed by solvent evaporation. This technique may be one of the simplest ways to integrate SCO compounds whichever is the solvent. Low material waste is also an advantage. However, this method produces heterogeneous thickness along the device, which makes difficult a reliable mechanical analysis.
- *Spin coating*: This technique produces homogeneous depositions with a thickness control and reproducibility. However, it works best on flat surfaces. Once the silicon is shaped it is difficult to obtain a homogeneous distribution, there is material wasting and may produce device stacking and/or breaking (**see Annexes A.3.2**).

- *Vacuum thermal evaporation*: This technique is based on the sublimation of molecules in high-vacuum at high temperature. Evaporated molecules travel in straight lines inside the chamber and they condense on the substrate. The growth rate is controlled by tuning the temperature and the thickness is monitored with a microbalance. This method produces the highest quality nanometric films (**See chapters 4-5**).The challenge with this technique is to conserve the integrity and functionality of the SCO material. Notably SCO compounds with counter-ions and/or lattice solvents are not adapted. For this reason very few of them are adapted to be integrated by this technique.
- *Dip deposition*: This technique may provide quite good uniformity with the possibility to produce very thin layers. However, it requires additional surface functionalization for a selective growth, material is wasted and the manipulation of the MEMS during the dipping process can become difficult. Additionally it may produce material stagnation between the device and the substrate or stacking (in particular in the case of silicon-on-insulator wafers) (s**ee Annexes A.3.3**.).

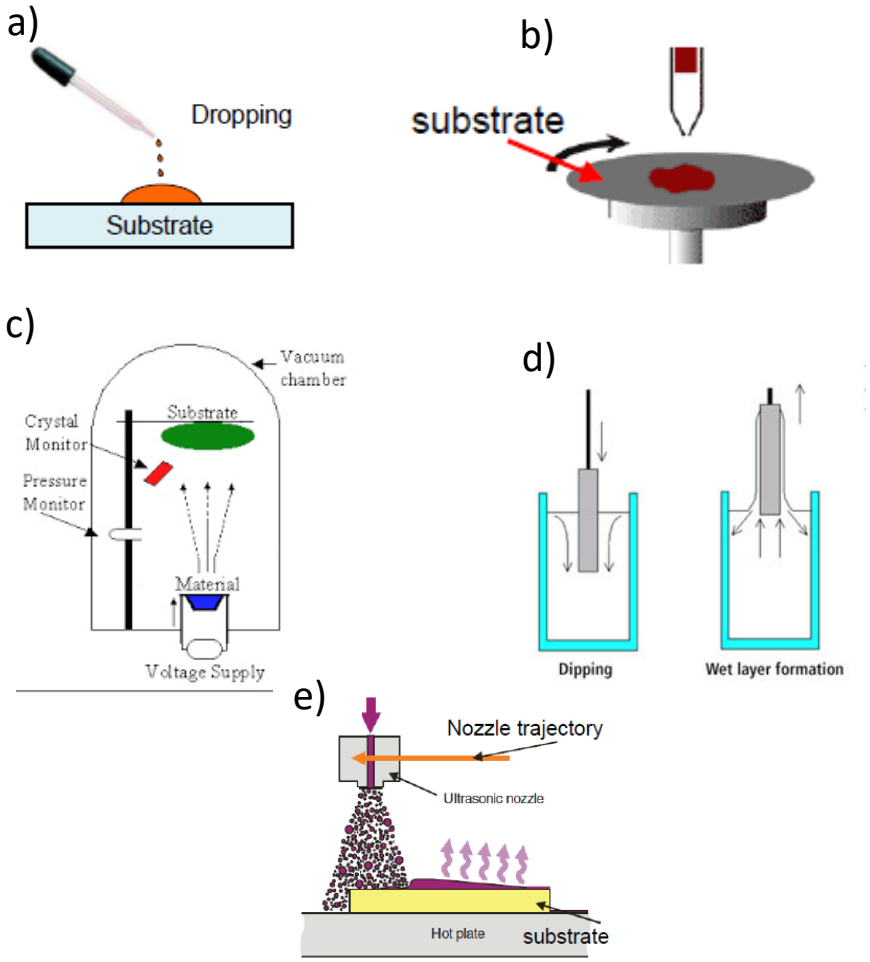

Figure 18: *Possible deposition methods to integrate SCO materials into MEMS devices: a) drop casting, b) spin coating, c) thermal evaporation, d) dip coating and e) spray coating.*

- *Spray coating*: This is a technique where wet droplets are sprayed on the substrate and merge into a full wet film before drying. It can be used with any substrate of different shapes and materials. It generates uniform films analogous to spin-coating with large area coverage. Thickness and morphology can be controlled by air pressure, solution viscosity, solvent properties, gun tip geometry, distance between nozzle and substrate. It is one of the most versatile integration techniques and it is suitable for the fabrication of micro and submicrometric films (**See Chapter 6**). However it is no suitable for the integration of homogeneous nanometer thick films.

Conclusions

In this chapter the general operation principles (static and dynamic) of MEMS devices have been reviewed, including the most common detection and actuation methods. The main challenges and possible approaches to integrate SCO materials into MEMS devices were also discussed. From preliminary experiments thermal evaporation and spray coating deposition appeared as the most reliable methods to integrate nanometer and micrometer thick SCO films, respectively. They will be discussed in chapters 4-6.

Chapter 4: MEMS integrating [Fe($H_2B(pz)_2)_2$(phen)] compound

The promising applications of SCO materials as actuators require a detailed knowledge of their mechanical properties, their effective integration in functional devices and appropriate strategies for transduction. In this chapter we describe the first achievement of this thesis to integrate spin crossover molecules as nanometric thin films into silicon MEMS devices with the aim to i) determine the mechanical properties of the SCO thin film and ii) detect the SCO using silicon mechanical devices. For this, a high quality thin layer of [Fe($H_2B(pz)_2)_2$(phen)] is deposited by thermal evaporation onto freestanding silicon bridges and cantilevers. From the mechanical response of the bilayer system in the dynamic regime it was possible to achieve a complete characterization of the mechanical properties of the thin layer using an optical interferometer. Additionally we also demonstrated the light-induced excited spin-state trapping (LIEEST) phenomenon by tracking the MEMS resonance frequency using piezoresistive detection. Details regarding the microfabrication process and the characterization set-up are discussed for each case. The results described in this chapter allow us to use MEMS for the first time as a new SCO detection method and as a straightforward tool to determine the mechanical properties of spin transition materials.

4.1 Generalities of [$Fe^{II}(H_2B(pz)_2)_2$(phen)]

The SCO compound we first integrated in MEMS devices is the [$Fe^{II}(H_2B(pz)_2)_2$(phen)] **1** complex (**Figure 19a**). This compound was selected for our experiments because of its ability to be conveniently deposited in a micromachining compatible process by thermal evaporation, leading to high quality and homogenous films. In addition, the spin-state of **1** can be easily altered by light irradiation.

The iron(II) mixed-ligand complex of formula [$Fe^{II}(H_2B(pz)_2)_2$(phen)] with $H_2B(pz)_2$ = dihydrobis-1-pyrazolylborate and phen = 1,10-phenanthroline (**1**) has been synthesized and structurally characterized by Real et al [**Real et al., 1997, Thomson et al., 2004**]. Magnetic susceptibility studies showed that **1** undergoes an abrupt spin transition in the 160−165 K temperature region (**Figure 19b**). Single crystal diffraction data have been recorded for **1** at 200 K, 100 K, 30 K and at 30 K after irradiation (LIESST). The crystal was found to be in the C2/c monoclinic space group at 200 K (HS), but it undergoes a loss of symmetry to a related, primitive structure ($P\bar{1}$), with unit cell volume approximately half that of the HS structure. This

loss of lattice symmetry in the LS state also leads to the loss of the C_2 molecular symmetry and this dramatic structural change explains the structural damage which is often observed with these crystals.

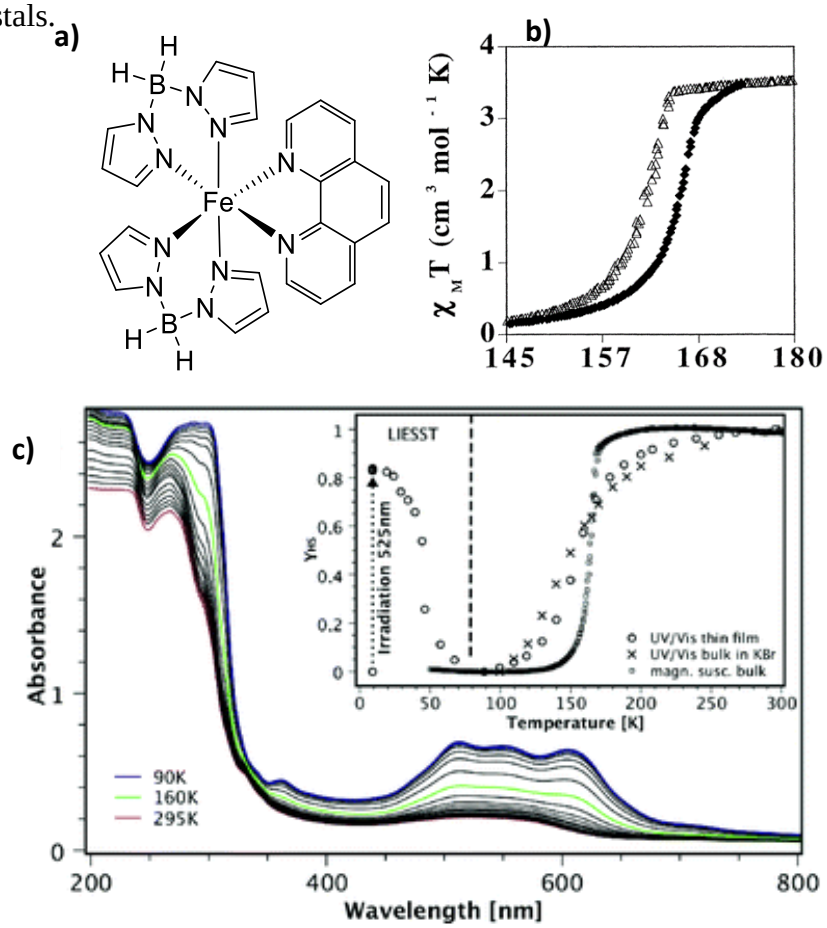

Figure 19: *a) Molecular structure of **1** and b) Variable temperature magnetic suceptibility of the powder of **1** showing thermal spin transition around 163 K [**Real et al., 1997**]. c) Variable temperature optical absorption of a 500 nm thick film of **1**. The inset shows the thermally (100-200 K) and phtotoinduced (<50 K) spin crossover phenomenon between the high spin and low spin states in the film in comparison with the bulk sample [**Naggert et al., 2011**].*

Thin films of complex **1** were deposited by vacuum evaporation first by Naggert et al. [**Naggert et al., 2011**], followed by numerous studies in different teams [**Zhang et al., 2014, Gopakumar et al., 2012, Pronschinske et al., 2013**]. Optical spectroscopy provided evidence that the deposited complex exhibits both thermal and light-induced SCO, but in comparison with the crystalline state, the transition in the film becomes very gradual, which is likely related to its reduced crystallinity [**Palamarciuc et al., 2012**]. As shown in **Figure 19c**, upon cooling from ca. 200 to 100 K, the HS electronic configuration of the molecules in the film is gradually

transformed into the ground LS state. However, below ca. 40 K, it is possible to fully depopulate the LS state by shining white light on the sample. The lifetime of the photo-induced metastable HS state at 10 K in the dark is ca. 11 days, [**Moliner et al., 2002**] i.e., the system remains trapped in the HS state long time after the photoexcitation.

4.2 Determining mechanical properties

4.2.1 Analytical approach to determine the mechanical properties of 1.

The mechanical properties of a monolithic cantilever beam are correlated with its resonance frequency f_r by **Equation 6**. In the case of a bilayer system f_r is given by **Equation 7a** [**Hoy-Benitez et al., 2012**] with λ_n as the modal coefficient related to the n^{th} vibrational mode, l the length, ρ the material density, A the cross-sectional area, $\hat{E}I$ the flexural rigidity, w the width, t the thickness and $\hat{E}$ the effective Young´s modulus. The subscripts Si and SCO refer to the silicon substrate and the SCO film, respectively.

$$\boldsymbol{f_n = \frac{(\lambda_n)^2}{2\pi l^2}\sqrt{\frac{\hat{E}I}{\rho A}}} \tag{6}$$

$$\boldsymbol{f_n = \frac{(\lambda_n l)^2}{2\pi l^2}\sqrt{\frac{\hat{E}I}{\rho_{Si}A_{Si} + \rho_{SCO}A_{SCO}}}} \tag{7a}$$

$$\boldsymbol{\frac{1}{\hat{E}I} = \frac{12\left(\hat{E}_{Si}t_{Si} + \hat{E}_{SCO}t_{SCO}\right)}{w\left(\hat{E}_{Si}^2 t_{Si}^4 + \hat{E}_{SCO}^2 t_{SCO}^4 + \hat{E}_{Si}\hat{E}_{SCO}t_{Si}t_{SCO}\left(4t_{Si}^2 + 6t_{Si}t_{SCO} + 4t_{SCO}^2\right)\right)}} \tag{7b}$$

$$\boldsymbol{\hat{E} = \frac{E}{(1-\nu^2)}} \tag{7c}$$

The elastic modulus of **1 (**E_{SCO}) can be obtained either by solving **Equations 7a-b** or by using the analytical expression (3), which considers a bilayer cantilever of rectangular cross section and correlates its experimental resonance frequency before (f_s) and after (f_{bi}) SCO deposition with the relative values of the elastic modulus ($E_r = E_{SCO}/E_{Si}$), thickness ($t_r = t_{SCO}/t_{Si}$) and density ($\rho_r = \rho_{SCO}/\rho_{Si}$) [**Hoy-Benitez et al., 2012, Withing et al., 1995**].

$$\left(\frac{f_{bi}}{f_s}\right)^2 = \frac{(E_r t_r^3+1)(E_r t_r+1)+3E_r t_r\,(t_r+1)^2}{(\rho_r t_r+1)(E_r t_r+1)} \tag{8}$$

Additionally, when the film is deposited on a double clamped cantilever (i.e. on a bridge), the residual stress (σ) due to a compressive or a tensile axial force *N* may lead to a downshift or upshift of the experimentally observed resonance frequency $f_r\,(N)$ with respect to the expected resonance frequency $f_r\,(0)$. Once E_{SCO} of the film is obtained from **Equation 8** using data obtained with the cantilever, we are able to quantify the residual stress using data obtained with the bridge by adapting the analytical expression described by Bowstra and Geijselaers [**Bouwstra and Geijselaers, 1991**] (**Equations 8 and 9a-d**) with *v* as the Poisson ratio and Υ_1 as coefficient for the contribution of the applied axial force for the first resonance mode.

$$f_r(N) = f_r(0)\sqrt{1+\Upsilon_1\frac{Nl^2}{12\hat{E}I}} \tag{9a}$$

$$N = (1-\nu_{bi})\sigma_{bi}A \tag{9b}$$

The Poisson ratio of the bilayer contribution can be expressed as:

$$\nu_{bi} = \frac{t_{Si}\nu_{Si}+t_{SCO}\nu_{SCO}}{t_{Si}+t_{SCO}} \tag{9c}$$

and the stress of the bilayer contribution as:

$$\sigma_{bi} = \frac{\sigma_{SCO}t_{SCO}+\sigma_{Si}t_{Si}}{t_{SCO}t_{Si}} \tag{9d}$$

4.2.2 MEMS fabrication and integration of the SCO complex 1

The powder of **1** was synthesized by Sylvain Rat (LCC-CNRS) following the method described in ref. [**Rat et al., 2016a**].

The fabrication and characterization of MEMS described in this section were carried out at the micro and nanotechnologies platform of LAAS-CNRS, in a clean room with controlled particulate concentration, temperature, humidity, and light intensity/spectrum (for certain operations), which permits the micro and nanoscale patterning and treatment of materials and device prototyping.

To validate and simplify this study, the most important considerations are the well-shaped devices and good dimensional characterization of the whole structure before and after deposition of **1**. Standard microfabrication process of bridges and cantilevers (9 µm width, 50 µm length, 2 µm thickness) was achieved using a SOI wafer (2 µm Si, 1 µm SiO_2, 400 µm thick Si from Soitec). The devices were patterned using UV-photolithography (ECI 3012 photoresist), followed by a vertical RIE (reactive ion etching) and wet HF etching. At the final step, 179 nm of **1** was deposited by thermal evaporation at 383 K under high vacuum (10^{-7} mbar) at a rate of 0.5 $A^{\circ}s^{-1}$ (**Figure 20a-d**). The device geometry and film quality were controlled by scanning electron microscopy (SEM) using a Hitachi S-400 instrument and atomic force microscopy (AFM) using a Bruker-Icon in amplitude-modulation mode. Film thickness and density were determined by X-ray reflectivity (XRR) and focused ion beam (FIB) using a Bruker-XRD (Cu Kα X-ray 1.54 Å) and a HELIOS 600i instrument, respectively.

As a result, well-shaped cantilevers and bridges were fabricated and high quality deposition was obtained (roughness 0.26 nm) (**Figure 20f-k**). Each chip includes more than 1600 devices/cm^2. At this point it may be worth to note that such high quality devices could be obtained only in a second fabrication run (**see Annexes A2 and A3** for more details of the encountered problems along the microfabrication process and their solutions).

4.2.3 Mechanical Characterization

4.2.3.1 Fabry-Perot Interferometer

The MEMS chips were mounted on a piezoelectric disk which was electrically actuated before and after deposition of **1** and the movement was followed by a Fabry-Perot interferometer at room temperature in controlled pressure conditions. Below is given a general description of the characterization set-up (**Figure 21**).

In order to produce the mechanical movement, the sample is mounted on a motorized piezo stage, this is placed inside a vacuum chamber which allows to reduce the effect of air damping. The piezo-shaker actuates in a collective manner all the devices on the chip.

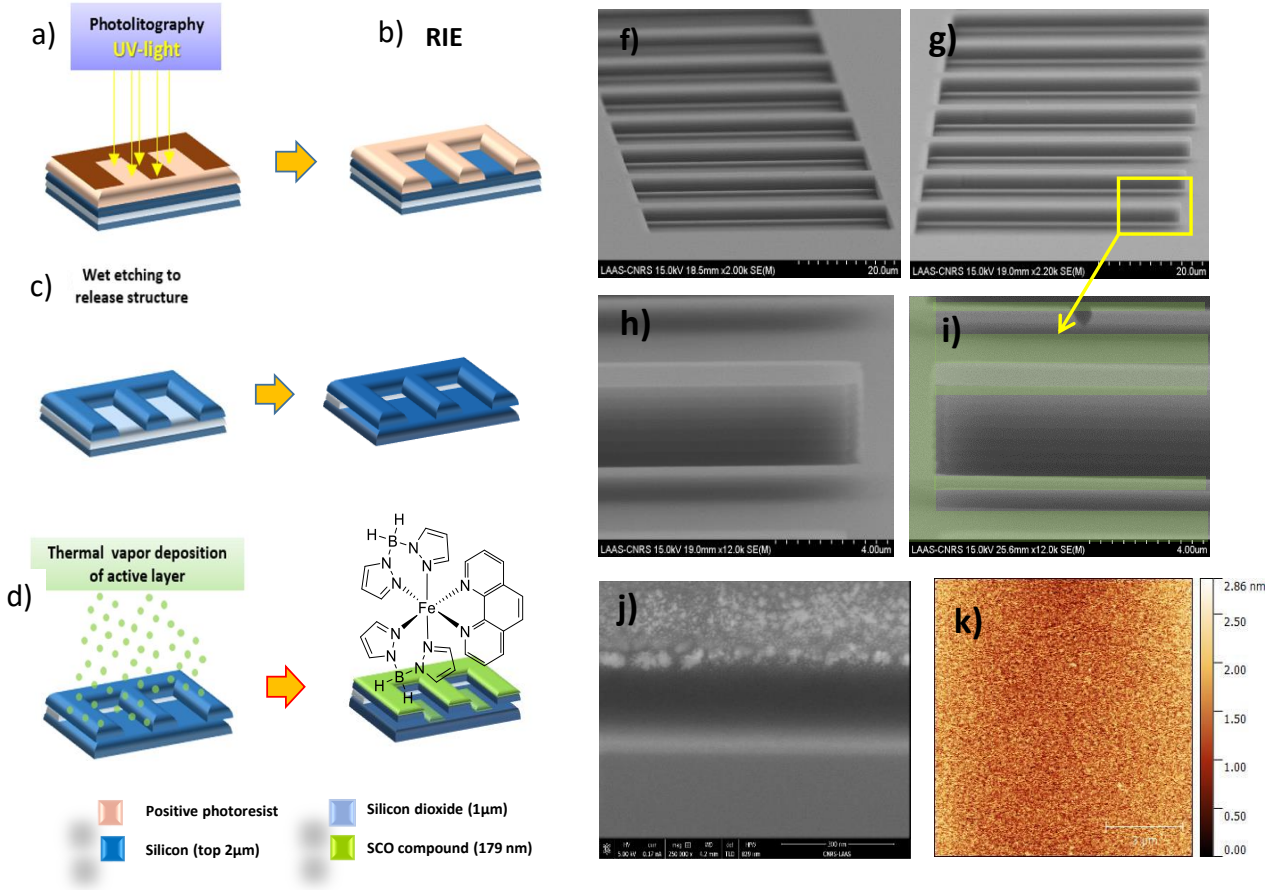

Figure 20: *Microfabrication process of MEMS a) photolitography, b) vertical RIE etching, c) HF wet etching, d) thermal evaporation of* ***1****. SEM images of f) bridges and g) cantilevers. Zoomed image of cantilever tip h) before and i) after the deposition of* ***1****. j) FIB milled cross section of a bilayer cantilever covered with an additional metal layer to observe the thickness of the deposited film of* ***1****. k) AFM topography image of the film (image size 10 x 10 µm²).*

The movement detection is based on an optical interferometry which consist on a He-Ne laser (30 mW rated power, λ = 632 nm) focalized by a beam expander (X5) and a microscope objective (x20, N.A. 0.28). The final position of the laser to the surface of the sample is defined by the motorized piezo stage system. The operation is observed on real time by a CMOS camera under a DEL (Diode Electro Luminescent) lightening (λ = 470 nm). The air gap between the

resonator and the substrate surface provide a Fabry-Perot cavity. The cantilever/bridge mechanical oscillations modify periodically the size of the optical cavity.

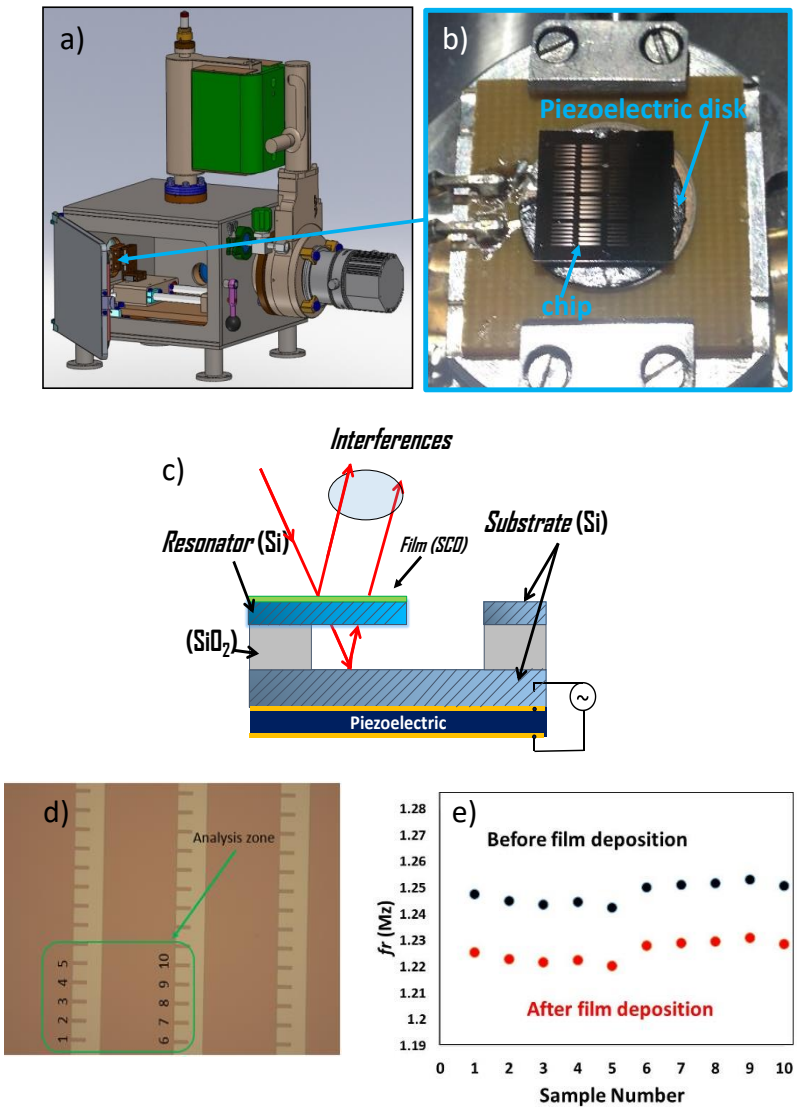

Figure 21: *MEMS characterization set-up, a) vacuum chamber, b) chip mounted on Motorized piezo-stage, c) Basic scheme of Fabry-Perot interferometer, d) Analysis zone and e) resonance shift before and after deposition of 1.*

The intensity of the resultant beam obtained from the interferences of the reflected beams of the two surfaces is then modulated by the vibration frequency of the mechanical structure and the amplitude is directly proportional to the resonator displacement. The beam is deflected towards a photo-detector (New Focus 1601) from which the AC signal is connected to a

Network Analyzer (Agilent 4395A) to track the response of single cantilevers at the excitation frequency [**Denis, 2015, Salomon et al., 2012**].

4.2.3.2 Young's modulus and Axial stress.

Table 3 summarizes the different material properties used in this study. In the case of silicon these values are well known from the literature [**Hopcroft et al., 2010**]. For compound **1**, most of parameters are obtained from the present study while *v* is an approximation for these materials [**Felix et al., 2015**]. The density value obtained by XRR for the SCO complex is ≈1.39 ± 0.01 kg/m^3 which is in good agreement with the one reported in the case of the powder [**Rat et al., 2016a**]. It is important to notice the mechanical values for **1** correspond to the high spin state as they were determined at room temperature. (N.B. The SCO from HS to the LS state occurs between 200 and 100 K). As the silicon thickness may vary depending on the analysis zone (±0.2µm according to the supplier), we use the experimentally determined value of f_r before deposition in conjunction with **Equation 6** to extract a more accurate thickness t_{Si}.

Table 3 : *Material properties and MEMS geometry for devices described in section 4.2.2.*

	Silicon	**SCO_{HS} (complex 1)**
Density $\boldsymbol{\rho}$ (kgm^{-3})	2330 [**Hopcroft 2010**]	1.39 ± 0.01
Young's modulus $\boldsymbol{E}$ (GPa)	169 [**Hopcroft 2010**]	6.9 ± 0.1
Poisson ratio $\boldsymbol{v}$	0.22 [**Hopcroft 2010**]	0.3 ± 0.05 [**Felix 2015**]
Residual stress **σ** (MPa)	N.A.	74.8
	Cantilever	**Bridge**
Modal coefficient $\boldsymbol{\lambda_1}$	1.875	4.71
Length $\boldsymbol{l}$ (µm)	50	50
Width $\boldsymbol{w}$ (µm)	9	9
Thickness $\boldsymbol{t}_{SCO}$ (µm)	0.179	0.179
Thickness $\boldsymbol{t}_{Si}$ (µm)	2.2	1.7
Coefficient $\boldsymbol{\Upsilon_1}$	NA	0.2949 [**Bouwstra and Geijselaers 1991**]
Resonance frequency substrate $\boldsymbol{f}$**s** (MHz)	1.2486	5.8
Resonance frequency bilayer $\boldsymbol{f}_{bi}$ (MHz)	1.2259	5.728

Figure 22 shows the resonance frequency of the cantilever (**Figure22a**) and bridge (**Figure 22b**) before and after the film deposition. 10 different devices were tested and regardless of the initial value of f_r, all of them present similar shifts of f_{r_shift} = 22.7 kHz (**Figure 21e**) corresponding to a mass addition of 0.113 ng. By using Eq. 3 we were able to extract the elastic modulus of the film E_{SCO} = 6.9 ± 0.1 GPa. If we introduce this value into Eq. 2a-b, the theoretical f_r shift (22.2 kHz) due to SCO deposition is very close to the experimental value (22.11 kHz).

When compare the elastic modulus of the film obtained in this thesis (6.9 GPa) Vs the powder obtained by NIS (4.8 GPa) [**Rat et al., 2016a**], the agreement is reasonable, in particular if one takes into account the fact that crystallinity is lost in the films [**Palamarciuc et al., 2012**]. By assuming that the elastic modulus variation between the two spin states is the same for the film as for the powder (ca. 8%), we can predict a LS elastic modulus of E_{SCO} = 7.5 GPa.

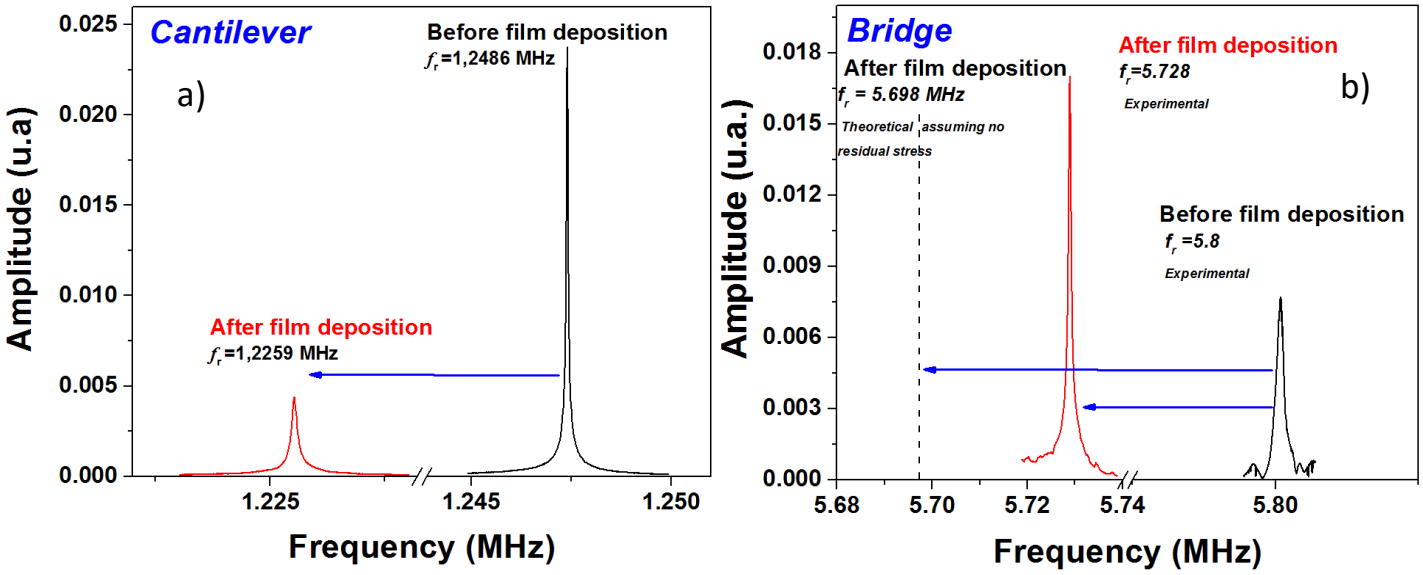

Figure 22: *Resonance frequency curves before and after film deposition for cantilevers a) and bridges b).*

In the case of bridges, as we can observe from **Figure 22b**, the experimental resonance frequency after the film deposition ($f_r(0)$ = 5.728 MHz) is higher than the theoretical one ($f_r(N)$ = 5.698 MHz obtained from **Equation 9a**) which allows us to evidence a residual stress in the material as consequence of an axial tensile force of N = 85.5 μN. By introducing these values in **Equations 9c-d**, the stress of the SCO film corresponds to σ_{SCO} = 74.8 MPa, which is a non-negligible value.

4.2.3.3 Work density.

Additionally we can also predict the work density which describes the maximum mechanical work output per unit volume of the active material ($W/V = E\varepsilon^2/2$). For this we consider the volume change determined previously for the crystalline powder upon the spin transition (4.5%). In the case of the film this change is isotropic (the film is amorphous) and we can expect a linear strain of $\varepsilon = 1.6\%$. This leads to a work density of $W/V = 0.93$ Jcm^{-3} (LS to HS) and $W/V = 0.97$ Jcm^{-3} (HS to LS). These values are in good agreement with those obtained for similar materials [**Shepherd et al., 2013**] and confirm their high actuating performance in terms of work density.

4.3 SCO Detection by MEMS using light energy.

4.3.1 MEMS characteristics

4.3.1.1 Electromagnetic Actuation/Piezoresistive Detection

The microelectromechanical devices used for the SCO detection are more complex since they integrate the actuation and detection elements into the same system. These devices were designed and fabricated by Liviu Nicu and Daisuke Saya (LAAS) in the frame of a parallel project. Only a general description about their function is described in this thesis (for more details on similar operation and fabrication principles see **Alava et al., 2010 and Dufour et al., 2011**). These devices consist of a silicon chip that includes two cantilevers: one is freestanding, thus free to move and vibrate, while the other one is fixed to the substrate (**Figure 23**). The latter serves as a reference to offset the environmental variations over the measurements. The general properties of the device are showed in **Table 4**.

Table 4: *MEMS geometry for devices described in section 4.3.1.*

Geometry	Free	Reference
Modal coefficient λ_1	1.875	
Length l (μm)	500	500
Width w (μm)	120	120
Thickness t_{SCO} (nm)	200	200
Thickness t_{Si} (μm)	20	546

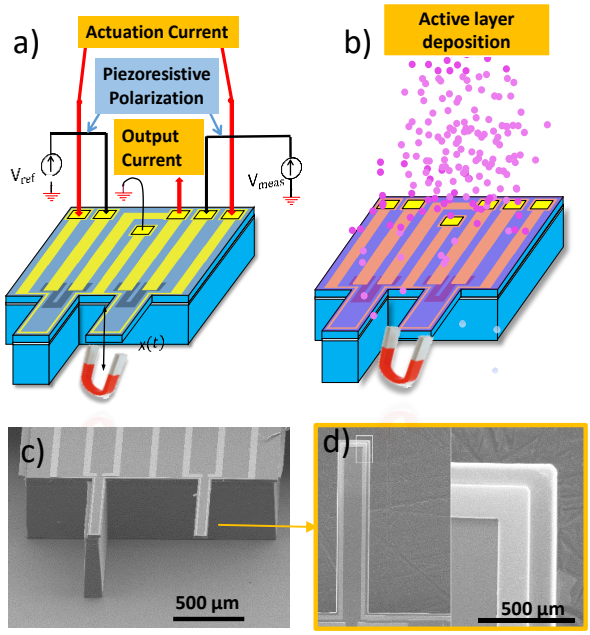

Figure 23: *a) Scheme of the MEMS device and the associated magnetic actuation-piezoresistive detection method. b) Scheme of the MEMS device covered with the SCO compound by thermal evaporation. c) A representative SEM image of the free-standing and reference cantilevers is also shown with a d) zoomed image of the cantilever tip showing the gold path for the actuation current.*

Magnetic actuation is used to drive the freestanding cantilever at its resonance frequency. To this aim, a sinusoidal current ***I*** is applied through a conducting path integrated onto the microcantilever, which is placed in the presence of a static magnetic field. The detection of the mechanical vibrations is performed by piezoresistors integrated at the clamped-end of the two microcantilevers where stress induced by displacement is maximal.

A home-built vector network analyzer (VNA) card is used to detect the piezoresistive response of the cantilever. For this, two complementaries polarization voltages are injected in free (V_{free}) and reference (V_{ref}) piezoresistances. The VNA card measures the output signal from the transimpedance amplifier. This amplified current (i_{out} (ω)) is the result of the sum of both I_{ref} + I_{free} (**see Equation 10**) which corresponds to the variation of the piezoresistance. This is transformed in a graphical signal. For a better description of the VNA card see **Annexes A4.2**.

$$i_{out} = I_{ref} + I_{free} = \frac{V_{ref}}{R_{ref}} + \frac{V_{free}}{R_{free} + \Delta R_{free}(\omega)} \qquad (10a)$$

$$With \quad \frac{V_{ref}}{R_{ref}} = -\frac{V_{free}}{R_{free}} \tag{10b}$$

$$i_{out}(\omega) \approx -I_{free}\frac{\Delta R_{free}}{R_{free}}(\omega) \tag{10c}$$

4.3.2 Characterization Set-up

The experiments were conducted by placing the MEMS devices, either coated with **1** or uncoated, on the cold finger of an Oxford Instruments OptistatCF liquid helium cryostat in a static He gas atmosphere. A fiber coupled halogen lamp (100 W) was used to shine white light on the device through the upper cryostat window, while a magnet was placed underneath for proper MEMS actuation (**see figure 24**).

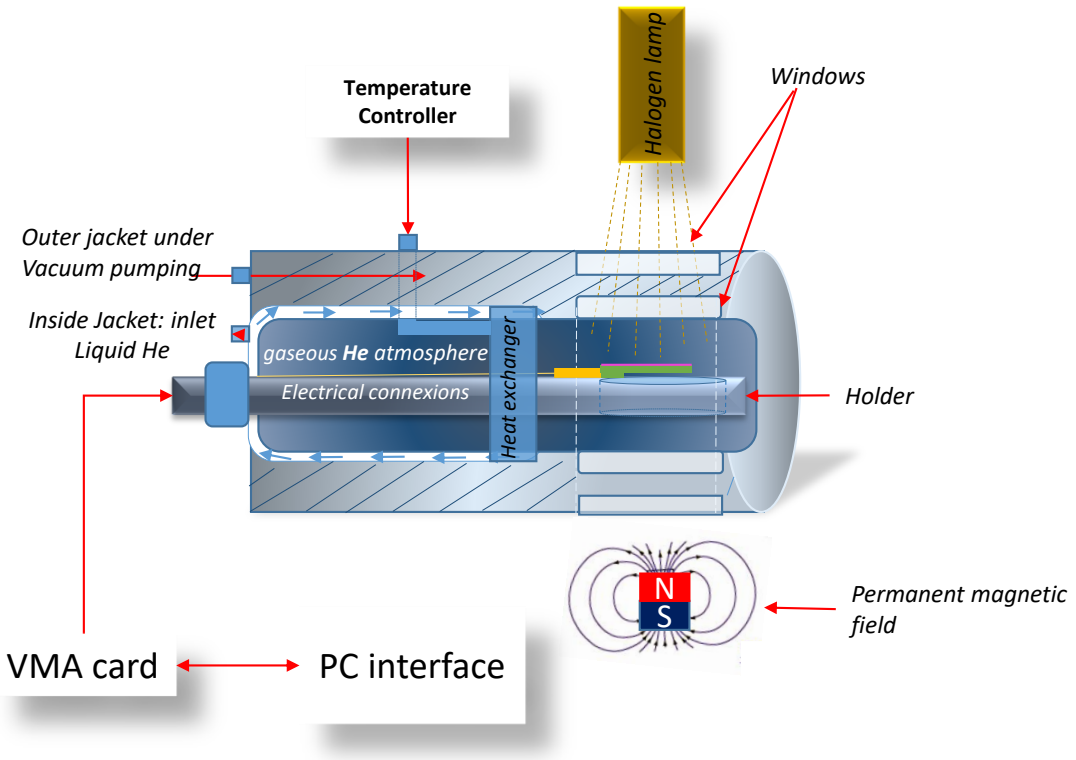

Figure 24: *Variable temperature MEMS characterization set-up allowing for light irradiation of the sample and magnetic actuation of the MEMS.*

4.3.3 Results and discussion

The advantage of using light excitation in this work is that the mechanical response (resonance frequency) of the MEMS cantilevers in the two spin states can be recorded in strictly the same temperature/ pressure conditions—before/after light irradiation—thus allowing us to study the sole influence of the SCO. Indeed, the resonance frequency of the silicon cantilever is extremely sensitive to temperature changes due to the substantial temperature dependence of the density and Young's modulus of Si. Hence, it is practically impossible to separate contributions from the temperature and spin-state changes on the mechanical behavior of the MEMS during the thermal spin crossover process (**See Figure 25**).

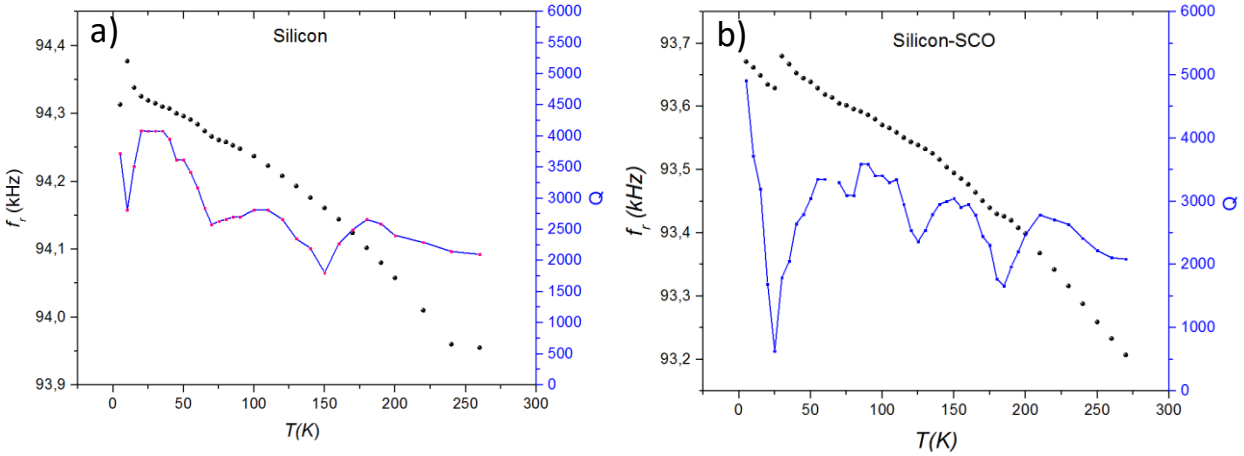

Figure 25 : *Temperature dependance of the resonance frequency and quality factor for uncoated a) and coated b) devices.*

To follow the light-induced excited spin-state trapping (LIESST) phenomenon in **1**, we used a similar procedure as described in [**Lefter et al., 2016**]. The device was first cooled down from 240 K to 10 K in the dark. At this temperature the ground state is LS, but the HS state can be easily populated by white light irradiation. The lifetime of this metastable HS state at 10 K is sufficiently long (several days) so as to characterize it even when the light is turned off. Once the temperature (and thus, the freestanding cantilever's resonance frequency) was stable, light was turned ON and OFF several times with intervals of 50 s. The variation of the resonance frequency (f_r) of the SCO-MEMS device during this experiment is shown in **Figure 26**. Upon the first irradiation cycle, one can observe a ca. 0.52 ± 0.1 Hz remnant drop of the resonant frequency (Δf_r LIESST in **Figure 26a**), which persists in the dark and which is not affected by further irradiation cycles. We thus assign this change to the LIESST effect.

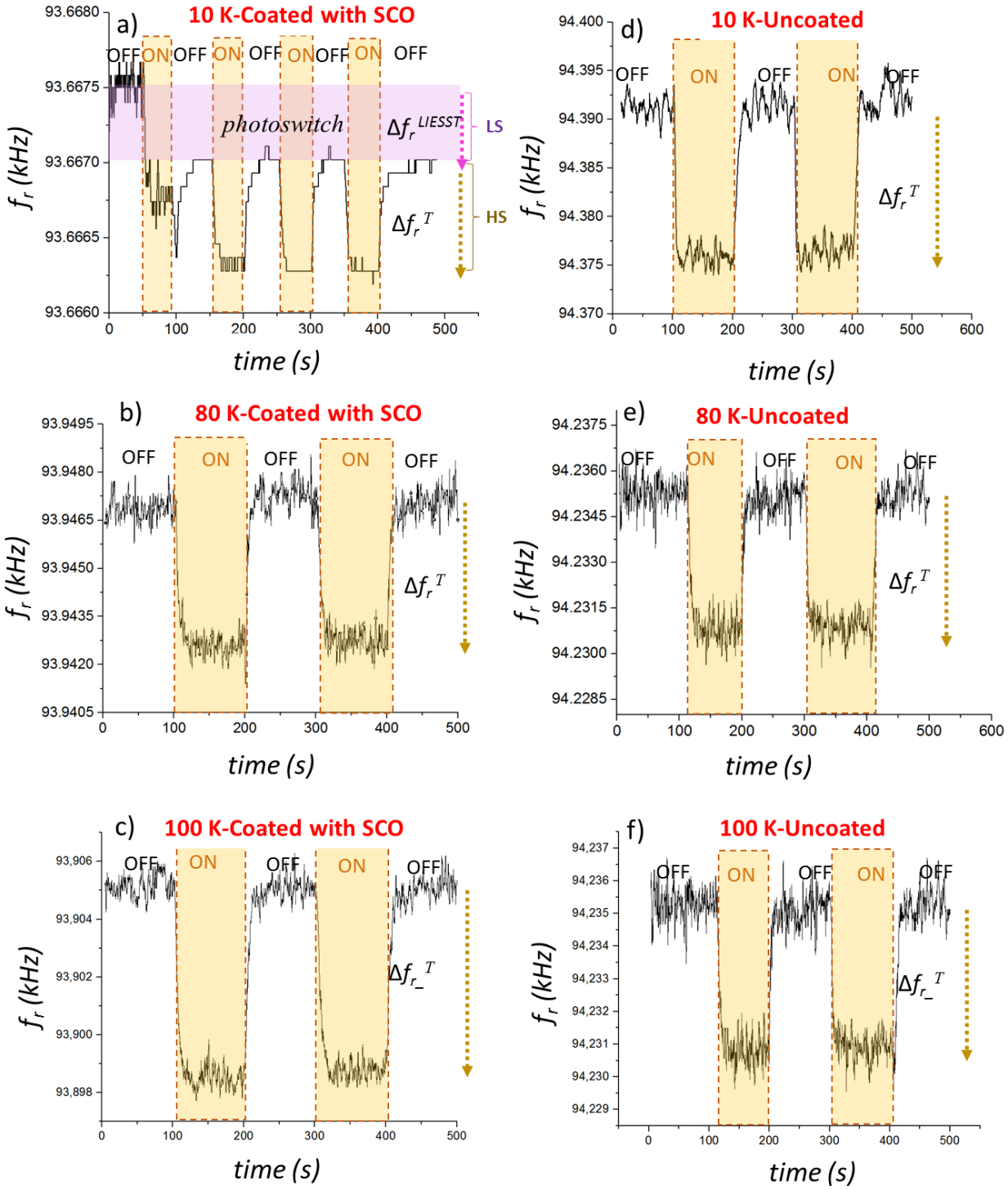

Figure 26: *Resonance frequency tracking of the MEMS at 10 K, 80K and 100 K upon successive light irradiation cycles (ON and OFF) for a device coated with a 200 nm thick of 1a)-c) and uncoated device d)-f).* Δf_r^{LIESST} *and* Δf_r^{T} *stand for the frequency shifts induced by the light induced spin-state switching (LIESST) and photothermal effect respectivelty.*

An additional, fully reversible resonance shift of 0.68 ± 0.1Hz is also observed during each successive irradiation cycle, which we attribute to the photo-thermal effect (Δf_r^{T} in **Figure 26a**). From the temperature dependence of f_r (**see Figure 25**, and more details in **Anexes A5.1**), we can estimate that the magnitude of the photo-thermal effect for this experiment is ca. 0.3–0.5 K. Above ca. 40 K, the lifetime of the metastable HS state drops quickly due to the thermal activation of the relaxation process [**Palamarciuc et al., 2012, Moliner et al., 2002**].

The device was heated up to 240 K to recover its initial state and then repeated the previous experiment at 80 K and 100 K where the LIESST effect is not efficient. Indeed, as shown in **Figure 26b-c** at these temperatures only the reversible photo-thermal effect could be detected, thus providing support for the assignment of the persistent resonance shift at 10 K to the LIESST effect. In order to assert that this phenomenon is related to the presence of the film of **1**, we repeated the three experiments (light irradiation at 10 K, 80 K and 100 K) with an uncoated device. This latter exhibited systematically the reversible photo-thermal effect (Δf_r^{T}) upon turning on and off the light source (**Figures 26d-f**), but we could not observe at any temperature the persistent resonance shift (Δf_r^{LIESST}) characteristic of the coated device. Further experiments at 7 K confirmed that the main observations are perfectly reproducible. (**See Annexes A4.3**). As a final remark, it is worth to compare these results with those we reported recently when monitoring the electrical current in thin (10–100 nm) junctions of **1** upon light irradiation [**Lefter et al., 2016**]. Of particular interest is that a persistent current drop in the junctions was systematically observed upon the first irradiation cycle at 5 K, while only a reversible photocurrent was detected at 100 K. The parallel between the two experiments (mechanical device and tunneling junction) is obvious.

The fact that the resonance frequency of the cantilever decreases when going from the LS to the HS state is consistent with the softening of the crystal lattice in the latter phase. Indeed, as discussed in Ref. [**Rat et al., 2016a**] the Young's modulus of **1** decreases by ca. 8% in the HS state. At the same time, the mass density decreases also by 5%. Obviously, this will also impact the geometry, primarily the thickness of the film. For a better understanding of the role of these different parameters in the coupling of molecular spin-states to the MEMS mechanical behavior, we can consider the analytical method described in the previous section **Equations 7a-c** which correlates the resonance frequency with the material properties and geometry in a bilayer beam [**Hoy-Benitez et al., 2012**].

Table 5 summarizes the relevant material properties for silicon and compound **1** in both spin states. In the case of **1** bulk values were used as a first approximation [**Rat et al., 2016a**]. Not only the material parameters are approximated in our calculations, but also the device geometry since we neglect the influence of metallic lines and the SiO_2 layer. Nevertheless, the magnitude and the sign of the changes should remain reliable. Indeed the calculated resonance shift obtained is -1.3 Hz, which is in fairly good agreement with the experimentally observed value (-0.52 Hz). These simple analytical calculations reproduce thus reasonably well the *relative* change of f_r since the *relative* change of ρ and E are expected to be similar for most SCO materials. It would be possible to further improve the calculated values by taking into account the "real" device geometry and the material parameters of the film, but this would require a considerable effort.

Table 5 : *Physical properties of bilayer cantilever materials used in the calculations.*

Properties	**Silicon**	**SCO_{HS}**	**SCO_{LS}**
Density $\boldsymbol{\rho}$ (kgm^{-3})	2330 [**Hopcroft 2010**]	1398 [**Rat 2016a**]	1471 [**Rat 2016a**]
Young's modulus $\boldsymbol{E}$ (GPa)	169 [**Hopcroft 2010**]	4.77	5.16
Poisson ratio $\boldsymbol{\nu}$	0.22 [**Hopcroft 2010**]	0.3 ± 0.05 [**Felix 2015**]	0.3 ± 0.05 [**Felix 2015**]
Modal coefficient $\boldsymbol{\lambda_1}$	1.875		

While the ensemble of these results clearly confirms the good mechanical coupling between the SCO molecules and the Si beam, still very significant scope remains to increase the magnitude of the resonance shift upon the spin-state switching. In particular, the ratio between the SCO and silicon film thickness and the cantilever dimensions can be tuned to achieve this goal.

Figure 27 shows simulation results based on **Equations 7a-c**, which allow us to estimate the effect of these parameters on the resonance frequency and, even more importantly, on the frequency shift associated with the SCO. For instance, if a thicker SCO film is deposited to obtain a ratio of 1 (SCO/Si), the SCO-induced resonance shift would be around 360 Hz.

Even higher sensitivity can be obtained with NEMS, for example, if we change dimensions (length: 8 μm, width: 2.5 μm, thickness: 340 nm) and maintain the same SCO film thickness, the mechanical device would resonate around 6.676MHz and one would expect a 4.786 kHz shift between the HS and LS states. Based on similar considerations, we can also assume that large displacements could be obtained with polymer MEMS structures, e.g., membranes or cantilevers, and that SCO materials could be particularly well suited for actuation of polymer MEMS due to the similarity of their mechanical properties (Young's modulus, etc).

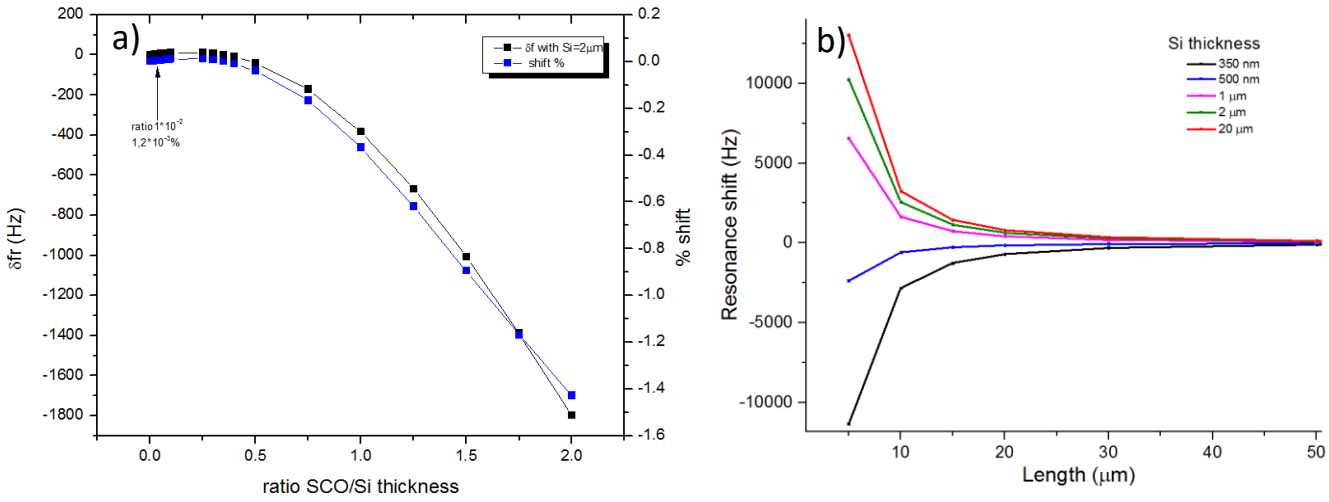

Figure 27: *Simulation results of resonance frequency shifts due to the SCO phenomenon: a) when the thickness ratio of the SCO/Si layer is tuned (Si thickness= 20 μm), b) when silicon cantilever dimensions are changed (SCO thickness = 200 nm).*

Conclusions

In the first part of this chapter we used a MEMS based methodology to characterize the mechanical properties of thin films of the molecular spin crossover compound $[Fe(H_2B(pz)_2)_2(phen)]$. Elastic moduli, residual stress and work density were evaluated. The feasibility of this study relied on the high quality of the films and the 'well-shaped' geometry of monolithic silicon microstructures. This work opens a new way for the analysis of mechanical properties of SCO materials for their reliable design in actuating devices. These values are later used in the second part of this chapter where the light-induced spin state switching of the molecules was correlated with a shift of the resonance frequency of the device. This correlation was substantiated by control experiments and analytical calculations. These later allowed us also to trace back the frequency shifts to the spontaneous strain and the associated softening of the material upon the spin crossover. In addition, they provide simple guidelines for more efficient harvesting of molecular motions. Such optimized devices would be very useful to assess accurately the mechanical properties of different molecular actuators, which, somewhat surprisingly, remain largely ignored in the literature. Based on these foundations, the actuating properties of these attractive "artificial molecular machines" could be established and optimized for a range of nanomechanical applications. In particular, the

integration of compounds which exhibit SCO around room temperature or the reverse-LIESST effect (from the HS to the LS at low temperatures) is some of the perspectives of this work. Even if the volume and stiffness change is a ubiquitous feature of SCO materials, one must note that the integration of different compounds calls for a case-by-case tailored fabrication process for reliable MEMS operation. In the next chapters some of these propositions are developed, either by integrating a room temperature tunable SCO material into smaller devices or a polymeric nanocomposite material for more for a more versatile use of these compounds.

Chapter 5: MEMS integrating $[Fe^{II}(HB(tz)_3)_2]$ compound

As a substantial step towards technological applications, we describe in this chapter a MEMS device in which the SCO molecules are not only used to tune the device mechanical properties, but also perform controlled and reversible macroscopic work. Furthermore, this actuation by the SCO molecules occurs not in a cryogenic environment, as seen in Chapter 4, but under ambient conditions. Whereas SCO compounds which work around room temperature are now readily available [**Salitros et al., 2009**], their deposition on fragile mechanical parts as well as their reliable operation represents a substantial challenge. To this aim we developed high-quality films of $[Fe^{II}(HB(tz)_3)_2]$ **2**, which provide significant advantages, since they can be deposited by thermal evaporation and they exhibit a fully reversible spin transition above room temperature in ambient air upon repeated thermal cycling. The results of this chapter are divided in two main sections, i) the synthesis and properties of the high quality thin films of **2** and ii) its integration and coupling with MEMS devices.

5.1 Sample preparation and characterization

5.1.1 Generalities on complex 2

The solvent-free crystals **2** crystallize in the orthorhombic space group Pbca with half a complex molecule in the asymmetric unit [**Rat et al., 2017**]. They exhibit a remarkably abrupt spin transition around 334 K between the high spin and low spin states (**Figure 28**). This isostructural spin transition is accompanied by a nearly isotropic change of the Fe^{II}-N bond lengths (8.3 %) and a highly anisotropic unit cell volume change (4.6 %). The very high cooperativity of the spin transition in **2** is rather unusual in mononuclear SCO compounds. This property can be related to the dense crystal packing and relatively high stiffness of the lattice (Debye temperature θ_D = 198 K), which involves numerous C–H···N hydrogen contacts between each molecule with fourteen neighboring molecules.

5.1.2 Sample preparation

Reagents and solvents used in this study are commercially available. The bulk powder $[Fe^{II}(HB(tz)_3)_2]$ was synthesized by Sylvain Rat (LCC-CNRS) as described in [**Rat et al., 2017**]. Thin films were grown by Victoria Shalabaeva (LCC-CNRS) by thermal evaporation using a

PREVAC thermal deposition system at a base pressure of ca. 2 x 10^{-7} mbar. The bulk powder was heated until 250 °C in a quartz crucible and evaporated at a rate 0.03 A/s. The evaporation rate and film thickness were monitored in-situ by a quartz crystal microbalance. The final control of the film thickness was carried out by AFM. The films were deposited onto fused silica, crystalline silicon (100) and polycrystalline gold (15 nm thickness) substrates, which were cleaned with acetone and isopropanol to remove contaminants.

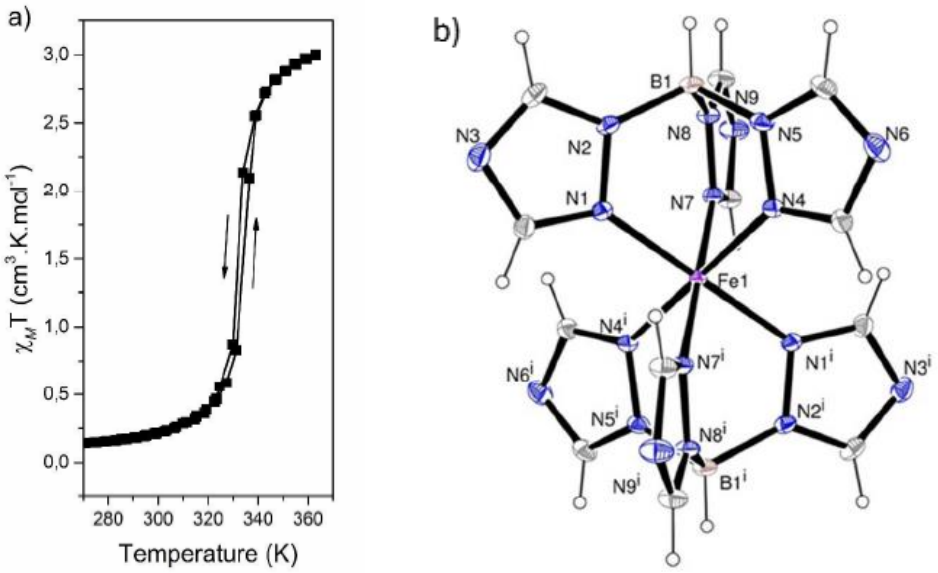

Figure 28: *a) Variable temperature magnetic behavior and b) structural view of complex* ***2.***

5.1.3 Sample characterization

The grazing incidence X-ray diffraction (GIXRD) experiments were carried out in a PANalytical X'Pert PRO MPD system using Cu-Kα radiation (45 kV and 40 mA) with a parallel-beam configuration. The incident beam optics consisted of a mirror with a 1/32° divergence slit. A parallel plate collimator (0.18°) and Soller slits (0.04°) were mounted on the path of the diffracted beam. An X'Celerator detector in receiving slit mode was used for X-ray collection. AFM topography measurements were done using a Cypher-ES microscope (Oxford Instruments) in amplitude-modulation mode at room temperature. Temperature dependent absorbance spectra of the thin films were collected at wavelengths between 250 and 800 nm using a Cary 50 (Agilent Technologies) spectrophotometer and a Linkam FTIR-600 liquid nitrogen cryostat. The sample chamber was purged by dry nitrogen and spectra were acquired

in the 293-393 K range with 1 K/min rate. Raman spectra were acquired using an Xplora (Horiba) Raman microspectrometer in conjunction with a Linkam THMS600 cryostage. All spectra were calibrated with respect to the first order silicon LO phonon peak at 521 cm^{-1}. The exciting laser beam (638 nm, 1 mW) was focused on the sample with a 50x (NA: 0.5) objective, which was also used to collect the backscattered light. The Rayleigh scattering was removed using an edge filter and the Raman scattering was analysed with a resolution of *ca.* 3 cm^{-1}. Magnetic susceptibility measurements were performed using a Quantum Design MPMS-XL magnetometer at heating and cooling rates of 2 K/min in a magnetic field of 10 kOe.

5.1.4 Pristine thermally evaporated thin films

The AFM analysis of the as-deposited films showed that the resulting films are smooth and continuous, but also rather heterogeneous in terms of morphology and roughness (**Figure 29a**). For example, the characterization of a film of ca. 1 cm^2 surface area and 75 nm thickness revealed different regions with roughness ranging between ca. 0.5 and 5 nm. Films were deposited on fused silica substrates in order to follow the thermal variation of the spin state of the complex by temperature dependent optical absorbance measurements. We found that the films are transparent in the visible range independently of the temperature, while they exhibit a pronounced absorbance change associated with the SCO in the UV (See **Figure 29b). Figure 29c** shows the UV absorbance change at 317 nm for a 75 nm thick pristine film of **2** along four heating-cooling cycles between 293 and 383 K. The abrupt spin transition, similar to the bulk powder [**Rat et al., 2017**], is apparent around 337 K. However, contrary to the powder sample, the spin transition in the pristine films is poorly reproducible: both the absorbance values and the shape of the curves change from cycle to cycle. In order to unveil the origin of this lack of stability, the films were further characterized by X-ray diffraction. The results in **Figure 29c** highlight that the freshly prepared films are amorphous. On the other hand, by prolonging the storage time (days/weeks) in ambient air, several peaks appear in the XRD pattern, i.e. the films evolve to a polycrystalline form. We did not carry out a detailed study of this ageing phenomenon, but it was observed repeatedly for different film thicknesses. The amorphous nature of the films can probably explain the lack of appreciable spin transition in the as-prepared samples, while the structural change observed upon prolonged storage may account for the evolving SCO behavior (in time and also from one cycle to another).

5.1.5 Crystallization by solvent-vapour annealing

In order to obtain stable films with reproducible SCO behavior, we tried to convert the amorphous films to the crystalline form. To this aim thermal and solvent-vapour annealing are the most frequently used methods reported in the literature [**Jin et al., 2017**]. As the films undergo a slow crystallization in ambient air, this fact suggested that water vapour (which is a moderate solvent for **2**) might be used to accelerate this process. (N. B. Other solvents may be also used here, but were not tested in our study. On the other hand we tested the possibility to recrystallize the films by thermal annealing, but we could not find any appropriate condition for this.) Indeed, the exposure of the fresh films of **2** to humid (ca. 75 – 80 %) air at room temperature led to their very efficient and fast crystallization. This spectacular process was followed by AFM, optical absorption and Raman measurements. The AFM image in **Figure 30a** shows the topography of a freshly evaporated film revealing a very low roughness (Ra = 0.45 nm). Then, a water drop (*ca.* 20 μL) was added into the AFM chamber and immediately another topography scan was acquired. As shown in **Figure 30b**, at the timescale of the measurement (*ca.* 2-3 min) the film experienced a dramatic morphological transformation: the initially rather featureless surface of the film evolved into a nano-crystalline morphology displaying well defined grain boundaries and a roughness (Ra) of *ca.* 6-7 nm. On the other hand, the addition of a water drop to another sample with the same thickness (150 nm), which was previously exposed to ambient air for 2 hours, did not induce any obvious change in the surface morphology (**Figure 30c-d**).

This means that 'irreversible' changes occur in the films in ambient air and the humidity treatment must be carried out on freshly prepared films in order to achieve a high degree of crystallinity. It is important to mention that the surface morphology depicted in **Figure 30b** does not represent the final stage of crystallization, as the humidity in the AFM chamber was not high enough for a complete transformation. Indeed, when the solvent annealing was carried out in a dedicated chamber for 75-80 % relative humidity we could obtain extremely well reproducible film morphologies with roughness (Ra) below 2.5 nm (150 nm thickness).

Perhaps even more importantly, in contrast to the pristine samples, these crystalline films cover uniformly the whole substrate surface and their morphology was found stable on storage in ambient air for several months (**see the inset of Figure 31, and Figure A5.1.1 in Annexes**).

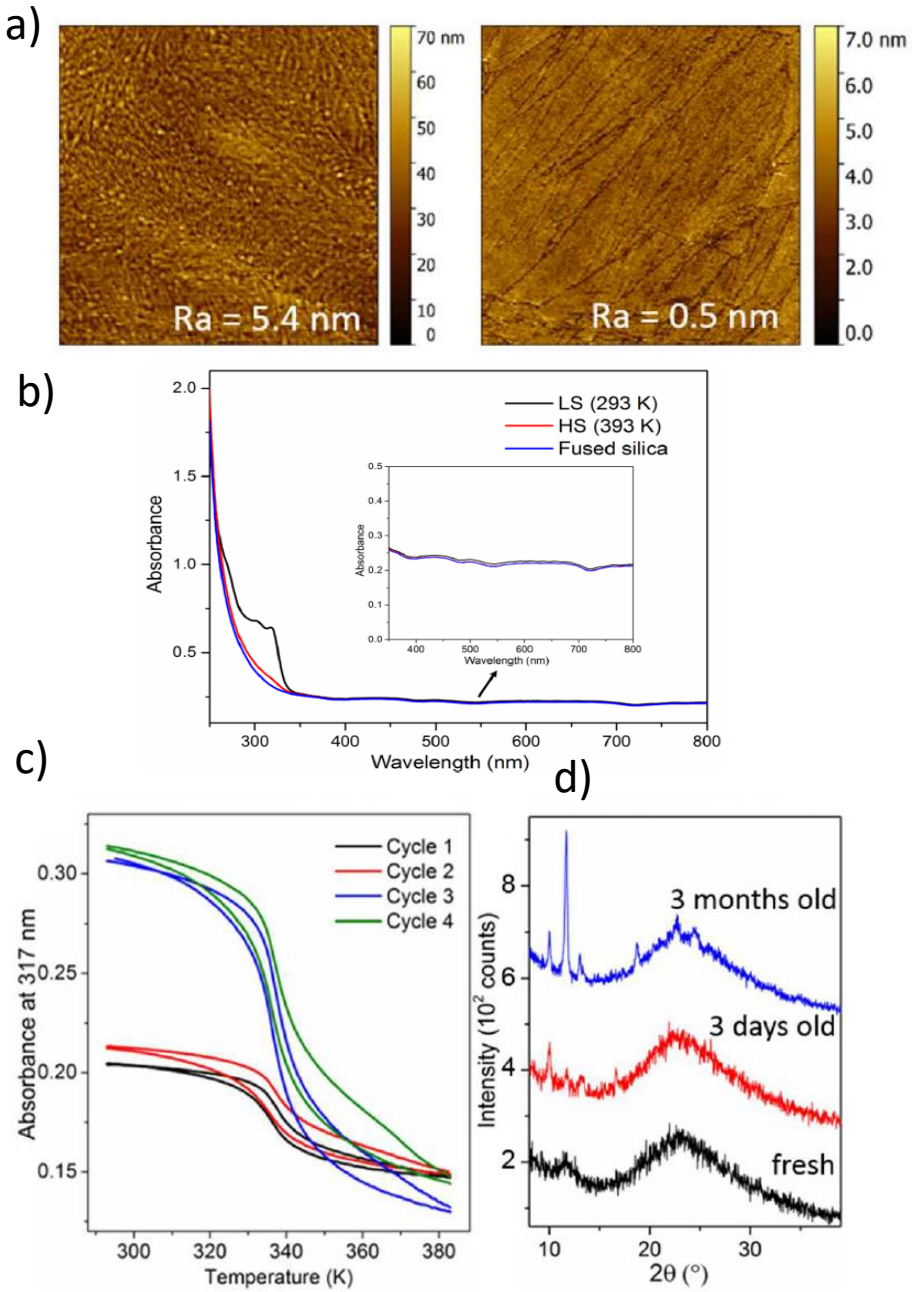

Figure 29: *Characterization of pristine thermally evaporated thin films, a) AFM topography images of a 75 nm thick film (images sizes are 10 x 10 µm², b), UV-vis spectra of a 90 nm crystalline film at 293 K (LS) and 393 K (HS) deposited on a fused silica substrate. Inset: zoom on the visible spectra range, c) Absorbance (λ = 317 nm) of a 75 nm thick film along four heating-cooling cycles, and d) Evolution of the XRD pattern for different storage times is ambient air (film thickness ca. 80 nm)*

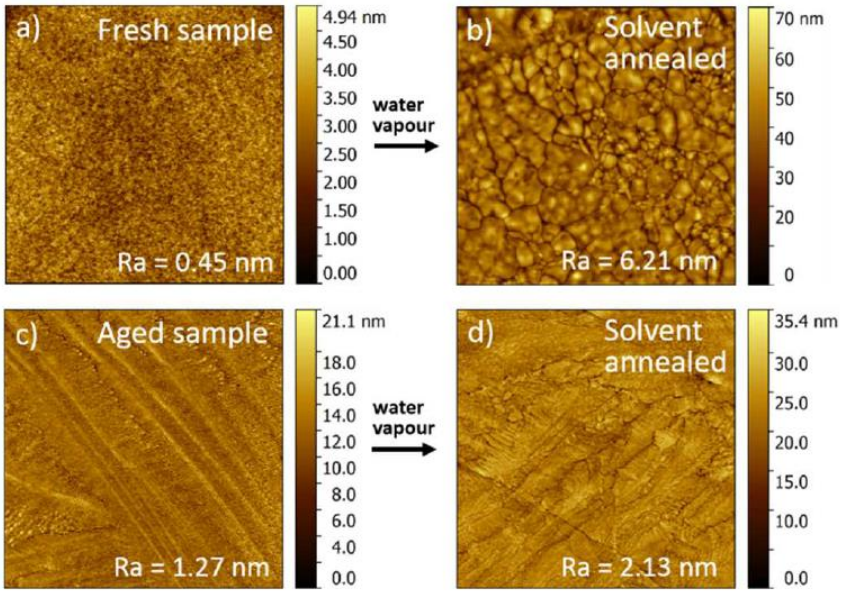

Figure 30: *AFM imaging of the crystallization of a film of 150 nm thickness. AFM topography of a fresh sample before a) and after b) exposure to humidity. The c) and d) images show the same treatment in a different film, which was storage previously in ambient air. Image sizes are 10 x 10 µm^2.*

The increase of the LS absorbance band upon exposure to humidity can be used to follow the crystallization process. For fully crystalline films it was found that the absorbance at 317 nm is closely proportional to the film thickness (**see Figure A5.1.2 in Annexes**). Hence it is possible to establish quantitatively the degree of crystallinity of the films from a simple room temperature UV absorption spectrum (provided the film thickness is known). As an example, **Figure 31** shows the UV absorbance of two 90 nm thick films, either stored in ambient air or annealed in 80 % humidity, revealing a crystallinity of *ca.* 45 % and 100 %, respectively.

Samples showing a complete and homogenous crystallization could be obtained with thicknesses ranging from approx. 20 to 200 nm. Thicker films crystallized only partially, most probably only in the proximity of the surface layers (leaving the underlying ones in amorphous/semi-crystalline form), while films with a thickness below *ca.* 20 nm formed a discontinuous layer of grains. Further work on the annealing process (e.g. multi-step annealing, etc.) will be required to obtain highly crystalline homogenous films in a broader thickness range.

The transformation of thin films from the amorphous to the crystalline form was also analyzed by Raman spectroscopy, which revealed three different spectral footprints.

A first spectral modification occurs upon exposure to water vapor, which can be attributed to the crystallization process. Then, a slight heating of the film to *ca.* 313 K allowed us to obtain a spectrum, which remained stable and reproducible upon thermal cycling as well as on storage

in ambient air. Since this latter spectrum corresponds closely to the spectrum of the bulk sample **2** [**Rat et al., 2017**] we can attribute this second spectral change to the loss of water. Interestingly, the Raman spectrum of the film in its stable (dehydrated crystalline) form matches more closely the spectrum of oriented single crystals of **2** than that of the polycrystalline powder [**Rat et al., 2017**].

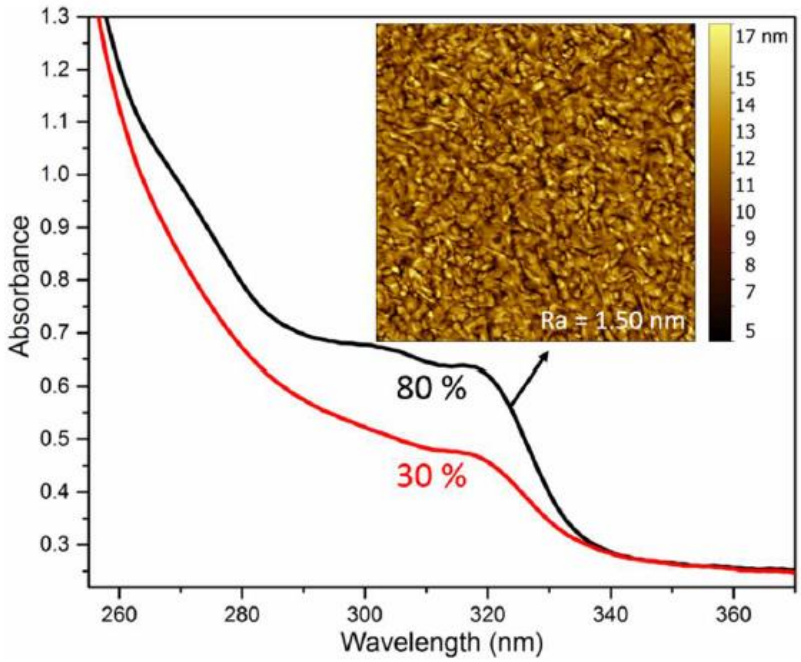

Figure 31: *Absorption spectra acquire at 293 K for 90 nm thick films stored either in 30 % (ambient air) or 80 % relative humidity. The inset shows the AFM image of the humidity treated film (image size is 10 x10 μm^2).*

This finding indicates that the crystalline films are possibly also oriented. To further investigate the crystallinity and texture of the films we acquired XRD data for humidity treated films. As shown in **Figure 33** the diffraction pattern of the films consists of a single peak at $2\theta = 10.02°$ indicating a preferential crystallographic orientation. (N.B. The very broad peak around $2\theta = 20° \div 25°$ is typical for amorphous fused silica substrates). The peak intensity approximately scales with the film thicknesses. This diffraction pattern of the crystalline films can be compared with that of the bulk powder, which exhibits a peak at $2\theta \sim 10.11°$ corresponding to the 002 reflection [**Rat et al., 2017**]. It should be noted also that no other 00l diffraction peaks have significant intensity in the simulated powder XRD data of **2** [**Rat et al., 2017**].

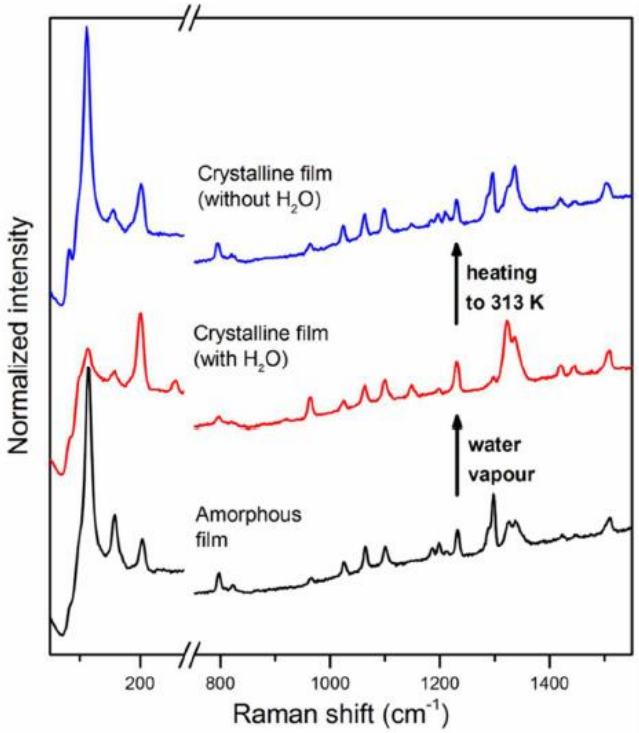

Figure 32: *Raman spectra of a thin film (138 nm thickness) at three stages of its synthesis: the pristine amorphous film, hydrated crystalline film (after humidity treatment) and the final dehydrated crystalline film (after annealing at 313 K).*

We can thus conclude that the crystalline domains in the films grow preferentially with their orthorhombic *c*-axis normal to the substrate surface. This finding was repeatedly observed for different film thicknesses and also for different substrates, such as single crystalline silicon and polycrystalline gold substrates (**see Annexes A5.1.3**). These results will be taken as representative guide for the discussion of their behavior when they are grown over silicon MEMS devices.

It is interesting to note that single crystals of **2** tend also to grow naturally with large *00l* facets suggesting these facets have relatively low surface energy. It is worth to mention also that the LS to HS spin transition in **2** leads to a very significant strain (ca. +5.6 %) along the orthorhombic *c*-axis, while in the other directions the changes are smaller or even opposite (*a*-axis: -2.3 %, *b*-axis: +1.0 %) [**Rat et al., 2017**]. Neglecting other contributions (e.g. micro-strain), it is possible to estimate the mean size of the ordered (crystalline) domains, which is directly linked to the peak broadening in the XRD diffraction patterns through the Scherrer Equation [**Langford and Wilson., 1978**]:

$$\tau = \frac{K\lambda}{\beta \cos\theta} \tag{11}$$

where τ is the mean size of the ordered (crystalline) domains, K is a dimensionless shape factor, with a value close to unity, λ is the X-ray wavelength, β is the line broadening at half the maximum intensity (FWHM), after subtracting the instrumental line broadening, in radians and θ is the Bragg angle (in degrees).

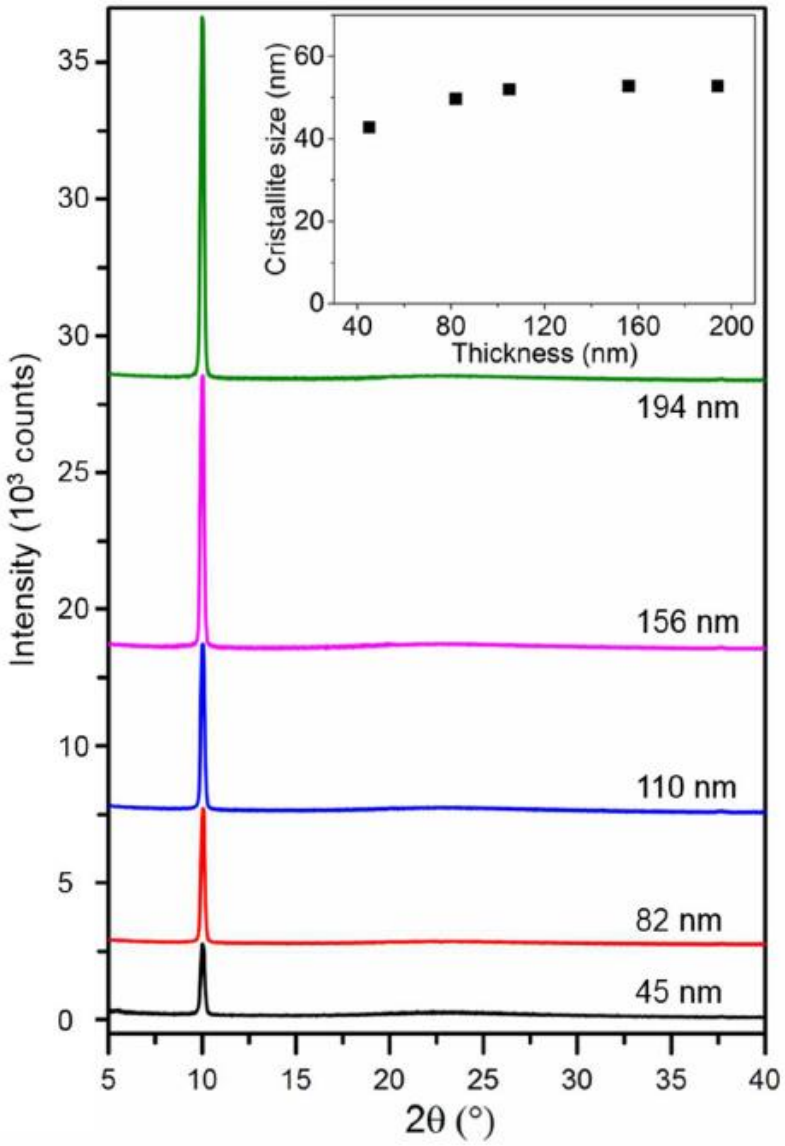

Figure 33: *XRD pattern of crystalline thin films of **2** for various thickness. The inset shows the size of the crystalline domains as a function of the film thickness.*

As shown in the inset of **Figure 33,** the size of crystalline domains remains quite similar (from 43 to 53 nm) for film thicknesses between *ca.* 45 and 200 nm. One may note that the Scherrer analysis of the bulk powder led to *ca.* 80-100 nm crystalline domain sizes [**Rat et al., 2017**].

5.1.6 Spin crossover properties of crystalline films

To follow the spin transition in a quantitative manner, variable temperature optical absorption measurements were performed over four heating - cooling cycles between 293 K and 393 K with a rate of 1 K/min. **Figure 34a** shows the absorbance spectra of a 90 nm thick crystalline film at different temperatures in the UV region. The intense absorption bands between 260 and 340 nm exhibit three maxima around 272, 305 and 317 nm at 293 K (see inset in **Figure 34a**). The absorption coefficients associated with these peaks are *ca.* 10^4 cm^{-1} indicating these are strongly allowed charge transfer transitions. These absorption bands are bleached upon increasing the temperature to 393 K, which we can obviously assign to the SCO phenomenon. Indeed the plot of the absorbance at 317 nm as a function of the temperature (**Figure 34b**) reveals an abrupt change around 338 K with a small hysteresis, which is virtually the same as the one observed for the bulk powder [**Rat et al., 2017**].

Since the spin transition is virtually complete in both directions (**see Annexes A5.1.2** for details) and the absorbance at 317 nm is directly proportional to the LS fraction (*nLS*) the plot in **Figure 34b** can be considered as a quantitative spin transition curve (*nLS vs. T*). It is interesting to note that during the first heating the transition temperature ($T_{1/2}up$ = 339.8 K) is slightly higher than in the successive cycles, which is the well-known 'run-in' phenomenon. However, beyond the first heating the transition temperatures ($T_{1/2}up$ = 338.1 K and $T_{1/2}down$ = 337.6 K) become perfectly reproducible, which can be well appreciated from the derivatives of the transition curves in the inset of **Figure 34b**. This SCO behaviour observed for the 90 nm thick film was perfectly reproduced for all other crystalline films with different thicknesses (**see Annexes A5.1.4** for a few examples) and no remarkable size effect has been observed. At first sight, this result might seem surprising, but actually the size of the crystalline domains in films of different thickness is not much different either (**see Figure 33**). In order to further investigate the SCO behaviour, temperature dependent Raman spectra were also acquired (**Figure 35**).

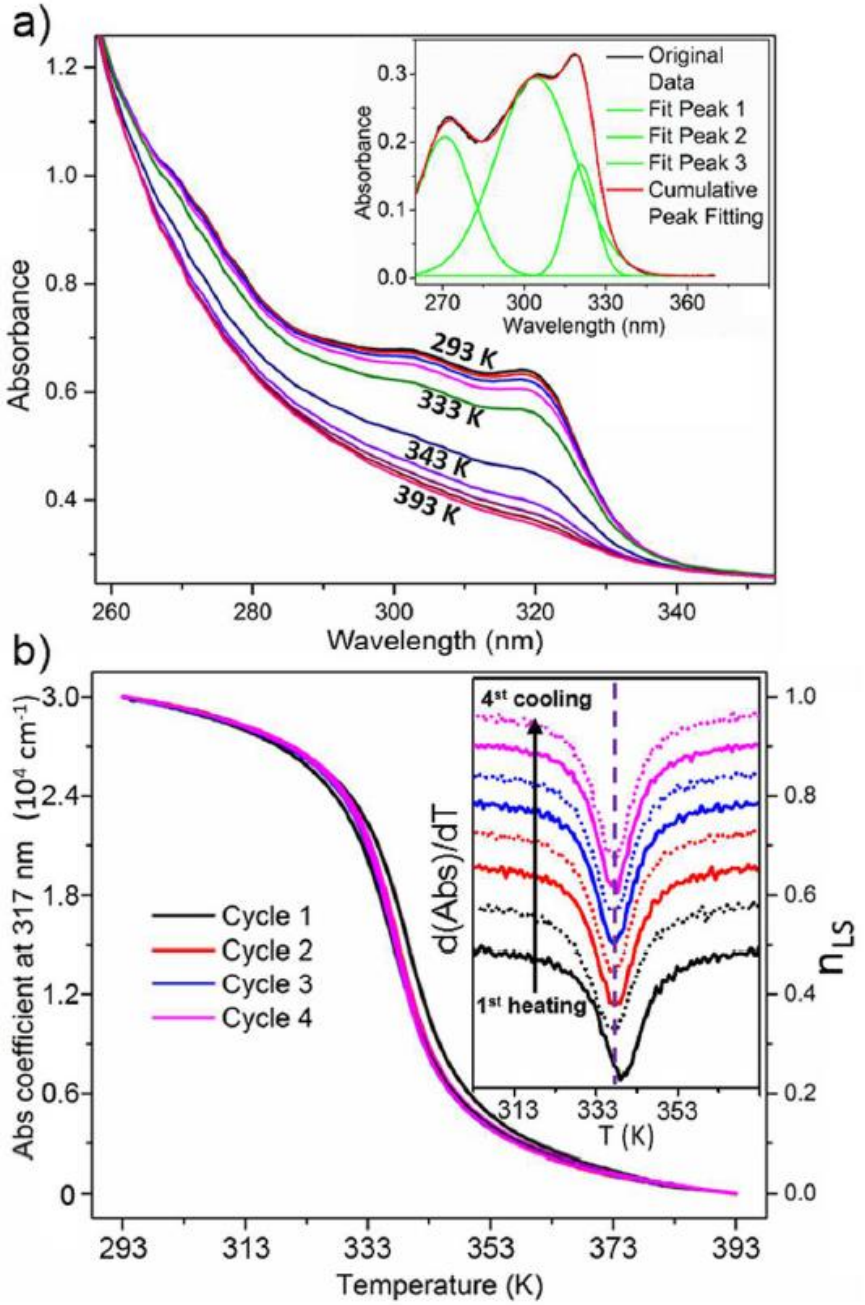

Figure 34: *Absorbance spectra of a 90 nm crystalline film (deposited on a fused silica substrate) acquired at different temperatures in the heating mode. The inset shows the peak fitting of the baseline subtracted spectrum at 293 K. b) Temperature dependence of the absorbance at 317 nm along four heating-cooling cycles recorded at 1K/min scan rate. The inset shows the derivatives of the transitions.*

During the spin transition, the Raman spectra of the films undergo characteristic changes in intensity and frequency in agreement with the spectra of the bulk powder **2** [**Rat et al., 2017**]. In particular, one can observe the increase in intensity of representative HS peaks around 1407, 1046, 123 and 102 cm^{-1}, while the LS markers around 1420 and 113 cm^{-1} loose in intensity.

Raman spectra enable also the observation of the coexistence of the LS and HS states at 338 K and confirm the completeness of the spin transition.

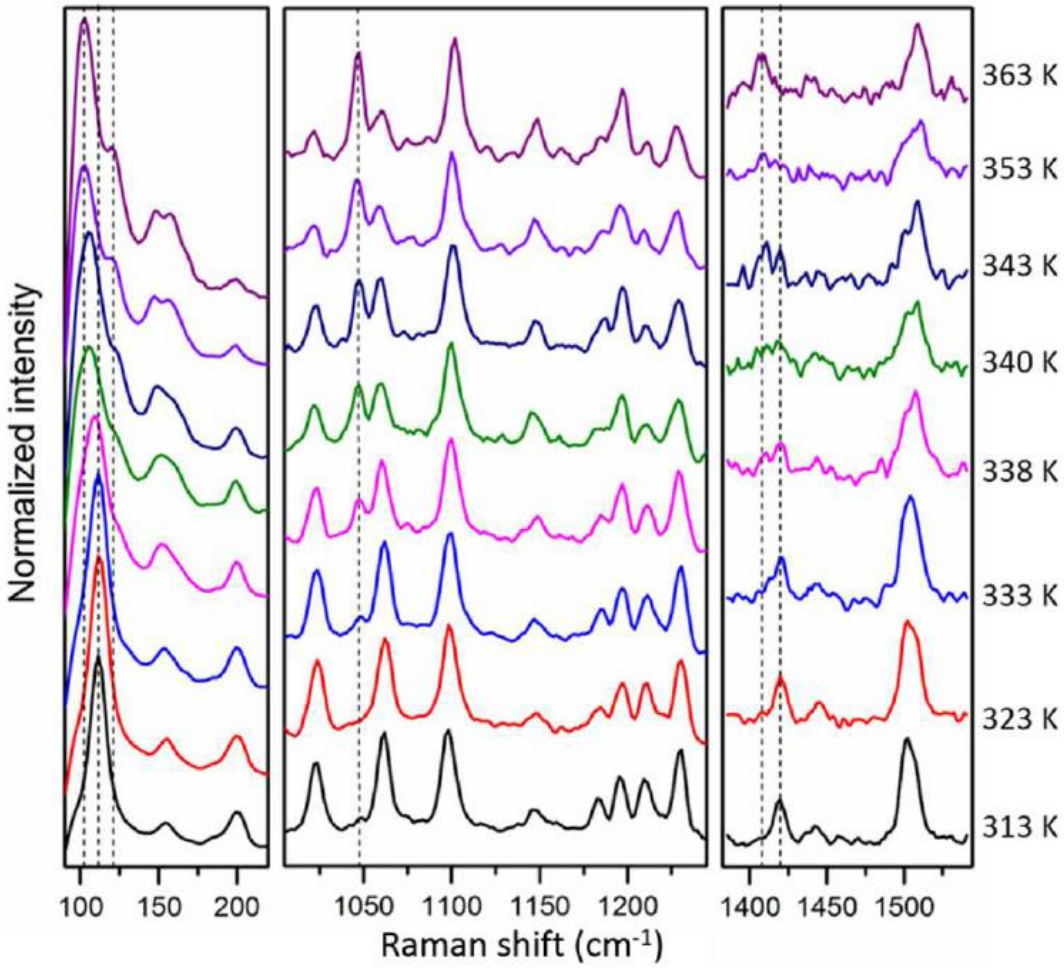

Figure 35: *Raman spectra of a 194 nm thick crystalline film acquired at different temperatures in the heating mode.*

5.2 MEMS: SCO detection and actuation by thermal energy

5.2.1 MEMS characteristics

To integrate compound **2**, new MEMS devices were used. They were fabricated by Jean Cacheaux from the MEMS team (LAAS) in the frame of his PhD thesis. These devices are suitable for the purpose of this project since they follow similar principles in terms of actuation-detection, as the ones described in section 4.3, the main difference relies on the reduced dimensions (200 µm length, 50 µm width, and 2 µm thickness) (**see Figure 36a**) which confers higher sensitivity to detect external perturbations.

A 140 nm thick film of **2** was deposited on the new device. The film deposition was done by thermal evaporation according with the procedure described in section 5.1. After deposition, a post annealing during 10 min with a relative humidity of approximately 80 % was carried out for the formation of the robust and fully crystalline coatings. SEM and AFM images of the final crystalline film of **2** are shown in **Figures 36b-c**. The film was smooth (with ca. 2.5 nm roughness) and covered the whole device in a uniform and continuous manner. The SCO associated changes in the crystal lattice of **2** are schematized in **Figure 36d**.

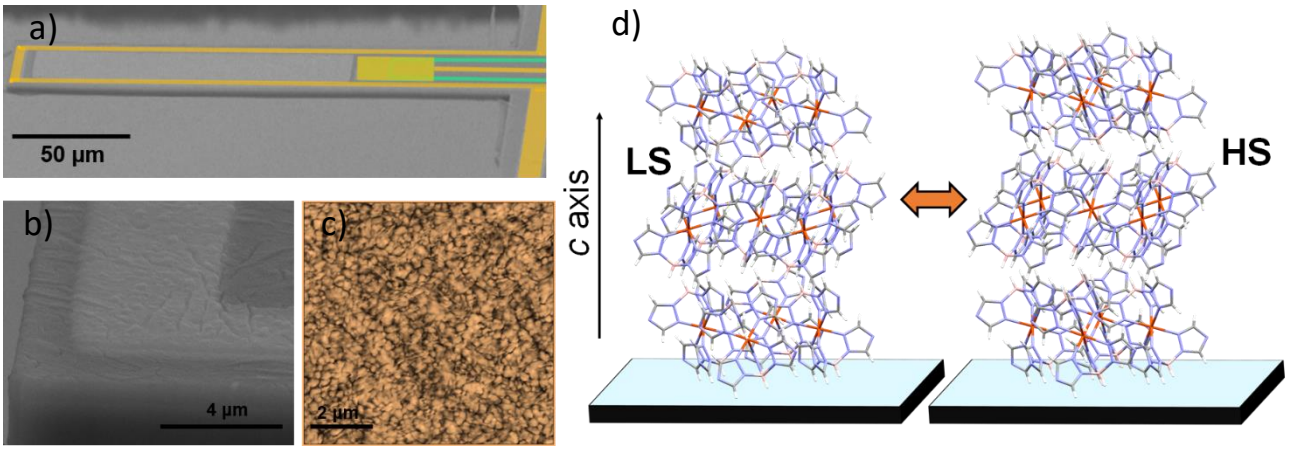

Figure 36: *Tilted SEM image of the microcantilever, b) AFM image of the film of **2** (z-scale 20nm), and c) schematic representation of the packing of molecules of **2** on the cantilever surface in the contracted (LS) and expanded (HS) states.*

5.2.2 Characterization set-up

With the help of Fabrice Mathieu (LAAS-CNRS) a new experimental set-up was put in place to characterize the MEMS devices covered by the film of **2**. The operational principles of this new set-up are the same as discuss previously for the set-up used to investigate the films of **1** (Chapter 4). The most important novelties of this new set-up are listed below and described further ahead:

- Considerable smaller characterization set-up, using a HFS350V (Linkam Scientific) cryostage (**Figure 37**).
- Possibility to control pressure, which allows maintaining this parameter constant during all the experiment.

- Possibility to extract both static and dynamic information in a simultaneous manner.

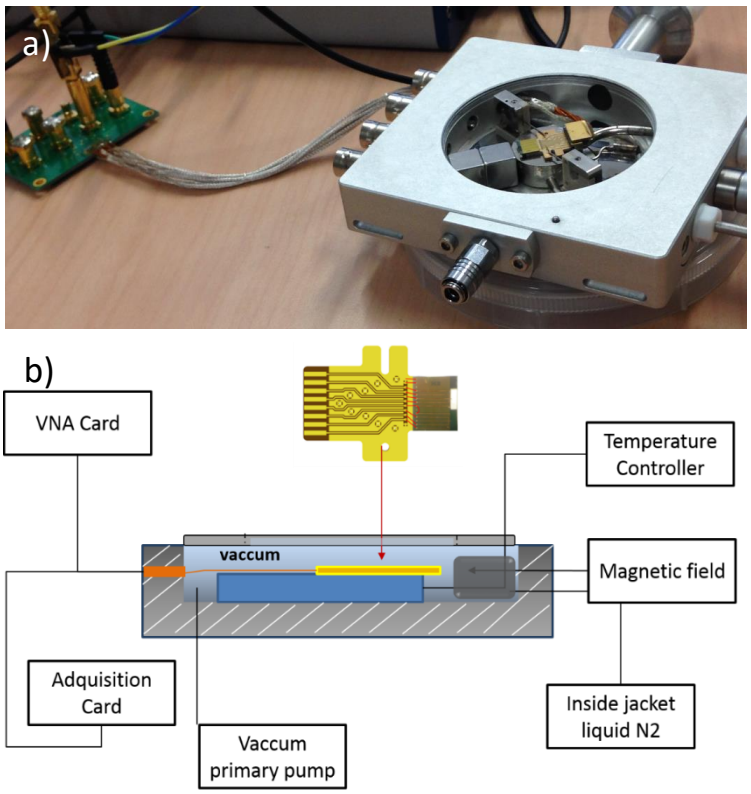

Figure 37: Set-up for MEMS characterization under controlled temperature and presure, a) Photo of the open chamber and b) Scheme of the main parts.

5.2.2.1 Dynamic and Static Measurements

For dynamic measurements, the mechanical device was actuated at its resonance frequency in a similar manner as for MEMS in section 4.3, using magnetic actuation and detecting the mechanical vibrations by piezoresistors. A reference cantilever was also attached to the substrate to offset the variations in the measurements. The home built VNA card (described in chapter 4.3) was used to track the mechanical response in terms of resonance frequency f_r and this time the quality factor Q was also accurately measured. For the static measurements, some considerations had to be taken: the resistance variation of the free cantilever can be affected by different external factors, the most important are temperature, mechanical properties and dimensional changes. The reference resistance is used to compensate all the environmental changes that influence directly over the measurement resistance, but it does not compensate the cantilever deformations which arise due to the altered mechanical properties and thermal

expansion coefficient of the device covered with the SCO film. Obviously the expansion/contraction due to the SCO is not compensated either.

For the simultaneous static measurements, which represent a real novelty in terms of signal processing, a parallel loop was used to control the static polarization state of the piezoresistors to maintain a perfect Lorentzian shape by a tuned voltage injected into the piezoresistors and generate the output current equal zero (i_{out} = 0, **see Equations 10a-c**). For this, the injected voltage on the reference is maintained fixed during all the experiment while the voltage on the free cantilever is tuned. By knowing the voltage on each resistance, it is possible to know the evolution of the measurement resistance over the time while SCO occurs. In this way it is possible to track and quantify the dynamic and static properties in a proper way.

For variable-temperature measurements, the device was placed on the heating/cooling block of a cryostat (**Figure 37**), which allowed us to control the sample temperature between 298 and 383 K at a heating/cooling rate of 2 K/min, while maintaining a constant pressure of 15 mbar during the whole experiment. We must stress that the experiments can also be run at higher or lower pressure, including atmospheric pressure, the key enabling point for reliable data acquisition being constant pressure while changing the temperature.

5.2.2.2 Static calibration

In order to calibrate the static amplitude variation, a similar silicon cantilever was actuated at its resonance frequency using our home-made electrical system and the movement was followed simultaneously by the piezoresistance variation (integrated on the device) and by an external optical interferometer (Polytec Scanning Vibrometer MSA-500). These experiments were run at the Institute of Electronics, Microelectronics and Nanotechnology (IEMN) located in Lille, France with the help of Olivier Thomas. We worked with an open chamber and an uncoated cantilever to obtain a better optical signal (**Figure 38b**). In a first approximation, we assume that the piezoresistance variation in these conditions follows a similar behavior as for the coated cantilever.

The optical detection system consists of a laser-based, non-contact optical interferometer for the analysis and visualization of structural vibrations and surface topography. It integrates a microscope with a scanning laser Doppler vibrometer, a stroboscopic video microscope and a scanning white light interferometer. The calibration was based on the Peak Hold of the chosen frequency taken at the mobile extreme of the cantilever, referring the amplitude of calibration

as the maximum amplitude registered on the whole mechanical structure at its resonance frequency.

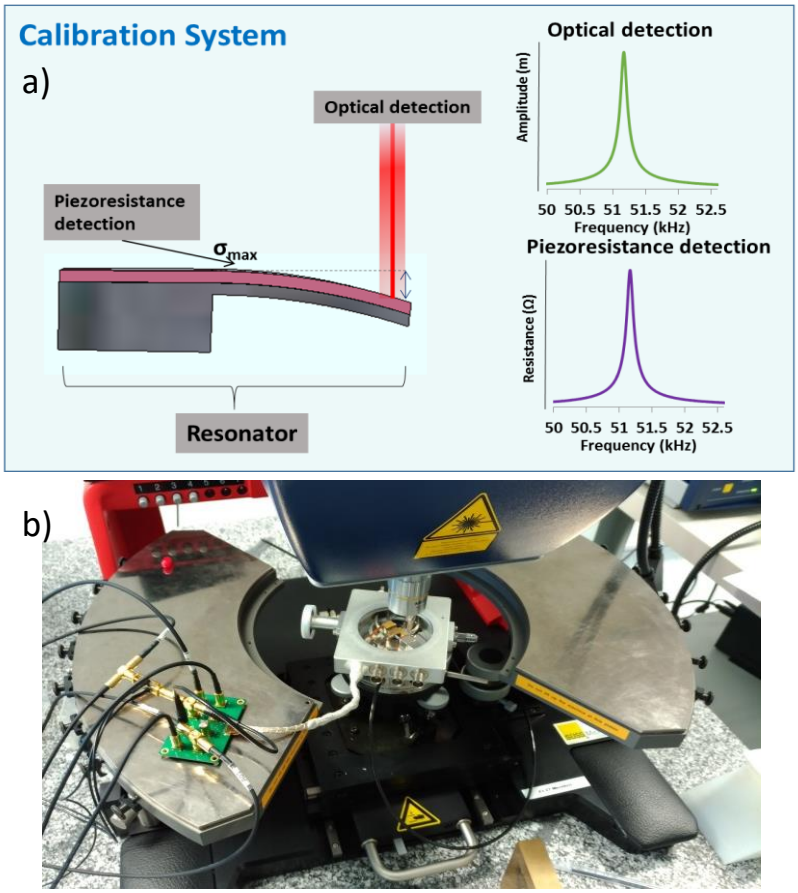

Figure 38 : *Coupling of the integrated piezoresistive detection with an external optical detection for the amplitude calibration of the MEMS device.*

The amplitude registered by the optical interferometer is correlated to a piezoresistance value registered by the electrical system. As shown in **Figure 39b** the same resonance frequency and the same quality factor were registered by the two independent detection systems (optical and electric). Information about the 3D mechanical structure was also obtained (**see Figure 39a**), but most importantly we could obtain the calibration of the piezoresistance values in terms of amplitude of movement of the cantilever (**Figure 39c**).

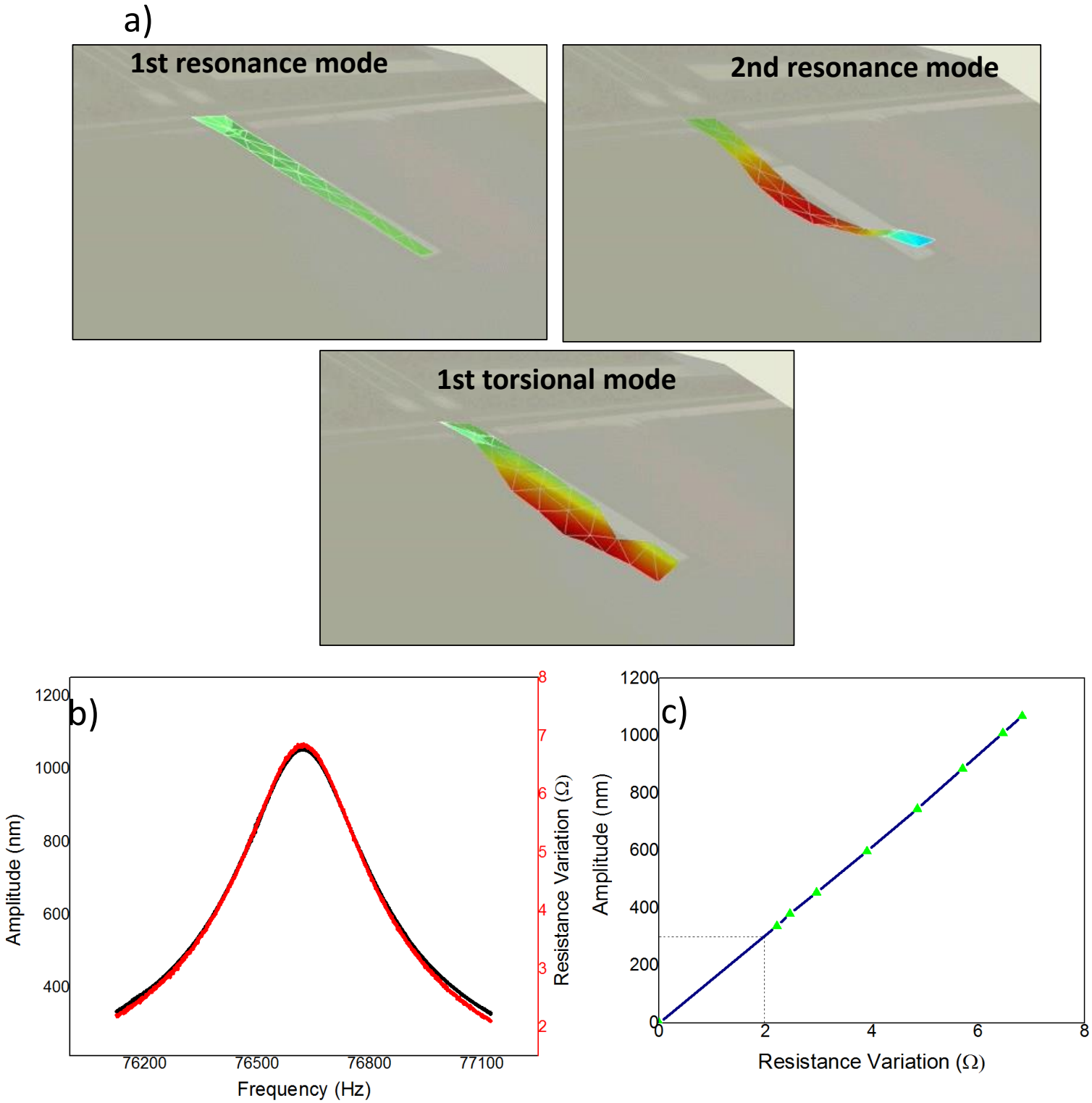

Figure 39: *a) 3D cantilever mapping of three different resonance modes. b) Amplitude of cantilever deflection and piezoresistance variation for the first resonance mode extracted from simultaneous optical and electrical measurements. c) The final calibration curve (Amplitude vs Resistance variation) obtained from figure b).*

5.2.3 Results and discussion

The SCO properties of the film were monitored by means of variable-temperature UV absorption measurements (**Figure 40a**), which confirmed the occurrence of the spin transition around 338 K with a hysteresis of 2 K. These results are comparable to our previous measurements on films of **2** deposited on thick glass substrates (Section 5.1.5). The detailed temperature dependence of the resonance frequency and the quality factor of our MEMS is shown in **Figure 40b-c**. Data were collected both before and after the deposition of the SCO layer. For the uncoated device, both f_r and Q decreased in a linear manner as the temperature increased. This downshift and broadening of the resonance peak reflects typical thermoelastic damping at constant pressure [**Kim et al., 2008**].

The deposition of the SCO layer on the cantilever resulted in a 409 Hz drop in the f_r value; the change can be attributed to the extra mass (ca. 2.2 ng). Thermal cycling of the coated device revealed clearly the spin transition around 338 K. The most important features are the negative (vs. positive) jump in f_r when the molecules are switched to the HS (vs. LS) state and the decrease in the Q factor around the transition temperatures. The spin-state dependence of f_r is in perfect agreement with our previous results obtained with MEMS coated with compound **1** (Chapter 4).

We were able to extract dynamic and static properties of film **2** simultaneously. See **Figure 40**. As mentioned previously, in the dynamic mode a decrease in the resonance frequency of MEMS can be expected when going from the LS to the HS state (heating), owing chiefly to the increase in the thickness of the SCO film as well as to the concomitant decrease in mass density and lattice stiffness. On the other hand, in the static mode a deflection of the cantilever is expected to occur due to the SCO, primarily as a result of the transformation strain and associated change in the surface stress.

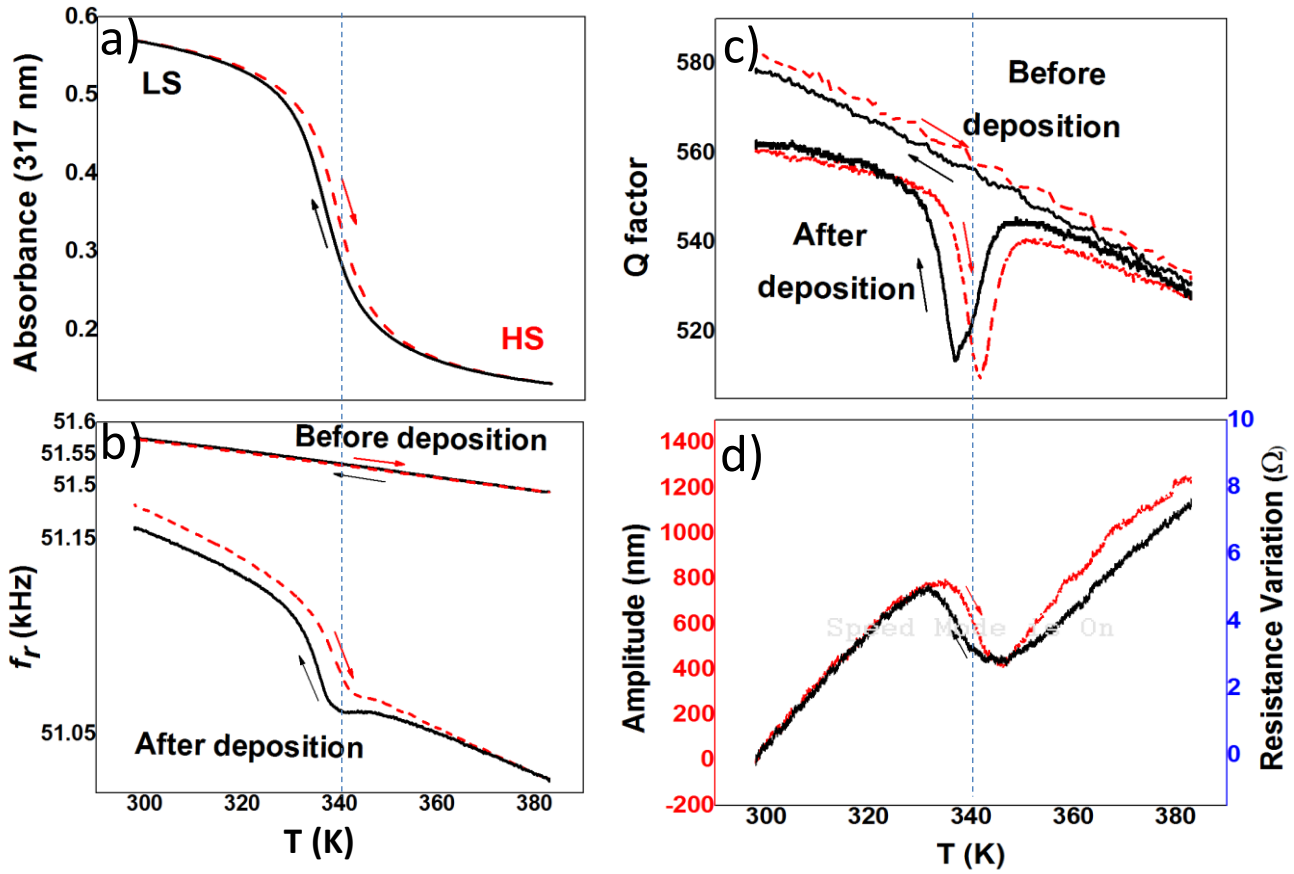

Figure 40: a) absorbance (317 nm), b) resonance frequency, c) quality factor and d) actuation of film **2** on heating (dashed red) and cooling (solid black line).

In order to extract the f_{r_shift} of the SCO contribution it is possible subtract the value at 298 K and 353 K from the resonance curve of cantilever before deposition (**see Annexes A5.2.1**). Remarkably, the frequency shift associated with the spin transition is approximately two orders of magnitude higher in the present case (66 vs. 0.5 Hz), presumably as a result of the reduced device dimensions. This effect was indeed predicted theoretically in our previous study (Chapter 4), and we can use the same analytical calculations to rationalize the spin-state dependence of the resonance by taking into account the different properties of the HS and LS lattices obtained previously (Section 5.1.4).

Table 6: *Material properties and MEMS geometry for devices described in section 5.2.1.*

		Complex **2**	
	Si	(LS)	(HS)
Young's Modulus (GPa)	169[Hopcroft 2008]	5.16[Rat 2016a]	4.77[Rat 2016a]
Poisson's ratio	0.22[Hopcroft 2008]	0.3[Felix 2015]	0.3[Felix 2015]
Density (kgm^{-3})	2330[Hopcroft 2008]	1568[Rat 2017]	1500[Rat 2017]
Length (μm)	200	200	200
Width (μm)	50	50	50
Thickness (μm)	2	0.140	0.146[a]

[a] To conserve the mass this analysis assumes the total volume change (4.5 %) is expanded in the *c*-direction as a thickness change.

As film **2** is deposited on the c-direction and it is highly oriented in the plane (001). Most of the volume change due to SCO of the crystal favored this direction (a:-2.3% b=1% and c: 5.6%) [**Rat et al., 2017**].

By using the bulk material properties extracted from NIS and XRD measurements (**Table 6**), these calculations lead to a theoretical frequency shift of 67 Hz (versus the experimental value of 66 Hz). As discussed in Chapter 4 these calculations do not take into account the effect of the metallic lines and that of the insulating SiO_2 layer. Nevertheless, they confirmed clearly the prevailing effect of the relative changes in the geometry (thickness) and mechanical properties (density, Young's modulus) of **2** between the HS and LS states on the shift of the MEMS resonance.

The drop in the quality factor around the transition temperature (**Figure 40c**) is indicative of internal frictions during the spin transition. In analogy with other first-order thermoelastic phase transitions, the origin of this dissipation phenomenon is most likely the formation, movement, and merging of phase boundaries during the nucleation and growth process. [**Perez-Saez et al., 1998**] We can also draw a parallel with a recent study of a hybrid polymer–SCO nanoparticle composite material, wherein dynamic mechanical analysis (DMA) provided evidence for a maximum of energy dissipation (loss modulus peak) around the spin-transition temperatures [**Rat et al., 2016b**].

The static response of the coated MEMS device is shown in **Figure 40d** and **Annexes A5.2.2**. Far from the spin transition, an increase in temperature leads to a linear increase in the

piezoresistance, in a very similar manner as for the uncoated device. On the other hand, the spontaneous strain associated with the spin transition gives rise to the opposite behavior. From the calibration of our system, the actuating deflection amplitude due to the SCO corresponds to -476 nm. This drop in the piezoresistance/amplitude around 338 K corresponds to the upward bending of the cantilever, which is indicative of a tensile surface stress. At first sight, this finding might seem rather surprising, since a tensile stress denotes the contraction of the SCO layer instead of its expansion, which could be expected during the LS to HS spin transition. Nevertheless, one has to also take into account the strong anisotropy of the transformation strain. Indeed, as it was mentioned previously, the X-ray diffraction study of films of **2** revealed their preferential growth with the orthorhombic (Pbca) c axis normal to the surface. The strain along this c direction due to the SCO is approximately +5.6%, whereas in the other directions the changes are smaller (b axis: +1.0%) or even opposite (a axis: -2.3%) (**Figure 41a-d**). [**Rat et al., 2017**] If a random lateral orientation of the crystalline domains is assumed, the LS-HS transition must lead to a compressive transformational strain of approximately -1.3 % along the cantilever length, in good agreement with the experimentally observed upward deflection of the cantilever (**Figure 40**). From **Annexes A5.2.2**, it is also highlighted the good reproducibility of the thermal actuation cycle in terms of the transition temperature and magnitude of actuation. Note that the hysteresis width becomes slightly reduced after the first cycle. This phenomenon was also observed in our previous optical investigation of films of **2** and most likely occurs as a result of the release of residual stress generated during film fabrication.

5.3 Extracting mechanical parameters and actuating performance

5.3.1 Young's modulus

5.3.1.1 Low Spin

By using the methodology explained in section 4.2 we extracted the Young's modulus and the axial stress for the film of compound **2** at room temperature. **Table 7** summarizes the general properties of devices prepared for this study. The obtained values for E_{LS} and residual σ_{LS} are highlighted in bold font. It is interesting to note the relatively high value of E (9.4 GPa) in comparison with complex **1** (6.9 GPa).

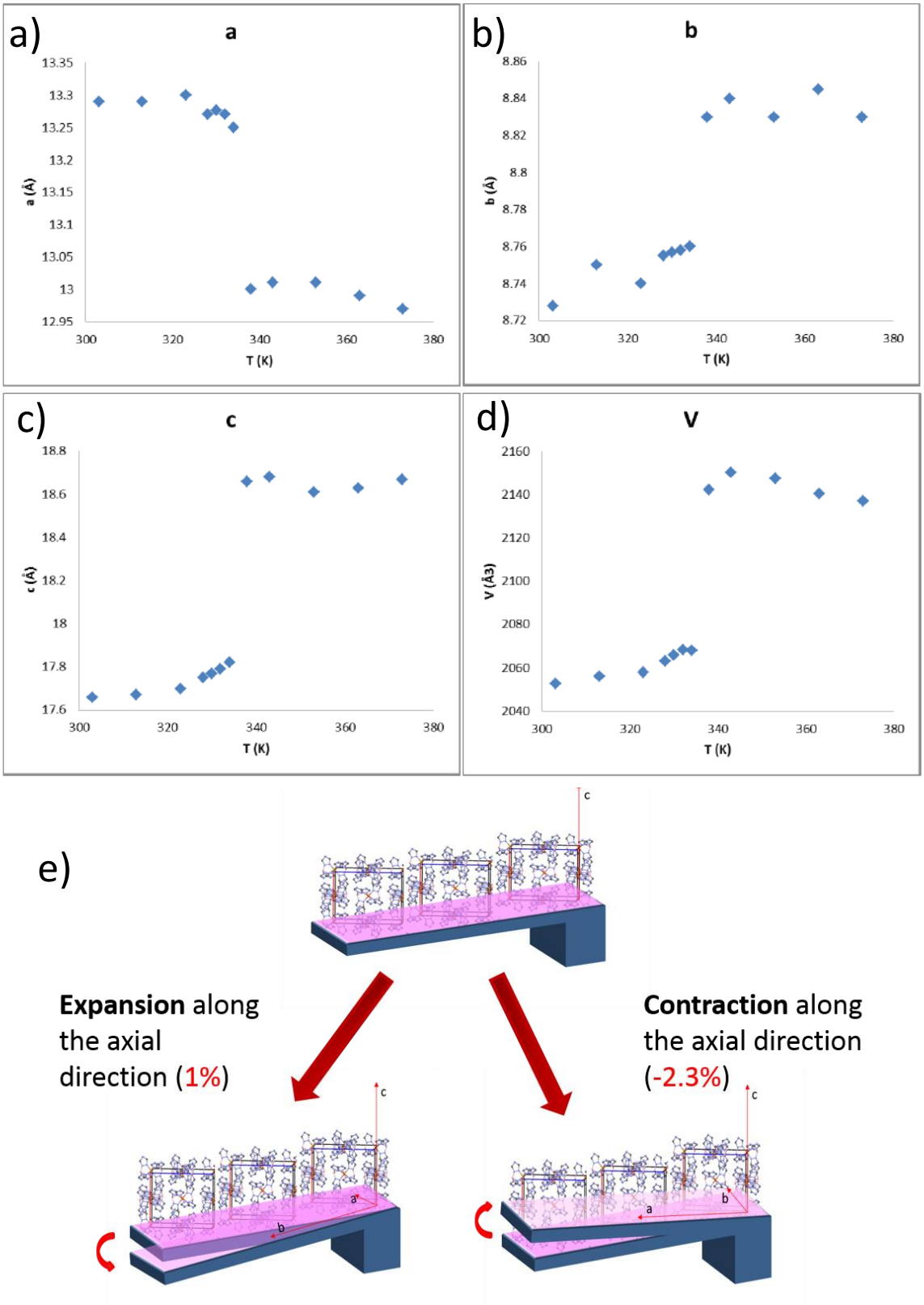

Figure 41: *a)-d) Thermal variation of the unit cell parameters and volume extracted from X-ray powder diffraction of bulk powder [$Fe^{II}(HB(tz)_3)_2$] sample in the heating mode. e) Diagram of MEMS deflection induced by the expansion or contraction of film of* ***2*** *along the cantilever length, when going from LS to HS state according to different deposition orientations.*

This finding is in line with the reported higher Debye temperature of **2** (198 K) when compared to complex **1** (146 K) [**Rat et al., 2017**]. We can speculate that the origin of this difference comes from the dense crystal packing of complex **2**. As for the film stress we cannot make such comparisons because of the different film fabrication processes. Nevertheless it is interesting to note the very high tensile stress (320 MPa) in the films of **2** in comparison with the case of **1** (75 MPa).

Table 7: *Material properties and MEMS geometry for devices described in section 5.4.*

	Silicon	Complex **2**	
		SCO_{LS}	SCO_{HS} (353 K)
Density ρ (kgm^{-3})	2330 [**Hopcroft 2008**]	1568 [**Rat 2017**]	1500 [**Rat 2017**]
Young's modulus E (GPa)	169[a] [**Hopcroft 2008**]	**9.4 ± 0.2**	**7.6**
Poisson ratio ν	0.22 [**Hopcroft 2008**]	0.3 ± 0.05 [**Felix 2015**]	0.3 ± 0.05 [**Felix 2015**]
Residual stress σ (MPa)	N.A.	**320.4**	
	Cantilever	Bridge	
Modal coefficient λ_1	1.875	4.71	
Length l (µm)	50	50	
Width w (µm)	9.5	9.5	
Thickness t_{SCO} (µm)	0.210	0.200	
Thickness t_{Si} (µm)	2.41	1.74	
Coefficient γ_1	NA	0.2949 [**Bowstra 1991**]	
Resonance frequency substrate f_s (MHz)	1.3598	5.7227	
Resonance frequency bilayer f_{bi} (MHz)	1.1994	6.1783	

[a] In this case for a silicon wafer with (100) surface we use E_{110} = 169 GPa

5.3.1.2 High Spin

The Young's modulus of the films in the HS state cannot be determined experimentally because we have not heating-cooling possibility in our Fabry-Perot set-up. Nevertheless taking into account the experimentally determined frequency shift of the MEMS when going from the LS to the HS state (Δf_r = -66 Hz, see **Figure 40b**) as well as the experimental value of the E_{LS}, we could obtain using **Equations 8 and 7a** E_{HS} = 7.6 GPa. This decrease of the Young's modulus (ΔE = -23.7 %) in the HS state is significantly higher than for compound **1** (ΔE = -8 %), but

comparable with other SCO compounds reported in the literature [**Felix et al., 2015, Hernandez et al., 2014**].

It is of course even more interesting to compare the values of E obtained from the film of **2** with those obtained for the corresponding bulk material. To this aim nuclear inelastic scattering (NIS) measurements were carried out at the ID18 beamline of ESRF with the help of Mirko Mikolasek on ^{57}Fe enriched powder samples of **2**. This technique allows us to determine the partial (only the iron atoms) vibrational density of states (VDOS) in the two spin states (**Figure 42a**). As explained in ref. [**Felix et al., 2015**] from the low frequency part of the VDOS it is possible to extract the Debye sound velocity and then calculate the Young's modulus. On the other hand variable pressure synchrotron X-ray diffraction experiments were carried out on a single crystal of **2** at the ID27 beamline of ESRF with the help of Helena Shepherd in order to determine the bulk modulus *B* of our sample (**Figure 42b**). Then taking into account the relationship between the Young's modulus and the bulk modulus the Poisson's ratio (v) was also determined. **Table 8** summarizes these results.

Table 8 : *Elastic properties of bulk and thin film samples of **2***

	Bulk	**Thin film**
E_{HS} (GPa)	10.8	9.4
E_{LS} (GPa)	7.8	7.6
B_{LS} (GPa)	10.4	-
ν_{LS}	0.32	-

Remarkably both the absolute value and the spin state dependence of the Young's modulus are in excellent agreement between the bulk and the film samples. In fact a closer agreement would be purely fortuitous since in the case of the bulk we measure a Young's modulus which corresponds to an average value for all crystallographic orientations, while for the film the Young's modulus extracted from the MEMS data corresponds to a specific crystallographic orientation (001). It is important to note also that for the first time we could determine Poisson's number for an SCO compound. The value we find (v = 0.32) confirms our initial hypothesis of using a value of 0.3 in our different calculations.

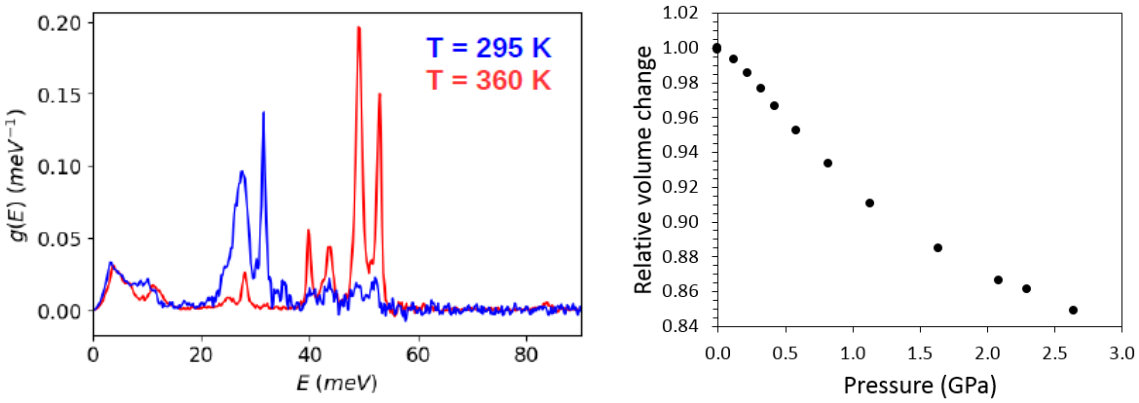

Figure 42: *a) Partial (Fe) vibrational density of states of the powder of* ***2*** *in the HS (360 K) and LS (295 K) states obtained from NIS measurements. b) Pressure dependence of the unit cell volume of compound* ***2*** *obtained from single crystal XRD.*

5.3.2 Work density

We can also predict the work density ($W/V = E\varepsilon^2/2$) as described in section 4.2.3.3. As discussed previously (Section 5.2.3), to obtain the strain we can estimate an average deformation of $\varepsilon = 1.3$ % along the cantilever length. This leads to a work density of $W/V = 0.645$ Jcm^{-3} (LS to HS) and $W/V = 0.794$ Jcm^{-3} (HS to LS). This work density is comparable with those reported for some electrostrictive polymers and shape memory alloys, confirming the expected high actuating performance of our SCO material.

5.3.3 Reactive force

The reactive force induced by the spin transition can be expressed as [**Shepherd et al., 2013**]:

$$F = \frac{3EI\delta}{l^3} \qquad (12)$$

where F is the bending force, EI the flexural rigidity expressed by **Equation 7b** (**Chapter 4**), δ the deflection amplitude obtained from the static MEMS measurements (476 nm) and L the cantilever length (50 µm).

The reactive force at the end of the cantilever corresponds to 1.07 µN. Since the force depends of the length, this will vary along the cantilever. For instance if we consider the position of the piezoresistances (l = 40 µm) we obtain a force of ca. 133 µN.

Conclusions

High quality thin films of the spin crossover complex $[Fe(HB(tz)_3)_2]$ have been deposited by high-vacuum thermal evaporation on different substrate materials with an accurate control of the film thickness between ca. 20-200 nm. The detailed temperature dependent UV absorption and Raman spectroscopic study demonstrated that the crystalline films display a cooperative, complete and tightly reproducible spin transition above room temperature, similar to the bulk material. No significant size effect was detected on the spin transition, which was attributed to the very similar crystalline domain sizes in the samples with different thickness. All these properties make the films of $[Fe(HB(tz)_3)_2]$ a very attractive candidate for integration into MEMS/NEMS and other nanoscale devices. Indeed we could show that spin-crossover molecules of $[Fe(HB(tz)_3)_2]$ can be used to actuate a silicon MEMS device, thus demonstrating good mechanical integration of the molecules to produce useful work under a controlled external stimulus. The MEMS devices integrating complex **2** exhibited spin-state dependent resonance frequency (similar to compound **1**) and we could evidence enhanced mechanical damping around the spin-transition temperature. The critical parameters for the successful integration are the robust, room temperature spin transition, the high quality of the films, the possibility to deposit them on delicate mechanical parts by thermal evaporation, the reduced and well-reproducible device dimensions, and the tightly controlled experimental conditions, including the simultaneous control of pressure and temperature. On the basis of this rigorous control of all relevant parameters, a detailed quantitative analysis of the mechanical properties and actuating performance (Young's modulus, work density and reactive force) of $[Fe(HB(tz)_3)_2]$ became possible. We could also obtain mechanical property data for the bulk compound **2** allowing us to extract for the first time the Poisson's number for an SCO complex. Additionally the implementation of an original set-up capable of tracking the dynamic and static mechanical behavior of MEMS devices opens also interesting technical perspectives.

Chapter 6: MEMS and artificial muscles based on SCO-polymer nanocomposites

In chapter 4 and 5 we discussed the first efforts to integrate SCO molecules on freestanding cantilevers to produce actuation at the microscopic scale. Even though the sublimation technique to integrate SCO materials is highly precise, it is limited to a few compounds capable to maintain their integrity while the molecules are sublimated. In this chapter a more versatile approach, the spray coating deposition is proposed. It consists of spraying micro-droplets of the desired material over the prefabricated MEMS device. To this aim we used nanoparticles of the SCO complex $[Fe^{II}(Htrz)_2(trz)](BF_4)$ mixed with the polymer SU8 in an appropriate solvent. By this approach it is possible to overcome the restriction of the sublimation method and to integrate a wide variety of SCO materials. Another advantage is that the nanoparticles are efficiently interconnected by the polymeric matrix for a reliable harvesting of their actuating properties. Besides MEMS integration we also extended this work for the fabrication of macroscopic soft actuators, the so-called artificial muscles.

6.1 SCO Polymeric Nanocomposite (SCO_PNC)

When individual materials and technologies achieve their limits in terms of application needs, new technological strategies are introduced to substitute or turn their value into a different manner. One of the ways to overcome the drawbacks of a given material is attained by making it work in combination with other materials in composites and nanocomposites. This requires obviously a more complex, interdisciplinary approach.

Basically, a composite material is defined as a material made from two or more constituents with different properties which, when combined, produce a material with different characteristics from the individual components. The individual components remain separate and distinct within the finished structure. Two main constituents are distinguished: matrix and reinforcement (also called filler or load). The matrix is generally in higher concentration and surrounds the reinforcement. The manner by which the individual phases are self-connected is described by the concept of connectivity [**Akdogan et al., 2005**].

Nanocomposites differ from conventional composites due to the exceptionally high surface to volume ratio of the reinforcing phase and/or its exceptionally high aspect ratio. In terms of

performance, nanocomposites are materials with a nanoscale structure that generally improve the macroscopic properties of products. For example nanoparticles in a polymeric matrix can affect local chemistry, degree of thermoset cure, polymer chain mobility, polymer chain conformation, degree of ordering, crystallinity and so forth.

In the literature several examples have been described wherein actuating materials, such as shape memory alloys or piezoelectrics, have been combined with a polymeric matrix [**Akdogan et al., 2005**]. For instance piezoelectric ceramics have been dispersed in polymeric matrices with the aim to maximize piezoelectric sensitivity and make the transducer mechanically flexible. These soft composite actuators allow for various mechanical and electromechanical couplings between the reinforcement and the polymeric matrix opening up several original applications for actuation, sensing, energy conversion and self-healing.

In this context spin crossover-based polymeric composites (SCO_PC) are of special interest for artificial muscles since they combine, in principle, the exceptional strain which accompany the SCO with the desirable mechanical properties of polymers (flexibility). Using a polymeric matrix it becomes possible to integrate virtually any SCO compound in actuating devices [**Shepherd et al., 2013**]. In addition this approach allows to shape SCO materials as micro- or macroscopic objects with specific sizes and shapes, which is in general impossible with the pure SCO compound [**Guralskyi et al., 2014**]. When combining SCO particles with a polymeric matrix original synergies and complementarities may also appear as a consequence of the volume change of the particles. For example, tunable electrical conductivity has been achieved either by the stress exerted on a piezoresistive polymer matrix [**Koo and Galan-Mascaros, 2014**] or as consequence of the stress induced on a piezoresistive element coupled to the SCO_PC in a bimorph object [**Chen et al., 2015**]. In order to implement these recent developments in functional artificial muscles, their actuating efficiency needs to be evaluated and proper synthesis and mechanical characterization need to be done. In the continuity of our work a polymeric spin crossover nanocomposite was first integrated into silicon MEMS devices as a micrometric film. Then this approach was extended to produce artificial muscles in form of centimeter scale objects (flowers and cantilevers).

The film integration method proposed in this chapter is based on spray coating deposition which has the advantage to produce homogeneous and high quality films on substrates of different type, shape and size. As polymeric matrix we chose the photoresist SU8, the most important reasons of this choice being: i) it is compatible with microfabrication technologies, ii) it has

physicochemical stability, iii) it has good adherence on the silicon substrate and iv) it has a high softening temperature [**Ru-Feng and Farris, 2003**]. The SU8 also helps to encapsulate and protect SCO nanoparticles from the external environment changes (humidity and other chemicals) and it is easy to characterize its optical properties by UV-vis spectroscopy due to its transparency. As reinforcing active material we have chosen nanoparticles (85 nm ±10 nm) of the complex $[Fe(Htrz)_2(trz)](BF_4)$ **3**. This compound is considered as one of the benchmark SCO materials [**Kahn and Martinez, 1998**], mainly due to its robustness, above room temperature transition, wide hysteresis loop and large volume change (≈11 %) on the SCO.

6.1.1 Generalities of $[Fe(Htrz)_2(trz)](BF_4)$

X-ray diffraction studies [**Grosjean et al., 2013**] have revealed that **3** contains one-dimensional coordination chains that are reinforced by inter-chain BF_4^- anions (**Figure 43a**). Each Fe^{II} cation is six-fold coordinated to nitrogen atoms of six triazole ligands in the bridging 1,2-coordination mode to form infinite 1D chains. The iron-ligand distances vary significantly upon the SCO (LS = 1.977 Å at 300 K to HS = 2.192 Å at 420 K), which give rise to a particularly large unit cell volume variation (ΔV = 11.5 %).

This compound is known to exhibit abrupt and complete SCO above room temperature with a large thermal hysteresis (≈40 K) (**Figure 43b**). Its pink to white color change associated to the SCO makes easy to characterize its properties by optical methods such as UV-vis absorbance and optical reflectivity [**Chen et al., 2015, Durand 2013**].

Compound **3** can be obtained as crystalline powder of different dimensions from the micro to the nanoscale. In general particles are formed of several coherent domains whose size was shown to be proportional to the particle size [**Grosjean et al., 2013**]. Remarkably it was shown that the cooperativity (hysteresis) in this compound is maintained even in very small objects [**Coronado et al., 2007, Durand 2013**]. Additionally they are able to form stable suspensions in organic solvents for longer periods of time [**Coronado et al., 2007**], which is an advantage for this work since the spray deposition involves a relatively long storage time prior to the coating.

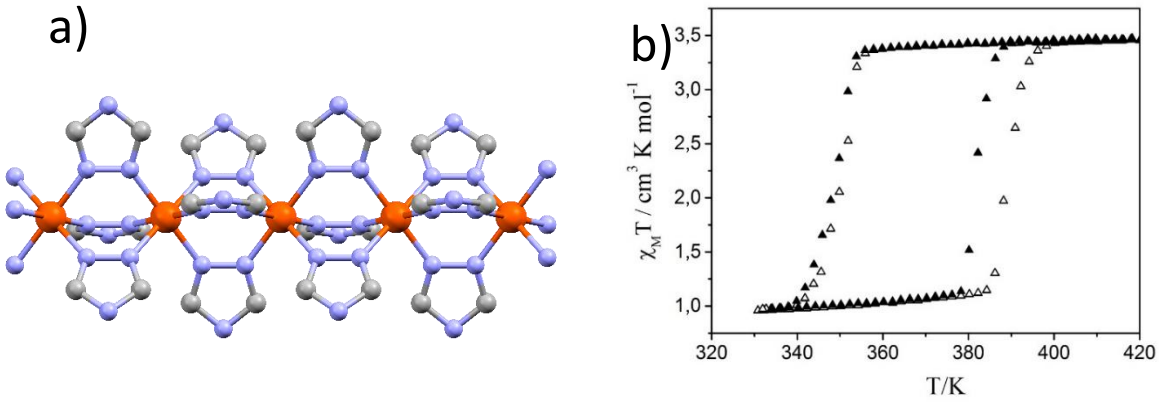

Figure 43: *a) 1D chain of **3** along the b axis, and b) typical temperature dependence of magnetic susceptibility vs. temperature of compound **3**.*

In summary for this project we choose nanoparticles of **3** because they offer i) high percentage of volume change, ii) stable suspensions, iii) homogeneous dispersion, iv) robust and abrupt spin transition with a wide hysteresis loop and v) the possibility to carry out measurements in air without any cryogenic equipment.

During this thesis we tried to elaborate thin films with particles of **3** without using any polymeric matrix. However it became clear that these films will be difficult to use for actuating purposes. In fact we observed that the morphology of the particles as well as the structure of the films are not stable and change from cycle to cycle [**Manrique-Juarez et al. 2016**]. Different phenomena, such as particle aggregation, stacking and surface degradation have been evidenced using variable temperature AFM measurements (**see Annexes A6.1-2**), which discouraged us to pursuit this way.

In order to profit of the outstanding properties of compound **3**, it was necessary combine it with a polymeric support (SU8), which helps to stabilize and "freeze" the nanoparticles and at the same time it protects it from undesirable environmental effects. The polymer provides also a good adhesion to the substrate and helps to transfer the mechanical strain from the particles to the structure.

6.1.2 Generalities of SU8 photoresist

In terms of microfabrication SU-8 provides well-defined resist profiles and it is suitable for use as permanent structure. It has been widely used in microfabrication processes. Among its advantages we can mention chemical inertness, thermal resistance and mechanical stability. Its final properties depend on the processing conditions for the specific desired application [**Ru-Feng and Farris, 2003**].

6.1.2.1 Chemistry

The SU8 resist is made of $C_{21}H_{24}O_4$ (bisphenol A diglycidyl ether) and consists of a multi-functional, highly branched polymeric epoxy novolac resin dissolved in an organic solvent, ϒ-butyrolactone (GBL). Along with the formulation there is a triaryl sulfonium salt which acts as photo-acid generator during the UV-light exposure. The resist has an average of 8 epoxy groups in each molecule, hence the name SU8 (**Figure 44**) [**Ru-Feng and Farris, 2003**].

A possible reaction mechanism for an epoxy group is represented on **Figure 45**. Photo-acid designated as H+ A- is photo-chemically produced in the solid photoresist film upon light absorption. The photo acid acts as catalyst in the subsequent cross-linking reaction that takes place during the post-exposure baking (PEB). This means the exposed resists contains acid catalyst, while the unexposed does not. The crosslinking reaction which is catalyzed happens when each epoxy group can react with another epoxy group, either in the same or different molecule and only occurs at high temperatures. The formed network is dense and insoluble in the developer (i.e. it is a negative resist).

6.1.2.2 Processing parameters

A complete SU8 process consists of resist coating, soft bake, UV-exposure, PEB and development. A controlled hard baking is recommended to further cross-link the SU-8 structures if they are supposed to remain part of the device. Process conditions are well established for commercial SU-8 in order to standardize and obtain the desired properties. However when a parameter in the formulation is changed, new protocols need to be established.

In our case the optimization of the process was based on the UV-exposure time and the PEB temperature.

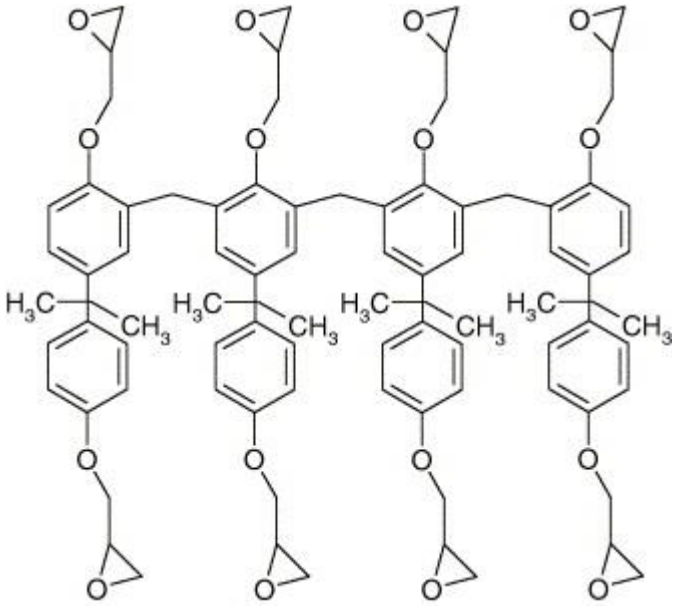

Figure 44: *Molecular structure of SU8*

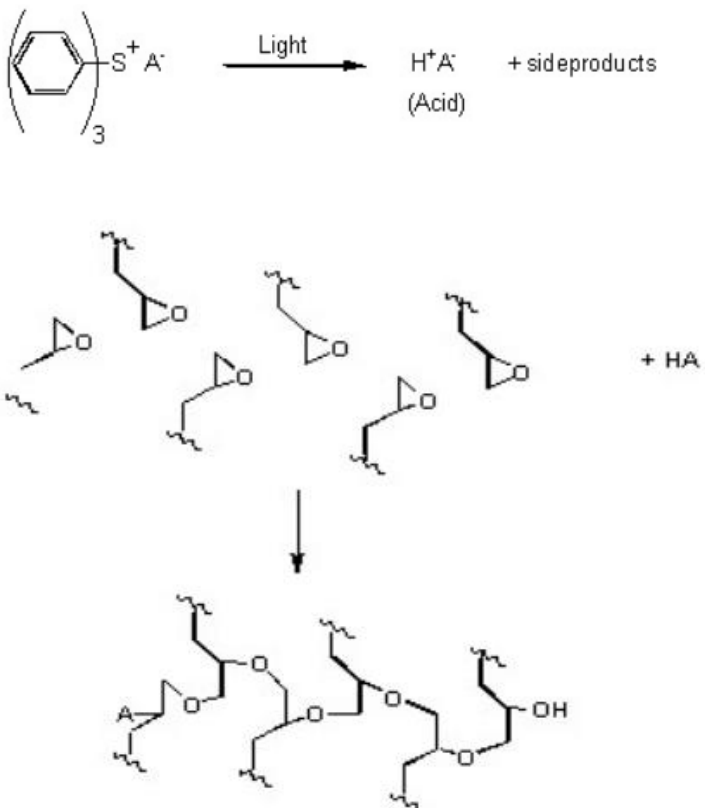

Figure 45: *Example of crosslinking reaction mechanism of SU8.*

During the preliminary tests, we observed that when SU8 is mixed with the SCO nanoparticles, the standard UV-exposure time required for polymerization was not enough (**Figure 46**), thus exposition time was prolonged as well as the hard baking temperature was increased. **Figure 47** summarizes the final parameters which were used in this work. Since the nanocomposite is deposited at the final step of the microfabrication process and the whole device is exposed to UV (except the masked electrode zones) no development is necessary. It may be worth to note that we used the same UV exposure for all samples independently of their thickness and their composition (with or without SCO_NPs).

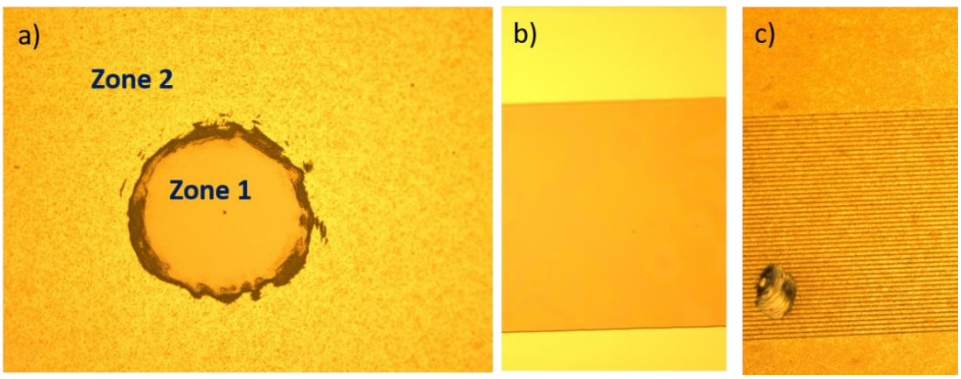

Figure 46: *a) Optical image recorded following polymerization crosslinking and development of a mixture of SU8 and SCO nanoparticles. The UV exposure time for zone1 (zone 2) was more (less) than 1 min. b)-c) Photolithography in standard conditions using SU8 photoresist and SU8 mixed with SCO_NPs. In the former (latter) case one obtains complete (incomplete) polymerization.*

6.1.2.3 Mechanical properties of SU8

One of the advantages when using SU8 is its thermo-mechanical stability after a hard baking processing. Several works report Young's modulus (***E***) values between 2.4 and 5.5 GPa at room temperature, depending on the fabrication and testing conditions. In the case of hard baking the reported values of ***E*** are in general higher (about 3.5-5 GPa) [**Chung and Park, 2013**]. SU8 displays has a Poisson's ratio (υ) of 0.22 and a glass transition temperature (Tg) of 323 K for the unexposed resin. In the case of crosslinked and hard-bake samples Tg can reach values above 473 K and a degradation temperature of 553 K, strongly depending on the post exposure conditions such as hard baking temperature. Obviously the mechanical properties are

temperature dependent, which will be important to consider in our work. [**Chung and Park, 2013, Ru-Feng and Farris, 2003**].

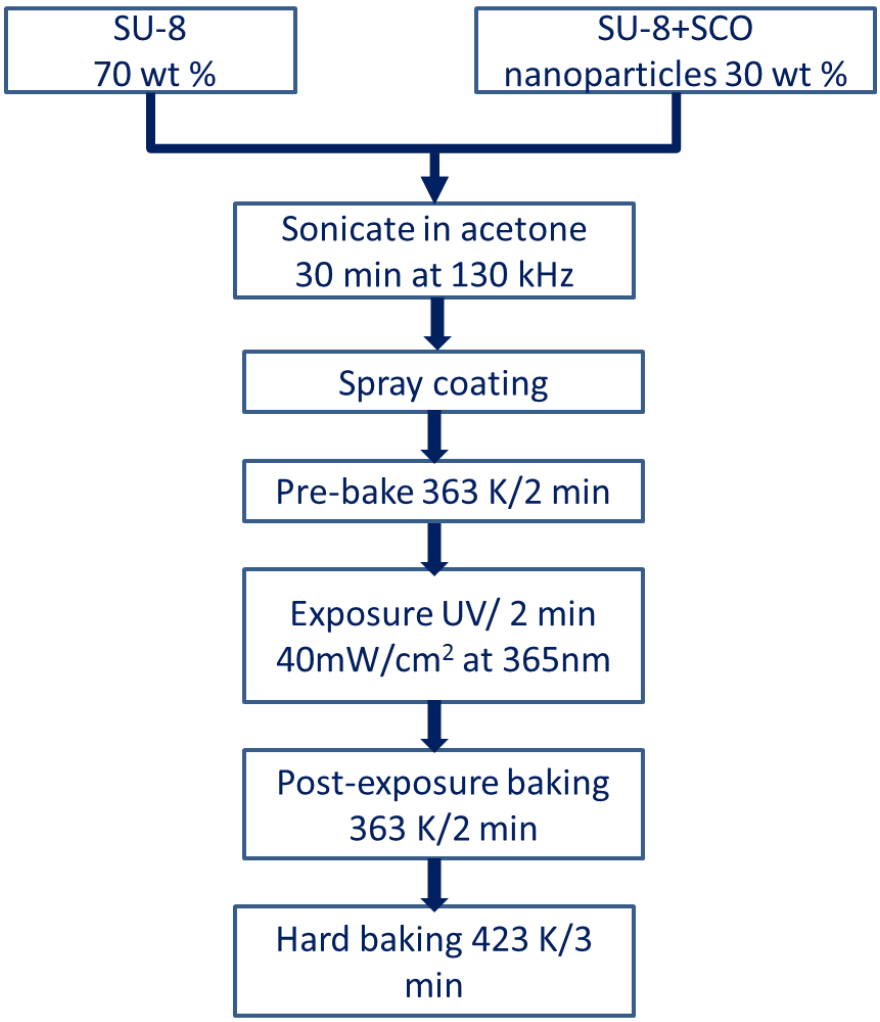

Figure 47: *Process SU-8 protocol for this work.*

6.1.3 Film: synthesis and deposition

For most nanocomposites a high ratio reinforcement/ matrix is required to produce a high impact over the desired final properties. Previous works with SCO polymer composites have reported up to 50 wt% loading, without much affecting the sample integrity [**Guralski et al., 2014**]. However higher concentrations seem also possible under specific preparation conditions [**Koo and Galan-Mascaros, 2014**]. For our work a lower concentration was used in order to

favor the dispersion stability, homogeneity and, therefore, to obtain a good distribution of the particles in the matrix. The SCO nanoparticles concentration was then compromised to 30 wt%, which we found as an acceptable charge to avoid agglomeration and/or brittleness, while at the same time it still allows to obtain a significant strain required for actuation purposes.

Since the aim of this research was to verify the actuation efficiency rather than the reinforcement ratio effect, no further concentrations were tested for actuation purposes. However as part of perspectives of this thesis, it will be interesting to analyze carefully this parameter, which may impact in a considerable manner not only the mechanical properties, but also the SCO properties.

6.1.3.1 Synthesis of SCO_NPs

The SCO nanoparticles of **3** were synthetized by Léa Godard (LCC-CNRS). For the synthesis of SCO_NPs, an aqueous solution of $Fe(BF_4)_2$ $6H_2O$ (424 mg, 1.25 mmol in 1 mL H_2O) was added dropwise to a mixture of 3.6 mL of Triton X-100, 3.6 mL pentanol and 8 mL of cyclohexane. An identical microemulsion was prepared with a solution of H-trz (262 mg, 3.75 mmol in 1 mL H_2O). These two microemulsions were mixed together and left to stir for 24 h. The obtained nanoparticles were separated and washed three times in ethanol. The observed average diameter of the SCO_NPs is 85 nm (**Figure 48a**).

6.1.3.2 Preparation of the SCO_NPs-SU8 solution and spray coating deposition

According to the process diagram presented on **Figure 47**, a solution of 1.4 g EPON^{TM} SU-8 (3050) from MicroChem Inc.) and 700 mg SCO_NPs in 80 g acetone was prepared by sonication (30 min at 130 kHz). The acetone is used as the liquid medium to allow the spraying. The solvent is evaporated during the deposition resulting in a charge of 30 wt% of nanoparticles inside the polymeric matrix. In parallel, control samples without nanoparticles were prepared as blank. The solution was deposited by a spray coater Delta AltaSpray (SUSS MicroTec). During the deposition the flow rate was 1ml/min and the devices were heated in a substrate plate at 60 °C to assure the acetone evaporation. The spray coater is designed to spray in four different directions during each cycle, which means 4 pass per cycle to assure a homogeneous

deposition. Sub micrometric films ≈0.430 μm are formed during each spray coating (≈1.77 μm per cycle) and the final thickness depended on the number of deposition cycles.

Two different depositions and structures were prepared for i) MEMS devices (**MEMS-PNC)** and ii) artificial muscles (**Polymer-PNC)**. In the first case 2 deposition cycles were performed achieving a thickness of 3.5 μm over the silicon cantilever structures with 20 μm thickness. Only the gold patches are masked. In the second case a bilayer film made of 22 μm SCO_PNC / 50 μm polyester was made. The polyester substrate consists of a commercial, optically transparent film (3M^{TM} 8211). It was chosen since it easily adheres on a silicon substrate and can be peeled away later when the SCO_PC deposition process is finished. After releasing from the silicon substrate, the bilayer-polymeric film can be cut in the desired shape.

In both cases, after the spray deposition (before peeling in the second case), samples were exposed during 90 s exposed to UV-irradiation using an EVG 620 machine (40mW/cm^2 at 365 nm). Then they were submitted to a PEB of 363 K during 2 minutes, followed by a hard baking at 423 K during 3 minutes to assure a complete cross-linking.

6.1.3.3 Sample characterization

The deposited film thickness was measured using a mechanical profiler KLA-Tencor/P-15. The film roughness was measured in ambient conditions using an AFM Cypher-ES microscope (Oxford Instruments) in tapping mode. Temperature dependent absorbance of the films were collected at 310 nm using a Cary 50 (Agilent Technologies) spectrophotometer and a Linkam FTIR-600 liquid nitrogen cryostat (equipped with fused silica windows). Spectra were acquired in the 293-423 K range. SEM images were acquired at room temperature using a Hitachi S-400 instrument. TEM images were acquired using a JEOL JEM-1400 (200 kV) instrument. Functional groups and interactions between compound **3** nanoparticles and SU-8 matrix were studied by infrared spectroscopy using an FT-IR spectrometer in the attenuated total reflectance mode (ATR), in the range of 4000-600 cm^{-1}.

In order to study the thermomechanical properties of composites two methods were used: i) MEMS resonance frequency tracking as described in section 5.2.2.1 and ii) dynamical mechanical analysis (DMA) in the case of artificial muscles. For this an ARES G2 rheometer from TA Instruments was used to perform DMA testing using a rectangular film tension geometry. The sample holder has two screw-down clamps that hold the film in tension while a

small amplitude oscillatory strain is applied to it. DMA tests were performed in the temperature range between 293 and 403 K with heating/cooling rates of 2 K min^{-1}. Samples were cut in a rectangular shape 24 x 7.5 mm with a thickness of 170 µm, and were loaded at a starting gap height of 10 mm. An oscillatory strain of 0.08 % was applied at a frequency of 1 Hz. In tension a static axial force of 2 N on the samples was set to be at least 20 % greater than the dynamic strain force applied to the film in order to prevent the sample buckling. Preliminary amplitude tests were performed at room temperature in dry nitrogen atmosphere to determine the linear viscoelastic range and optimal mechanical conditions.

The thermochromic (i.e. SCO) properties of the film and powder were acquired simultaneously by reflectivity measurements using a stereomicroscope and a liquid nitrogen cryostat (Linkam). Reflectivity data were acquired in a range between 293-423 K.

6.1.4 SCO properties of polymeric films

The sonicated mixture (polymer-nanoparticles-acetone) produces a good and stable dispersion of SCO nanoparticles in the matrix (**see Figure 48c**) and also attractive SCO properties. A smooth surface (Ra = 1 nm) was obtained (**Figure 48b**). The SCO properties of the composite were evaluated by UV-vis absorbance measurements at 310 nm (**Figure 48d**). The transformation from the low-spin to the high-spin state occurs around 389 K ($T_{1/2}$ up) during the first heating, shifting to 386 K in the second and third cycles. On the other hand the reverse transition from HS to LS occurs around 328 K ($T_{1/2}$ down) in all cases (**see Annexes A6.3** for the three first cycles). Comparing the spin transition of the nanocomposite with reported values for similar nanoparticles [**Moulet et al., 2016**], the composite material displays a hysteresis broadening effect of ca. 20-30 K. It appears that the matrix may affects thus the hysteresis width similar to what was reported previously by other authors [**Tissot et al., 2012, Durand et al., 2013**].

With the purpose to analyze this particular hysteresis behavior, variable temperature optical reflectivity measurements of the SCO nanoparticles both with and without the SU8 matrix were carried out simultaneously. As shown in **Figure 48e** the spin transition in the nanoparticles occurs with a hysteresis of 28 K width, while the same particles in the SU8 matrix display a hysteresis of ~58 K in the same experimental conditions. Additional experiments at different temperature ramps (1 K/min, 3K/min and 5 K/min) were performed to observe possible kinetic

effects on the SCO behavior (**see Annexes A6.4**), but the hysteresis remains the same in all cases. Let us know also other polymeric composite systems have been published by different authors using the same compound **3** (**see Table 9**), but with larger particle sizes, however, they do not report this hysteresis discrepancy between the powder and the composite film [**Guralsky et al., 2014, Chen et al., Rat et al., 2016b**].

In the case of the work developed by Pierrick Durand et al., the authors report on a very broad hysteresis loop of about 65 K in the case of nanoparticles of **3** smaller than 5 nm surrounded by a silica matrix, to be compared with the hysteresis of 28 K in the bare nanoparticles. They attribute this broadening to an elastic confinement effect on the embedded SCO NPs due to the matrix stiffness [**Durand et al., 2013**]. Besides the stiffness of the silica, the efficient contact between the matrix and nanoparticles was considered also as one of the main parameters responsible of the elastic interactions. In the case of our work, we used SU8, which is of course less stiff than silica, but its elastic modulus is relatively high with respect to other polymers. It is important to mention that SU8 crosslinking was made once the nanoparticles were inside the resin, which may also favor the mechanical interactions. Additionally the homogeneous particle distribution should improve the surface contact between the reinforcement and the matrix.

Table 9: *SCO properties of compound **3** inside different kinds of matrices*

Reference	Particle size	Matrix	Process	Percentage reinforcement	$T_{1/2}$ (LS)	$T_{1/2}$ (HS)	Hysteresis nanoparticles	Hysteresis Composite	Storage modulus Matrix (Gpa)
This work	85 nm	SU-8	Spray Coated suspension	30 %	328 K	386 K	28 K	60 K	~3.7 [Chung 2013]
Guralskyi 2014	micrometric	PMMA	Dispersed in organic solvent and Drop casted	50 %	≈331 K	≈363 K	30 K	32 K	~1.2 [Dixit 2009]
Durand 2013	3.5 nm	Silica (SiO_2)	Synthesis in presence of mesoporous silica	20 %	≈310 K	375 K	28 K	65 K	~74 [Pabst 2013]
Chen 2015	nanometric	Policarbonate	Dispersed in organic solvent and drop casted	50 %	332 K	370 K	Not reported	38 K	~1.5 [Amol 2009]
Koo 2014	450±50 nm	Poly-pyrrole	Synthered under isostatic pressure	71 %	343 K	396 K	Not reported	53 K	>1 [Shoa 2010]
Rat 2016b	1-5 µm	Cellulose	Aqueous solution mixure	50 %	353 K	385 K	Not reported	32 K	~0.5 [Rat 2016b]

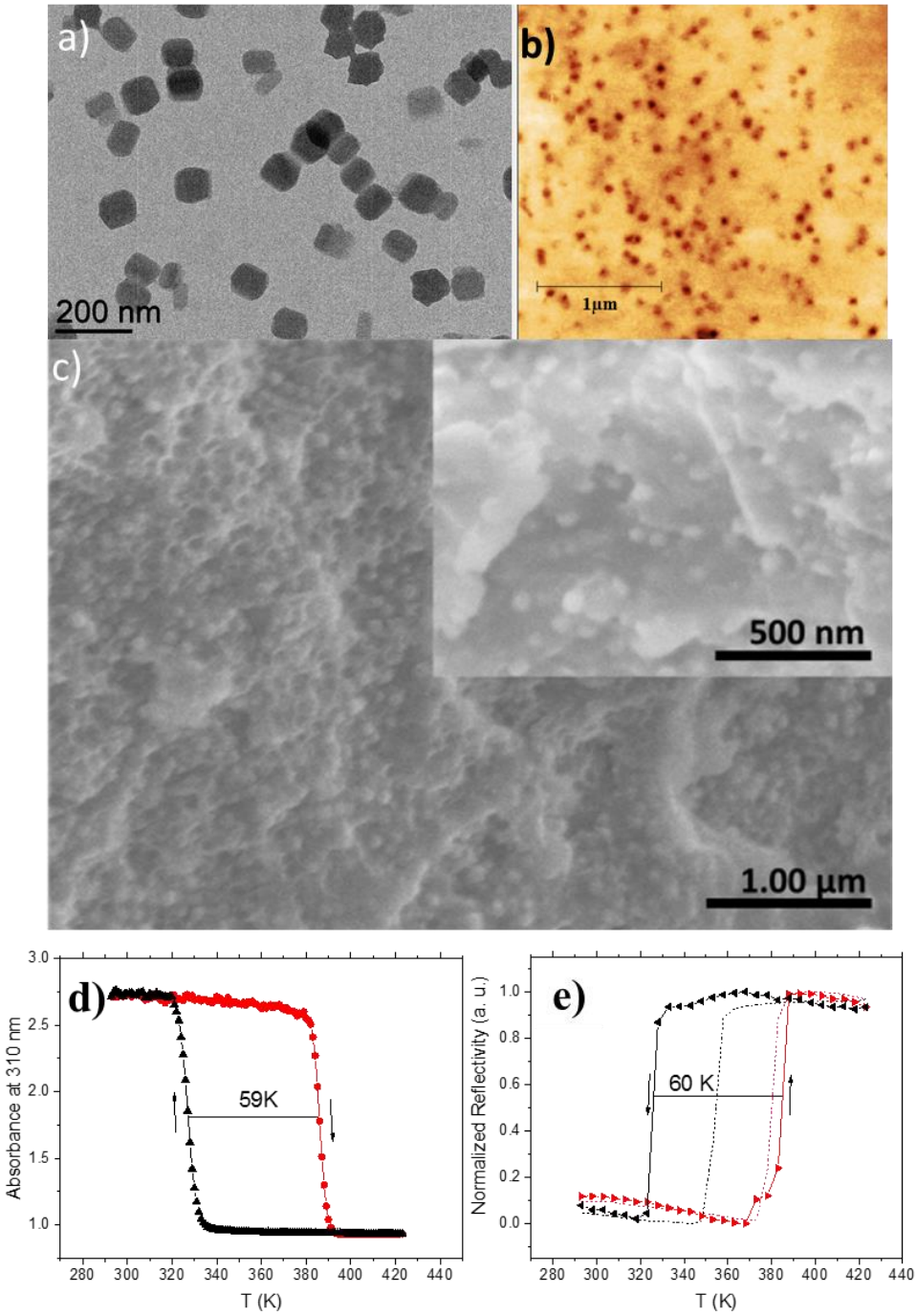

Figure 48: *a) TEM image of SCO nanoparticles of* ***3****, b) AFM images of the SCO-SU8 composite, c) SEM image of the cross-section of the SCO-SU8 composite, d) Optical absorbance vs. temperature curve of the SCO-SU8 composite (second cycle), e) Optical reflectivity vs. temperature of the SCO-SU8 composite (triangles) compared with that of the bare SCO (dashed line). Heating and cooling are indicated by arrows.*

FT-IR was used to try to observe the physico-chemical interactions between the reinforcement and the matrix. The room temperature IR spectra of the bare nanoparticles, matrix and nanocomposite are shown in **Figure 49**.

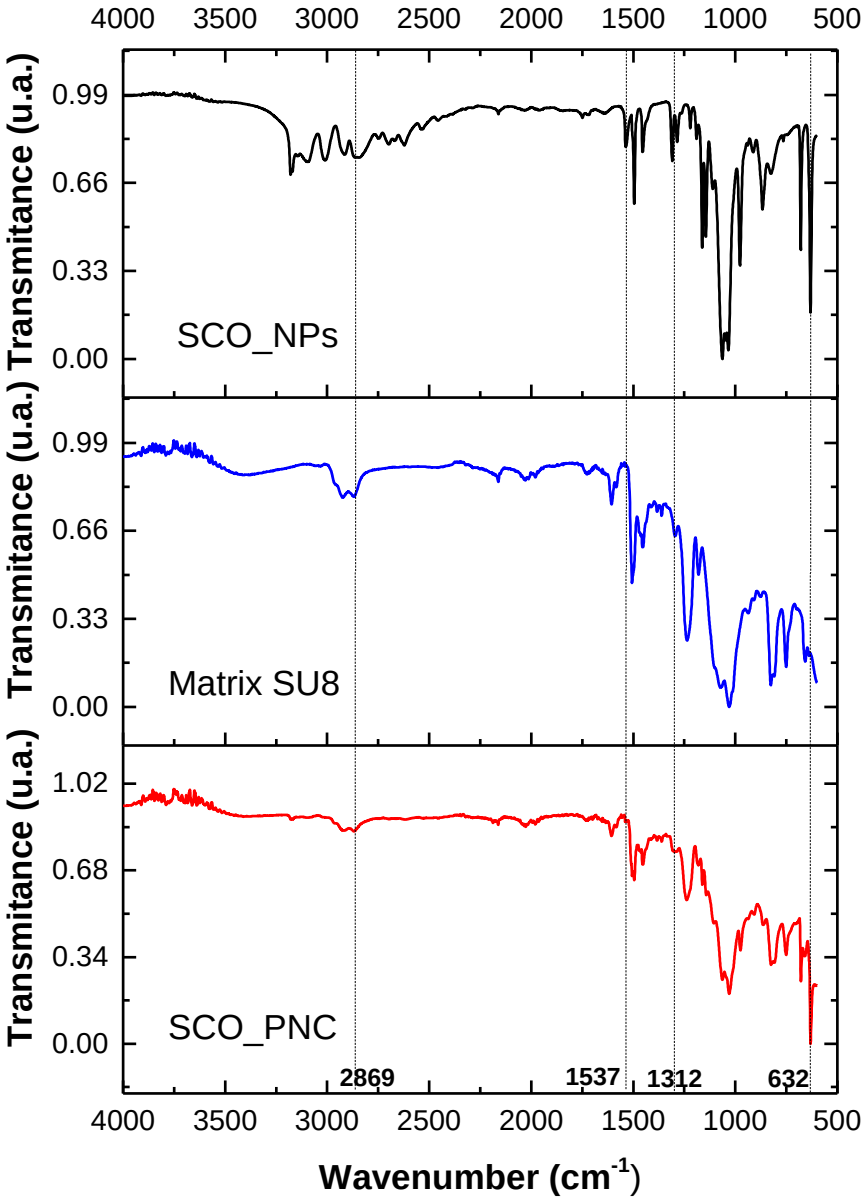

Figure 49: *FT-IR spectra of SCO nanoparticles of **3** (black line), the SU8 polymeric matrix (blue line) and the SCO-SU8 nanocomposite (red line) at room temperature.*

Several vibrational modes in the far IR (Fe-N stretching vibrations and FeN_6 distortion modes) and mid-IR (vibrational modes of the Htrz/Trz ligands) are very sensitive to the Fe^{II} spin state. This can be followed as a "fingerprint" of the material. Most of the bands observed in the pure SU8 and SCO_NPs coexist in the spectrum of the composite material. Several peaks of the nanoparticles are masked by the intense peaks of the polymer. More interestingly certain IR peaks of the nanoparticles are shifted when the particles are surrounded by the polymer, which might indicate the mechanical stress of the matrix over the particles (**see Figure in Annexes A6.5**). However, at this stage of our investigation it is difficult to conclude on the origin of

these spectral variations and further studies using variable temperature, FT-IR and Raman spectroscopies will be necessary.

6.2 MEMS: SCO detection and actuation by thermal energy

Overall we can say that high quality films of the SCO-SU8 nanocomposite could be deposited with favorable SCO properties. For the mechanical characterization of these nanocomposite films we used silicon MEMS similar to the ones described in section 4.3. As shown in the SEM image in **Figure 50b** the spray coating produces a continuous and smooth coverage on the surface of the MEMS.

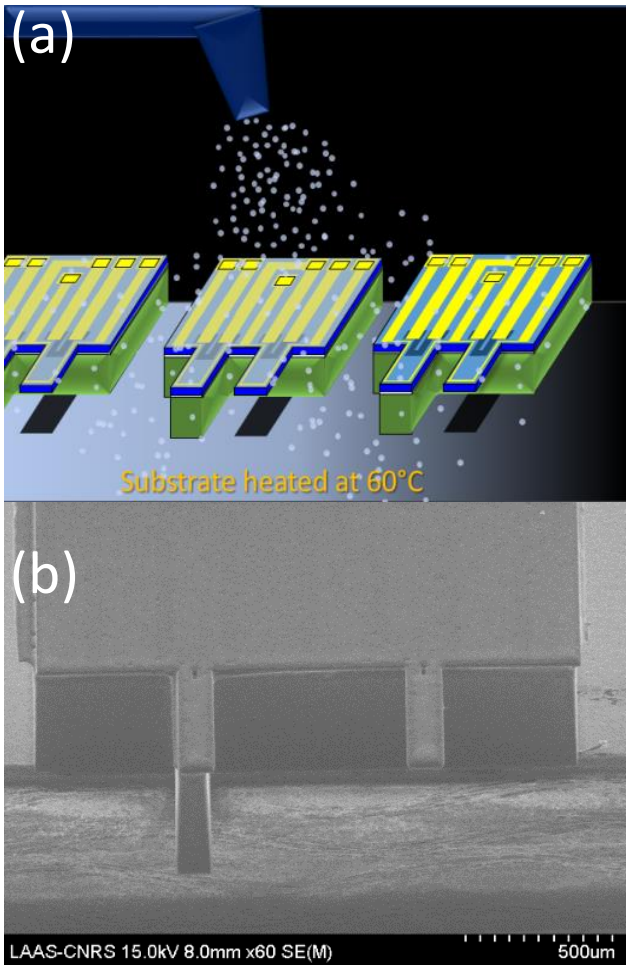

Figure 50: *a) Scheme of spray deposition on silicon cantilevers, b) SEM image of silicon cantilevers covered by the nanocomposite (3.5 µm SU8-SCO over 20 µm Si cantilever with 840 µm length and 100 µm width).*

The static and dynamical mechanical behavior of the MEMS was followed simultaneously by our home-made system as described in section 5.2.2. The temperature of the devices was cycled between 293 K and 423 K. **Table 10** summarizes the shifts of resonance frequency, quality factor, piezo-resistance and amplitude of the static bending detected between the HS and LS states. It is important to stress that all measurements were carried-out inside the hysteresis loop at the same temperature (353 K). By fixing a temperature inside the hysteresis we can analyze the effect of the spin transition on the mechanical properties of the device while discarding any temperature effect.

Table 10 : *MEMS: Static and dynamic response in the LS and HS states (both at 353 K)*

At 353K	f_r	Q	R	Amplitude
LS	30.159 kHz	610	536.38Ω	4.996µm
HS	30.166 kHz	694	537.19Ω	8.649µm
Shift	7 Hz	84	0.81 Ω	3.653µm

6.2.1 Static response

The amplitude variation was calibrated using the procedure described in section 5.2.2.2 (**See Figure 51a-c**). **Figure 51d** shows the static response of the mechanical device during the second heating-cooling cycling. The actuation induced by the spin transition is well identified thanks to the characteristic and well reproducible hysteresis loop associated with the SCO. (See first 3 cycles for the static and dynamic responses in **Annexes A6.6**) Ten thermal cycles were carried-out to verify the efficiency and reproducibility of the SCO in the static actuation regime. After the first cycle, the actuation amplitude becomes stable (≈0.8 Ω = 3.65 µm, **see Figure 52**). It is interesting to note that contrary to compound **2** (see Chapter 5) the LS to HS transition here induces a downward bending of the cantilever (i.e. an increase of the piezoresistance) which indicates and expansion of the nanocomposite film along the cantilever. This result is in agreement with the expected isotropic volumetric dilation of the composite.

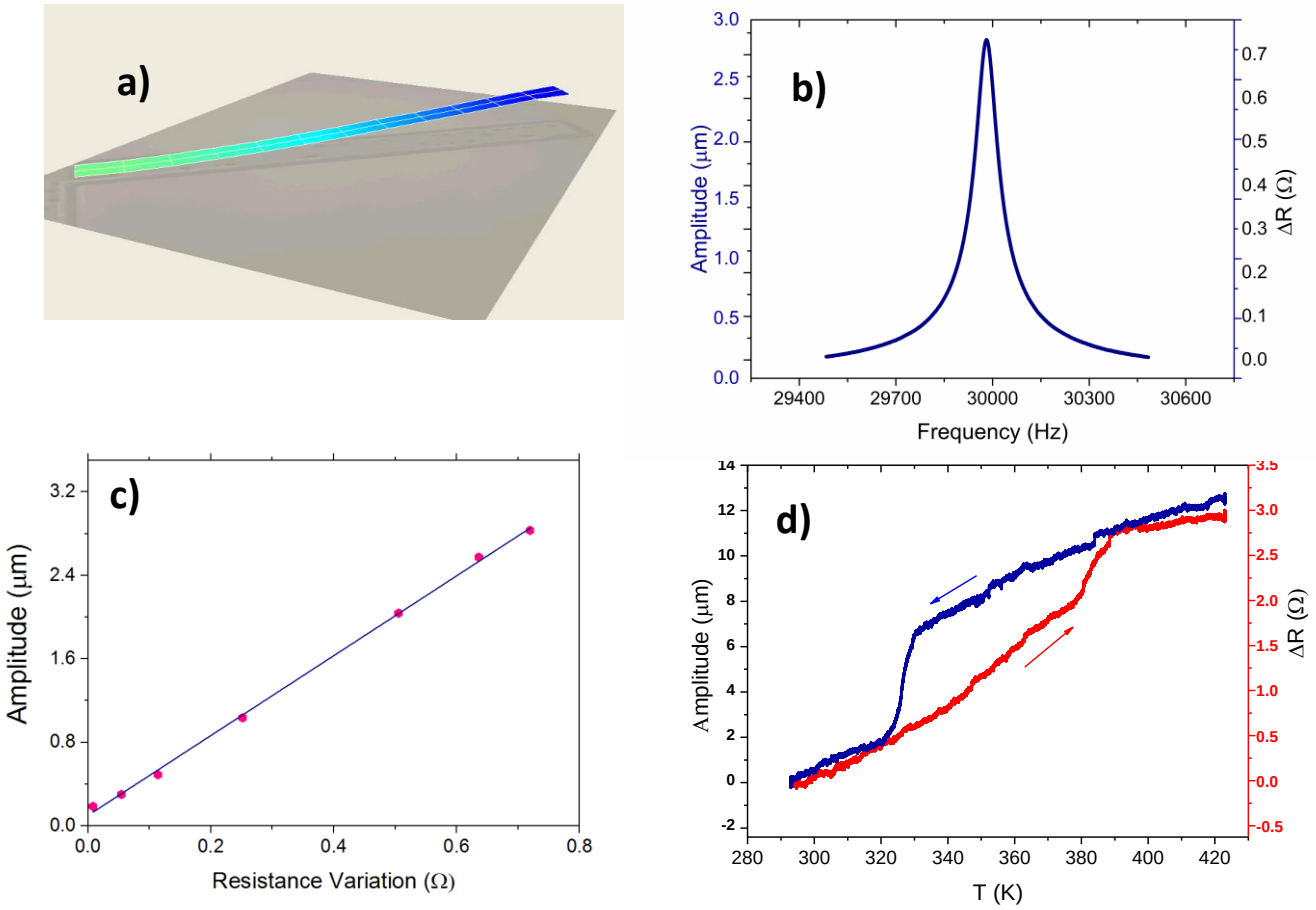

Figure 51: *a)-c) Static calibration of MEMS: a) 3D cantilever mapping of the 1st resonance mode, b) the corresponding resonance peak detected by both optical (bending amplitude) and electrical (piezoresistances) techniques, and c) the final calibration curve. d) The actuating response of the MEMS covered by the SCO_SU8 nanocomposite. Arrows indicate heating-cooling.*

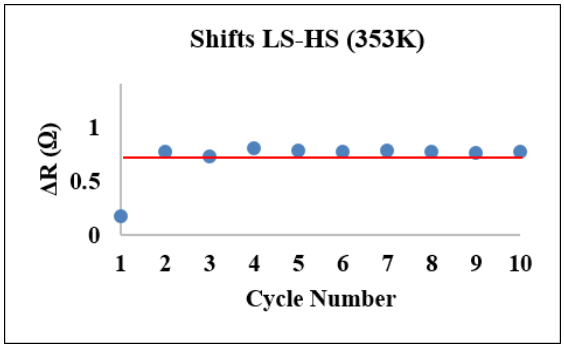

Figure 52: *Actuation reproducibility*

6.2.2 Dynamic response and thermomechanical properties (MEMS vs. DMA)

The dynamical-mechanical properties of the SCO-SU8 composite films at the microscopic scale were analized using the **MEMS** devices. These results were compared with the dynamical mechanical analysis (DMA) on the bilayer Polyester/SU8-SCO films (**see Figure 53** and systems without nanoparticles in **Annexes A6.7**).

DMA is widely used by the research community of polymeric materials to study their viscoelastic properties. Recently Rat et al. [**Rat et al., 2016b**] used this technique also to explore the viscoelastic response of a cellulose - $[Fe^{II}(Htrz)_2(trz)](BF_4)$ composite material and observed the variation of viscoelastic properties upon the SCO. DMA consists of applying a stress or strain to a sample upon a temperature program and analyzing the response to obtain phase angle and deformation data. These data allow the calculation of the damping or tangent delta (tanδ) as well as the complex dynamical modulus (E*). The complex modulus is composed of the storage modulus E' (elastic response) and the loss modulus E'' (viscous response).

The stiffness of the composite material is directly proportional to the resonance frequency f_r in MEMS and also to the storage modulus E' obtained with DMA. As for the energy dissipation we can compare the inverse of the quality factor (1/Q) obtained with the MEMS with the loss tangent (tanδ) in DMA. Lower the energy loss, higher the quality factor becomes (see sections 3.2.1.2, Chapter 3).

Overall, both approaches seem to be in agreement. In the case of the **MEMS** study, the drop of $\boldsymbol{f_r}$ is observed during the heating ramp far from the spin transition (**Figure 53a**), while the internal frictions **1/Q** increase (**Figure 53b**). This behavior is well known as the classical thermomechanical damping of silicon MEMS devices [**Kim et al., 2008**]. Overlapped to this intrinsic behavior of the silicon MEMS, the response of the system to the SCO is also detected. Notably a slight increase of f_r is observed at the LS to HS transition ($T_{1/2}$ up ≈ 387 K), which is reversible when the system returns to the LS state ($T_{1/2}$ down ≈ 328 K). The variation of 1/Q also reproduces the SCO with a clear hysteresis loop and a drop of 1/Q is evident in the HS phase (less friction). In the case of the DMA measurements on the bilayer film, $T_{1/2}$ up is masked by a relaxation process in the polyester component. Nevertheless the hysteresis is clearly observed through the variation of both E' and tanδ and $T_{1/2}$ down is easily detected (**Figure 53c-d**). In agreement with previous works on cellulose - $[Fe^{II}(Htrz)_2(trz)](BF_4)$ composites [**Rat et al., 2016b**], one can observe the softening of the matrix (i.e. decrease of E') while the

particles contract during the HS to LS transition. This means that the stiffening (or softening) of the polymeric composite is a consequence of the volume expansion (or contraction) of the particles, rather than the change of the mechanical properties of the particles as it was observed with pure SCO films in Chapters 4 and 5. (N.B. Actually the particles are stiffer in the LS phase.)

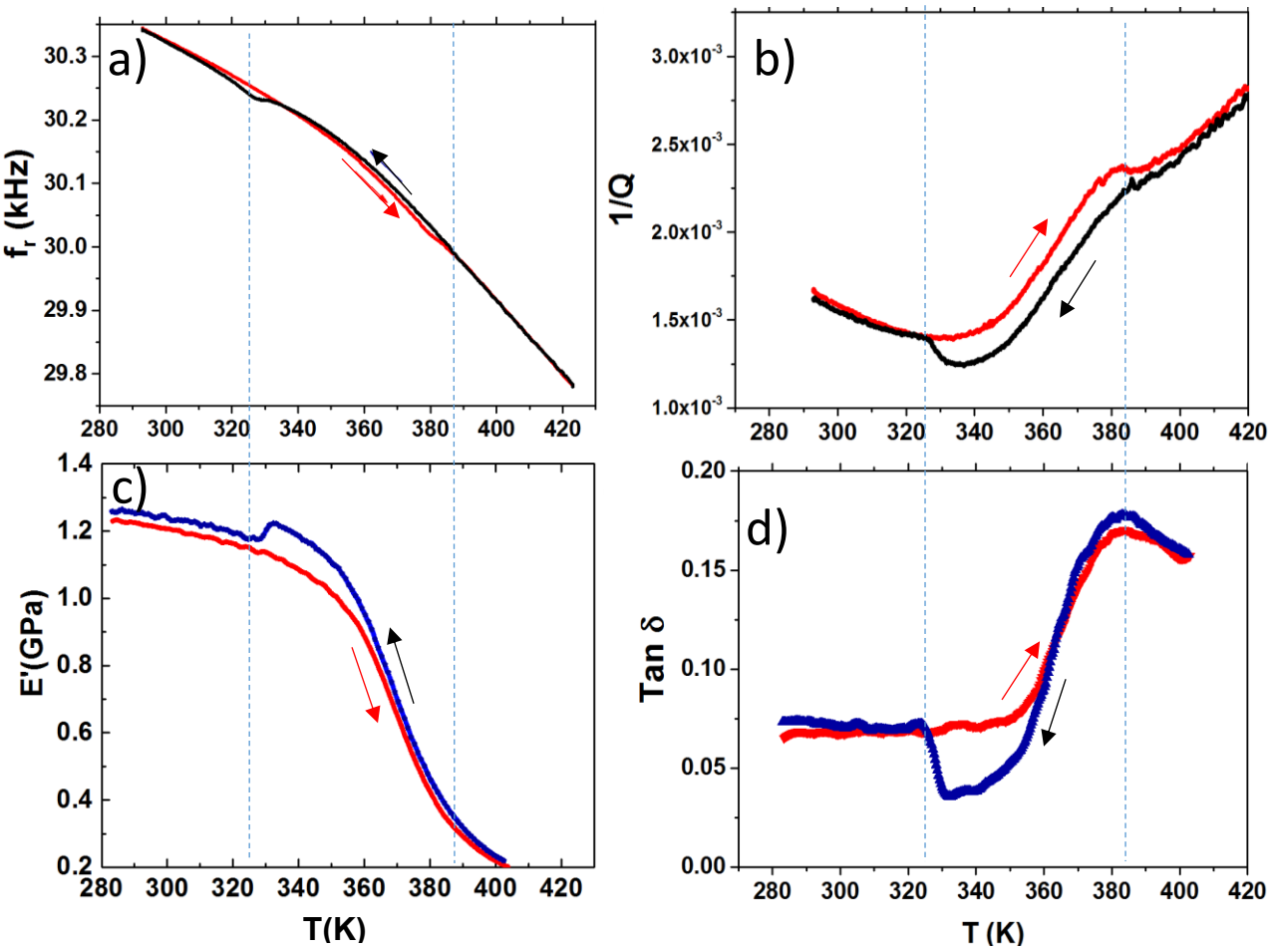

Figure 53 : *Thermomechanical response of SCO-SU8 polymer composites detected using MEMS (a-b) and DMA (c-d) techniques. Arrows indicate heating and cooling.*

It is possible correlate the amplitude of actuation δ with the mechanical properties of our active layer when the SCO occurs by using the curvature of the cantilever **k** (**Equation 13**) and the analogy of Timoshenko's equation for a bimetallic strip [**Shepherd et al. 2013**]. As the amplitude shift between the LS and HS state was measured at the same temperature inside the hysteresis curve (353 K), it is possible to exclude the thermal expansion contribution and consider only the effect of SCO on the behavior of the cantilever. From this data we can extract

the Young's modulus (E) of the composite material. Timoshenko's equation can be reduced in terms of **Equation 14**, where m = $t_{SCO\text{-}SU8}/t_{Si}$, n = $E_{SCO\text{-}PNC}/E_{Si}$ and h = $t_{SCO\text{-}PNC}+t_{Si,}$ t = thickness. See **Table 11** for the summary of bilayer properties.

Table 11: *MEMS properties in the case of SCO-SU8 polymer nanocomposite films*

	Substrate	SCO_PNC
Length ***l*** (µm)	840	840
Thickness ***t*** (µm)	20	3.5
Width ***w*** (µm)	100	100
Density ***ρ*** (kgm^{-1})	2330 [Hopcroft 2008]	SU8 (1220)/Nps_HS (1778)
Young's modulus ***E*** (Gpa)	169 [Hopcroft 2008]	1.69 (HS)
Amplitude ***δ*** (LS-HS) (µm)	3.65	3.65
Linear strain ***ε*** (LS-HS)	N.A.	0.022
Curvature ***k*** (m^{-1})	10.332	10.332
Work density **W/V** (Jcm^{-3})	N.A.	0.431 (HS)
Reactive Force **F** (µN)	N.A.	220

$$\delta = \frac{kl^2}{2} \tag{13}$$

$$k = \frac{6(\frac{\Delta l}{l_{LS}})(1+m)}{h[3(1+m^2)+(1+mn)\left(m^2+\frac{1}{mn}\right)]} \tag{14}$$

6.2.3.1 Linear strain

With the aim to obtain the linear strain ε = Δ*l*/*l* which arises due the SCO we consider the SCO nanoparticles display a volume change of 11 % upon the SCO [**Grosjean et al., 2016**]. The composite contains 30 %wt of nanoparticles. In order to obtain the volume fraction (Vf) for the matrix and reinforcement we consider **Equation 14**:

$$\frac{V_{SCO\_Nps\_LS}}{V_{comp\_LS}} = \frac{\frac{0.30}{\rho_{SCO\_Nps\_LS}}}{\frac{0.30}{\rho_{SCO\_Nps\_LS}} + \frac{0.70}{\rho_{SU8}}} \quad (15)$$

were $V_{SCO\_Nps\_LS}$, V_{comp_LS}, $\rho_{SCO\_Nps\_LS}$, are the volume of the SCO nanoparticles inside the matrix, the total volume of the composite material and the density of SCO nanoparticles, respectively in the LS state. ρ_{SU8} corresponds to the density of the SU8 matrix. Therefore the volume fraction of the nanoparticles and matrix are $Vf_{\_Nps}$ = 0.26 and $Vf_{\_matrix}$ = 0.74, respectively. In order to obtain the total volume of the composite material in the LS and HS states (V_{comp_LS} ,V_{comp_HS}) we use **Equations 15a-b**:

$$V_{comp\_LS} = V_{SU8} + V_{SCO\_Nps\_LS} \quad (16a)$$

$$V_{comp\_HS} = V_{SU8} + 1.11 * V_{SCO\_Nps\_LS} \quad (16b)$$

where V_{SU8} and $1.11 * V_{SCO\_Nps\_LS}$ correspond to the total volume of the SU8 matrix and that of the SCO nanoparticles in the HS state inside the composite. The total volume change of the composite material upon the LS→HS switch (ΔV_{comp_SCO}) is given by:

$$\Delta V_{comp\_SCO} = \mathrm{Vf_{Nps}} * 1.11 * V_{comp\_LS} \quad (16c)$$

Then, from **Equation 16a-d** it is possible to determine the linear strain associated with the LS→HS transition ($\varepsilon_{LS\rightarrow HS}$):

$$l_{SCO\_Nps\_LS} = \sqrt[3]{\mathrm{Vf\_Nps}} * l_{LS} \quad (17a)$$

$$l_{SCO\_Nps\_HS} = l_{comp\_LS} * \sqrt[3]{1.11} \quad (17b)$$

$$\Delta l = l_{SCO\_Nps\_HS} - l_{SCO\_Nps\_LS} \tag{17c}$$

$$\varepsilon_{LS\rightarrow HS} = \frac{\Delta l}{l_{comp\_LS}} = 2.2 * 10^{-2} \tag{17d}$$

where l_{comp_LS}, l_{comp_HS} are the total length of the composite material in the LS and HS states.

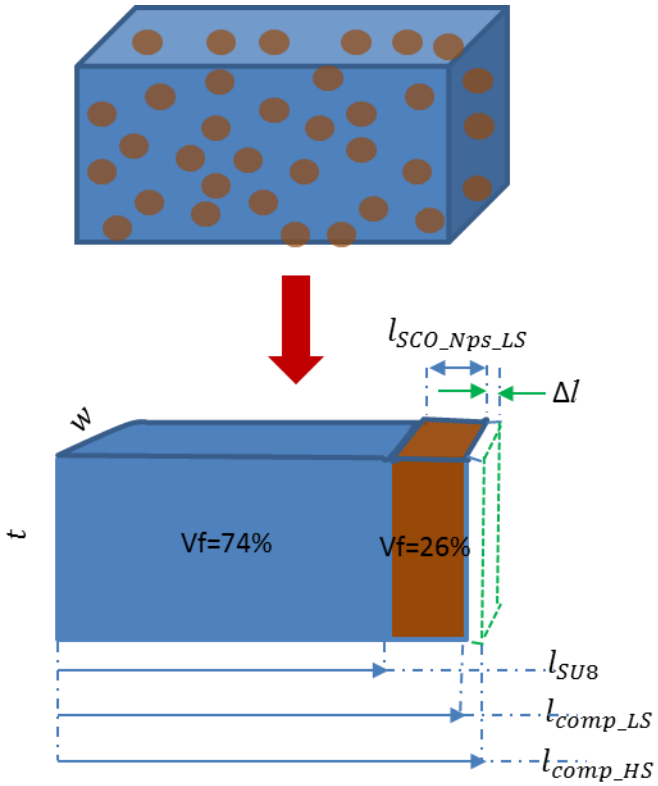

Figure 55: *Scheme to show the different components in a SCO composite and the contribution of the linear strain* $\varepsilon_{LS\rightarrow HS}$.

6.2.3.2 Young's Modulus

From **Equations 13 and 14** we obtained a Young's modulus value of 1. 69 GPa for the composite material in the HS state. This value seems reasonable if we compare it with the SU8 mechanical properties (1.2 GPa) at the same temperature [**Chung and Park 2013**]. Then, using the rule of mixtures (**Equation 18**) it is possible to estimate the Young's modulus of the SCO

particles in the HS state (3.0 GPa). This value might seem low for compound **3**, but one should consider that it corresponds to a relatively high temperature (353 K) and to the softer phase (HS).

$$E_{\_comp} = Vf\_Nps * E_{\_Nps} + Vf\_SU8 * E_{\_SU8} \quad (18)$$

6.2.3.3 Work density

As explained in Chapter 4, it is also possible to predict the work density ($W/V = E\varepsilon^2/2$) associated with the LS to HS transition, leading to a value of $W/V = 0.43$ J/cm^3, which is a remarkably high value if one takes into account the moderate volume fraction of the SCO nanoparticles (26 %) and the high temperature of the actuation.

6.2.3.4 Reactive Force

From **Equation 12** (chapter 5), it is also possible to obtain the reactive force of our device as F = 220 μm.

6.3 Actuation versatility

6.3.1 MEMS

The actuation was confirmed for two other silicon devices with the same thickness and width, but with different lengths (**see Figure 56**). They were tested in the static regime and all of them displayed similar behavior. Of particular interest is that the piezo-resistance variation ΔR values associated with the SCO at 353 K are nearly the same in each device. This means that the stress induced in the piezoresistances is nearly independent of the cantilever length. Hence we can reasonably assume that the curvature of bending k is similar for each device ($k = 10.3325$ m^{-1}). Then, the resulting bending amplitude δ at the end of the cantilever tip is directly proportional to the length (**see Equation 13**). Finally we obtain $\delta_1 = 1.29$ μm ($l = 500$ μm), $\delta_2 = 3.64$ μm ($l = 840$ μm) and $\delta_3 = 40.79$ μm ($l = 2810$ μm).

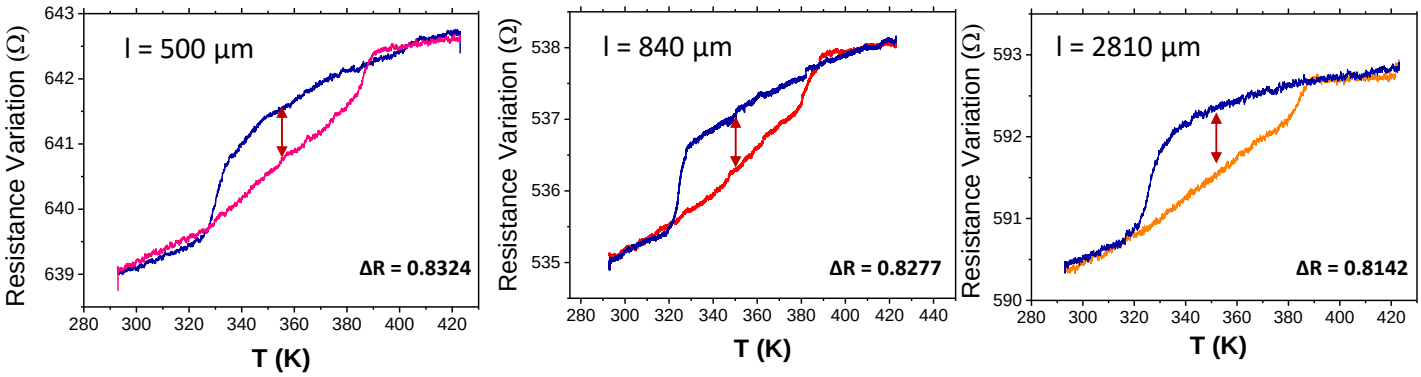

Figure 56: *Static behavior for three cantilevers with the same thickness and width, but different lengths (l).*

6.3.2 Soft artificial muscles

Two different soft systems, i) six-petal flowers and ii) cantilevers were cut out from the bilayer polyester/SCO-SU8 films. During the fabrication process the bilayer was submitted to different heat treatments (**see scheme in Figure 47**). Since the film was well attached to the silicon substrate, stresses were induced in the film.

When the film is released from the substrate and cut to the desired shape (**see Figure 57**), each system is heated from ≈293 K to ≈423 K (approximate temperature since the structure is not in direct contact with the heater). The residual stresses due to the fabrication process are released after the first thermal cycle and the final shape is obtained (**see Figure 57c).**

Thermal cycling of the flower triggers a gradual and reversible petal folding along with the characteristic color change between rose (LS) and yellow (HS) (**see Figure 58**). The yellow-transparent color in the high spin state can be seen as a camouflage effect. This phenomenon together with the thermal-induced petal folding open a perspective for the development of biomimetic soft actuators (**Whitesides and Grzybowski, 2002**).

For the second system, two cantilevers of the same bilayer composition were actuated, each of them in the presence of an additional mass of 4.785 mg and 9.57 mg, respectively. While heating, a larger deflection (δ = 2.9 mm vs. δ = 1.78 mm) is observed for the first cantilever as a consequence of the lower charge.

The movement due to the SCO confirms the effectiveness of the actuating system. The intrinsic mechanical properties can be estimated from the DMA data (Section 6.2.2.). However, further improvements regarding device design and heat distribution will need to be overcome in order

to quantify the actuation parameters, since a non-homogeneous heat distribution is encountered in these first experiments.

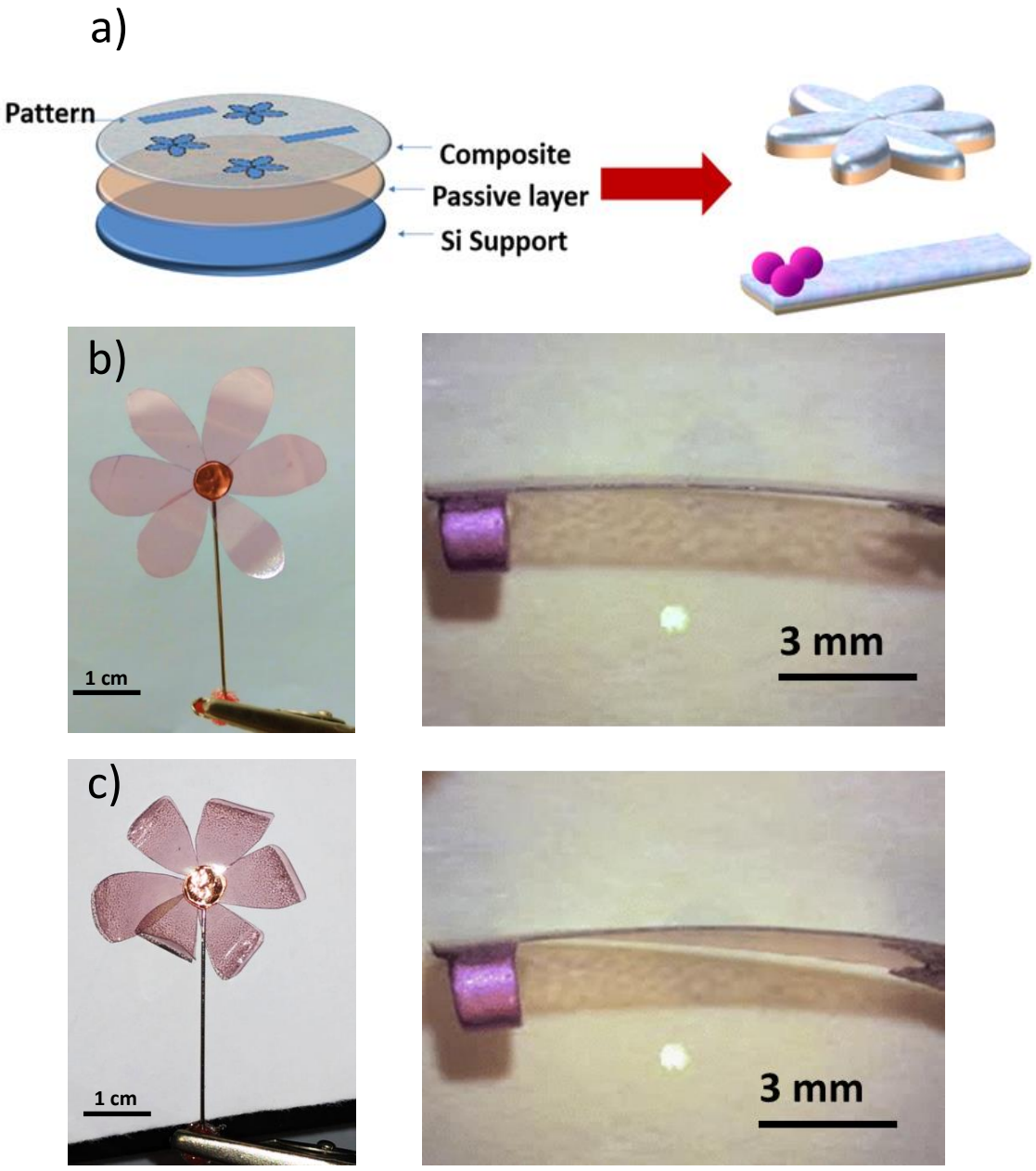

Figure 57 : *Flower and cantilever systems based on bilayer polymer composites: a) patterning scheme, b) Low spin before any heating, c) Low spin after cycling (i.e. after stress release). The violet balls were fixed at the end of the cantilever to provide a load.*

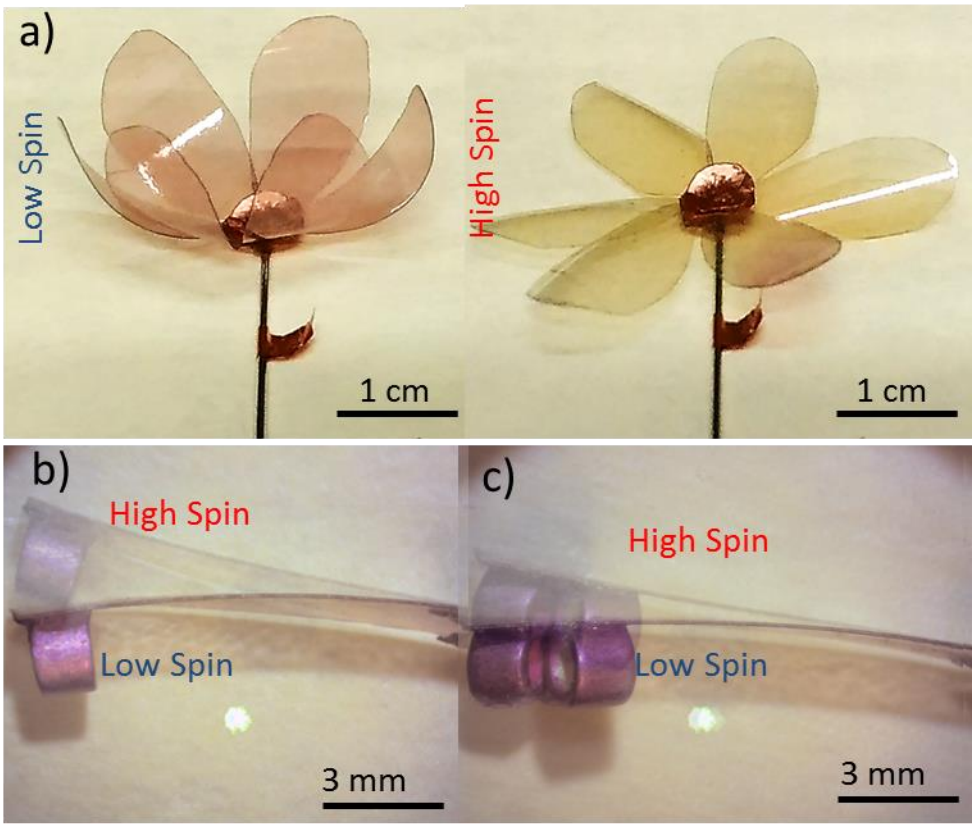

Figure 59 : *Artificial muscles actuated by SCO molecules: a) Flower opening and b-c) Cantilever bending with one ball and three balls. The cantilever dimensions are: w= 2 mm, t =0.0 75 mm, l = 11 mm.*

Conclusions

In this chapter we described a new, versatile approach for the integration of SCO materials into actuator devices. This approach is based on the spray coating of SCO nanoparticles in a polymeric matrix onto the desired surface. By optimizing the photo-thermal treatment of the polymeric matrix we succeeded in elaborating homogeneous and smooth nanocomposite films of $[Fe^{II}(Htrz)_2(trz)](BF_4)$ nanoparticles in an SU8 matrix with thicknesses in the micrometer range. Interestingly the composite films exhibited SCO with hysteresis loops twice as large as the initial nanoparticles. We believe this phenomenon occurs due to the mechanical stresses generated during the crosslinking and baking of the SU8 matrix, but this hypothesis awaits further investigations. The nanocomposite films were then deposited on silicon MEMS devices, which exhibited a well reproducible actuation upon the spin transition. By calibrating the actuating amplitude we were able to extract the main actuating properties of the composite

material (linear strain, Young's modulus, work density, reactive force). Of particular interest is the high work density (0.43 J/cm^3), which provides realistic scope for applications. Besides microsystems we also constructed macroscopic (cm scale) actuator devices based on bilayer polymer architecture. These soft actuators displayed large deflections and perceptible color changes upon the SCO, which might be exploited in biomimetic artificial muscles. In good agreement with the dynamical characterization of MEMS, DMA analysis of the thermomechanical properties of the bilayer system evidenced a stiffening of the composite in the HS phase and a concomitant decrease of the damping. These findings are somewhat counter-intuitive at a first glance, but can be explained by the dominant role of the change of volume fraction upon the SCO, which has been also reported for other SCO polymer composites in the literature. The versatility of the spray coating approach introduce here can be exploited to develop SCO based actuators with different compositions, sizes and shapes. A further important step towards this direction will be the integration of the thermal excitation into the device via Joule heating and assess the temporal behavior as a function of the system size.

General conclusions

As recognized also by the 2016 Nobel Prize in Chemistry [https://www.nobelprize.org/nobel_prizes/chemistry/laureates/2016/], switchable molecules have received many attention recently for the possibility to use them as molecular machines and actuators. To achieve this aim one has to be able to integrate and interface the molecules with their environment in order to connect them to an external source of energy, which is then transduced by the molecules to produce useful work in a controllable manner. In the literature several examples have been reported for proof of concept molecule-based actuators, but no methodical studies have been conducted in a technologically relevant context, nor the intrinsic material mechanical properties have been systematically investigated. The aim of this thesis work was to demonstrate that the switchable molecule can be efficiently integrated into state-of-the-art silicon microelectromechanical systems to produce actuation. Preceding the experiments different molecular systems with potentially useful actuating properties have been reviewed and the interest of molecular spin crossover complexes in this context has been highlighted. Selected spin crossover molecules were then processed, integrated into MEMS devices and their actuating performance as well as mechanical properties have been assessed.

As the first experimental step the well-known sublimable spin crossover complex $[Fe^{II}(H_2B(pz)_2)_2(phen)]$ was deposited by thermal evaporation on silicon MEMS devices, comprising also an integrated piezoresistive detection system. The devices showed spin-state dependent mechanical properties: at 10 K the molecules were in the ground low spin state, which was transformed by light irradiation through the LIEEST effect into the metastable high spin state, resulting in a sizeable and reversible drop of the MEMS resonance frequency. Using a straightforward analytical model this phenomenon could be linked to the change of the mechanical properties of the spin crossover compound (Young's modulus, mass density and strain). To avoid complications arising from the multilayer MEMS structure monolithic silicon MEMS devices (cantilevers and bridges) were also coated by the $[Fe^{II}(H_2B(pz)_2)_2(phen)]$ complex, which allowed us to determine the Young's modulus, the residual film stress and the work density of the coating. Overall the methodology developed here not only allows for detecting the spin crossover phenomenon in nanometric thin films, but provides also unrivaled accuracy to evaluate their mechanical properties.

In order to work at technologically more relevant temperatures thin films of the spin crossover complex $[Fe^{II}(HB(tz)_3)_2]$ were synthetized by thermal evaporation, optimized and characterized

for their morphology, structure and spin crossover properties. In the bulk this compound displays an abrupt spin transition around 333 K, which was also reproduced in the films (for thicknesses between 40 and 200 nm). The films were then deposited by thermal evaporation onto MEMS devices and their dynamical-mechanical properties were evaluated using the previously developed methodology. This study allowed us to determine the mechanical properties of the films in both spin states, which were also confirmed by independent measurements on the bulk sample leading to a complete set of elastic constants (Young's modulus, bulk modulus and Poisson's ratio). Notably a ca. 25 % variation of the Young's modulus between the two spin states was determined. Similar to the pyrazolyl derivative the resonance frequency of the MEMS decreased in the high spin state and this time we could also evidence a transient drop of the quality factor at the spin transition, which we attributed to internal frictions during the nucleation and growth phenomena. These experiments were carried out using an improved experimental set-up combining several advantages, such as the simultaneous control of temperature and pressure, improved resonance tracking and, most importantly, the possibility to acquire both dynamic and static mechanical data. Thanks to this original set-up we could, for the first time, observe actuation of a micromechanical device by spin crossover molecules. Unexpectedly, these experiments revealed an upward bending of the cantilever when going from the low spin to the high spin state. This denotes a compressive transformational strain along the cantilever, which is contradictory to the intuitive fact that the material expands in the high spin state. This apparent contradiction could be resolved using the crystallographic data, which showed a highly anisotropic transition, characterized by an increase of the film thickness and a concomitant decrease of the film dimensions in the plane of the substrate.

The main advantage of the thermal evaporation technique is that it allows for the deposition of very high quality films on the fragile mechanical parts. Yet, the number of evaporable spin crossover compounds remains relatively low. To overcome this limitation a method was established which used a mixture of spin crossover nanoparticles and an organic polymer in conjunction with a spray coating process. An advantage of this method is that it provides a large versatility for the choice of active molecules. Using $[Fe^{II}(Htrz)_2(trz)](BF_4)$ nanoparticles and a polymeric SU8 matrix we were able to deposit high quality nanocomposite films on the MEMS devices and demonstrate well-reproducible actuation. This approach was successfully extended also for the fabrication of macroscopic size actuators (artificial muscles). The dynamical-

mechanical properties of these centimeter scale actuators were characterized by DMA and the results were found in good agreement with the MEMS data.

Figure 60 summarizes and contextualizes the actuating properties of the different spin crossover compounds we investigated during this work. This diagram highlights two important issues. First of all the anticipated good actuating performance of spin crossover materials is confirmed in a technologically relevant context (MEMS). On the other hand it shows also that the highest possible actuating performance of the materials was not reached when they were integrated into the devices. The reasons vary from case to case: Compound **1** formed an amorphous film, while the film of compound **2** crystallized with a preferential orientation and compound **3** had to be dispersed in a polymeric matrix,. All these phenomena led to a reduced effective strain and/or Young's modulus.

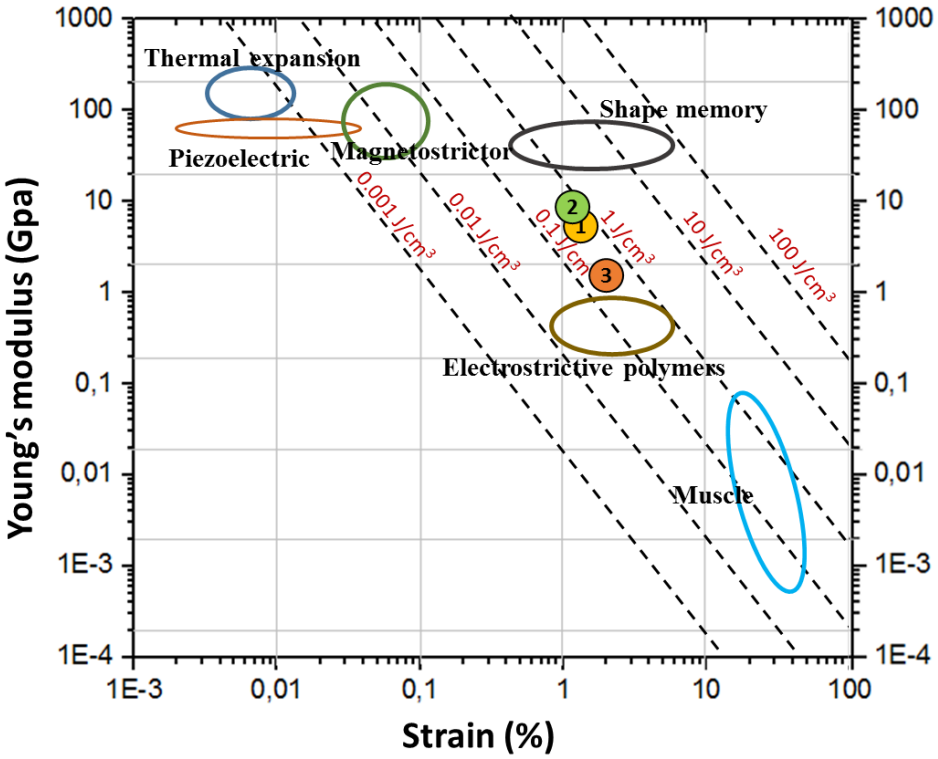

Figure 60: *Young's modulus versus linear strain plot for selected actuation material families [Adapted from* ***Liu et al., 2012****]. The contours of equal volumetric work density are also shown by dashed lines. Numbers represent the spin crossover compounds investigated in this thesis:* ***1****)* $[Fe^{II}(H_2B(pz)_2)_2(phen)]$ *thin film,* ***2****),* $[Fe^{II}(HB(tz)_3)_2]$ *thin film and* ***3****)* $[Fe^{II}(Htrz)_2(trz)](BF_4)$*-SU8 nanocomposite.*

Outlook

Based on the results of this thesis several appealing perspectives are open. In particular, the demonstrated actuating behavior of the spin crossover microcantilevers could be, in the future, promising for the integration of SCO-based NEMS devices in ultralow consumption, switch-type configurations [**Loh and Espinosa, 2012**]. In addition SCO-based devices provide scope for the development of nanoscale cyclic heat engines [**Pei et al., 2011**] and resonator or oscillator type devices [**Manca et al., 2017**] as well.

On one hand, the switching property inherent to SCO materials as well as the prospect they provide for size reduction are very appealing in the context of mechanical switches. In particular, nanoscale (NEMS) switch technologies are very attractive because they offer reduced leakage currents due to the physical separation of the components of the switch in the OFF state (**Figure 61**). This leads to reduced power consumption and improved ON/OFF ratios. To explore SCO materials in switch-type NEMS devices it will be of primary importance to study the size reduction capability of the integrated SCO layers by means of a simple nanomechanical structure before addressing more complex NEMS devices. To this aim, increasingly accurate and efficient modelling will be also indispensable.

Another outstanding prospect of SCO materials in the MEMS/NEMS context is their multifunctionality, including several smart features, such as self-regulating properties. In particular it seems possible to elaborate self-regulated mechanical oscillators assisted by SCO nanomaterials. The existence of auto-stimulated behavior in the spin transition systems has been recently analyzed theoretically [**Varret et al., 2013, Boukheddaden et al., 2014**].

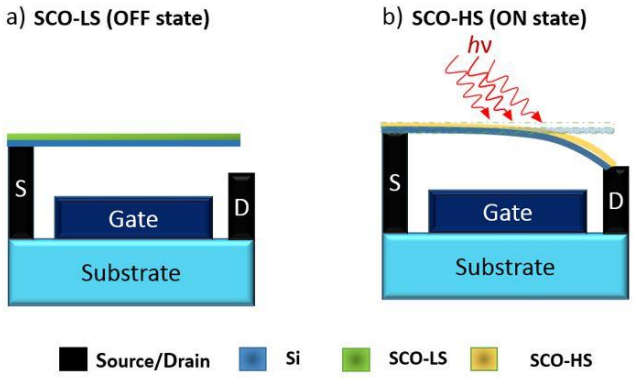

Figure 61: *Cantilever type SCO switch device in the OFF and ON states. The cantilever consists of a bilayer with an active SCO material actuated photothermally.*

For example, the application of a photothermal effect caused by a steady light irradiation in the regime of thermally induced hysteresis loop of SCO compounds should be able to generate the

necessary feedback for spatial and/or temporal oscillation phenomena of the spin transition, with a periodic switching between HS and LS states and associated material properties (**Figure 62**) - in particular the mechanical and structural properties. However, this autocatalytic behavior results from a subtle balance between the non-linear relaxation of the excited spin-state and the photothermal effect. Therefore, the regime where oscillations can emerge has to be specified in a first step. Then, the maximum frequency reached by this type of thermal powered oscillators depends on the characteristic size of the mechanical system and the speed at which the heat is transferred in/out of the device. Hence the heat dissipation and thus frequency bandwidth need to be carefully investigated and optimized using integrated heating/cooling systems.

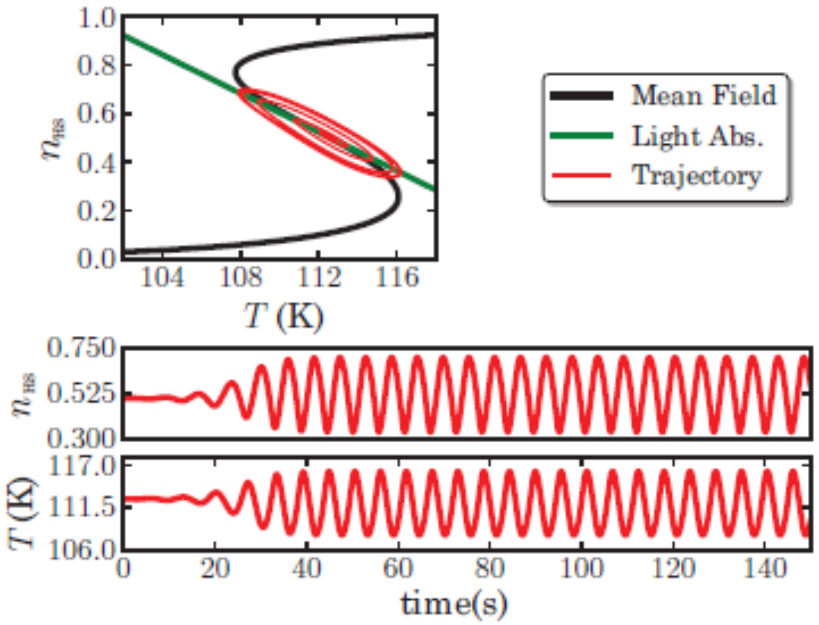

Figure 62: *Theoretical modelling of an oscillator based on a spin crossover compound [**Boukheddaden et al., 2014**]. The self-sustained oscillations of the high-spin fraction emerge spontaneously as a result of a subtle balance between the nonlinear relaxation of the HS fraction towards the low-spin state and the photothermal effect caused by a steady light excitation matching one of the characteristic absorption bands in the LS state of the material. Top (red): Time evolution of the system in the HS fraction (η_{HS}) - temperature (T) plane. Bottom: Time dependence of η_{HS} showing autocatalytic oscillations under constant light excitation.*

References

Abendroth J. M., Bushuyev O. S., Weiss P. S., and Barrett C. J., *Controlling Motion at the Nanoscale: Rise of the Molecular Machines, ACS Nano,* 8 (2015) 7746.

Agolini F. and Gay F. P., *Synthesis and Properties of Azoaromatic Polymers* Macromolecules 3, 3 (1970) 349.

Akdogan E. K., Allahverdi M and Safari A., *Piezoelectric Composites for Sensor and Actuator Applications*, IEEE Transactions on Ultrasonics, Ferroelectrics, and Frequency Control 52, 5 (2005) 746.

Alava T., Mathieu F., Mazenq L., Soyer C., Remiens D. and Nicu L., *Silicon-Based Micromembranes with Piezoelectric Actuation and Piezoresistive Detection for Sensing Purposes in Liquid Media*, Journal of Micromechanics and Microengineering 20, 7 (2010) 075014.

Al-Kaysi R. O., Müller A. M. and Bardeen J. C., *Photochemically Driven Shape Changes of Crystalline Organic Nanorods, Journal of the American Chemical Society* 128, 50 (2006)15938.

Baker W. A. and Bobonich H. M., *Magnetic properties of Some High-Spin Complexes of Iron(II)*, Inorganic Chemistry, 3 (1964) 1184.

Balzani V., Venturi M., Credi A., *Molecular Devices and Machines, Concepts and Perspectives for the Nanoworld*, Wiley-VCH, Weinheim, 2003.

Bargatin I, Kozinsky I and Roukes M L, *Efficient electrothermal actuation of multiple modes of high-frequency nanoelectromechanical resonators*, Appl. Phys. Lett. 90 (2007), 093116.

Boisen A., Dohn S., Keller S. S., Schmid S. and Tenje M., *Cantilever-like Micromechanical Sensors*, Reports on Progress in Physics 74, 3 (2011) 036101.

Boukheddaden K., Paez-Espejo M., Varret F. and Sy M., *Autocatalytic Spin-Crossover Transition: Nonlinear Dynamics Induced by a Photothermal Instability*, Physical Review B 89, 22 (2014).

Bousseksou A., Nasser J., Linares J., Boukheddaden K., and Varret F., *Ising-like model for the two-step spin-crossover*, Journal of Physics I France 2 (1992) 1381.

Bousseksou A., Varret F. and Nasser J., *Ising model for the two step spin-crossover of binuclear molecules*, Journal of Physics I France 3 (1993) 1463.

Bousseksou A., Molnar G., Salmon L. and Nicolazzi W., *Molecular spin crossover phenomenon: recent achievements and prospects*, Chemical Society Reviews, 40 (2011) 3313.

Bouwstra S. and Geijselaers B., On the resonance frequencies of microbridges", Dig. Tech. Papers 6th
Int. Conf. Solid-State Sensors and Actuators, San Francisco, USA, (1991), pp. 538-542.

Breuning E., Ruben M., Lehn J.-M., Renz F., Garcia Y., Ksenofontov V., Gütlich P., Wegelius E. and Rissanen K., *Spin Crossover in a Supramolecular Fe4II [2 X 2] Grid Triggered by Temperature, Pressure, and Light*, Angewandte Chemie, 39 (2000) 2504.

Browne W. R. and Feringa B. L., *Making molecular machines work***,** Nature Nanotechnology 1 (2006) 26.

Bruns C. J. and Stoddart J. F., *Rotaxane-Based Molecular Muscles*, Accounts of Chemical Research 47, 7 (2014) 2186

Bushuyev O. S., Singleton T. A. and Barrett C. J., *Fast, Reversible, and General Photomechanical Motion in Single Crystals of Various Azo Compounds Using Visible Light*, Advanced Materials 25, 12 (2013) 1796.

Cambi L. and Gagnasso A., *Polymorphie innerer Komplexalze: Eisensalze der Dithiocarbamidsauren*, Atti. Accad. Naz. Lincei, 13 (1931) 809.

Cavallini M., *Status and Perspectives in Thin Films and Patterning of Spin Crossover Compounds*, Physical Chemistry Chemical Physics 14, 34 (2012) 11867.

Chen Y.-C., Meng Y., Ni Z.-P. and Tong M.-L. *Synergistic Electrical Bistability in a Conductive Spin Crossover Heterostructure*, *Journal of Materials Chemistry C* 3, 5 (2015) 945.

Choi H. J., Jeong K.-U., Chien L.-C. and Lee M.-H., *Photochromic 3-Dimensional Actuator Based on an Uncrosslinked Liquid Crystal Elastomer*, Journal of Materials Chemistry 19, 38 (2009) 7124.

Chung S. and Park S., *Effects of Temperature on Mechanical Properties of SU-8 Photoresist Material*, Journal of Mechanical Science and Technology 27, 9 (2013) 2701.

Clark P. G., Day M. W. and Grubbs R. H., *Switching and Extension of a [C2] Daisy-Chain Dimer Polymer*, Journal of the American Chemical Society 131, 38 (2009) 13631.

Cleland A. N. and Roukes M. L., *Fabrication of high frequency nanometer scale mechanical resonators from bulk Si crystals*, Applied Physics Letters, 69 (1996) 2653.

Cobo S., Ostrovskii D., Bonhommeau S., Vendier L., Molnár G., Salmon L., Tanaka K. and Bousseksou A., *Single-Laser-Shot-Induced Complete Bidirectional Spin Transition at Room Temperature in Single Crystals of (Fe ^{II} (Pyrazine)(Pt(CN) $_4$))*, Journal of the American Chemical Society 130, 28 (2008) 9019.

Coronado E., Galán-Mascarós J. R., Monrabal-Capilla M., García-Martínez J. and Pardo-Ibáñez P., *Bistable Spin-Crossover Nanoparticles Showing Magnetic Thermal Hysteresis near Room Temperature*, Advanced Materials 19, 10 (2007) 1359.

Coskun A., Banaszak M., Astumian R. D., Stoddart J. F., and Grzybowski B. A., *Great Expectations: Can Artificial Molecular Machines Deliver on Their Promise?* Chemical Society Reviews 41(2012) 19.

Craighead H. G., *Nanoelectromechanical Systems*, Science 290 (2000) 1532.

Dawson R. E., Lincoln S. F. and Easton C. J., *The Foundation of a Light Driven Molecular Muscle Based on Stilbene and α-Cyclodextrin*, Chemical Communications, 34 (2008) 3980.

Decurtins S., Gutlich P., Kohler C. P., Spiering H. and Hauser A., *Light-Induced Excited-spin-State Trapping in Iron(II) Spin-Crossover Systems. Optical Spectroscopic and Magnetic Suceptibility Study*, Chemical Physics Letters, 105(1984)1.

Dezest D., *Nanosystèmes electromécaniques pour la biodétection : intégration d'un moyen de transduction et stratégies de biofonctionnalisation*, PhD Thesis, Universite de Toulouse 3, Toulouse France 2015.

Du G., Moulin E., Jouault N., Buhler E. and Giuseppone N., *Muscle-like Supramolecular Polymers: Integrated Motion from Thousands of Molecular Machines,* Angewandte Chemie International Edition 51, 50 (2012) 12504.

Dufour I., Maali A., Amarouchene Y., Ayela C., Caillard B., Darwiche A., Guirardel M., Kellay H., Lemaire E., Mathieu F., Pellet C., Saya D., Youssry M., Nicu L. and Colin A., *The Microcantilever: A Versatile Tool for Measuring the Rheological Properties of Complex Fluids*, Journal of Sensors 2012 (2012) 1.

Durand P., Pillet S., Bendeif E.-E., Carteret C., Bouazaoui M., El Hamzaoui H., Capoen B. Salmon L., Hebert S., Ghanbaja J., Aranda L. and Schaniel D., *Room Temperature Bistability with Wide Thermal Hysteresis in a Spin Crossover Silica Nanocomposite*, Journal of Materials Chemistry C 1, 10 (2013) 1933.

Durot S., Reviriego F. and Sauvage J.-P., *Copper-Complexed Catenanes and Rotaxanes in Motion: 15 Years of Molecular Machines,* Dalton Transactions 39, 44 (2010) 10557.

Eddy D. S. and Sparks D. R., *Application of MEMS Technology in Automotive Sensors and Actuators,* Proceedings of the IEEE 86, 8(1998): 1747.

Eelkema R., Pollard M., Vicario J., Katsonis N., Serrano Ramon B., Bastiaansen C. W. M., Broer D. J. and Feringa B. L., *Molecular Machines: Nanomotor Rotates Microscale Objects, Nature* 440, 7081 (2006) 163.

Feng R. and Farris R. J., *Influence of Processing Conditions on the Thermal and Mechanical Properties of SU8 Negative Photoresist Coatings*, Journal of Micromechanics and Microengineering 13, 1 (2002) 80.

Feringa B. L. and Browne W. R., ed. *Molecular Switches*. Wiley-VCH, Weinheim, 2011.

Félix G., Mikolasek M., Peng H., Nicolazzi W., Molnár G., Chumakov A. I., Salmon L. and Bousseksou A., *Lattice Dynamics in Spin-Crossover Nanoparticles through Nuclear Inelastic Scattering,* Physical Review B 91, 024422 (2015).

Forestier T., Kaiba A., Pechev S., Denux D., Guionneau P., Etrillard C., Daro N., Freysz E. and Létard J.-F., *Nanoparticles of [Fe(NH 2 -Trz) 3]Br 2 ·3 H 2 O (NH 2 -Trz=2-Amino-1,2,4-Triazole) Prepared by the Reverse Micelle Technique: Influence of Particle and Coherent*

Domain Sizes on Spin-Crossover Properties, Chemistry - A European Journal 15, 25 (2009) 6122.

Gentili D., Valle F., Albonetti C., Liscio F. and Cavallini M., *Self-Organization of Functional Materials in Confinement,* Accounts of Chemical Research 47, 8 (2014) 2692.

Good J. T., Burdett J. J. and Bardeen C. J., *Using Two-Photon Excitation to Control Bending Motions in Molecular-Crystal Nanorods*, Small 5, 24 (2009) 2902.

Gopakumar T. G., Matino F., Naggert H., Bannwarth A., Tuczek F. and Berndt R., *Electron-Induced Spin Crossover of Single Molecules in a Bilayer on Gold*, Angewandte Chemie International Edition 51, 25 (2012) 6262.

Granier T., Gallois B., Gaultier J., Real J. A., Zarembowitch J., *High-pressure single-crystal x-ray diffraction study of two spin-crossover iron(II) complexes: $Fe(Phen)_2(NCS)_2$ and $Fe(Btz)_2(NCS)_2$,* Inorgic Chemistry 32 (1993) 5305.

Grosjean A., Daro N., Pechev S., Moulet L., Etrillard C., Chastanet G. and Guionneau P., *The spin-crossover phenomenon at the coherent-domains scale in 1d polymeric powders: Evidence for structural fatigability*. European Journal of Inorganic Chemistry 2016 (2016) 1961.

Grosjean A., Négrier P., Bordet P., Etrillard C., Mondieig D., Pechev S., Lebraud E., Létard J.-F. and Guionneau P., *Crystal Structures and Spin Crossover in the Polymeric Material $[Fe(Htrz)_2(Trz)](BF_4)$ Including Coherent-Domain Size Reduction Effects*, European Journal of Inorganic Chemistry 2013, 5–6 (2013) 796.

Guionneau P., *Crystallography and spin-crossover. A view of breathing materials*. Dalton Trans. 43 (2014) 382.

Guionneau P., Lakhloufi S., Lemée-Cailleau M.-H., Chastanet G., Rosa P., Mauriac C. and Létard J.-F., *Mosaicity and Structural Fatigability of a Gradual Spin-Crossover Single Crystal*, Chemical Physics Letters 542 (2012) 52.

Gural'skiy, I. A., Quintero C. M., Sánchez Costa J., Demont P., Molnár G., Salmon L., Shepherd H. J., and Bousseksou A. *Spin Crossover Composite Materials for Electrothermomechanical Actuators,* Journal of Materials Chemistry. C, 16 (2014): 2949.

Gutlich P. and Goodwin H. A., *Topics in Current Chemistry. Spin Crossover in Transition Metal Compounds I.*, Springer-Verlag, Berlin, 2004.

Griffith J. S., *On the magnetic properties of some haemoglobin complexes*, Proceedings of the Royal Society of London A : Mathematical, Physical and Engineering Sciences, 235 (1956) 23.

Halcrow M. A., *Jahn–Teller Distortions in Transition Metal Compounds, and Their Importance in Functional Molecular and Inorganic Materials*, Chem. Soc. Rev. 42, 4 (2013) 1784.

Halcrow, M.A. Structure:function relationships in molecular spin-crossover complexes. Chemical Society Reviews 40 (2011) 4119.

Harzmann G. D., Frisenda R., van der Zant H. S. J. and Mayor M., *Single-Molecule Spin Switch Based on Voltage-Triggered Distortion of the Coordination Sphere,* Angewandte Chemie International Edition 54, 45 (2015) 13425.

Hauser A., *Reversibility of light-induced excited spin state trapping in the $Fe(ptz)_6(BF_4)_2$, and the $Zn1-xFex(ptz)_6(BF_4)_2$ spin-crossover systems,* Chemical Physics Letters, 124 (1986) 543.

Hauser A., *Intersystem crossing in the [Fe(ptz)6](BF4)2 spin crossover system (ptz=1-ropyltetrazole),* Journal of Chemical Physics, 94 (1991) 2741.

Hernández E. M., Quintero C. M., Kraieva O., Thibault C., Bergaud C., Salmon L., Molnár G. and Bousseksou A., *AFM Imaging of Molecular Spin-State Changes through Quantitative Thermomechanical Measurements,* Advanced Materials 26, 18 (2014) 2889.

Hmadeh M., Fang L., Trabolsi A., Elhabiri M., Albrecht-Gary A.-M. and Stoddart J. F., *On the Thermodynamic and Kinetic Investigations of a [C2]Daisy Chain Polymer*, Journal of Materials Chemistry 20, 17 (2010) 3422.

Hollauer Ch., *Modelling of thermal oxidation and stress effects*, Ph.D. dissertation, Vienna Univ. Technol., Vienna, Austria, 2007

Hoy-Benítez J A, Avilés F., Gamboa F., Peón-Escalante R. and Oliva A. I., *Vibration Modeling and Testing of Bilayer Beams for Determination of Film Elastic Modulus*, Measurement Science and Technology 23, 4 (2012) 045605.

Hopcroft M. A., Nix W. D. and Kenny T. W., *What Is the Young's Modulus of Silicon?* Journal of Microelectromechanical Systems 19, 2 (2010) 229.

Huang T. J., Brough B., Ho C.-M., Liu Y., Flood A. H., Bonvallet P. A., Tseng H.-R., Stoddart J. F., Baller M. and Magonov S., *A Nanomechanical Device Based on Linear Molecular Motors*, Applied Physics Letters 85, 22 (2004) 5391.

Irie M., Kobatake S. and Horichi M., *Reversible Surface Morphology Changes of a Photochromic Diarylethene Single Crystal by Photoirradiation*, Science 291 (2001) 1769.

Jia L. and Li M.-H., *Liquid Crystalline Polymer Vesicles: Thermotropic Phases in Lyotropic Structures,* Liquid Crystals 41, 3 (2014) 36884.

Jimenez-Molero M. C., Dietrich-Buchecker C. and Sauvage J.-P., *Towards Artificial Muscles at the Nanometric Level*, Chemical Communications, 14 (2003) 1613.

Jin C., Olsen B. C., Luber E. J. and Buriak J. M., *Nanopatterning via Solvent Vapor Annealing of Block Copolymer Thin Films*, Chemistry of Materials 29, 1 (2017) 176.

Jin Y., Harrington D., Rachford A. A. and Rack J. J., *Stimulating Changes in the Elastic Modulus of Polymer Materials by Molecular Photochromism*, RSC Adv. 4, 108 (2014): 62920–25.

Jin Y., Paris S. I. M. and Rack J. J., *Bending Materials with Light: Photoreversible Macroscopic Deformations in a Disordered Polymer*, Advanced Materials 23, 37 (2011) 4312.

Juluri B. K., Kumar A. S., Liu Y., Ye T., Yang Y.-W., Flood A. H., Fang L., Stoddart J. F., Weiss P. S. and Huang T. J., *A Mechanical Actuator Driven Electrochemically by Artificial Molecular Muscles, ACS Nano* 3, 2 (2009) 291.

Jung J., Bruchhäuser F., Feile R., Spiering H. and Gütlich P., *The cooperative spin transition in* $[Fex Zn_{1} - x(ptz)_{6}](BF_{4})_{2}$*: I. Elastic properties — an oriented sample rotation study by Brillouin spectroscopy*, Zeitschrift für Physik B Condensed Matter, 100 (1996) 517.

Kahn O. and Martinez C. J., *Spin-Transition Polymers: From Molecular Materials toward Memory Devices*, Science 279, 5347 (1998) 44.

Kim B., Hopcroft M. A., Candler R. N., Jha C. M., Agarwal M., Melamud R., Chandorkar S. A., Yama G. and Kenny T. W., *Temperature Dependence of Quality Factor in MEMS Resonators*, Journal of Microelectromechanical Systems 17, 3 (2008) 755.

Kim T., Zhu L., Al-Kaysi R. O. and Bardeen C. J., *Organic Photomechanical Materials* ChemPhysChem 15, 3 (2014) 400.

Kobatake S., Takami S., Muto H., Ishikawa T. and Irie M., *Rapid and Reversible Shape Changes of Molecular Crystals on Photoirradiation*, Nature 446, 7137 (2007) 778.

Koo Y-S and Galán-Mascarós J. R., *Spin Crossover Probes Confer Multistability to Organic Conducting Polymers*, Advanced Materials 26, 39 (2014) 6785.

Koshima H., Ojima N. and Uchimoto H., *Mechanical Motion of Azobenzene Crystals upon Photoirradiation*, Journal of the American Chemical Society 131, 20 (2009) 6890.

Krulevitch P., Lee A. P., Ramsey P. B., Trevino J. C., Hamilton J., Northrup M. A., *Thin Film Shape Memory Alloy Microactuators*, Journal of Microelectromechanical Systems, 5 (1996) 270.

Langford J. I. and Wilson A. J. C., *Scherrer after sixty years: a survey and some new results in the determination of crystallite size*, Journal of Applied Crystallography, 11 (1978) 102.

Lantada A. D., Handbook of Active Materials for Medical Devices: Advancesand Applications, CRC Press, 2011.

Lefter C., Tan R., Tricard S., Dugay J., Molnár G., Salmon L., Carrey J., Rotaru A. and Bousseksou A., *On the Stability of Spin Crossover Materials: From Bulk Samples to Electronic Devices*, Polyhedron 102 (2015) 434.

Lefter C., Rat S., Sánchez Costa J., Manrique-Juárez M. D., Quintero C. M., Salmon L., Séguy I., Leichle T., Nicu L., Demont P., Rotaru A., Molnar G. and Bousseksou A., *Current Switching Coupled to Molecular Spin-States in Large-Area Junctions*, Advanced Materials 28, no. 34 (2016) 7508.

Leondes, C. T., MEMS/NEMS Handbook Techniques & Applications, edited by C. T. (Springer, 2006).

Li M.-H., Keller P., Li B. and Wang X., Brunet M., *Light Driven Side-On Nematic Elastomer Actuators*, Advanced Materials 15 (2003) 569.

Li M., Tang H. X. and Roukes M. L., *Ultra-sensitive NEMS-based cantilevers for sensing, scanned probe and very high-frequency applications* Nature Nanotechnology 2 (2007) 114-120.

Liljeroth P., Repp J., Meyer G., *Current-Induced Hydrogen Tautomerization and Conductance Switching of Naphtalocyanine Molecules*, Science 317 (2007) 1203.

Liu K., Cheng C., Cheng Z., Wang K., Ramesh R. and Wu J., *Giant-Amplitude, High-Work Density Microactuators with Phase Transition Activated Nanolayer Bimorphs*, Nano Letters 12, 12 (2012) 6302.

Liu Y., Flood A. H., Bonvallet P. A., Vignon S. A., Northrop B. H., Tseng H.-R., Jeppesen J. O., Huang T. J., Brough B., Baller M., Magonov S., Solares S. D., Goddard W. A., Ho C.-M. and Stoddart J. F., *Linear Artificial Molecular Muscles*, Journal of the American Chemical Society 127, 27 (2005) 9745.

Loewy R. G., *Recent Developments in Smart Structures with Aeronautical Applications*, Smart Materials and Structures 6, 5 (1997) R11.

Loh O. Y. and Espinosa H. D., *Nanoelectromechanical Contact Switches*, Nature Nanotechnology 7, 5 (2012) 283.

Lorenc, M., Hébert J., Moisan N., Trzop E., Servol M., Buron-Le Cointe M., Cailleau H., Boillot M. L., Pontecorvo E., Wilff M., Koshihara S. and Collet E., *Successive Dynamical Steps of Photoinduced Switching of a Molecular Fe(III) Spin-Crossover Material by Time-Resolved X-Ray Diffraction*, Physical Review Letters 103, 2 (2009).

Manrique-Juárez M. D., Suleimanov I., Hernández E., Salmon L., Molnár G. and Bousseksou a., *In Situ AFM Imaging of Microstructural Changes Associated with The Spin Transition in [Fe(Htrz)2(Trz)](Bf4) Nanoparticles*, Materials 9, 7 (2016) 537.

McGravey J. J. and Lawthers I., *Photochemically-induced perturbation of the $^1A \rightleftharpoons ^5T$ equilibrium in Fe^{II} complexes by pulsed laser irradiation in the metal-to ligand charge-transfer absorption band*, Journal of the Chemical Society, Chemical Communications, (1982) 906.

Manca N., Pellegrino L., Kanki T., Venstra W. J., Mattoni G., Higuchi Y., Tanaka H., Caviglia A. D. and Marré D., *Selective High-Frequency Mechanical Actuation Driven by the VO 2 Electronic Instability*, Advanced Materials 29, 35 (2017) 1701618.

Masmanidis S. C., Karabalin R. B., Vlaminck I. D., Borghs G., Freeman M. R. and Roukes M. L. *Multifunctional Nanomechanical Systems via Tunably Coupled Piezoelectric Actuation* Science 317 (2007) 780-3.

Matejka L., Dusek K., Ilavsk´y M., *The termal effect in the Photomechanical Conversion of a Photochromic Polymer*, Polymer Bulletin 1 (1979) 659.

Mikolasek M., *Étude de la dépendance en taille des propriétés physiques des composés à transition de spin*. PhD Thesis, Universite de Toulouse 3, Toulouse France 2016.

Moliner N., Salmon L., Capes L., Muñoz M. C., Létard J.-F., Bousseksou A., Tuchagues J.-P., McGravey J. J., Dennis A. C., Castro M., Burriel R. and Real A., *Thermal and Optical Switching of Molecular Spin States in the {[FeL[$H_2B(Pz)_2]_2$} Spin-Crossover System (L = Bpy, Phen)*, The Journal of Physical Chemistry B 106, 16 (2002) 4276.

Morimoto M. and Irie M., *A Diarylethene Cocrystal That Converts Light into Mechanical Work*, Journal of the American Chemical Society 132, 40 (2010) 14172.

Moulet L., Daro N., Etrillard C., Létard J.-F., Grosjean A. and Guionneau P., *Rational Control of Spin-Crossover Particle Sizes: From Nano- to Micro-Rods of [Fe(Htrz)2(Trz)](BF4)*, Magnetochemistry 2, 1 (2016) 10.

Naggert H., Bannwarth A., Chemnitz S., von Hofe T., Quandt E., Tuczek F., *First observation of light-induced spin change in vacuum deposited thin films of iron spin crossover complexes*, Dalton Transactions 40 (2011) 6364.

Natansohn A. and Rochon P., *Photoinduced Motions in Azo-Containing Polymers*, Chemical Reviews 102, 11(2002) 4139.

Naumov P.e, Sahoo S. C., Zakharov B. A. and Boldyreva E. V., *Dynamic Single Crystals: Kinematic Analysis of Photoinduced Crystal Jumping (The Photosalient Effect)*, Angewandte Chemie International Edition 52, 38 (2013) 9990.

Naumov P., Chizhik S., Panda M. K., Nath N. K. and Boldyreva E., *Mechanically Responsive Molecular Crystals*, Chemical Reviews 115, 22 (2015) 12440.

Nicu L., *Etudes theoriques et experimentales du comportement mecanique de microstructures de type levier ou pont. Application a la mesure de la viscosite de liquids et a la caracterisation de nanostructures*, PhD Thesis, Universite de Toulouse 3, Toulouse France 2000.

Palamarciuc T., Oberg J. C., Hallak F. E., Hirjibehedin C. F., Serri M., Heutz S., Létard J.-F. and Rosa P., *Spin Crossover Materials Evaporated under Clean High Vacuum and Ultra-High Vacuum Conditions: From Thin Films to Single Molecules*, Journal of Materials Chemistry 22, . 19 (2012) 9690.

Pelesko J. A. and Bernstein D. H., *Modeling MEMS and NEMS* (CRC Press), 2002

Pei Y., Shi X., LaLonde A., Wang H., Chen L. and Snyder G. J., *Convergence of Electronic Bands for High Performance Bulk Thermoelectrics*, Nature 473, 7345 (2011) 66.

Pérez-Sáez R. B., Recarte V., Nó M. L. and San Juan J., *Anelastic Contributions and Transformed Volume Fraction during Thermoelastic Martensitic Transformations*, Physical Review B 57, 10 (1998) 5684.

Petersen, K. E., Silicon as a Mechanical Material, Proc. IEEE 70 (1982) 420.

Pierpont C.G., *Studies on Charge distribution and valence tautomerism in transition metal complexes on catecholate and semiquinonate ligands*, Coordination Chemical Reviews, 99 (2001) 216.

Pons J. L. *Emerging Actuator Technologies: A Micromechatronic Approach*. Chichester, England ; Hoboken, NJ: Wiley, 2005.

Priimagi A., Barrett C. J. and Shishido A., *Recent Twists in Photoactuation and Photoalignment* Control, J. Mater. Chem. C 2, 35 (2014) 7155.

Pronschinske A., Chen Y., Lewis G. F., Shultz D. A., Calzolari A., Buongiorno Nardelli M. and Dougherty D. B., *Modification of Molecular Spin Crossover in Ultrathin Films*, Nano Letters 13, 4 (2013) 1429.

Rat S., Mikolasek M., Sanchez Costa J., Chumakov A. I., Nicolazzi W., Molnar G., Salmon L. and Bousseksou A., *Raman and nuclear inelastic scattering study of the lattice dynamics of the [Fe(H2B(pz)2)2(phen)] spin crossover complex*, Chemical Physics Letters 653 (2016a) 131.

Rat, S., K. Ridier, L. Vendier, G. Molnár, L. Salmon and A. Bousseksou, *Solvatomorphism and Structural-Spin Crossover Property Relationship in Bis[Hydrotris(1,2,4-Triazol-1-Yl)Borate]Iron(ii)*, CrystEngComm 19, 24 (2017) 3271.

Real J. A., Munoz M. C., Faus J. and Solans X., *Spin Crossover in Novel Dihydrobis(1-pyrazolyl)borate [$H_2B(pz)_2$]-Containing Iron(II) Complexes. Synthesis, X-ray Structure, and Magnetic Properties of [FeL{$H_2B(pz)_2$}$_2$] (L = 1,10-Phenanthroline and 2,2‘-Bipyridine)* Inorganic Chemistry 36 (1997) 3008.

Reddy, C. M., Padmanabhan K. A. and Desiraju G. R., *Structure−Property Correlations in Bending and Brittle Organic Crystals*, Crystal Growth & Design 6, 12 (2006) 2720.

Reddy C. M., Krishna G. R. and Ghosh S., *Mechanical Properties of Molecular Crystals—applications to Crystal Engineering*, CrystEngComm 12, 8 (2010) 2296.

Saha S., Leung K. C.-F., Nguyen T. D., Stoddart J. F. and Zink J. I., *Nanovalves*, Advanced Functional Materials 17, 5 (2007) 685.

Sahoo, S. C., Sinha S. B., Kiran M. S. R. N., Ramamurty U., Dericioglu A. F., Reddy C. M. and Naumov P., *Kinematic and Mechanical Profile of the Self-Actuation of Thermosalient Crystal Twins of 1,2,4,5-Tetrabromobenzene: A Molecular Crystalline Analogue of a Bimetallic Strip, Journal of the American Chemical Society* 135, 37 (2013) 13843.

Salitros I., Madhu N. T., Boca R., Pavlik J., Ruben M., *Room-temperature spin-transition iron compounds*, Monatshefte für Chemie-Chemical Monthly. 140 (2009) 695.

Salomon S, Leïchlé T., Dezest D., Seichepine F., Guillon S., Thibault C., Vieu C. and Nicu L., *Arrays of Nanoelectromechanical Biosensors Functionalized by Microcontact Printing*, Nanotechnology 23, 49 (2012) 495501.

Sauvage J. P., *Molecular Machines and Motors*, Springer, Berlin, 2001.

Scansen D., How MEMS enable Smartphone Features: Engineering.com, (2013). http://www.engineering.com/ElectronicsDesign/ElectronicsDesignArticles/ArticleID/6124/How-MEMS-Enable-Smartphone-Features.aspx

Shepherd H. J., Rosa P., Vendier L., Létard J.-F., Bousseksou A., Guionneau P., Molnár G., *High-pressure spin-crossover in a dinuclear Fe(II) complex*, Physical Chemistry Chemical Physics 14 (2012) 5265.

Shepherd H. J., Gural'skiy I. A., Quintero C. M., Tricard S., Salmon L., Molnár G. and Bousseksou A., *Molecular Actuators Driven by Cooperative Spin-State Switching*, Nature Communications 4 (2013) 2607.

Shu W., Liu D., Watari M., Riener C. K., Strunz T., Welland M. E., Balasubramanian S. and McKendry R. A., *DNA Molecular Motor Driven Micromechanical Cantilever Arrays,* Journal of the American Chemical Society 127, 48 (2005) 17054.

Spearing S. M., *Materials issues in microelectromechanical systems (MEMS)*, Acta materialia 48 (2000) 179.

Spiering H., Meissner E., Koppen H., Muller E. W. and Gutlich P., *The effect of the lattice expansion on high spin Low spin transitions*, Chemical Physics 68 (1982) 65.

Sreenivasa M., Soueres P., and Laumond J., *Walking to Grasp: Modeling of Human Movements as Invariants and an Application to Humanoid Robotics*, IEEE Transactions on Systems, Man, and Cybernetics - Part A: Systems and Humans 42, 4 (July 2012) 880.

Takashima Y., Hatanaka S., Otsubo M., Nakahata M., Kakuta T., Hashidzume A., Yamaguchi H. and Harada A., *Expansion–contraction of Photoresponsive Artificial Muscle Regulated by Host–guest Interactions*, Nature Communications 3 (2012) 1270.

Tamayo J., Kosaka P. M., Ruz J. J., San Paulo A. and Calleja M., *Biosensors Based on Nanomechanical Systems*, Chemical Society Reviews 42, 3 (2013) 1287.

Tissot A., Enachescu C. and Boillot M.-L., *Control of the Thermal Hysteresis of the Prototypal Spin-Transition FeII(Phen)2(NCS)2 Compound via the Microcrystallites Environment: Experiments and Mechanoelastic Model*, Journal of Materials Chemistry 22, 38 (2012) 20451.

Thompson A. L., Goeta A. E., Real J. A., Galet A. and Muñoz M. C., Thermal and Light Induced Polymorphism in Iron(II) Spin Crossover Compounds, Chemical Communications, 12 (2004) 1390.

Varret F., Bleuzen A., Boukheddaden K., Bousseksou A., Codjovi E., Enachescu C., Goujon A., Linares J., Menendez N. and Verdaguer M., *Examples of molecular switching in inorganic solids, due to temperature, light, pressure, and magnetic field*, Pure and Applied Chemistry, 74 (2002) 2159.

Varret F., Paez-Espejo M., Boukheddaden, *Light-induced instability generated by photo-thermal effect in switchable molecular crystals*, Europhysics Letters 104 (2013) 27003.

Warren M. R., Easun T. L., Brayshaw S. K., Deeth R. J., George M. W., Johnson A. L., Schiffers S., Teat S. J., Warren A. J., Warren J. E., Wilson C. C., Woodall C. H. and Raithby P. R., *Solid-State Interconversions: Unique 100 % Reversible Transformations between the Ground and Metastable States in Single-Crystals of a Series of Nickel(II) Nitro Complexes*, Chemistry - A European Journal 20, 18 (2014) 5468.

Whitesides G. M. and Grzybowski B., *Self-Assembly at All Scales*, Science, 295 (2002) 2418.

Yamada M., Kondo M., Mamiya J., Yu Y., Kinoshita M., Barrett C. J. and Ikeda T., *Photomobile Polymer Materials: Towards Light-Driven Plastic Motors*, Angewandte Chemie International Edition 47, 27 (2008) 4986.

Yu Y., Nakano M. and Ikeda T., *Photomechanics: Directed Bending of a Polymer Film by Light,* Nature 6954 (2003)145.

Zhang X., Palamarciuc T., Létard J.-F, Rosa P., Lozada E. V., Torres F., Rosa L. G., Doudin B., Dowben P. A., *The spin state of a molecular adsorbate driven by the ferroelectric substrate polarization*, Chemical Communications 50 (2014) 2255.

Zhu L., Al-Kaysi R. O. and Bardeen C. J., *Reversible Photoinduced Twisting of Molecular Crystal Microribbons*, Journal of the American Chemical Society 133, 32 (2011) 12569.

Publications

- **Maria D. Manrique-Juarez**, Sylvain Rat, Laurent Mazenq, Fabrice Mathieu, Isabelle Séguy, Thierry Leïchlé, Liviu Nicu, Lionel Salmon, Gábor Molnár and Azzedine Bousseksou. "Spin Crossover Materials for MEMS actuation: film integration and characterization" *IEEE Dig. Tech. Papers 19th Int.* Conf. *Solid-State Sensors Actuators and Microsystems* **2017** (in press).

- **Maria D. Manrique-Juarez,** Fabrice Mathieu, Victoria Shalabaeva, Jean Cacheux, Sylvain Rat, Liviu Nicu, Thierry Leïchlé, Lionel Salmon, Gábor Molnár, and Azzedine Bousseksou, "A Bistable Microelectromechanical System (MEMS) Actuated by Spin Crossover Molecules", *Angewante Chemie* 56, **2017** 1-5.

- Victoria Shalabaeva, Sylvain Rat, **Maria D. Manrique-Juarez**, Alin C. Bas, Laure Ven-dier, Lionel Salmon, Gábor Molnár, Azzedine Bousseksou, "Spin crossover in bis[hydrotris(1,2,4-triazol-1-yl)borate]iron(II),Part II: Vacuum deposition of high-quality thin films", *Journal of Materials Chemistry C* 5 **2017**, 4419-4425.

- Lefter, Constantin, Sylvain Rat, José Sánchez Costa, **María D. Manrique-Juárez**, Carlos M. Quintero, Lionel Salmon, Isabelle Séguy, Thierry Leichle , Liviu Nicu , Philippe Demont , Aurelian Rotaru , Gábor Molnár , and Azzedine Bousseksou "Current Switching Coupled to Molecular Spin-States in Large-Area Junctions." *Advanced Materials* 28, **2016,** 7508.

- **Maria D. Manrique-Juarez**, Sylvain Rat, Fabrice Mathieu, Daisuke Saya, Isabelle Séguy, Thierry Leïchlé, Liviu Nicu, Lionel Salmon, Gábor Molnár, and Azzedine Bousseksou. "Microelectromechanical Systems Integrating Molecular Spin Crossover Actuators." *Applied Physics Letters* 109, **2016,** 061903.

- **Maria D. Manrique-Juárez,** Iurii Suleimanov, Edna Hernández, Lionel Salmon, Gábor Molnár, and Azzedine Bousseksou. "In Situ AFM Imaging of Microstructural Changes Associated with The Spin Transition in [Fe(Htrz)2(Trz)](Bf4) Nanoparticles." *Materials* 9, **2016,** 537.

- **Manrique-Juárez, María D.**, Sylvain Rat, Lionel Salmon, Gábor Molnár, Carlos M. Quintero, Liviu Nicu, Helena J. Shepherd, and Azzedine Bousseksou. "Switchable Molecule-Based Materials for Micro- and Nanoscale Actuating Applications: Achievements and Prospects." *Coordination Chemistry Reviews* 308, **2016,** 395.

Molecular Actuators

International Edition: DOI: 10.1002/anie.201702739
German Edition: DOI: 10.1002/ange.201702739

A Bistable Microelectromechanical System Actuated by Spin-Crossover Molecules

Maria D. Manrique-Juarez, Fabrice Mathieu, Victoria Shalabaeva, Jean Cacheux, Sylvain Rat, Liviu Nicu, Thierry Leïchlé, Lionel Salmon, Gábor Molnár, and Azzedine Bousseksou**

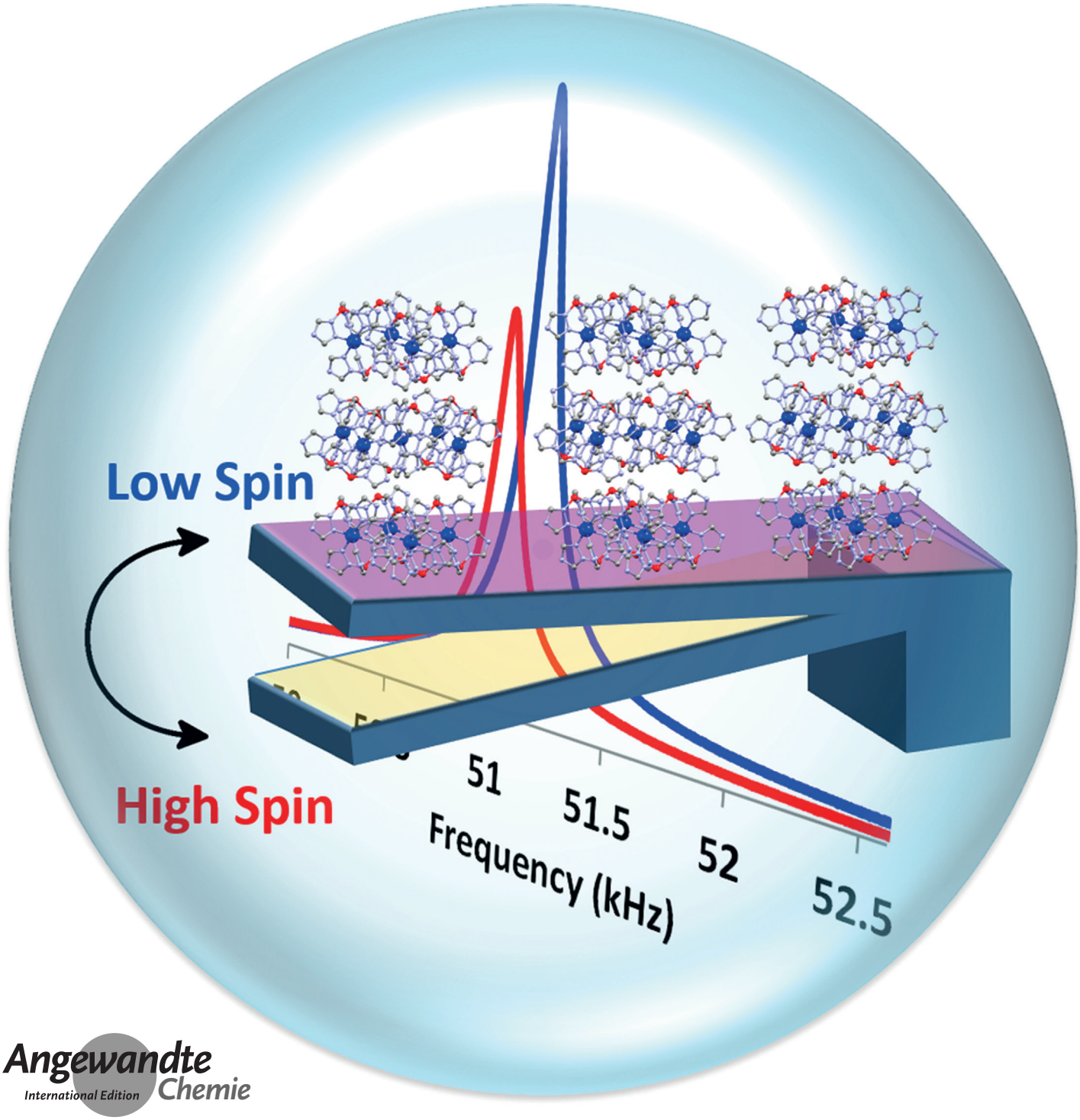

Annexes

Micro and nanoactuators based on bistable molecular materials

A1.-In the design of MEMS

A1.1 Resonance frequency predictions (1st resonance mode) when cantilever length (L), thickness (t) and SCO compound deposition are tuned.

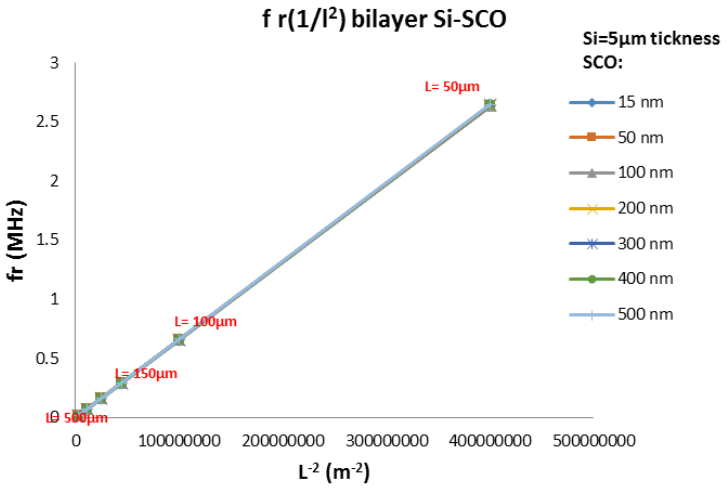

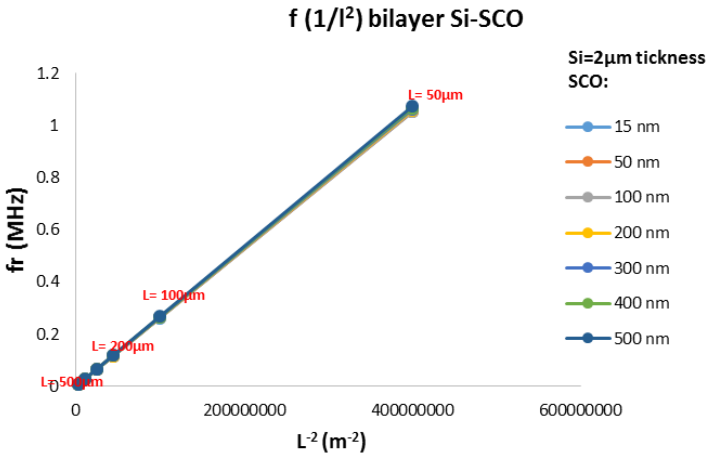

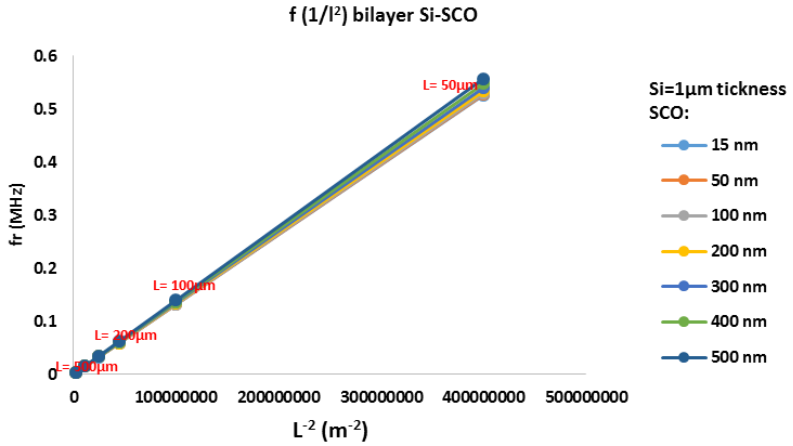

A1.2 Mask design with the layout editor Clewin for patterning during the photolithography process.

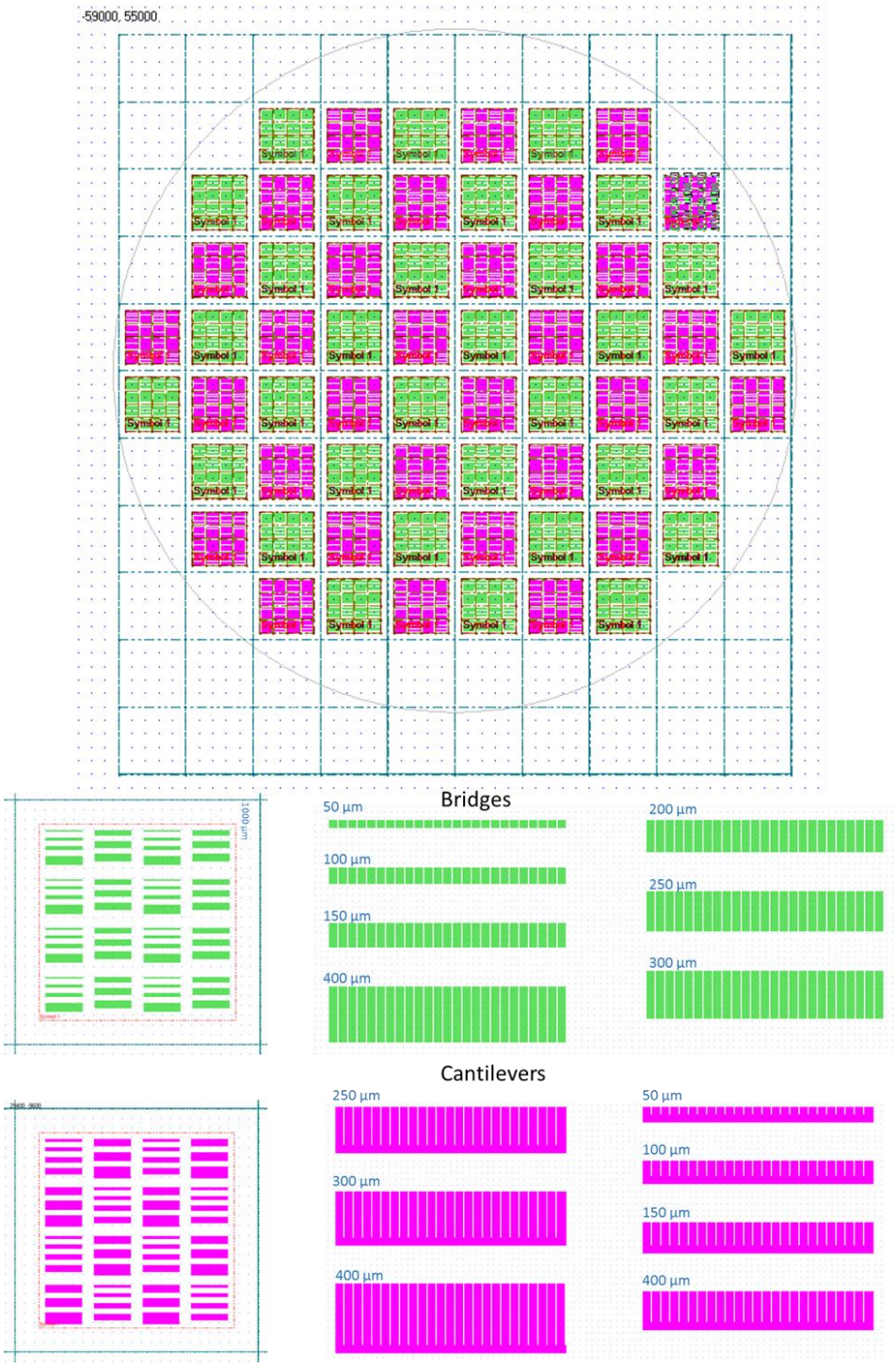

A1.3-Detailed microfabrication process.

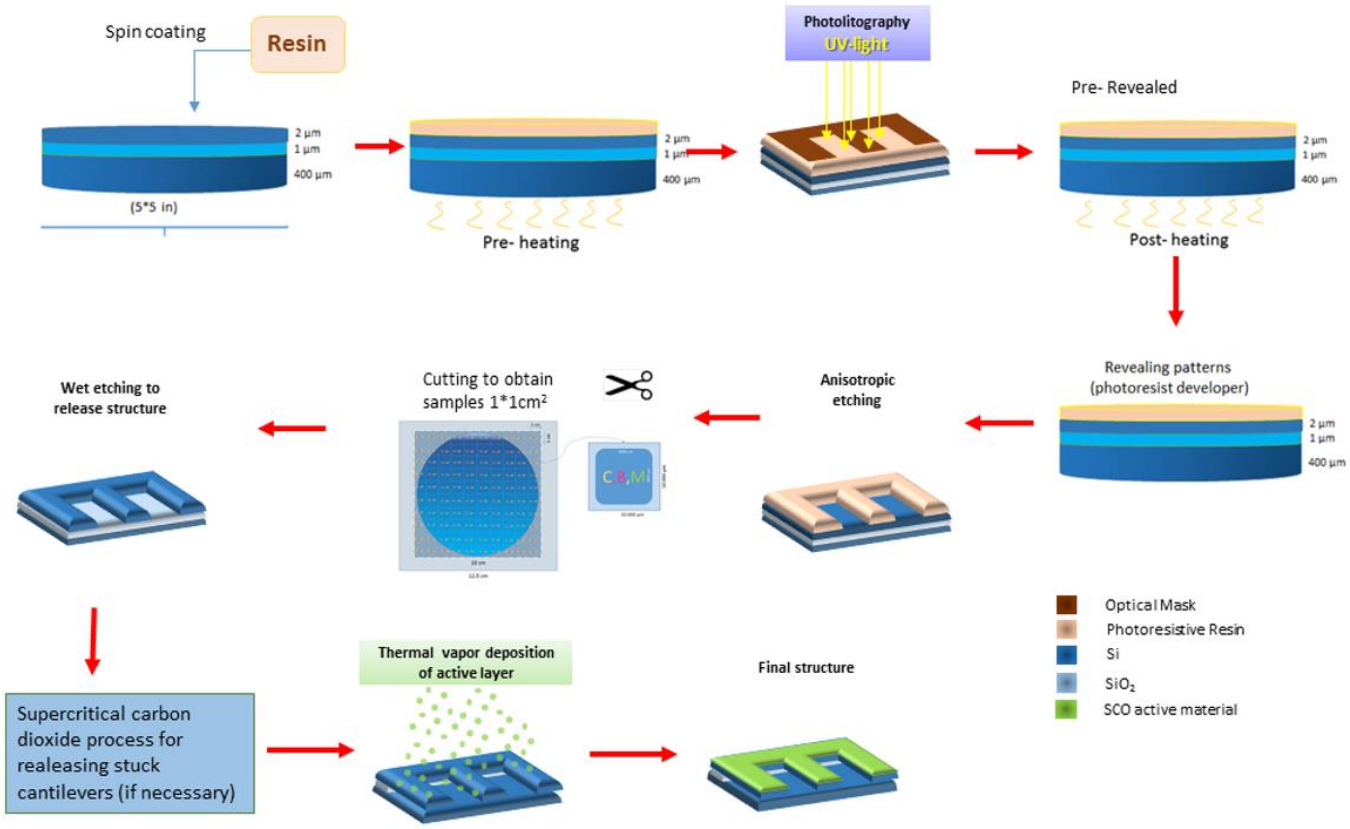

-SOI wafer, prepare surface.

-Spin coating of the positive resin ECI 3012 (1.1 microns), annealing of 90°C during 30s.

-Light exposure with MA6 (25mW/cm^2) during 8s.

-Post baking 110°C during 60s

-Revealing patterns with photoresist developer MFCD2 during 25s

-RIE etching (vertical etching), verify dimensions.

-Protect wafer with a fi

-Cut chips 1 cm^2.

-Clean chip with acetone and water followed by plasma O_2 (or piranha). (This step is done previous the SCO deposition, not before.

-Wet etching HF 5% (≈3.7 hrs). After HF etching dip the chip immediately in acetone at 60°C.

-Verify complete releasing with SEM.

-Prepare surface before the SCO deposition, a plasma O_2 is enough.

A2.-Some problems that may appear during the microfabrication process.

A.2.1 Structure stacking due to a bad wet-etching (it is necessary to survey releasing process HF-water-acetone 60°C).

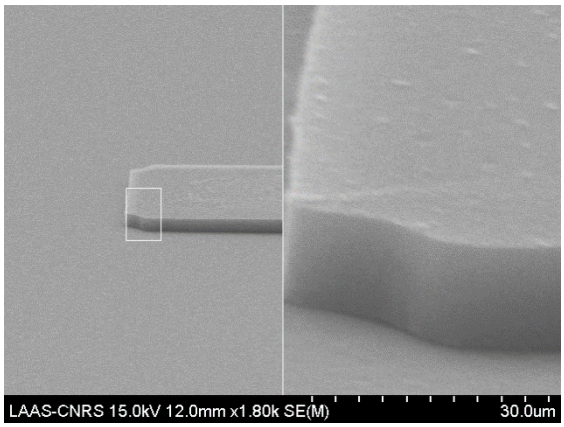

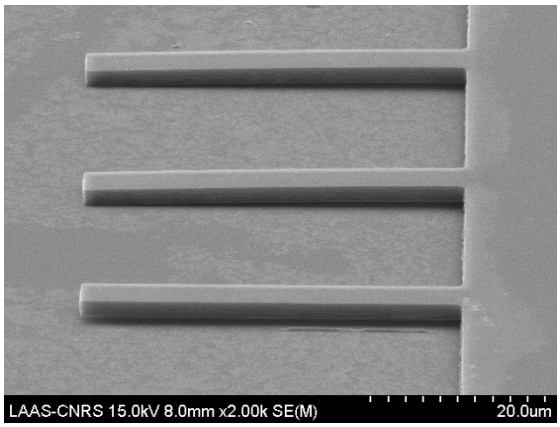

A.2.2 No released structures (necessary to optimize HF etching time, however it is also important to avoid over etching).

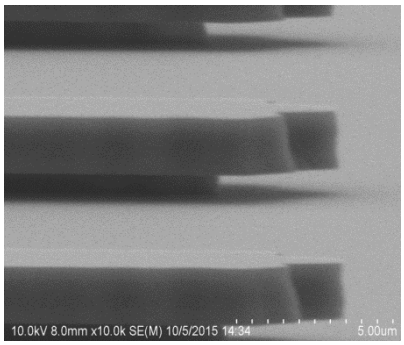

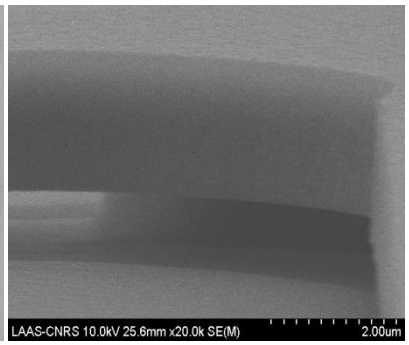

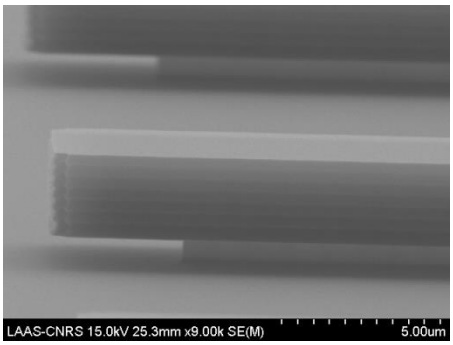

A.2.3 Bad shaped cantilevers (proximity artifact: diffraction effects during the photolithography process).

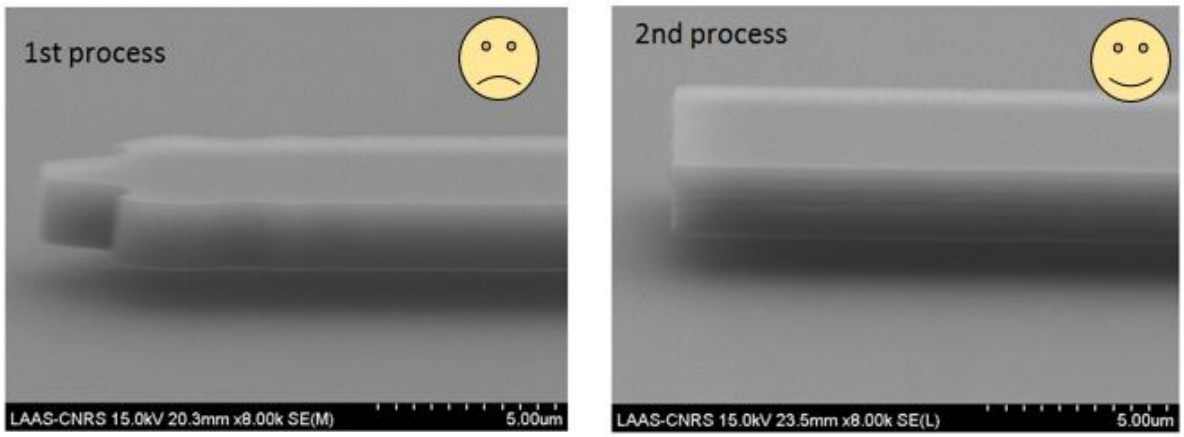

A.3 Low quality SCO deposition

A.3.1 Crystal nucleation and growing of compound 1 due to a bad surface preparation which induces bad untestable and bad quality deposition.

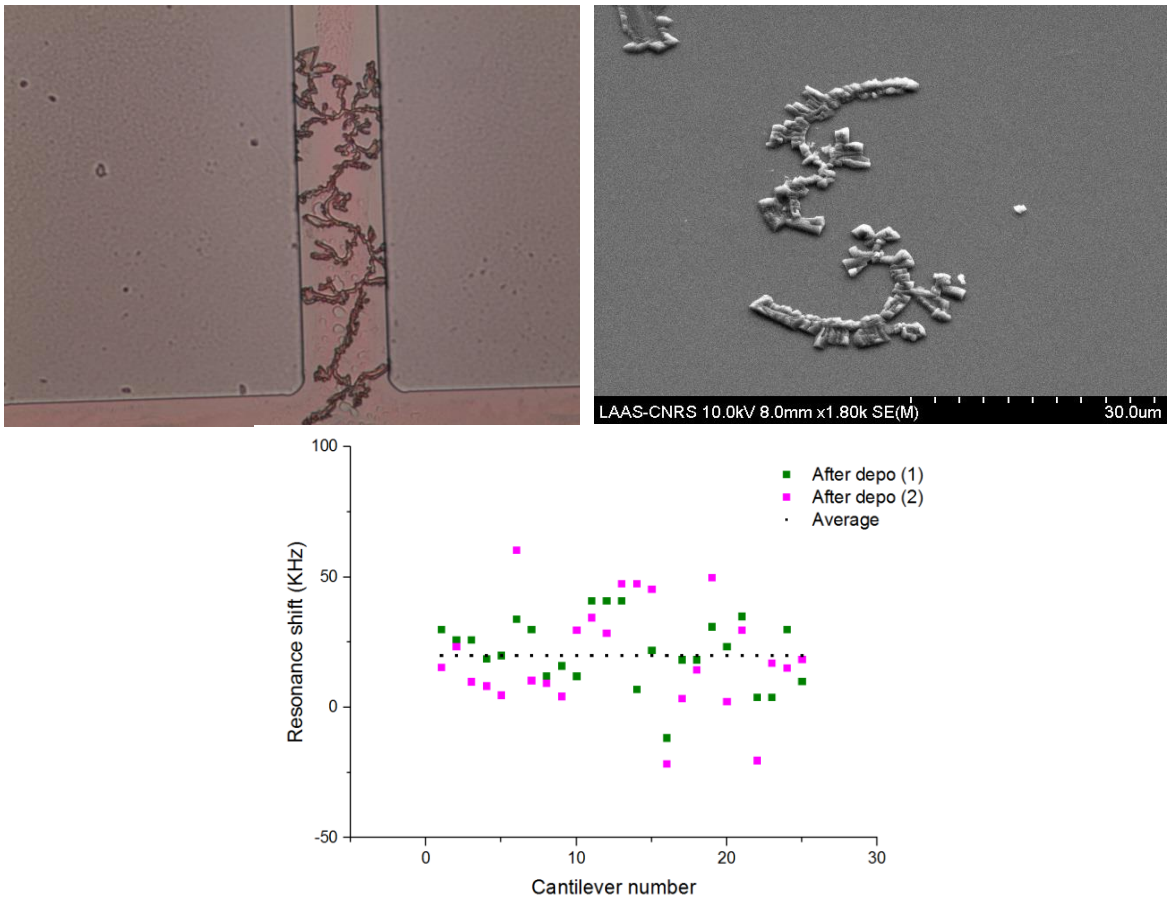

A.3.2 Heterogeneous SCO distribution resulted from spin coating.

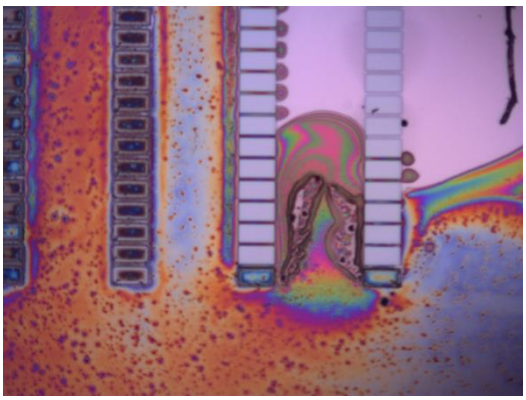

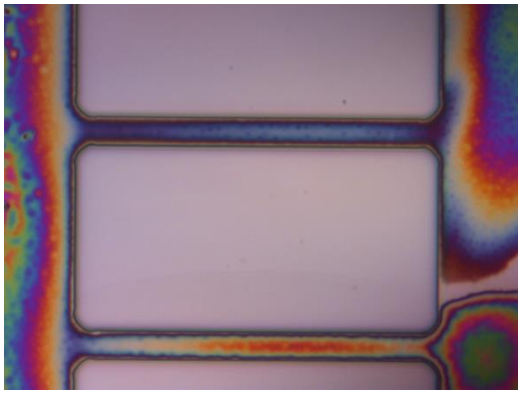

A.3.3 Bad quality deposition obtained by Dip-coating.

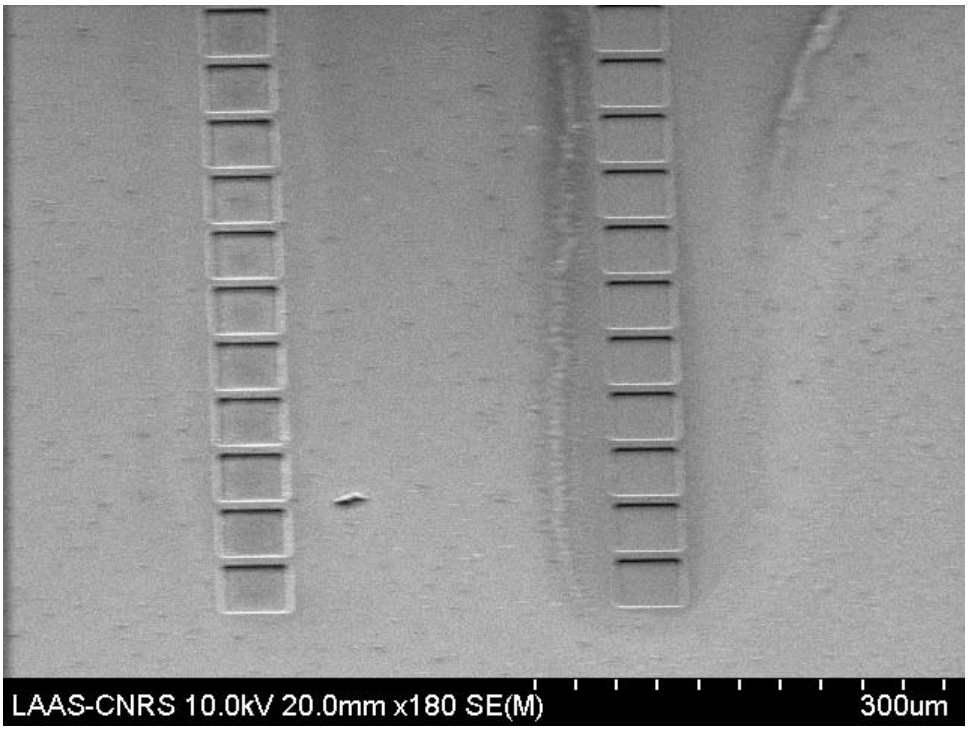

A.4. MEMS-Photoswitch [$Fe^{II}(H_2B(pz)_2)_2(phen)$]

A.4.1-Design of MEMS with integrated piezoelectric detection.

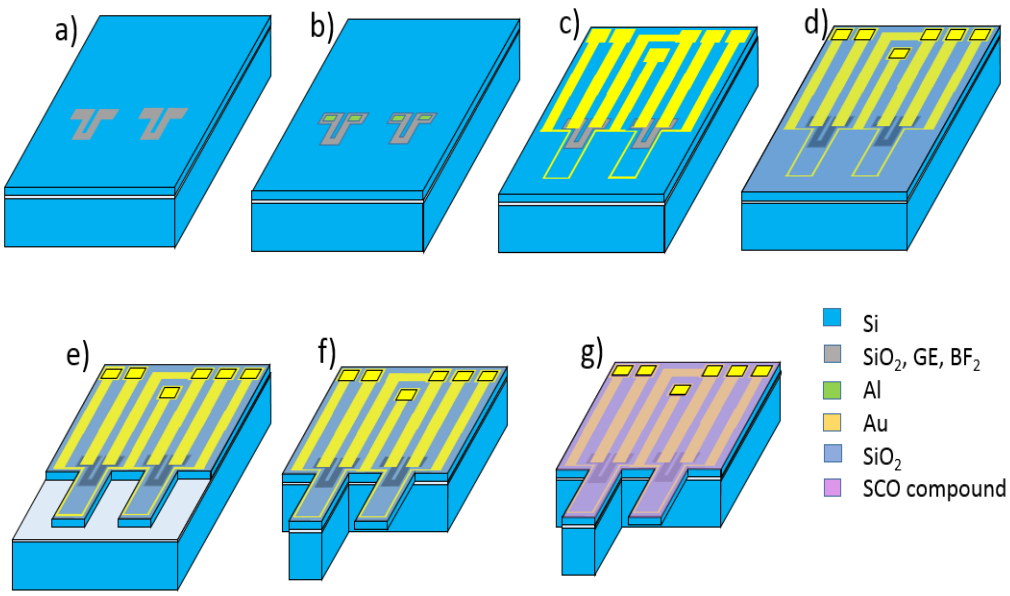

A.4.2-Scheme of VNA card

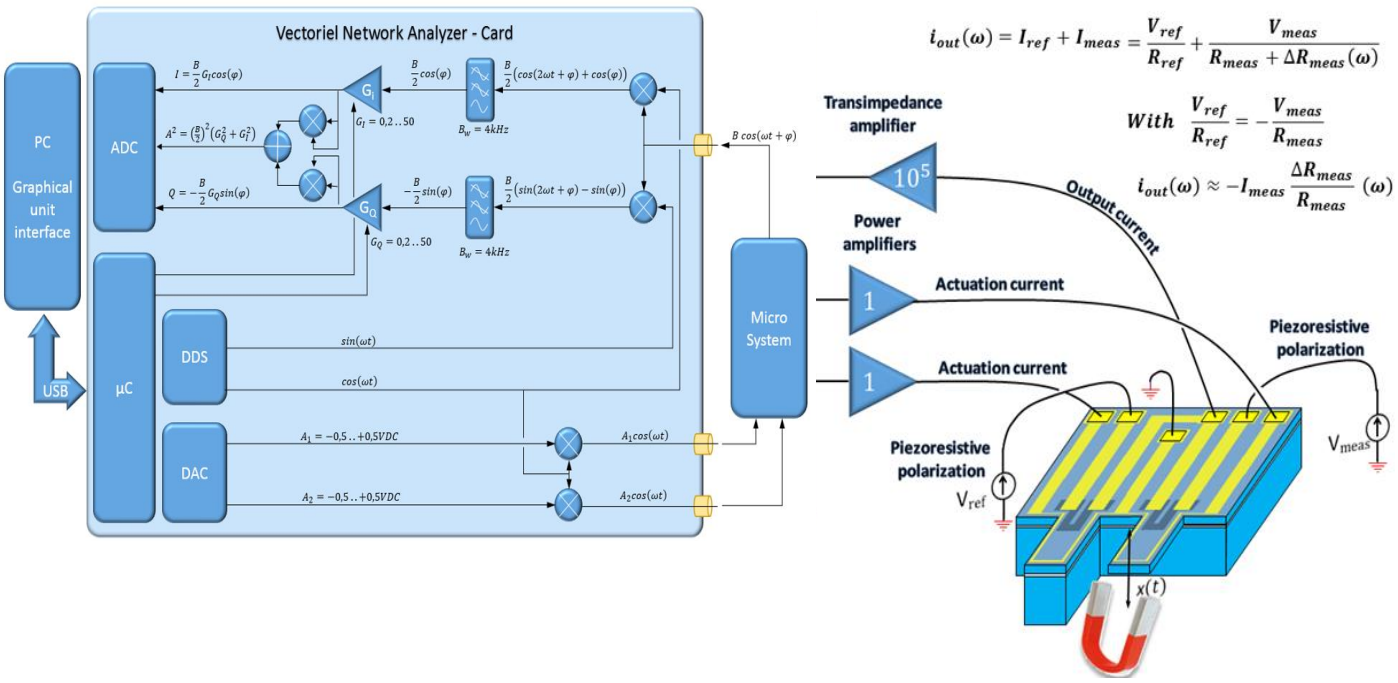

A.4.3 Photoinduced SCO using MEMS at 7 K:

Resonance frequency tracking of the MEMS at 7 K, upon successive light irradiation cycles (ON and OFF) for a device coated with a 200 nm thick of **1**, Δf_r^{LIESST} and Δf_r^{T} stand for the frequency shifts induced by the light induced spin-state switching (LIESST) and photothermal effect respectively.

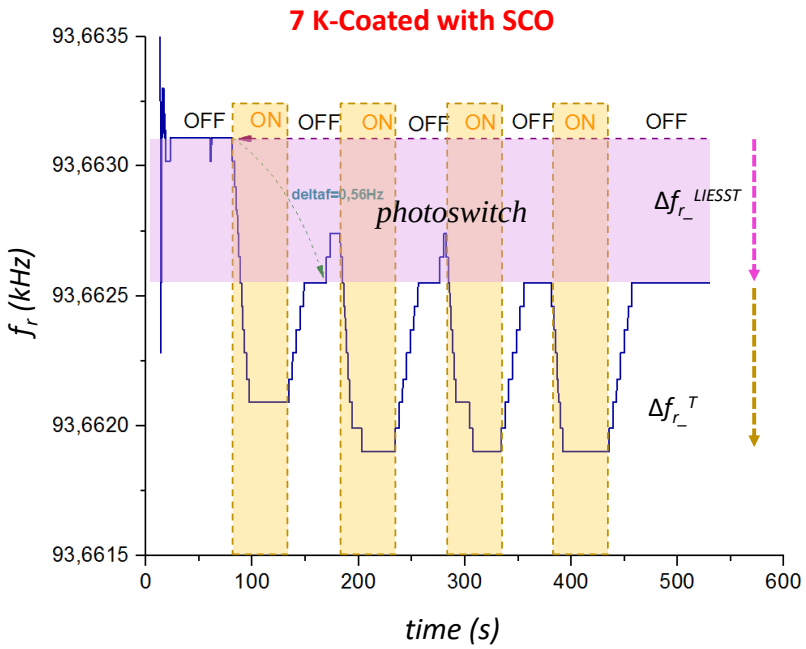

A.4.4 Light Contribution at different T (with and without SCO material)

It was observed that the resonance shift due to the light irradiation is not the same at different temperatures and it is not related to the magnitude of the resonance frequency neither. These observations are important since the mechanical response of the global system at a given temperature could play an important role related to the magnitude of the resonance frequency shifts under the SCO. Therefore the slight differences between the resonance shift at 7 K (0.56 Hz) and 10 K (0.52 K) may be as consequence of this phenomenon.

In the case of light it is observed a relationship with the slope of the resonance at each temperature. Both of them has similar tendency (this is true in the case of uncoated cantilevers). In the case of the cantilevers coated with SCO compound, the slope at each temperature was plotted and the corresponding shift produced by the light should be at least 3Hz but we can observe a shift less than 1 Hz for 5, 7 and 10 K. For a similar cantilever are obtained these shifts values between 290-75K in this range it seems to be in agreement with the slope tendency of its resonance curve.

A.4.4.1 Slope and Light Shifts at different temperatures for uncovered (left) and covered (right) with compound **1**.

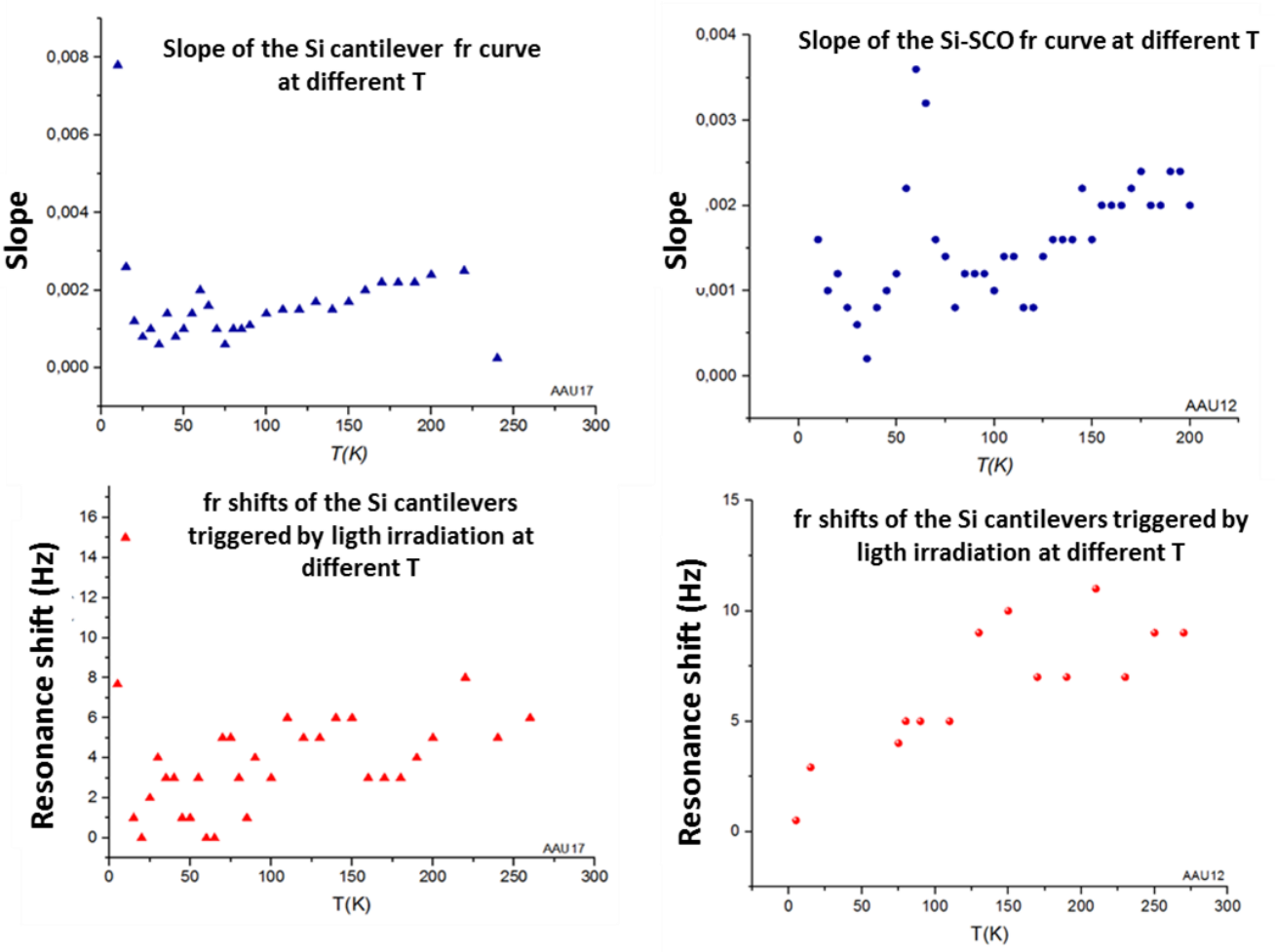

A.4.4.1 Photoresponse of MEMS (f_r) at room temperature when the light irradiation intensity (I) is tuned.

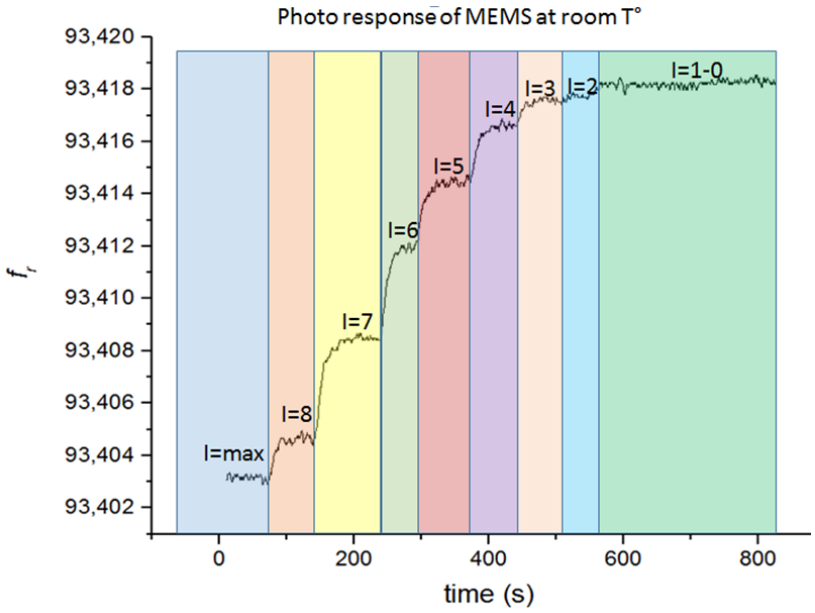

A5. MEMS integrating $[Fe^{II}(HB(tz)_3)_2]$ compound

A5.1 Films characterization

A5.1.1. Selected AFM images of crystalline films obtained by solvent vapour annealing: (a)-(b) two different zones of 90 nm film; (c) 90 nm film after 3 months of storage in ambient air;(d) 150 nm film with roughness 2.5 nm; (e) film thickness evaluation.

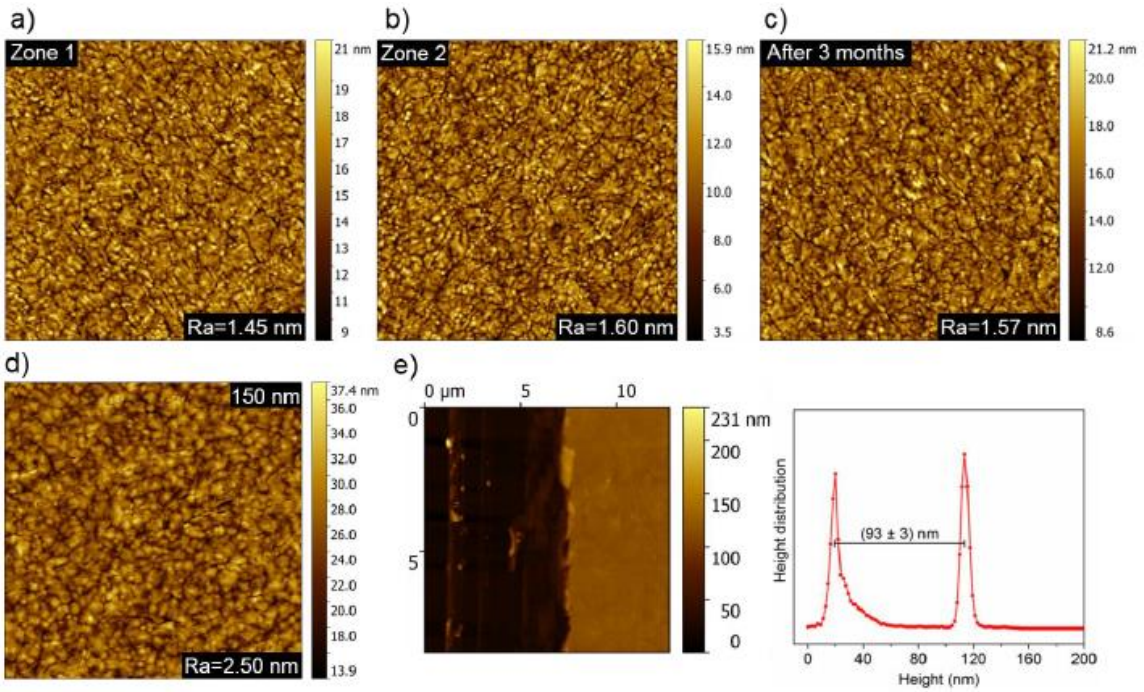

A5.1.2 Evaluation of the degree of crystallinity and the completeness of the spin transition in the films. The graph shows the variation in absorbance between the LS and HS states ($Abs_{LS}$$Abs_{HS}$) for various film thicknesses. The black squares correspond to the experimentally measured values, while the red line corresponds to the theoretically expected values for a fully complete spin transition. This evaluation is based on the assumption that the 194 nm film displays a complete spin transition, which was inferred from the temperature dependent Raman analysis of this film.

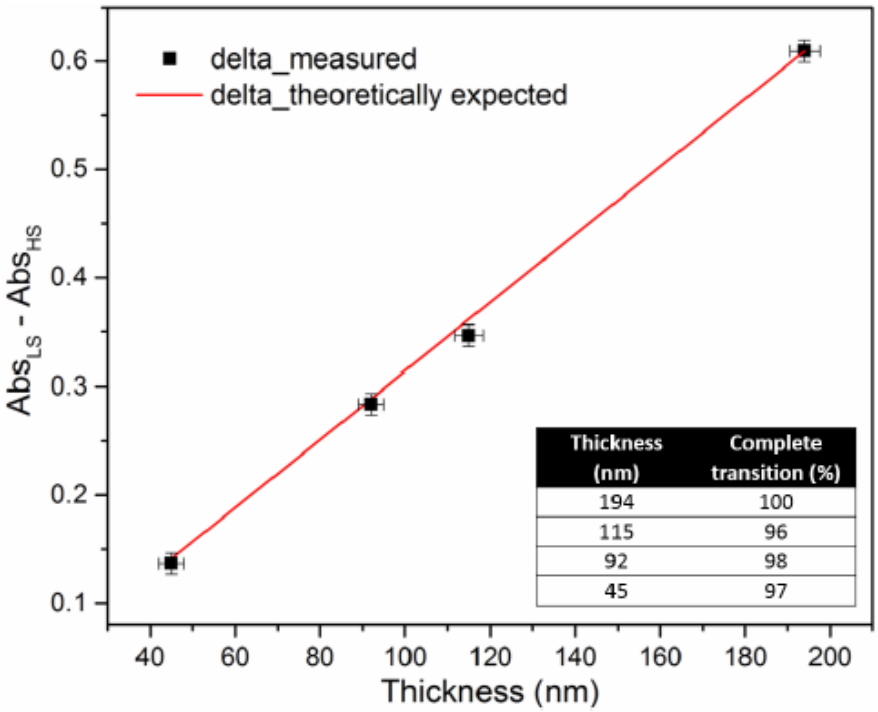

Thickness (nm)	Complete transition (%)
194	100
115	96
92	98
45	97

A5.1.3 XRD patterns of solvent annealed films on different substrates (fused silica, single crystalline silicon and polycrystalline gold).

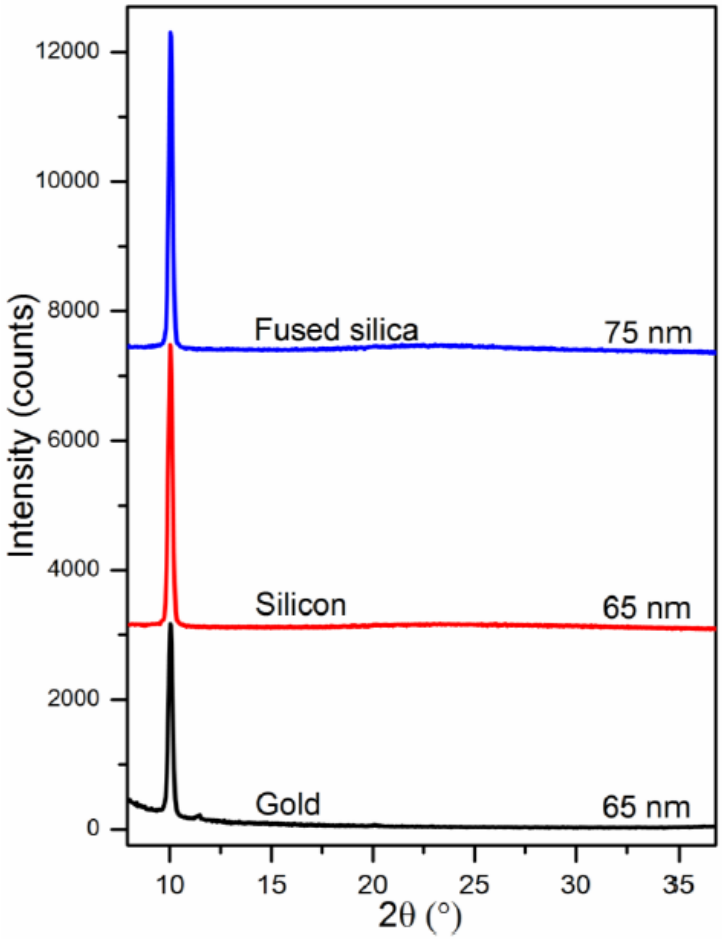

A5.1.4. Temperature dependence of the absorbance at 317 nm along four heating-cooling cycles recorded at 1 K/min scan rate for films with thickness of 45 nm (a) and 194 nm (b).

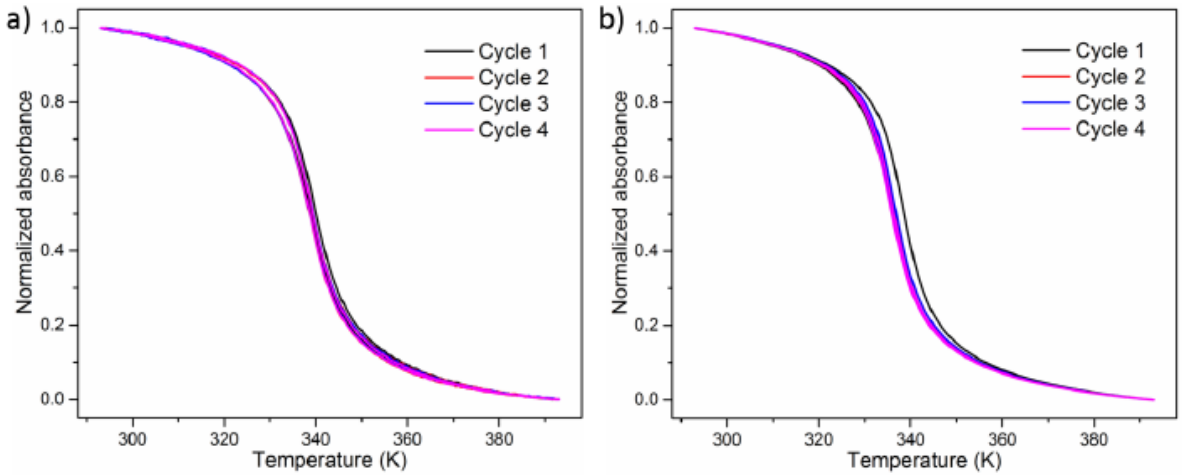

A5.2 MEMS: SCO detection and actuation by thermal energy

A5.2.1 Resonance frequency on heating and cooling of MEMS devices before and after the SCO film.

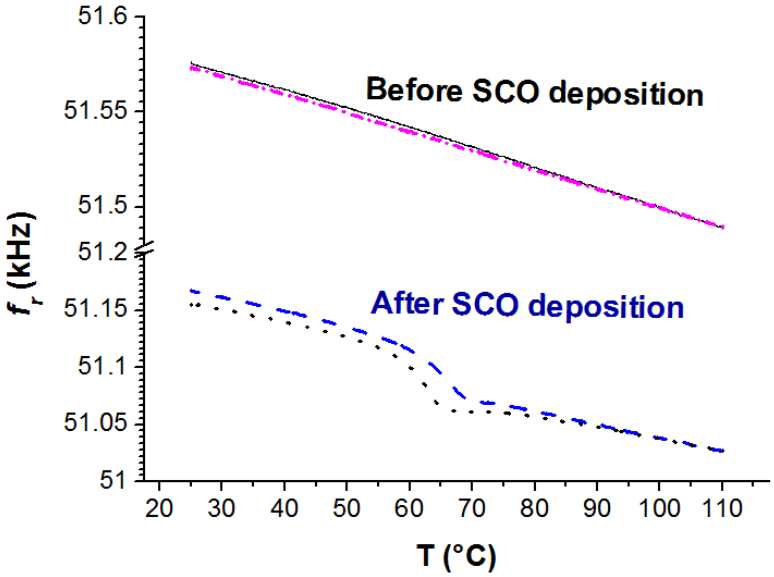

A5.2.2 Static response upon two cycles heating-cooling of MEMS devices with and without deposition of compound **2**.

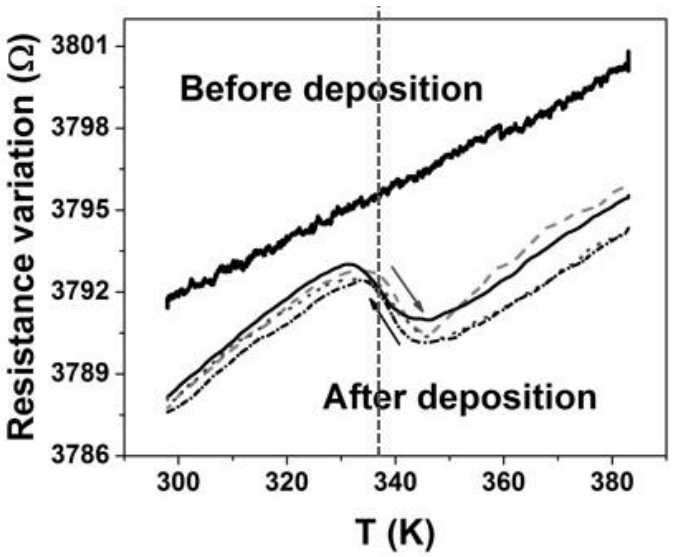

A6. MEMS and artificial muscles based on SCO-polymer nanocomposites

A6.1 Stacking a-c) and surface degradation d-f) of 3 particles.

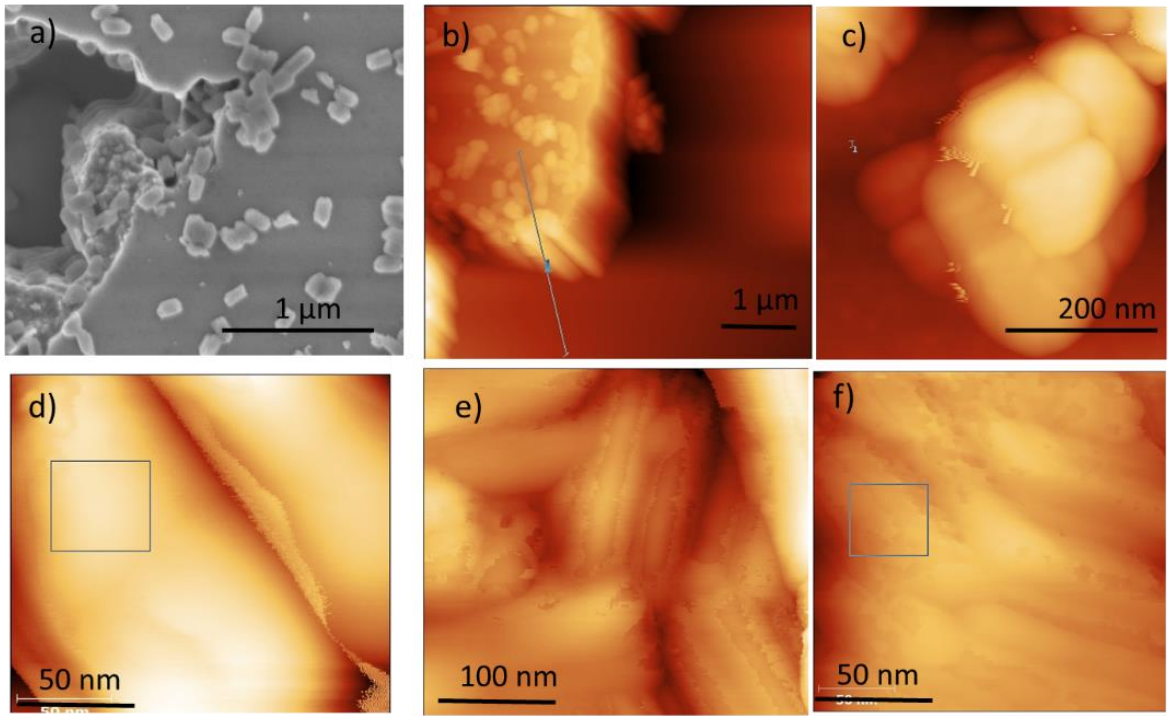

A6.2. AFM images 3 aquired during a complete thermal cycle, from left to right: LS(353K); HS (358K) and LS(353K)states.

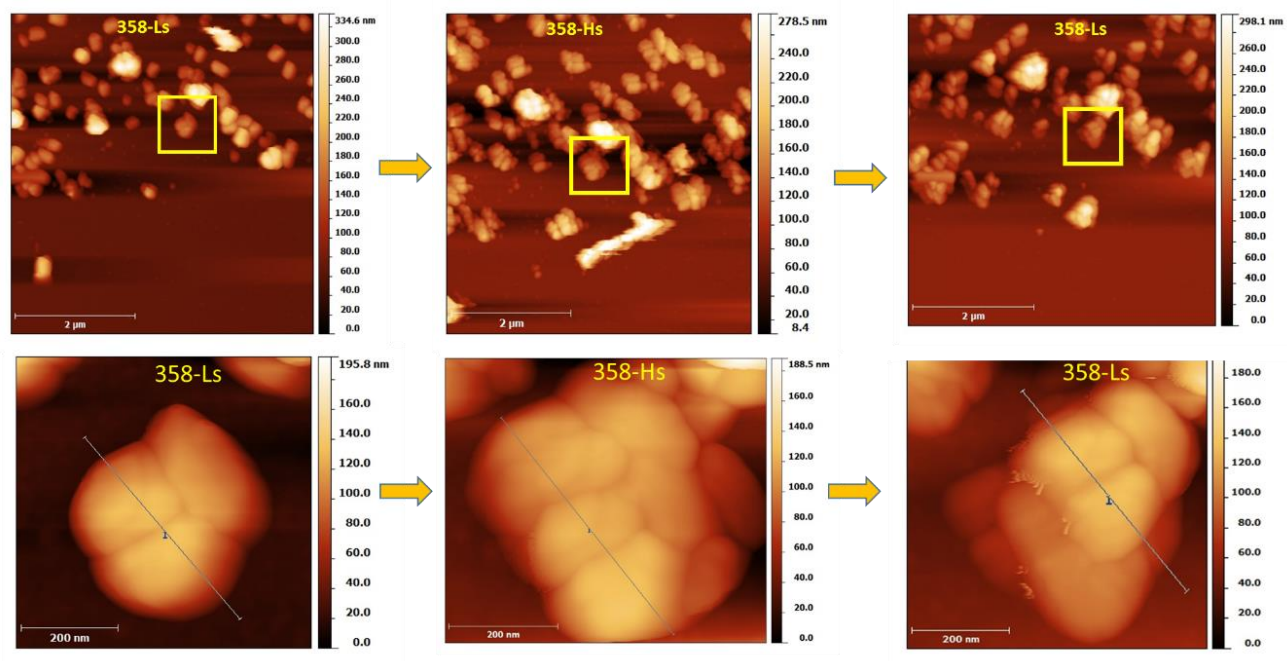

A6.3 Hysteresis curve at 30 wt% of SCO-SU8 nanocomposite upon the three first thermal cycles at 2 K/ min measured by optical absorbance vs. temperature.

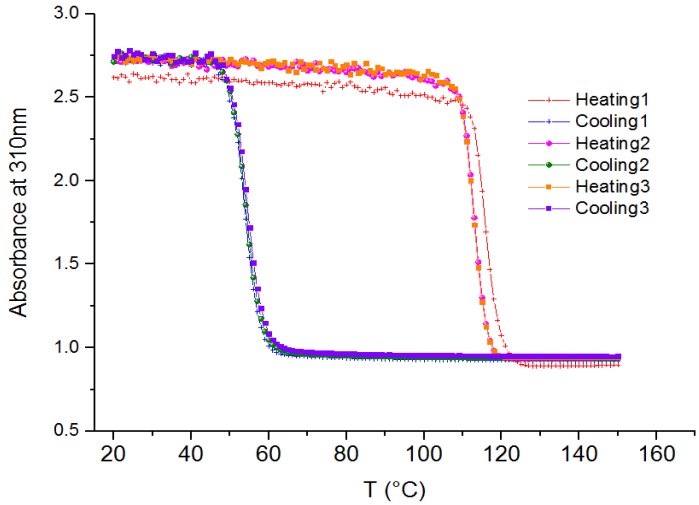

A6.4 Optical reflectivity vs. temperature measurements for the bare SCO and the nanocomposite. They were submitted together at different temperature ramps (1 K/min, 3 K/min and 5 K/min). For each set of experiments fresh powder and film were used.

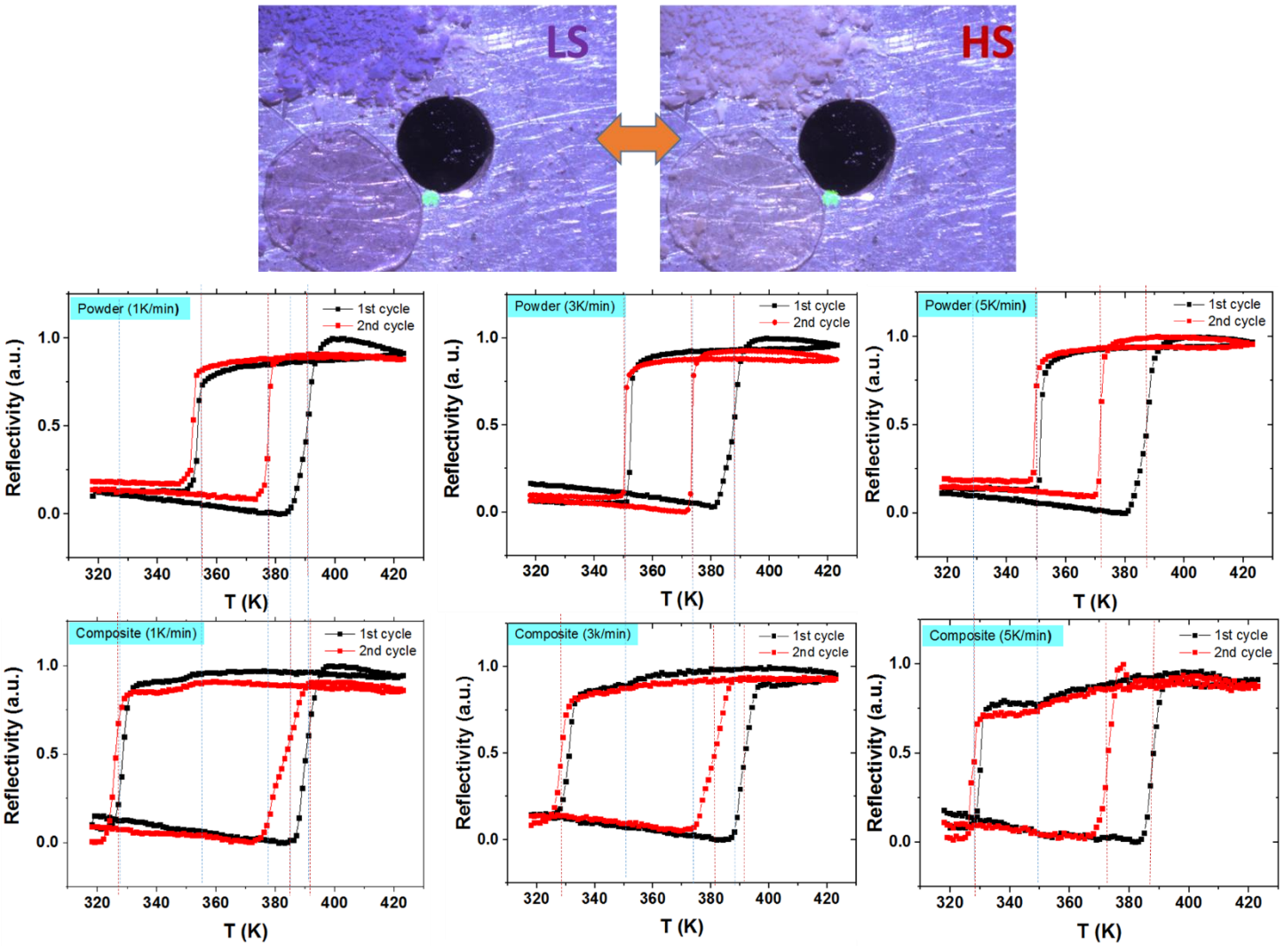

A6.5 Zoomed FT-IR spectra of SCO nanoparticles of **3** (black line), the SU8 polymeric matrix (blue line) and the SCO-SU8 nanocomposite (red line) at room temperature. In the case of the nanocomposite, some vibrational modes of the SCO nanoparticles are hidden by the matrix as consequence of the particles concentration. Nevertheless other bands result shifted to higher wavenumbers in the case of the composite respect to the powder (dashed vertical lines).

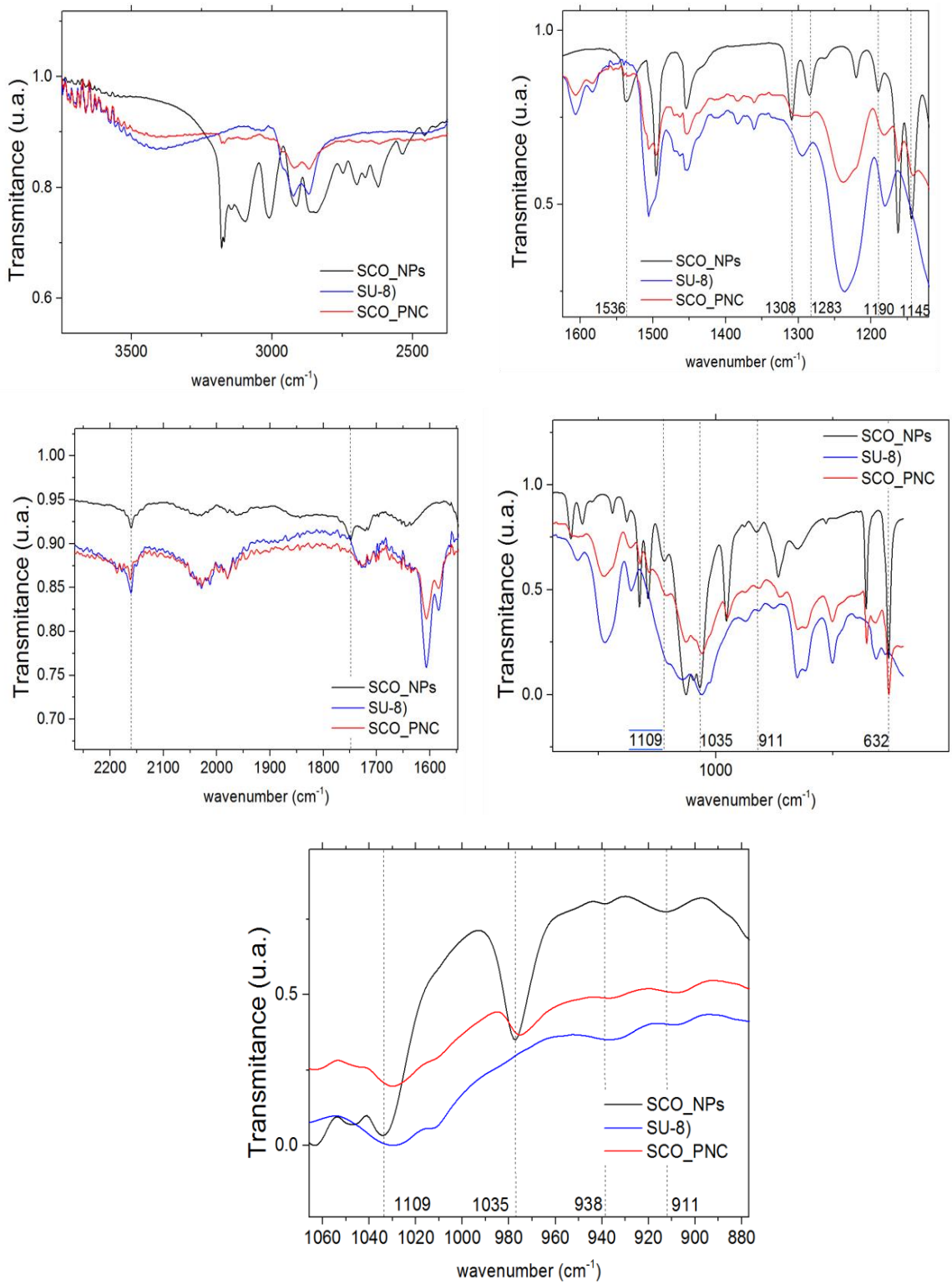

A6.6 Three first cycles of the thermomechanical response (resonance frequency, quality factor and static response) of SCO-SU8 polymer nanocomposites detected using MEMS b-d) compared with optical absorbance measurements a).

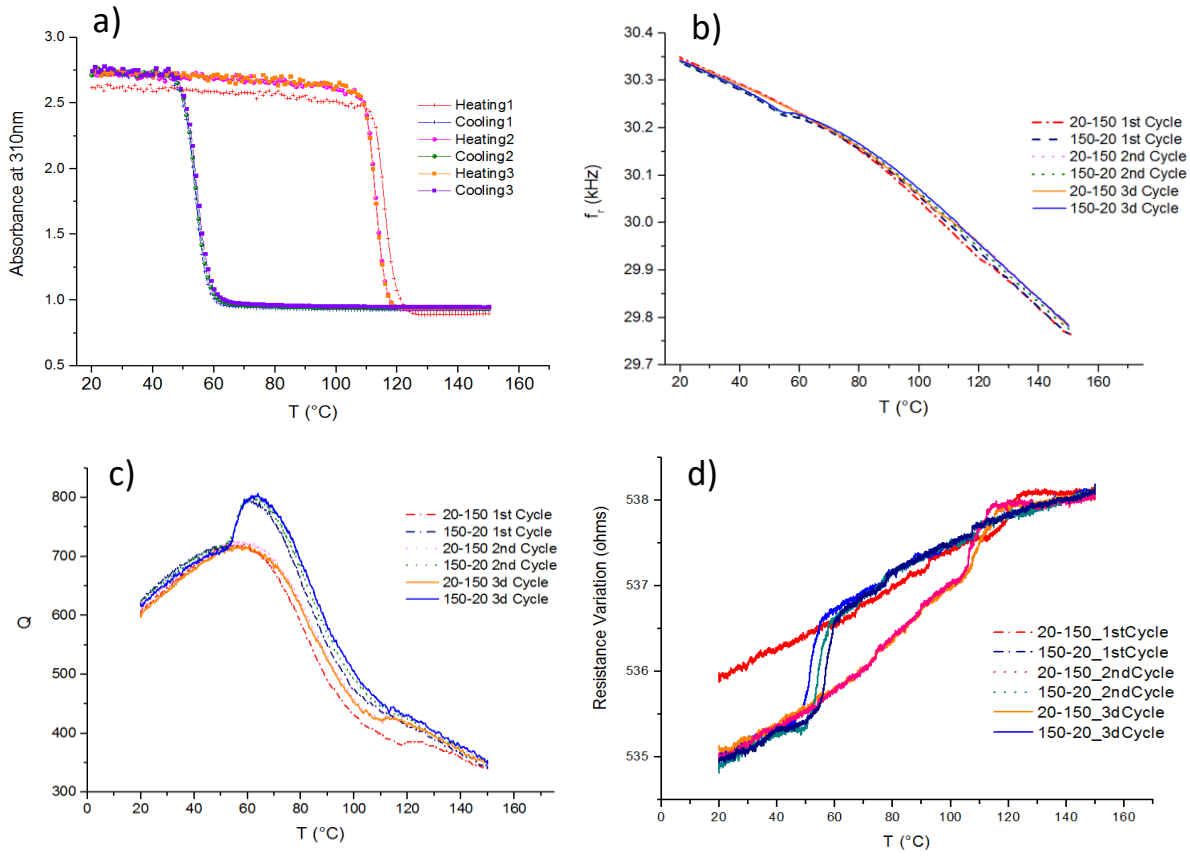

A6.7 Comparison of the thermomechanical dynamic response of MEMS coated with SU8 and SU8-SCO nanoparticles.